Collective Radiation of Coupled Atomic Dipoles and the Precise Measurement of Time

Dissertation
zur Erlangung des akademischen Grades
Doctor of Philosophy

eingereicht an der

Fakultät für Mathematik, Informatik und Physik
der Leopold-Franzens-Universität Innsbruck

von

Mag. rer. nat. Laurin Ostermann

Betreuer: Univ.-Prof. Dr. Helmut Ritsch, Institut für Theoretische Physik

Innsbruck, Juni 2016

Abstract

Ultracold optical lattice atomic clocks have made it to the forefront of timekeeping and spectroscopy over the last decade. A prominent example, that features a relative precision of $2 \cdot 10^{-18}$ in the measurement of one second, is the ^{87}Sr lattice clock at NIST in Boulder, CO. A plethora of fundamental shifts and perturbations has been successfully dealt with in order to arrive at such an admirable measurement accuracy. Yet, there are still phenomena that have not played a limiting role so far, but will become prevalent in the next decade. One of these is dipole-dipole interaction, which constitutes the main subject of this work.

Quantum emitters in close proximity to each other can exchange energy through free space vacuum modes and thus feature shifts and altered spontaneous emission rates in their collective states. Collective spontaneous emission exhibits a drastically different behaviour than emission from a single source: constructive interference can lead to increased spontaneous emission rates, i.e., superradiance, and destructive interference to decreased rates, i.e., subradiance, respectively. As these emission processes are stochastic they constitute a fundamental, inherently uncontrollable perturbation in spectroscopy setups such as atomic clocks.

In this work, we investigate the effect of super- and subradiance on to the Ramsey signal obtained from interacting quantum emitters with a particular focus on ^{87}Sr. We show that even small numbers of atoms at high densities can lead to large detrimental effects on precision. Consequently, we suggest an alteration to the Ramsey measurement scheme, where we use phase separation between the individual emitters in order to replace their superradiant behaviour by a subradiant one. This allows for a vast increase in probing time and ultimately a much better sensitivity in the spectroscopic procedure. We investigate our proposed technique for larger systems and find that the increase in probing time scales almost exponentially with the system size, indicating promising results for clock setups.

Furthermore, we develop a procedure that allows subradiant states to be prepared directly as opposed to preparing them by phase alteration. We use phase imprinting in the excitation laser or a large magnetic field gradient to realize almost perfect Rabi oscillations between the collective ground state and the slowest decaying, most subradiant, states in the single- and double-excitation manifold.

And, we employ our findings to study a superradiant laser, whose active medium is given by atoms sitting in a magic wavelength optical lattice. Here, we find that, at magic wavelength distance, the negative effects of dipole-dipole interaction can be largely ignored, while they become prominent at smaller lattice constants.

In additional research conducted during my doctoral studies, we use a mean-field treatment to calculate collective shifts and rates for realistically large systems of emitters in various geometries and find that square or hexagonal lattices seem to suppress collective emission, i.e., feature subradiance, the most.

In a conceptually similar fashion, closely collaborating with the Innsbruck-based experimental photonics group, we investigate emission properties from a quantum dot, where exciton and biexciton emission form a cascade of decay. This setup is aimed at creating time-bin entangled photons, yet other procedures like a Rabi oscillation or a Ramsey scheme have been implemented as well.

Zusammenfassung

Über die letzten Jahrzehnte wurden Atomuhren, die auf ultrakalten Atomen in optischen Gittern basieren, zur Speerspitze der Zeitmessung und der Spektroskopie. Ein sehr prominentes Beispiel dafür ist die ^{87}Sr-Gitteruhr am NIST in Boulder, Colorado, mit der sich eine relative Messgenauigkeit von $2 \cdot 10^{-18}$ bei der Messung einer Sekunde erzielen lässt. Um diese beinahe unvorstellbare Genauigkeit zu erreichen war es notwendig, eine Vielzahl von störenden Effekten zu beachten und erfolgreich zu kontrollieren. Es gibt allerdings weitere Phänomene, die in den nächsten Jahren für eine erneute Verbesserung der Gitteruhren relevant sein werden, wenn sie auch bis heute noch keine allzu große Rolle spielen. Eines dieser Phänomene ist die Dipol-Dipol-Wechselwirkung, das Hauptaugenmerk dieser Arbeit.

Kollektive Zustände individueller Quantensysteme, die sich räumlich sehr nahe beieinander befinden, können durch Energieaustausch mittels Vakuummoden des freien Raums, Energieverschiebungen oder veränderte spontane Emissionsraten ausbilden. Kollektive Emission verhält sich dabei im Vergleich zu Emissionen von Einzelquellen sehr unterschiedlich: konstruktive Interferenz kann zu erhöhten spontanen Emissionsraten, der sog. Superradianz, führen, während destruktive Interferenz in verringerten Raten, der Subradianz, resultiert. Nachdem es sich bei diesen spontanen Emissionen um stochastische Prozesse handelt, die intrinsisch unkontrollierbar sind, stellen sie eine fundamentale Schranke für die Spektroskopie und damit für Atomuhren dar.

Diese Arbeit untersucht die Auswirkungen von Super- und Subradianz auf das Ramsey-Signal eines Ensembles von wechselwirkenden Quantensystemen, wobei wir einen Fokus auf ^{87}Sr legen. Wir zeigen, dass sich sogar bei einer kleinen Anzahl von Atomen hoher Dichte nachteilige Effekte feststellen lassen. Daher schlagen wir ein verändertes Ramsey Messschema vor, indem wir Phasenseparation zwischen den einzelnen Quantensystemen ausnutzen, um superradiantes Verhalten durch subradiantes zu ersetzen. Dadurch erreichen wir einen beachtlichen Zuwachs der Interrogationszeit und letztlich eine verbesserte Sensitivität der spektroskopischen Prozedur. Wir untersuchen die vorgeschlagene Technik für größere Systeme und stellen fest, dass sich der Gewinn in der Interrogationszeit beinahe exponentiell zur Systemgröße verhält, ein vielversprechendes Ergebnis für Atomuhren.

Des weiteren entwickeln wir ein Verfahren, mit dem sich subradiante Zustände direkt präparieren lassen, anstatt diese durch Veränderungen der Phasen zu erzeugen. Mittels einer im Anregungslaser eingeschriebenen Phase oder eines Magnetfeldgradienten lassen sich beinahe perfekte Rabi-Oszillationen zwischen dem kollektiven Grundzustand und den am langsamsten zerfallenden, den subradiantesten, Zuständen im Subraum von

ein und zwei Anregungen erreichen.

Außerdem untersuchen wir einen superradianten Laser, dessen aktives Medium durch in einem 'magic wavelength' Gitter befindliche Strontium-Atome gegeben ist. Wir zeigen, dass negative Effekte durch Dipol-Dipol-Wechselwirkung bei einem magic wavelength Gitter nahezu vernachlässigt werden können, während sie bei kleineren Gitterabständen relevante Störungen darstellen.

In weiteren Forschungsarbeiten, die während meines Doktorats entstanden sind, benützen wir einen molekularfeldtheoretischen Formalismus, um Frequenzverschiebungen und Zerfallsraten in realistisch großen Systemen unterschiedlicher Geometrien zu berechnen. Es zeigt sich dabei, dass quadratische und hexagonale Gitter spontanen Zerfall am besten zu unterdrücken scheinen, also am ehesten subradiante Zustände ausbilden.

In einer konzeptionell verwandten Arbeit untersuchen wir, gemeinsam mit experimentellen Photonikern, Emissionseigenschaften eines Quantum Dot, in dem Exziton- und Biexziton-Emissionen eine Zerfallskaskade bilden. Dieser Aufbau dient vornehmlich zur Erzeugung von zeitgeordnet verschränkten Photonen, wobei auch andere Prozeduren, wie Rabi-Oszillationen oder ein Ramsey-Schema, umgesetzt werden konnten.

Danksagung

In erster Linie bedanke ich mich herzlich bei Prof. Helmut Ritsch für seine exzellente Betreuung meiner Arbeit, sein offenes Ohr für Ideen und Diskussionen, das tolle und entspannte Klima in seiner Arbeitsgruppe und für seine kollegiale Art. Des Weiteren möchte ich Dr. Claudiu Genes, der viele meiner Arbeiten mitbetreut hat, meinen Dank für sein unermüdliches Motivieren und die vielen erkenntnisreichen Diskussionen aussprechen. Auch das ein oder andere Feierabend-Bier, bei dem unsere Unterhaltungen manchmal auch etwas von der Physik abwichen, sei hier erwähnt.

Ich bedanke mich bei allen anderen aktuellen und ehemaligen Mitgliedern der Ritsch-Gruppe, die mich während meiner Dissertation begleitet haben: Wolfgang Niedenzu, Matthias Sonnleitner, Raimar Sandner, Kathrin Sandner, Tobias Grießer, Erez Boukobza, Francesco Piazza, Stefan Ostermann, Valentin Torggler, Daniela Holzmann, Dominik Winterauer und ganz speziell bei meinen Koautoren Hashem Zoubi, David Plankensteiner, Thomas Maier und Sebastian Krämer. Die vielen Stunden, die ich mit Euch in den letzten Jahren mit und auch abseits der Physik verbracht habe, haben mich sehr geprägt. Ein besonderes Danke richte ich an Wolfgang und David für ihre Kommentare und das Korrekturlesen. Auch Kollegen aus anderen Gruppen, speziell Prof. Gebhard Grübl und Markus Penz, Prof. Gregor Weihs, Ana Predojevic, Tobias Huber und Maximilian Prilmüller, sowie meinen Kommilitonen Stefan Huber, Stefan Walser, Daniel Plörer, Alex Murr und Florian Pranger sei gedankt.

Auf privater Seite sei als allererstes meine Familie erwähnt. Meinen Eltern Rudolf und Hildegard danke ich von ganzem Herzen für ihre moralische und materielle Unterstützung und vor allem dafür, dass sie mich überhaupt Physiker werden ließen. Ebenso danke ich meinen Großeltern Hermann und Elfriede sowie meiner Großmutter Thekla. Auch meiner Schwester Teresa möchte ich herzlich danken, nicht zuletzt dafür, dass sie mich hin und wieder zur Selbstreflexion animiert. Ich danke Nicole für unsere gemeinsame Zeit.

Stellvertretend für all meine Freunde möchte ich Leo Gruber für unsere gemeinsamen Erlebnisse, sein offenes Ohr im Wissenschaftlichen, Politischen, Gesellschaftlichen und Privaten meinen aufrichtigen Dank und meine Anerkennung ausdrücken. Ohne Dich, ohne Euch, würde ich mich nicht halb so wohl fühlen!

Ich danke allen Komusikern in meinen Bands Tapedeck, Nova Cosmos, Parasoul, Kings of the UK, David Blum & Band und Farbarena sowie in allen Projekten für die beizeiten notwendige Ablenkung von der Physik und die phantastischen Momente, die wir gemeinsam im Proberaum, auf Tour, auf der Bühne und an Backstage-Bars verbringen durften.

Abschließend möchte ich meiner erweiterten Familie, allen meinen Freunden, Arbeitskollegen, Mitmusikern und allen anderen Wegbegleiterinnen und Wegbegleitern danken, die nicht explizit erwähnt wurden.

Contents

1 General Introduction

In this thesis we analyze the effect of dipole-dipole interaction on the measurement precision in ultracold optical lattice atomic clocks. We suggest and study an improvement to the standard measurement procedure, that can lead to a superior accuracy. We investigate a close cousin of optical lattice clocks, namely a superradiant laser, where the same physics is present, but used to build a laser with a very narrow linewidth. Some other related subjects, like state preparation or optimizing geometries, are touched as well.

1.1 Historical Introduction

Measuring and keeping time has always been a crucial capability for humanity. From ancient cultures to the modern day, having an accurate sense of time has been of great importance. Be it in simple every-day life, communication, navigation, or even warfare, knowing the time and having it synchronized among multiple places has been the key to carrying out all these efforts.

Departing from very simple observations of the stars and the earth's relative orientation towards the sun throughout a day, early cultures soon constructed more involved clocks and could tell the time of the day fairly precisely. During the epoch of renaissance and also in the age of enlightenment great advances in terms of clocks were made. Mechanical oscillators with springs or pendulums came into play. In the last century, two significant discoveries lead to an even more accurate measurement of time: first, the piezo-electric properties of quartz were found, which allowed for building clocks that would surpass the mechanical devices by orders of magnitude and secondly, the insight that electronic transitions in atoms could be used as frequency standards.

This lead to the construction of atomic clocks with a first proof of concept experiment in 1949 and a working device shortly thereafter. Atomic clocks advanced in their precision over the last decades, with more and more perturbations accounted for and corrected, and every so steadily increasing experimental and technical skill. Ultimately, we stand at a level of a relative precision of $2 \cdot 10^{-18}$ in the measurement of one second in current state of the art Strontium optical lattice clocks.

At this level, fundamental interactions among the atoms start to constitute perturbations that need to be dealt with. One of these is dipole-dipole interaction and its resulting collective decay, the main focus of the present thesis. Through the inherent

coupling of electronic transition dipoles to the free space vacuum modes of light, a coherent and dissipative exchange of energy amongst them is possible. In this work, we focus on understanding and quantifying the phenomenon as well as investigating possibilities to exploit it in order to help increase the clock precision even further.

1.2 Motivation

As stated above, the prime motivation for this work is contributing to an increase in measurement precision in ultracold optical lattice atomic clocks. At a relative uncertainty of about 10^{-18}, one fundamental perturbation is constituted by energy exchange and collective spontaneous emission facilitated through the interaction among atomic transition dipoles.

Depending on the geometry of the clock setup, dipole-dipole interaction can have various, almost diametrically opposite, effects. Generally, apart from the shift of collective electronic levels mediated by coherent dipole-dipole energy exchange, the phenomena of super- and subradiance start to appear. Superradiance is the result of constructively interfering spontaneous emission and features an overall increased collective spontaneous emission rate, that can be as large as N^2 times the single emitter decay rate with N being the number of interacting emitters. On the other hand, subradiance due to destructive interference can facilitate an almost zero effective decay rate, yielding extremely long-lived states. It is important to realize that both these processes are stochastic and thus, a precise control over them is inherently impossible. Therefore, the concrete aim lies in reducing the negative effects of the collective spontaneous emission on the measurement as far as possible.

In that fashion the idea to use subradiant collective states in order to increase the precision in optical lattice clocks could be viewed as the main goal of this work. A thorough study of the consequences of super- and subradiance in clock systems precedes this goal and various other investigations around it, e.g., its scalability, its feasibility and suggestions for implementations need to be performed as well.

1.3 Outline of this Thesis

We begin by briefly introducing the mathematical formalism and the concepts that we need to perform quantum mechanical and quantum optical calculations. This provides the framework for all the investigations we carry out in the course of this work.

In chp. 3 we move on to time keeping and atomic clocks in particular. We shortly discuss time keeping in general and give a historical overview of how time has been measured throughout the ages, finally arriving at atomic clocks and optical lattice clocks. We discuss their setup and their limitations in detail and conclude with a description of the Ramsey measurement technique, that sits at the heart of atomic

clocks.

Chapter 4 is devoted to the phenomenon of spontaneous emission. We begin with a heuristic treatment following Einstein's original work and transition to quantum electrodynamics and consider the spontaneous emission from a single quantum emitter as well as from an ensemble of emitters, which ultimately forms the basis for a large part of our investigations. Here, dipole-dipole interaction is introduced and we discover super- and subradiance, which is discussed in great detail for two emitters and will be generalized in the following chapters.

Moving on to the publications that make up this thesis, chp. 5 studies super- and subradiance at the example of extended toy models. In addition, this paper highlights the effect of dipole-dipole interaction and collective decay to the Ramsey measurement scheme. The next publication, presented in chp. 6 suggests an alteration of the Ramsey measurement technique, employing subradiant states, which allow for a longer interrogation time and ultimately an increased measurement precision. This investigation is continued in chp. 7, where the focus lies on scaling laws and implementations of the suggested technique.

Next, in chp. 8 we look at the possibility to address these subradiant or 'protected' states directly by means of imprinted phases in the excitation or external fields. The last publication, chp. 9 constituting the bulk of this work deals with superradiant lasers, which are methodologically very similar to what we have done before, except for the fact that a cavity and a pump are added.

We round up our findings with conclusions and suggestions for further investigations that could be based upon this work.

Chapter 11 and chp. 12 are two publications that are somewhat connected to the rest of this work, conceptually or methodologically. But they would rather qualify as additional research that was conducted during my doctoral studies. The first deals with optimizing geometries for optical lattice clocks, where a mean-field formalism could be used in order to calculate shifts and collective decay rates for realistically large systems, while in the latter we have investigated emission properties from a quantum dot, largely using the same methods as in the rest of this thesis.

2 Methodological Overview

Before we begin to discuss physical systems, this chapter aims at giving a short summary of the methodological and mathematical background of the research constituting the present thesis. Overall, we deal with open quantum systems and rely on a full quantum treatment of these. Calculations were performed analytically where ever possible, yet larger system sizes or more involved expressions needed to be evaluated numerically. A comprehensive introduction to the methodology can be found in any standard quantum mechanics textbook, e.g. [1–4].

2.1 Systems under Consideration

A large part of this work deals with ensembles of quantum emitters modelled as two-level systems, where the Hilbert space of the ensemble can be written as $\mathcal{H} = \left(\mathbb{C}^2\right)^{\otimes N}$, with N being the number of individual emitters. Each of these two-level systems has two distinct states, one of lower energy and one of higher energy. Usually, we call the lower state the ground state $|g\rangle$ and the upper state the excited or inverted state $|e\rangle$. This is mathematically equivalent to the description of a spin-1/2 system, which we will often use synonymously.

On the level of the individual systems dynamics and measurements can be written by using superpositions of the three Pauli matrices and the identity matrix with

$$\sigma_x = |e\rangle\langle g| + |g\rangle\langle e|\,, \tag{2.1a}$$
$$\sigma_y = i\left(|e\rangle\langle g| - |g\rangle\langle e|\right), \tag{2.1b}$$
$$\sigma_z = |e\rangle\langle e| - |g\rangle\langle g|\,, \tag{2.1c}$$
$$\mathbb{1} = |e\rangle\langle e| + |g\rangle\langle g|\,. \tag{2.1d}$$

Dynamics and observables on the compound systems are then realized by writing down the tensor product of the desired operators in the combined Hilbert space, e.g.

$$S^z = \frac{1}{2}\sum_j \sigma_z^j = \frac{1}{2}\left(\sigma_z \otimes \mathbb{1} \cdots \otimes \mathbb{1} + \mathbb{1} \otimes \sigma_z \otimes \cdots \otimes \mathbb{1} + \dots\right) \tag{2.2}$$

and so on, where any combination of operators can be used. The commutation relation among the individual Pauli matrices can be extracted from the relation

$$\sigma_\alpha \sigma_\beta = i\sum_\gamma \epsilon_{\alpha\beta\gamma}\sigma_\gamma + \delta_{\alpha\beta}\mathbb{1}, \tag{2.3}$$

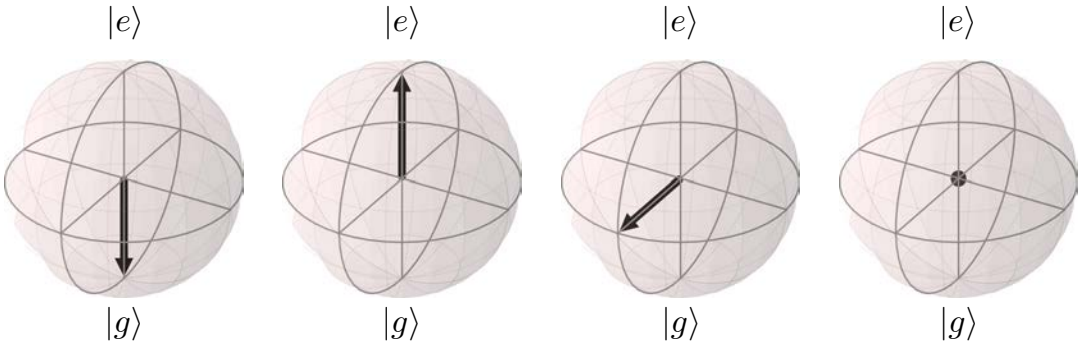

Figure 2.1: *Example of Bloch spheres.* Their south pole represents the ground state $|g\rangle$ and their north pole the excited state $|e\rangle$. The visualized states (from left to right) are the three pure states $|g\rangle$, $|e\rangle$ and $1/\sqrt{2}\,(|g\rangle + |e\rangle)$ as well as the mixed state $|e\rangle\langle e| + |g\rangle\langle g|$.

with the Levi-Civita symbol $\epsilon_{\alpha\beta\gamma}$ and the Kronecker Delta $\delta_{\alpha\beta}$. There are two further, non-Hermitian, operators that we will use frequently, namely

$$\sigma^+ = |e\rangle\langle g| \tag{2.4a}$$
$$\sigma^- = |g\rangle\langle e|\,, \tag{2.4b}$$

the so-called rising and lowering operators.

A typical picture that is used in the context of two-level systems is the Bloch sphere, where the pure state of a system can be visualized as a point on the surface of the sphere and any mixed state will appear as a point inside the sphere. This results from the fact that any (pure) state can be written as

$$|\psi\rangle = \exp(i\varphi/2)\cos(\theta)\,|g\rangle + \exp(-i\varphi/2)\sin(\theta)\,|e\rangle \tag{2.5}$$

with the polar angle θ and the azimuth angle φ. Mixed states will appear as superpositions of projectors onto several pure states. Figure 2.1 depicts different states of a two-level system using Bloch spheres. Besides allowing for the visual representation of the state of a system, Bloch spheres can also be used to visualize dynamics within the system. An operation generated by any of the Pauli matrices will result in a rotation about the respective axis of the sphere.

Similarly, the different states of a light field can be represented by using a Fock space [5]. Put simply, the Fock states $|n\rangle$, where $n \in \mathbb{N}_0$, describe a system where n photons are present in a particular light mode given by its wave vector $\vec{k}$ and polarization λ. If the light field in second quantization is viewed as a harmonic oscillator the quadrature components of the kinetic and potential energy parts can be expressed in terms of ladder operators a and $a^\dagger$ with the following properties,

$$a\,|n\rangle = \sqrt{n}\,|n-1\rangle\,, \tag{2.6a}$$
$$a^\dagger\,|n\rangle = \sqrt{n+1}\,|n+1\rangle \tag{2.6b}$$

and $a|0\rangle = 0$. Of course, a quantum system can be in superpositions of different Fock states, with the coherent state $|\alpha\rangle = D(\alpha)|0\rangle$ being a prime example for such a superposition. $D(\alpha)$ is called the displacement operator and reads

$$D(\alpha) = \exp\left(\alpha a^\dagger - \alpha^* a\right). \tag{2.7}$$

In this work, we will deal with two very different cases of light fields. When deriving the spontaneous emission rates of single atoms and ensembles of emitters we will rely on a light field that permits any wave vector and both polarizations, i.e., we allow for all free space light modes. When investigating the superradiant laser, however, only one single mode chosen through the properties of the laser cavity will be relevant.

2.2 Coherent and Dissipative Dynamics

With these two elementary quantum optical building blocks, we are now able to describe the behaviour of a system made up by two-level emitters and light modes. Typically, we will find two types of interactions within such a system: coherent, energy-conserving processes and dissipative, lossy processes.

The energy-conserving processes and the underlying dynamics can be captured by writing down the Hamiltonian operator. This operator describes all the energies and energy-conserving interactions that are present in the system. We will encounter many different Hamiltonians throughout this work, but, as an example, let us mention a fairly typical one, involving one two-level system and one light mode, i.e., the Jaynes-Cummings Hamiltonian [6]. It reads

$$H = \frac{\omega_0}{2}\sigma_z + \omega_l a^\dagger a + g\left(\sigma^- a^\dagger + \sigma^+ a\right), \tag{2.8}$$

with the atomic transition frequency ω_0, the frequency of the light mode ω_l and the coupling strength between the atom and the light mode g. In a reduced subspace, we could now diagonalize this expression in order to find the eigenstates and energies present in the system and study its behaviour under variation of the model parameters, etc. With a Hamiltonian at hand, the dynamics in the system can be calculated by means of the Schrödinger equation [7],

$$i\partial_t|\psi\rangle = H|\psi\rangle, \tag{2.9}$$

which allows us to model a system in a pure state. A formal solution of this equation is

$$|\psi(t)\rangle = U(t)|\psi(0)\rangle = \exp(-iHt)|\psi(0)\rangle, \tag{2.10}$$

where $U(t)$ is usually called the evolution operator. However, if the system is in a mixed state, we will need to describe its properties by the use of a density operator

ρ, which is a weighted superposition of projectors onto different (not necessarily orthogonal) states, i.e.

$$\rho = \sum_j c_j \left|\psi_j\right\rangle \left\langle\psi_j\right| , \tag{2.11}$$

with the properties $\mathrm{tr}\,(\rho) = 1$, $\rho_{jj} \geq 0$ and $\rho_{jk} = \rho_{kj}^*$. For this case, we will employ a sort of generalization of the Schrödinger equation to mixed states, the so-called von Neumann equation,

$$\partial_t \rho = i\,[\rho, H] , \tag{2.12}$$

where the square brackets represent the commutator $[\rho, H] = \rho H - H\rho$.

The von Neumann equation can easily be generalized to include incoherent dissipative processes, that will reduce or increase the overall energy in the system or manipulate its coherences, while ensuring that the total population in the system is preserved. This equation is called master equation [8] and besides the commutator present above it includes a second term that is usually called the Liouvillian. It reads

$$\partial_t \rho = i\,[\rho, H] + \mathcal{L}\,[\rho] . \tag{2.13}$$

A master equation in our case is derived by writing down a complete model of the system (e.g., atoms + free space modes) and then eliminating part of the model by partially tracing out subsystems from the Hilbert space. In the case of spontaneous emission of a single atom, which we discuss below, the Liouvillian would read

$$\mathcal{L}\,[\rho] = \frac{\Gamma}{2}\left(2\sigma^- \rho \sigma^+ + \sigma^+ \sigma^- \rho + \rho \sigma^+ \sigma^-\right) . \tag{2.14}$$

In this case excited state population will decay to the ground state $|g\rangle$ with a rate of Γ. The last two terms in the Liouvillian are responsible for the actual exponential decay of the state $|e\rangle$, while the first term, dubbed 'recycling term' ensures that the overall population of the system is constant. This means that when the excited state loses amplitude, this amplitude needs to end up in the ground state, so that the overall normalization of the system $\mathrm{tr}\,(\rho) = 1$ is satisfied.

Now, knowing the entire dynamics of the system, we can extract information from it by calculating expectation values and their rms deviations which corresponds to an average over measurements and their uncertainties. Given an operator A that represents a certain observable, for instance 'What is the energy in my non-interacting two-level system?', where A would be $A = (\omega_0/2)\sigma_z$, the expectation values and their root mean square (rms) deviations can be calculated as

$$\langle A\rangle = \langle\psi|A|\psi\rangle , \qquad \Delta A = \sqrt{\langle A^2\rangle - \langle A\rangle^2} \tag{2.15}$$

for pure states and

$$\langle A\rangle = \mathrm{tr}\,(\rho A) \tag{2.16}$$

for mixed states.

With this, we would like to conclude the short methodological overview of the mathematical concepts that lie at the foundations of quantum mechanics as it seems, this compact illustration will suffice for an understanding of the next chapters. At any point, each publication or chapter will define and explain the necessary tools in a much more involved, yet less general way, than it has been done here. For a comprehensive treatment or extensive discussions we would like to refer to quantum mechanics [1–4] or quantum optics [9–15] textbooks as mentioned in the beginning.

3 Atomic Clocks

The precise measurement of time has always been at mankind's interest. In ancient times mathematicians and astronomers employed the planetary motion of both the earth around the sun and the earth's precession about its axis to come up with a calendar and ultimately a time standard based on the time between sunrise and sunset resulting in the construction of reasonably precise sundials [16].

The first workable concept of a mechanical clock involving the use of an oscillator powered by an escapement, which would allow for a controlled release of energy determining the overall rate at which a clock device moves, was proposed around 1250 by the French architect Villard de Honnecourt [17] and some historians claim that such a device was built at the court of Louis IX [18]. This clock did not have any hands yet, but was rather used to sound a bell at regular intervals.

In the 16th century, Galileo Galilei discovered [19] that the frequency of a pendulum is not influenced by its amplitude or velocity, but rather a fairly constant property, involving the length of the pendulum l and material properties only. In the simplifying mathematical model of a pendulum its frequency is given by

$$2\pi \cdot \nu = \sqrt{\frac{g}{l}}, \tag{3.1}$$

with g being the gravitational acceleration, while in the more involved physical pendulum the frequency yields

$$2\pi \cdot \nu = \sqrt{\frac{mgd}{I}} \tag{3.2}$$

with the moment of inertia I, its mass m and d the distance between the pendulum's point of suspension and its centre of mass [20].

From that point on time keeping was dominated by mechanical oscillators and a first patent for a spring-based pendulum clock was granted to Christian Huygens in 1657 [21]. Over the next 200 years, the mechanics became more and more precise [22,23] culminating in a marine chronometer built by John Harrison [24] with a relative precision of $\pm 5\,\mathrm{s}$ in 10 weeks, i.e., $\approx 2 \cdot 10^{-6}$.

In the 1880s the piezo-electric properties of crystalline quartz were discovered by Jacques and Pierre Currie [25], which lead to a new generation of time keeping devices with the first quartz clock being built in 1927 [26]. From 1929 to the 1960s NIST (then called NBS) in Boulder, CO, USA based their primary time standard on a quartz oscillator [27].

During the 1940s, the MKS (meter, kilogramme, second) system [28], employing C. F. Gauss' suggestion to use the second as the primary unit for measuring time from 1832 [29] backed up by a so to say international agreement upon the second as the principal unit of time put forward by the British Association for the Advancement of Science in 1862 [30], became the de facto international standard for measurement units. The second was then defined as $1/(24 \cdot 60 \cdot 60) = 1/86400$ of a mean solar day, basing it upon the precession of the earth around its axis.

In 1960, the Eleventh General Conference on Weights and Measures, which established the International System of Units [31] ratified a refined version of the second's definition using the earth's revolution around the sun as 'the fraction 1/31,556,925.9747 of the tropical year for 1900 January 0 at 12 hours ephemeris time' [32], because it had been realized that looking at a mean day would be too imprecise and 200 years of astronomical data were available which allowed for accurate calculations.

Meanwhile, with the advent of quantum physics and one of its fundamental results [33], namely that energy differences of electronic states in an atom are directly associated with frequencies by the relation

$$\Delta E = h\nu, \tag{3.3}$$

where h is the Planck constant, it became evident very quickly that a vast improvement in time measurements could be possible. After a theoretical proposal by Isidor Rabi [34], where he suggested to build a clock based upon magnetic resonance, the first atomic clock employing ammonia was built in 1949. This clock served as a proof of principle and a later version with Caesium atoms demonstrated the atomic clock's superiority in precision in 1955 [27].

In October 1967 the SI second was redefined [35] as $9,192,631,770$ times the frequency of radiation emitted from the transition between the two hyperfine structure levels of the ground state of ^{133}Cs with a relative measurement precision of 10^{-10} at that time. The number was chosen so that the Cs-based second would match the ephemeral second [36], which it replaced. This definition still holds today. In 1997, it was added that the previous definition 'refers to a caesium atom at rest at a temperature of 0 K' [37], thereby compensating for black-body radiation or external magnetic fields.

Since then, Caesium clocks have advanced steadily and the most accurate Cs clock today features a relative precision of 10^{-16} [38], while other suitable elements started being used in atomic clocks as well. This includes Rubidium and Hydrogen, where a comparable precision could be achieved.

The ultimate advancement was brought about by the invention of the frequency comb and the possibility to use optical transitions in earth alkaline elements for building an optical atomic clock [39]. A concrete realization was first achieved at the National Metrology Institute of Japan [40] and featured ^{87}Sr atoms trapped in an optical lattice [41], which allows for a well controlled motional degree of freedom in

Type	Time	Frequency	Precision
NH_3	1948/49	$2.2 \cdot 10^9$ Hz	10^{-8}
^{133}Cs	1960s	$9.1 \cdot 10^9$ Hz	10^{-13}
^{87}Rb	2000s	$6.8 \cdot 10^9$ Hz	10^{-15}
^{87}Sr	2014	$4.2 \cdot 10^{15}$ Hz	10^{-18}

Table 3.1: Overview of different atomic species used for building clock devices. Data due to [42–45].

the atoms, eliminating all kinds of shifts and noises [42], which will be discussed in detail below.

Table 3.1 gives an overview of different atomic clocks based upon Ammonia or Caesium and finally optical atomic clocks using Strontium.

Time measurements based on atomic clocks have been used in tests of general and special relativity or particle physics [46–49]. But, the usefulness of these clocks is not restricted to just fundamental research. For instance, their remarkable precision is exploited in the Global Positioning System (GPS), which consists of a set of atomic clocks mounted on satellites [50]. They send signals to small and cheap receivers like phones, watches or dedicated navigation devices. By measuring the arrival times of these clock signals the receiver can determine its location with an accuracy of a couple of meters. Nowadays, almost any travel or logistics effort is carried out with the help of such navigation instruments, be it on a plane, a ship, in the car or when hiking and we are not surprised to be guided from the sky anymore.

3.1 Concept and Implementations

As mentioned above, one of the fundamental results of quantum physics is the discovery that the energies of electrons in atoms are directly associated with frequencies, see eq. (3.3). In that sense atoms can absorb and emit light at well-defined never changing frequencies, characteristic of the particular atomic specie used [51].

In early realizations of atomic clocks this insight has led to the construction of clocks, where a radio source is locked to the radio frequency hyperfine transition of Caesium atoms propagating in an atomic beam [52]. As a predecessor to the Ramsey measurement scheme, which sits at the heart of current atomic clocks, these early clocks relied on the Rabi measurement technique [53]. Thermal atoms would interact with a probe field when passing through it as a beam and depending on how well the probe frequency would be in tune with the targeted atomic transition, one could see more or less inversion in the atomic states from the ground state to the excited state, which would be detected by counting the inverted atoms or the amount of absorbed radiation.

Since not long after the initial Rabi-based setups, the atomic resonance has been

observed by using an interferometric method, the Ramsey measurement technique, discussed in detail below. In principle, the atoms successively interact with two microwave pulses as they travel along the beam. By sweeping the microwave frequency and detecting one of the two hyperfine states downstream, a modulated signal, called the Ramsey fringe pattern, is obtained. The pattern's centre, where the microwave frequency is perfectly in tune with the atomic transition frequency, is determined with a precision that depends on the fringe spacing, which is inversely proportional to the time between the two microwave pulses [3].

Our discussion and overview here will focus on atomic clocks that were and are built at NIST in Boulder, CO, USA. However, let us emphasize that many other research facilities around the world have also constructed atomic clocks and, most importantly, have played a key role in the advancement of this setup as well, e.g., in Germany, France, the United Kingdom, Japan or India [54–58].

In a concrete realization like NBS-1 to NBS-6 and NIST-7 [59] the transition between $F = 3$ and $F = 4$ for $m_F = 0$ in ^{133}Cs is used [60, 61] .The atoms are heated up to their gas phase in an oven and a beam of atoms at a temperature of roughly 300 K emerges from it. The beam is guided through a magnetic field, where it is split up into two beams depending on the respective electronic state. One beam is absorbed by the getter and is of no further interest, while the second beam is deflected into the microwave interrogation cavity, the so-called Ramsey cavity. Inside this cavity the Caesium beam interacts with a microwave frequency generated by a Quartz-based frequency synthesizer. If the microwave frequency is in tune with the atomic resonance, some of the atoms will have changed their internal state upon leaving the Ramsey cavity. Now, the beam is exposed to a second magnetic field, which will separate the atoms that have changed their state from those that did not. One half is again absorbed and the other half is guided to the detector, which sends a feedback signal to a servo circuit, that continually tunes the Quartz synthesizer in such a way that the maximum number of atoms reach the detector. This keeps the oscillator frequency locked to the Caesium resonance as tightly as possible. The setup is illustrated in fig. 3.1.

In the last two decades, laser-cooled atoms [62] have replaced the thermal atoms used in previous clock setups. The interval between the two individual pulses has been increased considerably and thus, the clock's precision could be improved by a couple of orders of magnitude. A prominent example of a clock that employed laser-cooling in its setup is NIST-F1 [63], a Caesium fountain clock. In this clock, the Caesium atoms move from below to above the interaction region and then being subject to gravity fall down again, passing the interaction region a second time. By means of laser cooling the atoms are slowed down to a few centimetres per second in contrast to several hundred meters per second in a thermal setup. This allows for a much longer time interval between the two pulses and thus a more narrow fringe spacing, yielding a higher precision.

The fountain setup was first suggested by Zacharias in the 1950s [44, 64], yet

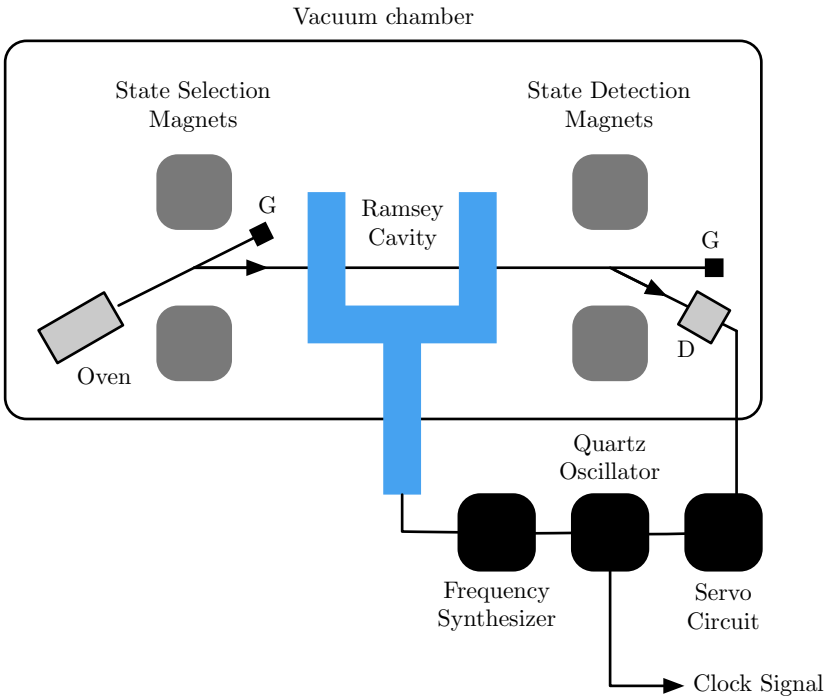

Figure 3.1: *Schematic of a beam-based atomic clock.* The atoms are heated up in the oven, those with the desired internal state are directed into the interrogation region, where they pass through the Ramsey cavity. Another set of magnets prepares the atoms which have flipped their state for being counted at the detector (D). In both sets of magnets about half of the passing atoms are lost and collected by the getter (G). The servo circuit optimizes the frequency of the cavity, which is generated by a Quartz oscillator and modulated by the frequency synthesizer so that the maximum number of atoms will be counted. A clock signal can be derived from the Quartz oscillator.

without the availability of sufficiently powerful cooling techniques, first attempts of an experimental realization did not yield any signal at all. Essentially, all the slow Caesium atoms were scattered out of the beam by faster ones, that overtook them.

In 1978 Dave Wineland demonstrated the feasibility of laser cooling [65], which had been proposed three years earlier [66]. In the late 1980s Steven Chu and his team built the first working fountain clock based upon Sodium [67] and later implemented a Caesium version of it [68]. The first primary frequency standard employing a Caesium fountain setup was built at BNM-SYRTE in Paris not long after that [69].

As mentioned, laser cooling constitutes a fundamental prerequisite for a fountain clock and those clocks usually use a technique called optical molasses [70]. Three pairs of identical counter-propagating laser beams exert a damping force on the atoms. The lasers are tuned to a frequency slightly below the atomic resonance and atoms at the intersection of the six beams can be cooled to a temperature of $< 1\,\mathrm{mK}$ at timescales of about 100 ms. As if the atoms were moving through a very viscous fluid, the atoms slow down to a bout 1 cm/s, hence the name 'molasses'. In that way a large sample of atoms can be accumulated in one place. In a mechanical picture, atoms preferentially absorb photons from the laser beam, which they are moving toward, as a result of the Doppler effect. The absorbed photons carry momentum in the opposite direction of the atomic motion. When the photon is spontaneously re-emitted with a random phase and in a random direction, the atom emits slightly more energy than it absorbed, as the lasers are red-detuned with respect to the atomic transition. This process is repeated many times ($\sim 10^7$ per second) facilitating a cooling cycle.

In 1998 NIST-F1 [71], that relies on the above concept, was built. In a nutshell, its measurement procedure can be described as follows. About 10^8 Caesium atoms in a volume of about one cubic centimetre are laser-cooled to $\sim 0.5\,\mu\mathrm{K}$ by an optical molasses. By detuning the frequency of the lasers in the z-direction the molasses starts to move upward and at this point shutters extinguishing the laser light make sure that the sample is no longer subject to any optical interactions during its ballistic flight. A short microwave pulse drives the internal state of the Caesium to $F = 3$ and an optical blast removes any access atoms still in $F = 4$. Now, the atoms undergo their first interaction with the microwave cavity, i.e., their first $\pi/2$-Ramsey pulse when they pass through the cavity at about 3 m/s. About 1 m above the resonator the atoms turn around and fall down due to gravity. They pass through the cavity again and are subjected to the second $\pi/2$-pulse, before they are detected via the probe laser and an optical transition from $F = 4$ to $F = 5$. The apparatus is illustrated in fig. 3.2.

With this vast increase in interrogation time from a few ten milliseconds to about one second, relative clock precision reached a level of $4 \cdot 10^{-16}$. At this level two fundamental perturbations seem to hinder a further increase in the clock's precision: the black-body shift and a density shift due to collisions of the atoms. In NIST-F2 [72], the successor of NIST-F1, these issues are accounted for by a cryogenic vacuum source and the implementation of an idea where not one, but several clouds of Caesium are

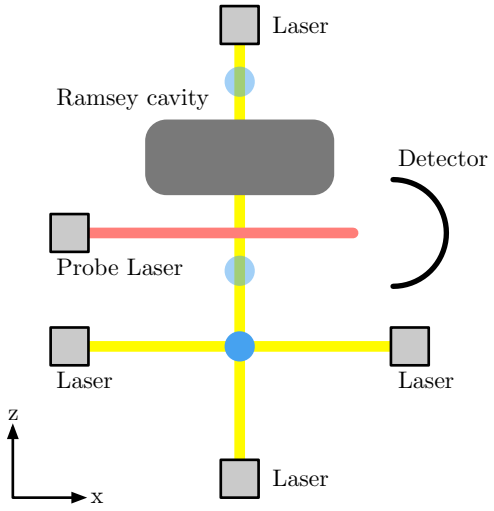

Figure 3.2: *Schematic of a Fountain Clock Setup (y-dimension omitted).* The atoms are laser-cooled in an optical molasses, then launched upwards and pass through the Ramsey cavity before they fall down again due to gravity and pass through the cavity a second time. They are then optically detected by a probe laser and a detector.

launched with different initial velocities, respectively [73].

Figure 3.3 gives an overview of relative atomic clock precision from the first setups in the 1950s to right before the advent of optical lattice atomic clocks, which will be discussed below.

For completeness, several review articles and books are available where actual measurement data is depicted [3, 44, 75].

3.2 Limits of Ultra High Precision Atomic Clocks

At a relative precision of 10^{-16} tweaking and improving the fountain clock setup became harder and harder and a new suggestion to use an optical lattice [40] instead of a thermal beam or ballistic cloud promised new clocks that would feature an accuracy some orders of magnitude better than the fountain setups.

Two main questions need to be addressed for an optical lattice clock. First, it is necessary to think about which atomic specie should be used in such a setup. This requires finding elements with a feasible level structure for trapping, manipulating and measuring. And secondly, all kinds of perturbations and external shifts need to be examined and taken into account. This ranges from shifts induced by the trapping or other external electric or magnetic fields to shifts due to black body radiation, i.e., finite temperatures in the setup. A very detailed treatment can be found in [74].

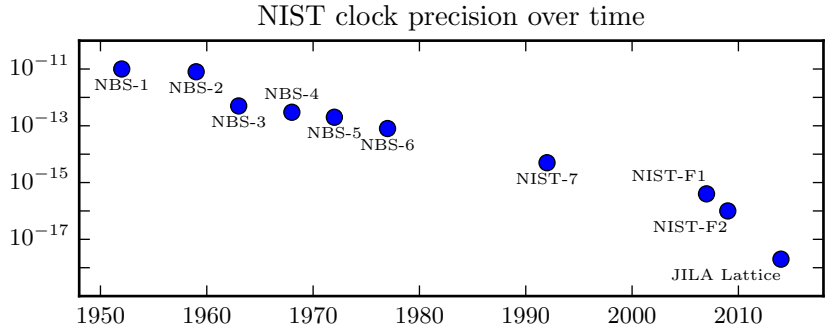

Figure 3.3: *Overview of atomic clock precision at NIST/JILA.* Qualitatively, an almost exponential increase in precision can be observed. (Almost) all of these clocks have served as primary frequency standards. Data due to NIST/JILA [59, 74].

To begin with, let us discuss, which atomic species feature a level structure that is most useful in optical lattice clocks. Besides implementations with trapped ions [76–78], recently, neutral atoms seem to dominate the clock business, as they possess the advantage of enhanced clock signals even down to the quantum projection noise limit.

While Cs in beam or fountain setups and H in Hydrogen masers have been most prominent in atomic clocks for the last decades their 'relatively small' microwave transition frequencies between ground and excited state of roughly 9.2 GHz and 1.42 GHz, respectively, ultimately hinder a further improvement of Caesium based clocks. Hence, the suggestion to use alkaline earth(-like) atoms that possess two valence electrons was made [79]. With two electrons in the outermost s-orbital their respective spins can add up parallel or anti-parallel, which results in singlet and triplet states. There are strong transitions within the singlet and triplet manifolds and a lot weaker ones between them. The ${}^1S_0 \rightarrow {}^1P_1$ cycling transition can be used for trapping, cooling and state detection. Cooling can be enhanced by employing the ${}^1S_0 \rightarrow {}^3P_1$ spin-forbidden transition. And further transitions from ${}^3P$ to ${}^3S_1$ or the ${}^3D$ manifold aid in repumping the cooling transition or in optical pumping for state detection. The most interesting transition in these atoms, however, is without a doubt, the doubly-forbidden ${}^1S_0 \rightarrow {}^3P_0$ transition, oftentimes dubbed 'clock transition', present in isotopes with nuclear spin. On the one hand, this transition features a frequency in the laser-accessible optical regime in the order of 100 THz and a very narrow linewidth of well below 1 Hz and on the other hand, there is no electronic angular momentum, which reduces the magnitude of many perturbations in the clock setup. In that sense, these species seem ideal for clocks, which is further underpinned by the existence of differential light shift free trapping wavelengths, the so-called 'magic wavelengths' and because of the minute dependence of the clock frequency on the light polarization. The level structure with a particular attention to ^{87}Sr is shown in fig. 3.4 and a detailed listing of all the transitions with their properties is given in tbl. 3.2.

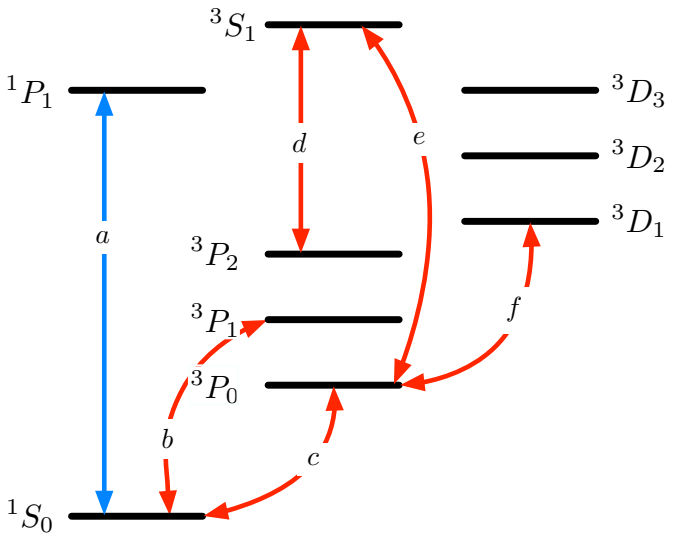

Figure 3.4: *Simplified level structure of* ^{87}Sr. In the outer-most orbitals various transitions are involved in cooling and trapping the atoms. The transition $^1S_0 \rightarrow ^3P_0$ (c) is the actual clock transition. For details see tbl. 3.2.

	Type	Levels	Transition	Linewidth
a	strong cooling	$^1S_0 \rightarrow ^1P_1$	460.9 nm	32 MHz
b	narrow cooling	$^1S_0 \rightarrow ^3P_1$	689.3 nm	7.5 KHz
c	clock	$^1S_0 \rightarrow ^3P_0$	698.4 nm	1 mHz
d	repump	$^3S_1 \rightarrow ^3P_2$	707.2 nm	
e	repump	$^3S_1 \rightarrow ^3P_0$	679.3 nm	
f	repump	$^3P_0 \rightarrow ^3D_1$	2603 nm	

Table 3.2: Transitions present in the outermost s-orbitals of ^{87}Sr that are used in an optical atomic clock. Data due to [74].

Before we go on to discuss the various systematic effects in the clock setups, let us briefly touch on the idea of a magic wavelength. Optical lattices confine atoms by inducing a dipole moment in them and then exerting a force on this dipole by a laser field gradient. Generally, the induced polarizabilities will vary for different states, so that the lattice will induce an AC Stark shift in the levels constituting the clock transition, which is detrimental to the clock's accuracy. Additionally, as the light field is inhomogeneous, atomic motion within the trap will result in a coupling of external and internal degrees of freedom, compromising coherence for spectroscopy. Of course, the Stark shifts of each individual level depend on the trapping wavelength and the polarization of the trap lasers. For some transitions it is however possible to find a trapping configuration so that the polarizability of the lower and upper clock state is equal, resulting in a net Stark shift of zero as well as a clear separation of motional and electronic degrees of freedom. This idea was first suggested by Katori in 2003 [80].

Without going into too much detail, let us present a short calculation of the lattice-induced AC Stark shift following [81]. In a one-dimensional optical lattice the lattice potential can be expressed as a longitudinal standing wave with a Gaussian distribution along the radial axis, i.e.

$$U(r,z) = \frac{4P\alpha}{\left(\pi c\epsilon_0 w(z)\right)^2} \exp\left(\frac{-2r^2}{w(z)^2}\right) \cos\left(k_L z\right) \tag{3.4}$$

with P the average laser power, $w(z)$ the laser waist along the propagation direction, k_L its wave number and α the polarizability of the state under consideration given by

$$\alpha = 6\pi\epsilon_0 c^3 \sum_j \frac{\Gamma_{j,\lambda}}{\Delta\omega_j^2\left(\Delta\omega_j^2 - \omega_L^2\right)}, \tag{3.5}$$

where we sum over all states with non-vanishing transitional dipole moments. $\Gamma_{j,\lambda}$ is the spontaneous emission rate of the respective target states when exposed to light of polarization λ. $\Delta\omega_j$ is the transition frequency between the considered and the target state and ω_L is the laser frequency. Now knowing the potential, we can calculate the electric field and obtain the scalar AC Stark shift

$$\Delta\omega = -\frac{\alpha\left|\vec{E}\right|^2}{2\hbar}. \tag{3.6}$$

In our considerations, where we deal with ^{87}Sr, a differential light shift of zero between the two clock states $^1S_0$ and $^3P_0$ is achieved at a 'magic' trapping wavelength of $\lambda_m = 813.428\,\mathrm{nm}$ [40, 82].

Now, let us discuss some systematic effects that need to be taken into account in an optical lattice clock. We largely follow [74].

To begin with, we realize that the Stark shift polarizable neutral atoms experience in the laser field of the optical trap, in fact, has three contributions: a scalar, a

vector and a tensor part. Since we are dealing with $J = 0$ ground states for the clock transition, the scalar contribution dominates and a typical shift would be on the order of 1 MHz. Yet this shift is cancelled by the use of a magic wavelength lattice, as discussed above. This shift is fairly insensitive to the actual trapping frequency and as long as the lattice trap frequency is within about 500 kHz of the magic wavelength, a cancellation of the shift with the consequence of a fractional frequency precision at the order of 10^{-18} is possible. Now, the fact that the clock states do not have an identical zero angular momentum due to state mixing from hyperfine interactions, does not allow for the vector and tensor contribution of the polarizability of the upper clock state to the Stark shift to vanish as well [83]. This shift can reach magnitudes of the order of 100 Hz [84], but in practise, the use of mostly linearly polarized light reduces the effect of the vector shift to a level, where it does not play any role in current 1D and 2D setups. The tensor contribution could be shown to influence the clock precision at the 10^{-16} level, yet can be straight-forwardly controlled to reduce its effect below the 10^{-17} regime [84]. Another systematic perturbation is brought about by the hyper-polarizability of the clock states, where its corresponding shift scales with E^4 as opposed to E^2. Hyper-polarizability includes one and two photon resonances [85] and it remains finite at the magic wavelength [86] resulting in a shift of about 10^{-17} in fractional frequency with an uncertainty well below that [84, 87]. Besides these dipole-based effects, higher order electric quadrupole or octopole shifts as well as magnetic shifts have been studied [88]. For the JILA Sr clock it could be shown that a purely linear intensity-dependent model allows for a characterization of the shifts below the 10^{-18} level [42].

Not only electric fields will cause a shift of the clock transition frequency, but magnetic fields can result in a Zeeman shift of the levels as well. In an optical lattice clock, both first and second order Zeeman shifts need to be taken into account. In fermionic Strontium the nuclear spin I will introduce $2I + 1$ magnetic sub-levels in the $J = 0$ clock states facilitating a Zeeman shift with linear dependence on the magnetic field. The challenge here is to accurately measure and calculate the differential g-factors of the clock states in order to correct this shift [83, 89–93]. A precise measurement places this differential g-factor at $\Delta g \mu_B/\hbar = -11084\,\mathrm{Hz}/\mu\mathrm{T}$ with the Bohr magneton μ_B [83]. In addition, a second-order Zeeman shift arising from levels separated in energy by the fine structure splitting of about $-2.33 \cdot 10^{-5} B^2\,\mathrm{Hz}/\mu\mathrm{T}^2$ is present [83, 88, 94, 95].

Another source of imprecision is given by black-body radiation that causes shifts on the atomic levels. The static and dynamic polarizability as well as the radiative temperature of the environment of the atoms are to be held accountable. At the value of $2.7 \cdot 10^{-15}$ for room temperature the black-body frequency shift constitutes the largest uncancelled systematic shift of the clock transition frequency. The uncertainty of this shift, however, is the actual problem. Expensive ab initio calculations [96] have brought this uncertainty down to 1% for Sr and direct measurements of the polarizability have contributed as well [97–99]. Recent coupled-cluster all-order calculations have demonstrated a good agreement with these measurements [100, 101].

Dynamic corrections to the static polarizability of the clock states need to be taken into account as well, where the $^3P_0$ state experiences the most significant correction, which is dominated by its coupling to the $^3D_1$ state. A recent measurement [102] allowed to reduce this uncertainty to below the 1% level and the mentioned new theoretical considerations are in good agreement with this value [100, 101]. The third cause of uncertainty in the black-body shift stems from the radiative environment bathing the atoms, i.e., temperature inhomogeneities, the optical and infrared transparency of viewports, complex geometries and non-uniform emissivities of the vacuum apparatus. This leads to an uncertainty of $7 \cdot 10^{-17}$. Cryogenic environments can be used to drive this down to the 10^{-18} regime, given the T^4 dependence of this effect [103]. In the last years in situ thermal probes have been used to monitor the radiative thermal bath resulting in an uncertainty below $2 \cdot 10^{-18}$ [42, 102].

In contrast to beam or fountain clocks (see sec. 3.1), where shifts induced by high densities and consequent collisions play a major role [68, 75, 104–106], optical lattice clocks are usually subject to much less atomic interactions. In 3D lattices, which typically feature a filling factor of less than one,, with the exception of tunnelling, collisions are virtually non-existent. Rather, long-range dipole-dipole interactions, which are the main subject of this thesis, start to play a role [107] given a sufficient clock precision. In 1D lattices, where sites are multiply occupied, the situation is very different, though. Even in fermionic ^{87}Sr, where the anti-symmetric wave function eliminates collisions from even partial wave collision channels (including lowest order s-wave) and lowest order odd p-wave collisions can be suppressed well, collisions have been observed [95, 108]. This seems to be the case due to the fact that finite temperatures in the atomic ensemble prohibit a full suppression of the p-wave collisions and the fact, that indistinguishable fermions evolved into non-identical superpositions of clock states during spectroscopy, allowing for s-wave interactions. A large body of theoretical [109–112] and experimental [108, 113–117] investigations of this phenomenon has been published and numerous techniques for cancellation or suppression of scattering are available [86, 115, 116, 118]. Currently, the uncertainty caused by collisions can be controlled at the level of 10^{-18} [42, 117].

As the differential light shift is zero for the trapping laser only, Stark shifts induced by the probe laser due to off-resonant couplings to intermediate states will occur in the system. This depends on the clock states' polarizability at the clock frequency and the laser power used to detect the clock transition. The effect resides at the order of 10^{-17} [82, 95, 119, 120], with new measurements placing it even below 10^{-18} [42]. With increasing laser coherence times it is possible to reduce the laser power required for detection, which also reduces this effect.

Doppler and recoil frequency shifts can usually be well avoided in optical lattices. However, there are some mechanisms that still lead to atomic motion. Tunnelling of the atoms between lattice sites is still possible, especially in shallow lattices [121], where tunnelling along the interrogation axis poses a problem. This can be hindered by aligning the interrogation axis along gravity, which lifts the degeneracy among

lattice sites and reduces the overall effect to the order of 10^{-17}. Relative vibrations between the lattice and clock lasers can cause residual Doppler shifts as well, which can be avoided by actively phase-stabilizing the clock and/or lattice lasers [122] or detection in two counter-propagating directions. Switching RF power in an acousto-optic modulator [123] for turning the interrogation of the clock laser on and off results in residual Doppler effects caused by phase chirps from RF ringing and thermal effects [124], which need to be characterized and controlled very well or actively stabilized [125]. Additionally, a relativistic Doppler shift due to thermal motion of the atoms is present as well, yet influences the clock's precision below the order of 10^{-20}.

Similar to the AC Stark shifts, static electric fields can introduce static DC Stark shifts. In optical lattices the atoms are usually far removed from surfaces, where stray charges may accumulate. Metallic components in the system are usually grounded, yet charge can built up on insulator surfaces, which influence the clock precision at the 10^{-17} level with some reports of exceptions, where a charge build-up lead to an effect on the order of 10^{-13} [126]. In recent experiments the DC Stark shift's effect could be reduced to about $2.1 \cdot 10^{-}18$ [42].

Finally, a number of other minor systematic effects have been looked into. These include line pulling, servo error, stray laser Stark shifts, AC Zeeman shifts among others [40, 42, 82, 94, 95, 120], which at current measurement precision do not pose fundamental limits.

3.3 Ramsey Measurement Procedure

Let us now discuss the Ramsey measurement technique first used in 1949 [64], that constitutes the core of an atomic clock setup, in more detail. We loosely follow [3].

In analogy to a Mach-Zehnder interferometer in classical optics [127], where an interference pattern is obtained by splitting up a beam into two sub-beams, manipulating each in a different way and then bringing them back together again, the Ramsey procedure can be understood as a time-based interferometer in quantum optics. Instead of different optical path lengths caused by an intrinsic time delay or actually different real space paths, two atomic states and their coherent superposition will serve as the basis for our interferometric procedure.

To be more precise, the Ramsey technique employs two consecutive $\pi/2$ Rabi pulses. The first pulse R_1 creates a coherent superposition of the two atomic states. Then, a tunable phase shift is acquired by the atomic coherence, before it is probed by the second pulse R_2.

For a system initially in the state $|g\rangle$, the first pulse will create a coherent superposition of ground and excited state, i.e.

$$R_1 |g\rangle = \frac{1}{\sqrt{2}} \left(|g\rangle + |e\rangle \right). \tag{3.7}$$

In the rotating frame, through a difference $\Delta = \omega_0 - \omega_l$ between the atomic transition frequency ω_0 and the probe field ω_l, a phase shift of $\varphi = \Delta\tau$ with probing time τ can be imprinted on the excited state (neglecting an irrelevant global phase). This is achieved by either detuning the probe field, i.e., the probe laser, or applying a transient electric or magnetic field to shift the atomic transition frequency. Our atomic state now reads

$$\frac{1}{\sqrt{2}}\left(|g\rangle + \exp\left(i\varphi\right)|e\rangle\right) \tag{3.8}$$

and upon applying the second Ramsey pulse R_2 we get

$$\frac{1}{2}\left[\left(1 - \exp\left(i\varphi\right)\right)|g\rangle + \left(1 + \exp\left(i\varphi\right)\right)|e\rangle\right] \tag{3.9}$$

and the probability for finding the atom in $|e\rangle$ or $|g\rangle$ after the probing sequence is given by

$$P_{|e\rangle} = \frac{1}{2}\left(1 + \cos\left(\varphi\right)\right) \qquad P_{|g\rangle} = \frac{1}{2}\left(1 - \cos\left(\varphi\right)\right), \tag{3.10}$$

a result that is identical to the output signals at the two arms of a Mach-Zehnder device.

The interpretation of this result is straight-forward: for $\varphi = 0$, where there is no evolution of the atomic coherence between the two pulses, they will simply add their effects and two $\pi/2$ pulses will result in one effective π pulse, flipping the atomic state from $|g\rangle$ to $|e\rangle$. For $\varphi = \pi$, R_2 will undo the effect of the first pulse and the atom will come back to $|g\rangle$.

These oscillations in the detection probabilities can also be understood as an atomic interferometer. The transition from $|g\rangle$ to $|e\rangle$ by absorption of photons from the probe beam may either occur during R_1 or R_2, two indistinguishable quantum paths, that will lead the atom from the initial to its final state. Thus, the corresponding amplitudes must be summed to obtain the final transition probability and the Ramsey fringes demonstrate the interference between these amplitudes.

The Ramsey interference is a very sensitive probe of any phase disturbance acting on the system between the two pulses. If an external perturbation produces an extra phase shift of the atomic coherence between R_1 and R_2 the Ramsey fringes are shifted accordingly and φ becomes $\varphi + \varphi'$, where φ' is an additional phase shift due to external circumstances.

For a practical implementation it is much more convenient to introduce a relative phase between the pulses R_1 and R_2, instead of tuning the phase of the atomic coherence between the two pulses. Again in the rotating frame, it is much easier to use one field source for both pulses R_1 and R_2 instead of two separate fields. The relative phase can then be adjusted by tuning the probe field ω_l relative to ω_0, as mentioned above.

The atom will undergo two interactions with the probe field, one from t_i to $t = 0$ and one from $t = \tau$ to t_f. We assume $|t_i|, |t_f - \tau| \ll \tau$, i.e., that the duration of the

pulses R_1 and R_2 is much shorter than the time of free evolution between the two pulses, a reasonable approximation for most measurement schemes. The Hamiltonian corresponding to this process with respect to the atomic transition frequency is then

$$H = \frac{i\Omega}{2}\,\Theta\left(t\right)\left(\exp\left(i\Delta t\right)\sigma^{+} - \exp\left(-i\Delta t\right)\sigma^{-}\right), \tag{3.11}$$

where $\Theta\left(t\right) = 1$ during the pulses and $\Theta\left(t\right) = 0$ otherwise.

Realizing that the spectral width (inverse pulse duration) of the two probe pulses is much smaller than Δ, we can neglect the phase effects of the pulses and set the phase of the first pulse to $\varphi = 0$ and the phase of the second pulse to $\varphi = \Delta\tau = \left(\omega_0 - \omega_l\right)\tau$. From this, we recover the Ramsey fringe signal as

$$P_{|e\rangle} = \frac{1}{2}\left(1 + \cos\left(\Delta\tau\right)\right). \tag{3.12}$$

When the probe frequency ω_l is swept, the spacing of the Ramsey fringes is given by $1/\tau$. The spectroscopic resolution of the Ramsey interferometer is thus proportional to the total interrogation time, not the duration of the actual probing pulses.

These features underpin the importance of the Ramsey interferometry procedure for high resolution spectroscopy experiments. During most of the interrogation time the atom can be shielded from the outside world and from the action of the probe field efficiently, thereby minimizing light shifts and power broadening. Most modern atomic clocks are based upon Ramsey interferometry.

Figure 3.6 demonstrates the fringe spacing, so to say the resolution of the spectroscopic procedure, for different interrogation times τ. The longer the period of free evolution in between the probing pulses, the closer the fringes are to each other. This favours precision in the experiment as smaller changes in Δ have a much larger effect on the signal and therefore can be measured more easily.

More formally, this idea is captured by the definition of the signal sensitivity, which gives a means for quantifying the smallest change in Δ, that can be resolved by a given setup and reads

$$\delta\Delta = \min_{\Delta} \frac{\Delta\sigma_z}{\left|\partial_\Delta \left\langle\sigma_z\right\rangle\right|}, \tag{3.13}$$

where we have chosen $\langle\sigma_z\rangle$ as our signal and $\Delta\sigma_z$ denotes its rms deviation. Heuristically, this formula results from a simple slope triangle deliberation as illustrated in fig. 3.7. As said, the smaller $\delta\Delta$, the better the resolution of the measurement when sweeping Δ. So, a small rms deviation $\Delta\sigma_z$ and an as large as possible slope $\left|\partial_\Delta \left\langle\sigma_z\right\rangle\right|$ will return the best measurement results.

In a perfect experiment, where there is no dissipation (discussed in detail in chp. 4) with a signal $\langle\sigma_z\rangle = \cos\left(\Delta\tau\right)$ the expression for the sensitivity will become

$$\delta\Delta = \min_{\Delta} \frac{\cos\left(\Delta\tau\right)}{\left|\tau\sin\left(\Delta\tau\right)\right|} = \frac{1}{\tau} \tag{3.14}$$

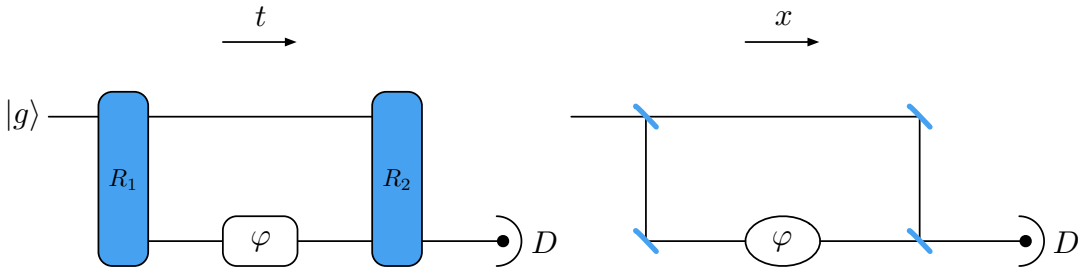

Figure 3.5: *Illustration of the Ramsey interferometry procedure.* In comparison to a Mach-Zehnder interferometer in classical optics (right). In a Ramsey procedure (left) the interference fringes are created by a phase imprinted on the coherence between $|g\rangle$ and $|e\rangle$, while in a classical interferometric experiment the interference pattern stems from combining the two split up fields of different optical path lengths again before detection.

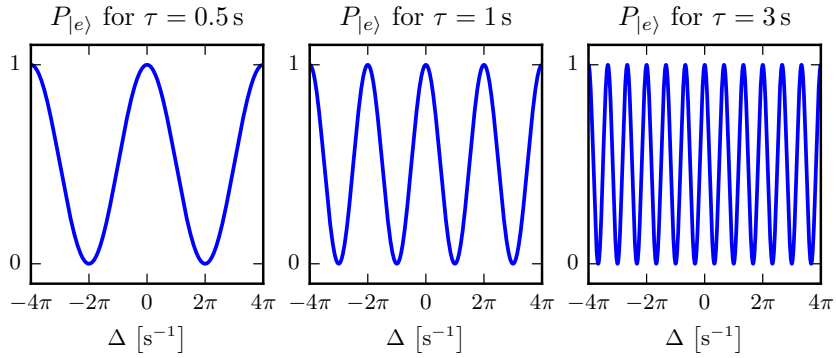

Figure 3.6: *Ramsey fringes for different interrogation times τ.* The longer the probing time, the closer the fringe spacing, which increases the discernibility or resolution of the individual fringes.

and we see that the longer the interrogation time, the smaller a difference in Δ we can resolve, which agrees with our qualitative discussion from above.

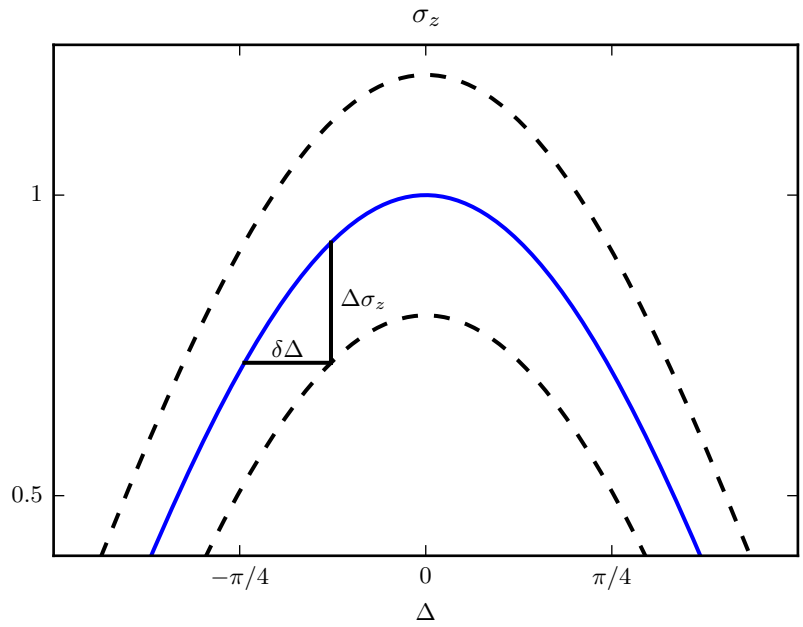

Figure 3.7: *Illustration of the meaning of the signal sensitivity $\delta\Delta$.* The solid blue curve depicts the signal $\langle\sigma_z\rangle$, while the two dashed curves illustrate the signal boundaries in the sense of its rms deviation. At any chosen point the sensitivity can be extracted from the slope triangle between the signal curve and signal plus/minus its rms deviation.

4 Spontaneous Emission

With our focus on measuring the frequency difference between two electronic states most precisely, it is very clear that the spontaneous decay of an electronic excitation within the atom constitutes a fundamental limitation to our spectroscopy procedure, which crucially relies on bringing as many atoms as possible into the excited state. When this is hindered by spontaneous, in that sense uncontrollable and unpredictable, emission from the atoms, our setup suffers from reduced accuracy and reproducibility.

4.1 Phenomenon and Concept

Spontaneous emission occurs when a quantum system like an atom, molecule, quantum dot, NV centre, etc., modelled by its two relevant states, moves from an excited state $|e\rangle$ to a state of lower energy, the ground state $|g\rangle$, and thereby emits a photon with the angular frequency $\omega = (E_e - E_g)/\hbar$, satisfying energy conservation. This photon is of unknown polarization and will propagate in a random direction as shown in fig. 4.1.

But why does such a two-level system decay after all? Based upon simple quantum mechanical considerations, we would argue that the excited state $|e\rangle$ is an eigenstate of the system and thus it's time evolution is simply given by

$$|e(t)\rangle = \exp(-i\omega_e t)\,|e\rangle\,, \tag{4.1}$$

only acquiring a (global) phase and thus $P_e(t) = 1$ for all times. This definitely does not explain the phenomenon of spontaneous decay.

In order to understand spontaneous emission, we need to look at a larger Hilbert space than just the one of our two-level system. Quantum Electrodynamics does this by including the free radiation field and its inherent interaction with the atomic states. As any atom is inevitably coupled to all vacuum modes of the radiation field, i.e., to photonic modes of any wave vector $\vec{k}$ and both polarizations λ, probabilities of the joint system to shift excitations from the atom to the field become finite. Now, when observing the reduced atomic system only, a transfer of energy from the atom to the field will appear as loss of energy or dissipation from the atomic system, thereby clarifying the meaning of spontaneous emission.

A first phenomenological treatment of these processes has been proposed by Einstein in 1916 [128,129], which resulted in the postulation of the then undetermined Einstein A- and B-coefficients.

Einstein realized that in radiative equilibrium there are three processes that are responsible for energy exchange between particles, e.g., atoms, and the radiation field. Those processes were famously dubbed

1. Absorption: by absorbing a photon from the radiation field an electron in an atom is lifted into a higher energy state $|e\rangle$.
2. Stimulated (or Induced) Emission: a mode populated by n photons stimulates the emission of another photon into that very same mode, i.e., same direction and polarization, while the atomic electron transitions into a lower state $|g\rangle$
3. Spontaneous Emission: the atom spontaneously emits a photon into an empty mode and transitions to a lower energy state $|g\rangle$. Particularly in free space that means that the direction of the emitted photon is random.

With this, we recognize that all three processes depend on the number of atoms in the respective states, N_g and N_e and absorption and stimulated emission also incorporate the spectral energy density $\rho(\omega)$ of the surrounding radiation field. Einstein introduced the coefficients A_{eg}, B_{eg} and B_{ge} (called A_{21}, etc. in his original work). Thus, the processes can be quantified by the probabilities of

1. absorption of a photon from the field $N_g \cdot B_{ge} \cdot \rho(\omega)$
2. stimulated emission into a certain mode $N_e \cdot B_{eg} \cdot \rho(\omega)$
3. spontaneous emission into an arbitrary mode $N_e \cdot A_{eg}$.

The rate equation for the number of atoms in the ground state $|g\rangle$ and the excited state $|e\rangle$ reads

$$\dot{N}_g = -\dot{N}_e = -N_g \cdot B_{ge} \cdot \rho(\omega) + N_e \cdot B_{eg} \cdot \rho(\omega) + N_e \cdot A_{eg}, \tag{4.2}$$

which in thermal equilibrium is equal to zero and it follows

$$\frac{N_e}{N_g} = \frac{B_{ge}\rho(\omega)}{A_{eg} + B_{eg}\rho(\omega)}. \tag{4.3}$$

The relation between the states' occupation and their respective energies is given by the Boltzmann distribution,

$$\frac{N_e}{N_g} = \frac{g_e}{g_g} \cdot \frac{\exp(-E_e/k_BT)}{\exp(-E_g/k_BT)} = \frac{g_e}{g_g} \exp(-\Delta E/k_BT), \tag{4.4}$$

where g_e and g_g quantify the degree of degeneracy of the states $|g\rangle$ and $|e\rangle$, E_e and E_g with $\Delta E = E_e - E_g$ denote their respective energies, k_B is the Boltzmann constant and T represents the temperature. Solving for the spectral energy densities leaves us with

$$\rho(\omega) = \frac{A_{eg}}{B_{eg}} \cdot \frac{1}{\frac{g_g B_{ge}}{g_e B_{eg}} \exp(\Delta E/k_BT) - 1}, \tag{4.5}$$

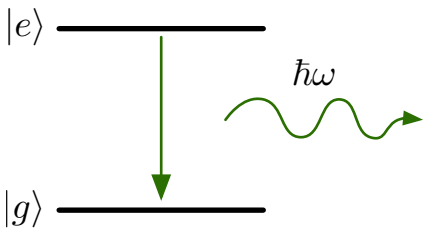

Figure 4.1: Spontaneous emission. A two-level quantum system decays from the excited state $|e\rangle$ to the ground state $|g\rangle$ and emits a photon of the energy $\hbar\omega = E_e - E_g$ with random polarization into a random direction.

which by comparison of coefficients to Planck's law of radiation or the Rayleigh-Jeans law [130] results in the following relations between the Einstein coefficients,

$$g_g \cdot B_{ge} = g_e \cdot B_{eg}, \tag{4.6a}$$

$$B_{eg} = A_{eg} \cdot \frac{\lambda^3}{8\pi h}, \tag{4.6b}$$

where h is the Planck constant and $\lambda = 2\pi\omega/c$ is the wavelength of the transition.

In this derivation the actual expression for the Einstein coefficients cannot be determined, such that they remain an abstract quantifier for absorption and emission probabilities, which solely depend on the chosen atomic specie and transition. The A- and B-coefficients are independent from temperature as the temperature dependence of the radiation is usually caused by different occupation probabilities N_e and N_g and is accounted for by the Boltzmann distribution.

We will now concentrate on the process of spontaneous emission, while both stimulated emission and absorption would be fairly similar to deal with.

The advent of quantum electrodynamics allowed for a more rigorous approach. Based upon the insight that the electromagnetic radiation field is quantized and the creation and annihilation of single electromagnetic quanta of energy, the so-called photons, is possible, a refined mathematical treatment of spontaneous emission emerged. Additionally, those photonic modes will suffer from random fluctuations, which are ultimately responsible for spontaneous emission as well as many other effects (e.g., the Casimir effect [131]).

In the following, we will derive the QED result for the rate of spontaneous emission from a single two-level system, before we extend our deliberations to an ensemble of two-level systems. Lastly, we will observe that, when more than one emitter is present, the emitted light from an extended system can interfere constructively and destructively depending on the system's geometry, which will lead us to super- and subradiance.

4.2 Single Atom

We will now derive the spontaneous emission rate from a dipole-facilitated transition between two electronic levels in an atom, following [132]. In second quantization the Hamiltonian describing the joint systems of a two-level atom and the free radiation field can be written as

$$H = H_{\mathrm{A}} + H_{\mathrm{F}} + H_{\mathrm{int}}, \tag{4.7}$$

where

$$H_A = \omega\sigma^+\sigma^- \text{ and } H_F = \sum_{\vec{k},\lambda} \omega_k a^\dagger_{\vec{k},\lambda} a_{\vec{k},\lambda} \tag{4.8}$$

describing the bare energies of the atom and the radiation field, where $\omega_k = c\left|\vec{k}\right|$, while

$$H_{\mathrm{int}} = -\vec{d}\cdot\vec{E}\left(\vec{r}\right) \tag{4.9}$$

denotes the interaction of the field with the atom treated in dipole approximation.

Now, substituting for the dipole and field operators of eq. (4.9) we end up with the fully quantized interaction

$$H_{\mathrm{int}} = i\sum_{\vec{k},\lambda} g_{\vec{k},\lambda}\left[a_{\vec{k},\lambda}\exp\left(i\vec{k}\vec{r}\right) - a^\dagger_{\vec{k},\lambda}\exp\left(-i\vec{k}\vec{r}\right)\right]\left(\sigma^+ + \sigma^-\right) \tag{4.10}$$

with the mode function $g_{\vec{k},\lambda} = \sqrt{\omega_k/2\epsilon_0 V}\vec{e}_{\vec{k},\lambda}\cdot\vec{\mu}$, where $\vec{e}_{\vec{k},\lambda}$ is the polarization vector and the dipole matrix element $\vec{\mu} = \left\langle e\middle|\vec{d}\middle|g\right\rangle$ is assumed real without loss of generality. V denotes the quantization volume.

Let us now expand and set $\vec{r}$ to be the position of the atom as the centre of mass, since the phase factor $i\vec{k}\vec{r}$ will vanish later on anyway. We obtain

$$H_{\mathrm{int}} = i\sum_{\vec{k},\lambda} g_{\vec{k},\lambda}\left(a_{\vec{k},\lambda}\sigma^+ + a_{\vec{k},\lambda}\sigma^- - a^\dagger_{\vec{k},\lambda}\sigma^+ - a^\dagger_{\vec{k},\lambda}\sigma^-\right), \tag{4.11}$$

where we have four distinct terms that characterize the possible interactions between the radiation field and our two-level atom. The first and the last term correspond to absorption and emission, respectively, where the energy of the combined system is conserved. The second and third term, however, denote processes where the initial state does not have the same energy as the final state as illustrated in fig 4.2 and we will therefore neglect them in the fashion of the rotating wave approximation.

Thus, we end up with an effective coupling between the atom and the radiation field that reads

$$H_{\mathrm{int}} = i\sum_{\vec{k},\lambda} g_{\vec{k},\lambda}\left(a_{\vec{k},\lambda}\sigma^+ - a^\dagger_{\vec{k},\lambda}\sigma^-\right). \tag{4.12}$$

With this proper interaction Hamiltonian we can now write down Fermi's Golden Rule [133], that allows for calculating transition rates between states in a first order

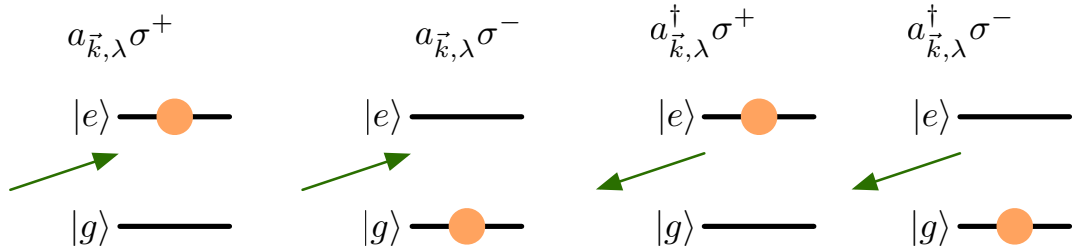

Figure 4.2: *Processes involved* In dipole-approximation there are four processes that can occur, when a two-level atom interacts with a field. Two of them are energy-conserving and are kept in the rotating wave approximation, while the other two are dropped, as discussed in the text.

time-dependent perturbation theory manner. The transition rate is proportional to the transition probability between an initial state $|i\rangle$ and all possible final states $|f_{\vec{k},\lambda}\rangle$ that are coupled by our interaction and reads

$$\Gamma = 2\pi \sum_{\vec{k},\lambda} \left| \left\langle f_{\vec{k},\lambda} \middle| H_{\text{int}} \middle| i \right\rangle \right|^2 \delta\left(\omega_i - \omega_f\right). \tag{4.13}$$

As we aim to study emission from the atom the initial state will be $|i\rangle = |e\rangle \otimes |n_{\vec{k},\lambda}\rangle$ and the final state, where the atom has lost its excitation to the creation of a photon will be $|f\rangle = |g\rangle \otimes |(n+1)_{\vec{k},\lambda}\rangle$. The only non-vanishing contribution to the matrix element will therefore be

$$\begin{aligned} \left\langle f_{\vec{k},\lambda} \middle| H_{\text{int}} \middle| i \right\rangle &= -i \sum_{\vec{k}',\lambda'} g_{\vec{k}',\lambda'} \left\langle f_{\vec{k},\lambda} \middle| a^\dagger_{\vec{k}',\lambda'} \sigma^- \middle| i \right\rangle \\ &= -i g_{\vec{k},\lambda} \sqrt{n_{\vec{k},\lambda} + 1.} \end{aligned} \tag{4.14}$$

Inserting that result back into eq. (4.13) we find

$$\Gamma = 2\pi \sum_{\vec{k},\lambda} \frac{\omega_k}{2\epsilon_0 V} \left| \vec{e}_{\vec{k},\lambda} \cdot \vec{\mu} \right|^2 \left(n_{\vec{k},\lambda} + 1 \right) \delta\left(\omega_i - \omega_f\right), \tag{4.15}$$

where $\omega_i = \omega_0 + n_{\vec{k},\lambda}\omega_k$ and $\omega_f = \left(n_{\vec{k},\lambda} + 1\right)\omega_k$, so $\omega_i - \omega_f = \omega_0 - \omega_k$ ensuring energy conservation.

We now identify two distinct contributions to the emission rate: one that is linear in the number of photons $n_{\vec{k},\lambda}$ present in a particular mode and a term independent of $n_{\vec{k},\lambda}$. The first term corresponds to stimulated emission, where the emitted photons matches the surrounding photons in wave vector and polarization. The second term describes the process of spontaneous emission, which allows for the emerging photon to assume any wave vector and polarization. As we are interested in the rate of this

spontaneous emission only, we will now set $n_{\vec{k},\lambda} = 0$, effectively choosing the vacuum mode $|0_{\vec{k},\lambda}\rangle$ for our initial state.

Next, we need to find a way to sum over all possible wave vectors $\vec{k}$ and both polarizations λ. By calculating the mode volume in reciprocal space to be $(2\pi)^3/V$ and the argument that our quantization volume is much larger than any other involved length scale, we can replace the above sum by the following integral

$$\begin{aligned}
\Gamma =& 2\pi \frac{V}{(2\pi)^3} \sum_{\lambda} \int \mathrm{d}^3k \, \frac{\omega_k}{2\epsilon_0 V} \left| \vec{e}_{\vec{k},\lambda} \cdot \vec{\mu} \right|^2 \delta(\omega_0 - \omega_k) \\
=& \frac{1}{8\pi^2\epsilon_0} \sum_{\lambda} \int \mathrm{d}k \, k^2 \int \mathrm{d}\theta \sin\theta \int \mathrm{d}\varphi \left| \vec{e}_{\vec{k},\lambda} \cdot \vec{\mu} \right|^2 \delta(\omega_0 - \omega_k) \\
=& \frac{1}{8\pi^2\epsilon_0 c^3} \sum_{\lambda} \int \mathrm{d}\omega_k \, \omega_k^2 \int \mathrm{d}\theta \sin\theta \int \mathrm{d}\varphi \left| \vec{e}_{\vec{k},\lambda} \cdot \vec{\mu} \right|^2 \delta(\omega_0 - \omega_k) \\
=& \frac{\omega_0^3}{8\pi^2\epsilon_0 c^3} \sum_{\lambda} \int \mathrm{d}\theta \sin\theta \int \mathrm{d}\varphi \left| \vec{e}_{\vec{k},\lambda} \cdot \vec{\mu} \right|^2
\end{aligned} \tag{4.16}$$

Lastly, it remains to resolve the sum involving the polarizations. To do this, we consider our dipole $\vec{\mu}$ to be oriented along the z-axis and formulate the direction of the wave vector $\vec{k}$ to be $(\sin\theta\cos\varphi, \sin\theta\sin\varphi, \cos\theta)$. Now, we can always rotate our coordinate system about its tangential angle φ in such a way that $\vec{\mu}$ and $\vec{k}$ will have an overlap of $\cos\theta$. For the two polarization vectors it holds, that they must be orthogonal to $\vec{k}$, i.e., $e_{\vec{k},\lambda} \cdot \vec{k} = 0$ and to each other, $e_{\vec{k},\lambda} \cdot e_{\vec{k},\lambda'} = \delta_{\lambda\lambda'}$. There is an additional degree of freedom involved, namely the choice of how the two polarization vectors are rotated about $\vec{k}$ in the plane that is spanned by them. Thus, we can rotate the polarizations so that one of them lies in the plane spanned by $\vec{\mu}$ and $\vec{k}$ and the other one is oriented perpendicularly to that plane. This will yield scalar products of $\mu \cdot e_{\vec{k},1} = \sin\theta$ and $\mu \cdot e_{\vec{k},2} = 0$. For a more visual impression these deliberations are illustrated in fig. 4.3. We have

$$\begin{aligned}
\Gamma =& \frac{\omega_0^3}{8\pi^2\epsilon_0 c^3} \int \mathrm{d}\theta \sin\theta \int \mathrm{d}\varphi \sin^2\theta \mu^2 \\
=& \frac{\omega_0^3 \mu^2}{8\pi^2\epsilon_0 c^3} \int \mathrm{d}\theta \sin\theta \int \mathrm{d}\varphi \sin^2\theta \\
=& \frac{\omega_0^3 \mu^2}{8\pi^2\epsilon_0 c^3} \frac{8\pi}{3} = \frac{\omega_0^3 \mu^2}{3\pi\epsilon_0 c^3}.
\end{aligned} \tag{4.17}$$

Having retrieved the known Wigner-Weisskopf literature result [134] of the spontaneous emission rate Γ, let us finally emphasize its cubic dependence on the transition frequency ω_0 and its quadratic scaling with the atomic transition dipole μ. In the following we will discuss atomic clock transitions that are not necessarily dipole facilitated transitions, but the general principle for deriving the spontaneous emission rate would be largely similar for quadropole or octopole transitions.

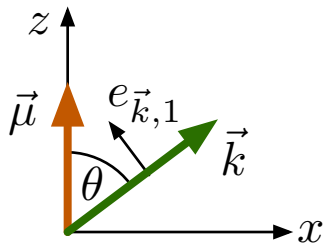

Figure 4.3: *Angles between $\vec{k}$ and $\vec{\mu}$.* This figure visualizes the resolution of the polarization sum of eq. (4.16).

4.3 Ensemble of Emitters

Let us now turn to an ensemble of two-level emitters coupled to the quantized free vacuum and investigate the modifications to the individual single-atom decay rates and emerging collective energy shifts. Again, we will do this in the framework of second quantization. We assume N identical point-like two-level systems with a transition frequency of ω_0, which are placed inside a fixed geometry given by the position vectors $\{\vec{r}_i\}_{i=1}^N$. The emitters are assumed to remain at their position at any time, effectively neglecting atomic motion or collisions. This scenario can be realized almost perfectly in an experiment, where atoms or molecules are loaded into a well-engineered optical lattice and driven to the so-called Mott insulator state [135].

Our approach here follows the original work by Lehmberg in 1970 [136, 137] and is largely based upon the derivation provided in ref. [138]. Again we depart from a Hamiltonian of the form

$$H = H_\mathrm{A} + H_\mathrm{F} + H_\mathrm{int}, \tag{4.18}$$

where

$$H_\mathrm{A} = \omega_0 \sum_{i=1}^{N} \sigma_i^+ \sigma_i^-, \tag{4.19a}$$

$$H_\mathrm{F} = \sum_{\vec{k},\lambda} \omega_k \, a_{\vec{k},\lambda}^\dagger a_{\vec{k},\lambda}, \tag{4.19b}$$

$$H_\mathrm{int} = -\sum_{i=1}^{N} \vec{d}_i \cdot \vec{E}\left(\vec{r}_i\right). \tag{4.19c}$$

We rewrite the interaction Hamiltonian in second quantized form to obtain

$$H_\mathrm{int} = i \sum_{i=1}^{N} \sum_{\vec{k},\lambda} g_{\vec{k},\lambda} \left[a_{\vec{k},\lambda} \exp\left(i\vec{k}\vec{r}_i\right) - \mathrm{h.c.} \right] \left(\sigma_i^+ + \sigma_i^-\right) \tag{4.20}$$

with $g_{\vec{k},\lambda} = \sqrt{\omega_k / 2\epsilon_0 V}\, \vec{e}_{\vec{k},\lambda} \cdot \vec{\mu}$ where we assume an equal orientation and amplitude for the atomic transition dipoles $\vec{\mu}_i = \vec{\mu}$. From that we obtain the equation of motion

for the field operators by writing down their corresponding Heisenberg equation, i.e.

$$\partial_t a_{\vec{k},\lambda} = i\left[H, a_{\vec{k},\lambda}\right] = -i\omega_k a_{\vec{k},\lambda} - g_{\vec{k},\lambda}\sum_{i=1}^{N}\exp\left(-i\vec{k}\vec{r}_i\right)\left(\sigma_i^+ + \sigma_i^-\right), \tag{4.21}$$

which can be solved by means of a retarded Green function and yields

$$\begin{aligned} a_{\vec{k},\lambda}(t) =& a_{\vec{k},\lambda}(t_0)\exp\left(-i\omega_k\left(t-t_0\right)\right) \\ &- \int_{t_0}^{t}\mathrm{d}t'\exp\left(-i\omega_k\left(t-t'\right)\right) g_{\vec{k},\lambda}\sum_{i=1}^{N}\exp\left(-i\vec{k}\vec{r}_i\right)\sigma_i^x\left(t'\right) \end{aligned} \tag{4.22}$$

with, of course, $\sigma_i^x = \sigma_i^+ + \sigma_i^-$. Now, we can put down the equation of motion for any atomic operator O as

$$\begin{aligned} \partial_t O =& i\left[H, O\right] = i\omega_0\sum_{i=1}^{N}\left[\sigma_i^+\sigma_i^-, O\right] - i\sum_{i=1}^{N}\left[\vec{d}\cdot\vec{E}\left(\vec{r}_i, t\right), O\right] \\ =& i\omega_0\sum_{i=1}^{N}\left[\sigma_i^+\sigma_i^-, O\right] - \sum_{\vec{k},\lambda}\sum_{i=1}^{N} g_{\vec{k},\lambda} \\ &\cdot\left(\left[\sigma_i^x, O\right] a_{\vec{k},\lambda}\exp\left(i\vec{k}\vec{r}_i\right) - a_{\vec{k},\lambda}^\dagger\exp\left(-i\vec{k}\vec{r}_i\right)\left[\sigma_i^x, O\right]\right), \end{aligned} \tag{4.23}$$

where we have split up the electric field to introduce normal ordering for the ladder operators, i.e., $a_{\vec{k},\lambda}$ to the left and $a_{\vec{k},\lambda}^\dagger$ to the right. We can now make use of eq. (4.22) and obtain

$$\begin{aligned} \partial_t O =& i\omega_0\sum_{i=1}^{N}\left[\sigma_i^+\sigma_i^-, O\right] \\ &- \sum_{\vec{k},\lambda}\sum_{i=1}^{N} g_{\vec{k},\lambda}\left(\left[\sigma_i^x, O\right] a_{\vec{k},\lambda}(t_0)\exp\left(-i\omega_k\left(t-t_0\right) + i\vec{k}\vec{r}_i\right)\right. \\ &\left. - a_{\vec{k},\lambda}^\dagger\left(t_0(\exp\left(i\omega_k\left(t-t_0\right) - i\vec{k}\vec{r}_i\right)\left[\sigma_i^x, O\right]\right)\right. \\ &+ \sum_{\vec{k},\lambda}\sum_{i=1}^{N}\left(g_{\vec{k},\lambda}\right)^2\int_{t_0}^{t}\mathrm{d}t'\exp\left(-i\omega_k\left(t-t'\right)\right) \\ &\cdot\sum_{i,j}\exp\left(i\vec{k}\vec{r}_{ij}\right)\left[\sigma_i^x(t), O(t)\right]\sigma_j^x\left(t'\right) \\ &- \sum_{\vec{k},\lambda}\sum_{i=1}^{N}\left(g_{\vec{k},\lambda}\right)^2\int_{t_0}^{t}\mathrm{d}t'\exp\left(i\omega_k\left(t-t'\right)\right) \\ &\cdot\sum_{i,j}\exp\left(-i\vec{k}\vec{r}_{ij}\right)\sigma_j^x\left(t'\right)\left[\sigma_i^x(t), O(t)\right] \end{aligned} \tag{4.24}$$

with $\vec{r}_{ij} := \vec{r}_i - \vec{r}_j$ being the distance between the positions of atoms i and j. Now, let us replace the sum over the modes $\vec{k}, \lambda$ by an integral over the entire mode space, similar to what we did for a single atom in sec. 4.2, i.e., $\sum_{\vec{k},\lambda} \to V/(2\pi)^3 \int \mathrm{d}^3k$. Furthermore, we will use the fact that $\vec{k} \perp e_{\vec{k},1} \perp e_{\vec{k},2}$ and thus

$$\sum_{\lambda} \left| \vec{\mu} \cdot e_{\vec{k},\lambda} \right|^2 = \mu^2 \left(1 - \left(e_{\vec{\mu}} \cdot e_{\vec{k}} \right)^2 \right), \tag{4.25}$$

where we define the unit vectors $e_{\vec{\mu}} = \vec{\mu}/\mu$ and $e_{\vec{k}} = \vec{k}/k$, and continue abbreviating the contribution from the incident field by $\mathcal{E}_{\mathrm{in}}(t)$,

$$\begin{aligned}
\partial_t O =& \mathcal{E}_{\mathrm{in}}(t) \\
&+ \frac{\mu^2}{2\epsilon_0 (2\pi c)^3} \sum_{i,j} \int_\Omega \mathrm{d}\Omega_{\vec{k}} \left(1 - \left(e_{\vec{\mu}} \cdot e_{\vec{k}} \right)^2 \right) \int_{t_0}^{t} \mathrm{d}t' \int_0^\infty \mathrm{d}\omega \\
&\quad \cdot \omega^3 \exp\left(-i\omega \left(t - t' - e_{\vec{k}} \vec{r}_{ij}/c \right) \right) \left[\sigma_i^x(t), O(t) \right] \sigma_j^x\left(t'\right) \\
&- \frac{\mu^2}{2\epsilon_0 (2\pi c)^3} \sum_{i,j} \int_\Omega \mathrm{d}\Omega_{\vec{k}} \left(1 - \left(e_{\vec{\mu}} \cdot e_{\vec{k}} \right)^2 \right) \int_{t_0}^{t} \mathrm{d}t' \int_0^\infty \mathrm{d}\omega \\
&\quad \cdot \omega^3 \exp\left(i\omega \left(t - t' - e_{\vec{k}} \vec{r}_{ij}/c \right) \right) \sigma_j^x\left(t'\right) \left[\sigma_i^x(t), O(t) \right].
\end{aligned} \tag{4.26}$$

Next, we neglect the retardation and perform the Markov approximation [139] by substituting

$$\sigma_j^x\left(t'\right) \to \sigma_j^+(t) \exp\left(i\omega_0 \left(t' - t \right) \right) + \sigma_j^-(t) \exp\left(-i\omega_0 \left(t' - t \right) \right), \tag{4.27}$$

which leads us to

$$\begin{aligned}
\partial_t O =& \mathcal{E}_{\mathrm{in}}(t) \\
&+ \frac{\mu^2}{2\epsilon_0 (2\pi c)^3} \sum_{i,j} \int_\Omega \mathrm{d}\Omega_{\vec{k}} \left(1 - \left(e_{\vec{\mu}} \cdot e_{\vec{k}} \right)^2 \right) \int_0^\infty \mathrm{d}\omega \\
&\cdot \omega^3 \exp\left(i\omega e_{\vec{k}} \vec{r}_{ij}/c \right) \left[\sigma_i^x(t), O(t) \right] \\
&\cdot \left[\left(-i\mathcal{P} \frac{1}{\omega + \omega_0} + \pi\delta\left(\omega + \omega_0\right) \right) \sigma_j^+(t) \right. \\
&\left. + \left(-i\mathcal{P} \frac{1}{\omega - \omega_0} + \pi\delta\left(\omega - \omega_0\right) \right) \sigma_j^-(t) \right] \\
&- \frac{\mu^2}{2\epsilon_0 (2\pi c)^3} \sum_{i,j} \int_\Omega \mathrm{d}\Omega_{\vec{k}} \left(1 - \left(e_{\vec{\mu}} \cdot e_{\vec{k}} \right)^2 \right) \int_0^\infty \mathrm{d}\omega \\
&\cdot \omega^3 \exp\left(-i\omega e_{\vec{k}} \vec{r}_{ij}/c \right) \left[\left(i\mathcal{P} \frac{1}{\omega - \omega_0} + \pi\delta\left(\omega - \omega_0\right) \right) \sigma_j^+(t) \right. \\
&\left. + \left(i\mathcal{P} \frac{1}{\omega + \omega_0} + \pi\delta\left(\omega + \omega_0\right) \right) \sigma_j^-(t) \right] \left[\sigma_i^x(t), O(t) \right].
\end{aligned} \tag{4.28}$$

Now, we integrate over the solid angle (cf. below) and applying the rotating wave approximation neglect fast oscillating terms, so that

$$\begin{aligned}\partial_t O =&\mathcal{E}_{\text{in}}(t)\\ &+\sum_{i,j}\left[\sigma_i^x(t), O(t)\right]\frac{\Gamma}{k_0^3}\int_0^\infty \frac{\mathrm{d}k}{2\pi}k^3\, F\left(kr_{ij}\right)\\ &\cdot\left[\left(-i\mathcal{P}\frac{1}{k+k_0}+\pi\delta\left(k+k_0\right)\right)\sigma_j^+(t)\right.\\ &\left.+\left(-i\mathcal{P}\frac{1}{k-k_0}+\pi\delta\left(k-k_0\right)\right)\sigma_j^-(t)\right]\\ &-\sum_{i,j}\frac{\Gamma}{k_0^3}\int_0^\infty \frac{\mathrm{d}k}{2\pi}k^3\, F\left(kr_{ij}\right)\\ &\cdot\left[\sigma_j^+(t)\left(i\mathcal{P}\frac{1}{k-k_0}+\pi\delta\left(k-k_0\right)\right)\right.\\ &\left.+\sigma_j^-(t)\left(i\mathcal{P}\frac{1}{k+k_0}+\pi\delta\left(k+k_0\right)\right)\right]\left[\sigma_i^x(t), O(t)\right],\end{aligned} \tag{4.29}$$

where we have implicitly defined

$$F\left(kr\right) := \frac{3}{2}\int_\Omega \frac{\mathrm{d}\Omega_k}{4\pi}\left(1-\left(e_{\vec{\mu}}\cdot e_{\vec{k}}\right)^2\right)\exp\left(i\vec{k}\cdot\vec{r}\right). \tag{4.30}$$

From this we can now abbreviate the quantities corresponding to collective energy shifts and emission rates as

$$\Gamma_{ij} =\Gamma F\left(k_0 r_{ij}\right) \tag{4.31}$$

$$\Omega_{ij}^{\pm} =\frac{\Gamma}{k_0^3}\,\mathcal{P}\int_0^\infty \frac{\mathrm{d}k}{2\pi}\frac{k^3 F\left(kr_{ij}\right)}{k\pm k_0}, \tag{4.32}$$

where we have anticipated the result for Γ_{ij} upon integration with $\delta\left(k-k_0\right)$, while the integration with $\delta\left(k+k_0\right)$ will yield zero. Now, our equation of motion simplifies drastically and reads

$$\begin{aligned}\partial_t O =&\mathcal{E}_{\text{in}}(t)\\ &+\sum_{i,j}\left[\sigma_i^x(t), O(t)\right]\left[\left(-i\Omega_{ij}^+\right)\sigma_j^+(t)+\left(-i\Omega_{ij}^-+\frac{\Gamma_{ij}}{2}\right)\sigma_j^-(t)\right]\\ &-\sum_{i,j}\left[\left(i\Omega_{ij}^-+\frac{\Gamma_{ij}}{2}\right)\sigma_j^+(t)+\left(i\Omega_{ij}^+\right)\sigma_j^-(t)\right]\left[\sigma_i^x(t), O(t)\right].\end{aligned} \tag{4.33}$$

Finally, we drop fast oscillating terms like $\sigma_i^+\sigma_j^+$ and $\sigma_i^-\sigma_j^-$ when resolving $\sigma^x =$

$\sigma^+ + \sigma^-$ and we get

$$\begin{aligned}\partial_t O =& \mathcal{E}_{\text{in}}(t) \\ &+ \sum_{i,j} \left[\sigma_i^-(t), O(t)\right] \left(-i\Omega_{ij}^+\right) \sigma_j^+(t) \\ &+ \sum_{i,j} \left[\sigma_i^+(t), O(t)\right] \left(-i\Omega_{ij}^- + \frac{\Gamma_{ij}}{2}\right) \sigma_j^-(t) \\ &- \sum_{i,j} \left(i\Omega_{ij}^- + \frac{\Gamma_{ij}}{2}\right) \sigma_j^+(t) \left[\sigma_i^-(t), O(t)\right] \\ &+ \sum_{i,j} \left(i\Omega_{ij}^+\right) \sigma_j^-(t) \left[\sigma_i^+(t), O(t)\right]\end{aligned} \tag{4.34}$$

and by collecting terms we obtain the final form of our equation, which is often referred to as a 'Quantum Langevin equation', i.e.

$$\begin{aligned}\partial_t O =& i \sum_i \left[\left(\omega_0 - \Omega_{ii}^+\right) \sigma_i^+(t)\sigma_i^-(t) - \Omega_{ii}^- \sigma_i^-(t)\sigma_i^+(t), O(t)\right] \\ &+ i \sum_{i \neq j} \left[\Omega_{ij}\, \sigma_i^-(t)\sigma_j^+(t), O(t)\right] \\ &+ \frac{1}{2} \sum_{i,j} \Gamma_{ij} \left(2\sigma_i^+(t) O(t) \sigma_j^-(t)\right. \\ &\left. - \sigma_i^+(t)\sigma_j^-(t) O(t) - O(t)\sigma_i^+(t)\sigma_j^-(t)\right).\end{aligned} \tag{4.35}$$

At this point we go back to the Schrödinger picture and put down the equation of motion for our density operator ρ describing the (mixed) state of our system and we end up with the 'Optical Bloch equations'

$$\partial_t \rho = i\,[\rho, H] + \mathcal{L}\,[\rho] \tag{4.36}$$

where the first part containing the Hamiltonian

$$H = \sum_i \omega_0\, \sigma_i^+ \sigma_i^- + \sum_{i \neq j} \Omega_{ij}\, \sigma_i^- \sigma_j^+ \tag{4.37}$$

describes the coherent energy-conserving part of the interaction, while the second part, often referred to as 'Liouvillian super-operator',

$$\mathcal{L}\,[\rho] = \frac{1}{2} \sum_{i,j} \Gamma_{ij} \left(2\sigma_i^- \rho \sigma_j^+ - \sigma_i^+ \sigma_j^- \rho - \rho \sigma_i^+ \sigma_j^-\right) \tag{4.38}$$

accounts for the dissipation from the system into its environment. Its first term, the so-called recycling term ensures that the overall population in the system remains constant by shuffling population that is reduced in higher energy states to those with

a lower energy, while the second and third term decrease the population in higher energy states. In this form the equation is also dubbed 'master equation'. The two geometry-dependent model parameters Γ_{ij} and Ω_{ij} can be written compactly as

$$\Omega_{ij} = \Gamma G\left(k_0 r_{ij}\right) \qquad \Gamma_{ij} = \Gamma F\left(k_0 r_{ij}\right) \tag{4.39}$$

with

$$G\left(\xi\right) = -\frac{3}{4}\left[\left(1-\cos^2\theta\right)\frac{\cos\xi}{\xi} - \left(1-3\cos^2\theta\right)\left(\frac{\sin\xi}{\xi^2}+\frac{\cos\xi}{\xi^3}\right)\right] \tag{4.40}$$

$$F\left(\xi\right) = \frac{3}{2}\left[\left(1-\cos^2\theta\right)\frac{\sin\xi}{\xi} + \left(1-3\cos^2\theta\right)\left(\frac{\cos\xi}{\xi^2}-\frac{\sin\xi}{\xi^3}\right)\right] \tag{4.41}$$

and $\cos\theta = e_{\vec{\mu}} \cdot e_{\vec{r}_{ij}}$ as defined above.

Let us now quantitatively discuss the system's behaviour as a function of its geometry, i.e., the distance dependence of the couplings Ω_{ij} and Γ_{ij}. Fig 4.4 demonstrates this for $\theta = 0$ (dipoles oriented along the direction of their alignment) and for $\theta = \pi/2$ (dipoles oriented perpendicularly to their alignment). We can clearly see that the interactions in the intermediate range of $0.2 < \xi < 1$ are much more pronounced when $\theta = \pi/2$.

Additionally, we observe that $F\left(\xi\right) \to 1$ for $\xi \to 0$ and $G\left(\xi\right)$ will diverge to $\pm\infty$ for $\xi \to 0$. Both functions will approach zero, i.e., $F\left(\xi\right) = G\left(\xi\right) = 0$ for $\xi \to \infty$. In essence, these properties lead to two prominent limiting cases. First, for $\xi \to 0$, we neglect the diverging energy shifts and realize that because of $F\left(\xi\right) = 1$ the collective decay rates become identical, $\Gamma_{ij} = \Gamma$, which is oftentimes referred to as the Dicke model [140], in which one can reduce the Hilbert space of N two-level systems to one effective spin $N/2$. The other limiting case, where $F\left(\xi\right)$ both vanish and $\Gamma_{ij} = \delta_{ij}\Gamma$ describes two-level emitters infinitely far apart from each other and thus as effectively independent.

4.3.1 Auxiliary relations

For the time integral, we rewrite the expression as a Cauchy principal value and retrieve an additional Dirac delta distribution according to the Sokhotski-Plemelj theorem [141–143]. We have

$$\int_{t_0\to-\infty}^{t} \mathrm{d}t' \exp\left(-i\left(\omega - i\epsilon \pm \omega_0\right)\left(t-t'\right)\right) = \frac{1}{i\left(\omega - i\epsilon \pm \omega_0\right)} \tag{4.42}$$

and when integrating over ω this becomes

$$\frac{1}{i\left(\omega \pm \omega_0\right)} \to -i\mathcal{P}\frac{1}{\omega \pm \omega_0} + \pi\delta\left(\omega \pm \omega_0\right) \tag{4.43}$$

as well as

$$\int_{t_0\to-\infty}^{t} \mathrm{d}t' \exp\left(i\left(\omega - i\epsilon \pm \omega_0\right)\left(t-t'\right)\right) = \frac{1}{-i\left(\omega - i\epsilon \pm \omega_0\right)}, \tag{4.44}$$

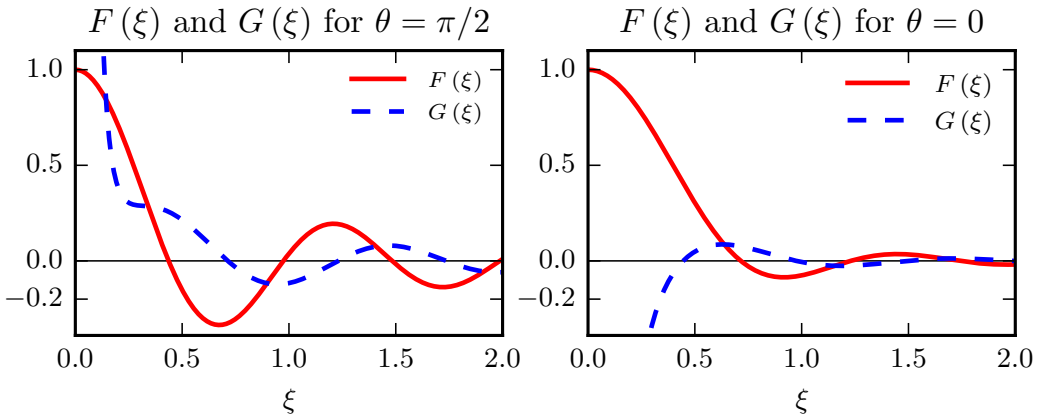

Figure 4.4: *Dissipative and coherent couplings $F(\xi)$ and $G(\xi)$.* Here, $\xi = r_{ij}/\lambda_0$ and $\lambda_0 = 2\pi/k_0$, i.e., we have scaled the arguments with a factor of 2π for the plots.

which in the ω-integral becomes

$$\frac{1}{-i(\omega \pm \omega_0)} \to i\mathcal{P}\frac{1}{\omega \pm \omega_0} + \pi\delta(\omega \pm \omega_0). \tag{4.45}$$

For the angular integral we pull out the derivative with respect to $\vec{r}$ and get

$$\begin{aligned} F(kr) &= \int_\Omega \mathrm{d}\Omega_{\vec{k}} \left[1 - \left(e_{\vec{\mu}} \cdot e_{\vec{k}}\right)^2\right] \exp\left(i\vec{k}\cdot\vec{r}\right) \\ &= \left[1 - \frac{\left(e_{\vec{\mu}}\cdot\nabla_r\right)^2}{k^2}\right] \int_\Omega \mathrm{d}\Omega_{\vec{k}} \exp\left(i\vec{k}\cdot\vec{r}\right) \\ &= \left[1 - \frac{\left(e_{\vec{\mu}}\cdot\nabla_r\right)^2}{k^2}\right] \int_0^{2\pi} \mathrm{d}\varphi_{\vec{k}} \int_0^{\pi} \mathrm{d}\theta_{\vec{k}} \sin\theta_{\vec{k}} \exp\left(ikr\cos\theta_{\vec{k}}\right) \\ &= \left[1 - \frac{\left(e_{\vec{\mu}}\cdot\nabla_r\right)^2}{k^2}\right] \frac{4\pi\sin(kr)}{kr}, \end{aligned} \tag{4.46}$$

where we have used $\vec{k}\cdot\vec{r} = kr\cos\theta$ and solved the integration as the spherical Bessel function of the first kind. Now, for evaluating the gradient we choose $e_{\vec{\mu}} = e_z$ and have

$$\begin{aligned} \left(e_z\cdot\nabla_{\vec{r}}\right)^2 \frac{\sin(kr)}{kr} &= \left(e_z\cdot\nabla_{\vec{r}}\right)\left(e_z\cdot e_r\partial_r\right)\frac{\sin(kr)}{kr} \\ &= \left(e_z\cdot\nabla_{\vec{r}}\right) k\,\cos\theta\cdot\left(\frac{\cos(kr)}{kr} - \frac{\sin(kr)}{(kr)^2}\right) \end{aligned} \tag{4.47}$$

and for the second derivative

$$\begin{aligned}\cdots &= \left(e_z \cdot \left(e_r\partial_r + e_\theta \frac{1}{r}\partial_\theta\right)\right) k\,\cos\theta \cdot \left(\frac{\cos(kr)}{kr} - \frac{\sin(kr)}{(kr)^2}\right) \\ &= \left(\cos\theta\partial_r - \frac{\sin\theta}{r}\partial_\theta\right) k\,\cos\theta \cdot \left(\frac{\cos(kr)}{kr} - \frac{\sin(kr)}{(kr)^2}\right) \\ &= k^2\cos^2\theta\left(-\frac{\sin(kr)}{kr} - \frac{2\cos(kr)}{(kr)^2} + \frac{2\sin(kr)}{(kr)^3}\right) \\ &+ k^2\sin^2\theta\left(\frac{\cos(kr)}{(kr)^2} - \frac{\sin(kr)}{(kr)^3}\right).\end{aligned} \tag{4.48}$$

Collecting terms and inserting into the original equation in eq. (4.30) with $\xi := kr_{ij}$ we obtain

$$F(\xi) = \frac{3}{2}\left[\left(1-\cos^2\theta\right)\frac{\sin\xi}{\xi} + \left(1-3\cos^2\theta\right)\left(\frac{\cos\xi}{\xi^2} - \frac{\sin\xi}{\xi^3}\right)\right], \tag{4.49}$$

where now $\cos\theta := e_{\vec{\mu}} \cdot e_{\vec{r}_{ij}}$ is the angle the vector connecting the emitters i and j draws with the direction of the transition dipole moment.

For the calculation of $\Omega_{ij} = -\Omega_{ij}^+ - \Omega_{ij}^-$, we realize that

$$\int_0^\infty \mathrm{d}k\, k^3 \frac{F(kr_{ij})}{k+k_0} = \int_{-\infty}^0 \mathrm{d}k\, k^3 \frac{F(kr_{ij})}{k-k_0}, \tag{4.50}$$

since $F(kr_{ij})$ is an even function. Thus, we can combine the two integrals to write down

$$\Omega_{ij} = -\frac{\Gamma}{\xi_0^3}\int_{-\infty}^\infty \frac{\mathrm{d}\xi}{2\pi}\xi^3 \frac{F(\xi)}{\xi-\xi_0} \tag{4.51}$$

with $\xi_0 := k_0 r_{ij}$ and reinterpret the expression as the real part of a complex path integral

$$\begin{aligned}\Omega_{ij} = &-\frac{\Gamma}{\xi_0^3}\lim_{\epsilon\to 0}\Re\oint\frac{\mathrm{d}\xi}{2\pi}\frac{1}{\xi-\xi_0-i\epsilon} \\ &\cdot\frac{3}{2}\left[\left(1-\cos^2\theta\right)\xi^2\frac{\exp(i\xi)-\exp(-i\xi)}{2i} + \left(1-3\cos^2\theta\right)\right. \\ &\left.\cdot\, s\left(\xi\frac{\exp(i\xi)+\exp(-i\xi)}{i} - \frac{\exp(i\xi)-\exp(-i\xi)}{2i}\right)\right].\end{aligned} \tag{4.52}$$

For the terms involving $\exp(i\xi)$ we close the integration path in the upper half-plane and pick up the residue at $\xi = \xi_0 0 + i\epsilon$. For the terms involving $\exp(-i\xi)$ we need to

close the integration path in the lower half-plane, where there is no residue. We get

$$\begin{aligned}\Omega_{ij} =& -\frac{\Gamma}{\xi_0^3}\frac{1}{2\pi}\lim_{\epsilon\to 0}\Re\, 2\pi i\left[\left(1-\cos^2\theta\right)\xi^2\frac{\exp\left(i\xi\right)}{2i}\right.\\ &+\left(1-3\cos^2\theta\right)\left.\left(\xi\frac{\exp\left(i\xi\right)}{2}-\frac{\exp\left(i\xi\right)}{2i}\right)\right]_{\xi=\xi_0+i\epsilon}\\ =& -\frac{3\Gamma}{4}\left[\left(1-\cos^2\theta\right)\frac{\cos\xi_0}{\xi_0}\right.\\ &-\left.\left(1-3\cos^2\theta\right)\left(\frac{\sin\xi_0}{\xi_0^2}+\frac{\cos\xi_0}{\xi_0^3}\right)\right],\end{aligned} \tag{4.53}$$

which concludes our derivation.

4.4 Super- and Subradiance

In order to illustrate the concept of enhanced (decreased) collective spontaneous emission by virtue of constructive (destructive) interference of the emitted light, we will particularize our general formalism from above to two two-level emitters. The bare atomic states present in the system can be written as

$$\left\{|gg\rangle, |eg\rangle, |ge\rangle, |ee\rangle\right\}, \tag{4.54}$$

where the position of g and e indicates, whether we are referring to the first or the second atom. The Hamiltonian of our system reads

$$H = \omega_0\left(\sigma_1^+\sigma_1^- + \sigma_2^+\sigma_2^-\right) + \Omega\left(\sigma_1^+\sigma_2^- + \sigma_1^-\sigma_2^+\right), \tag{4.55}$$

which by diagonalization provides us with the system's eigenstates introduced by the dipole-dipole interaction $\Omega = \Gamma G\left(k_0 r\right)$. They are given by

$$|G\rangle = |gg\rangle \tag{4.56a}$$

$$|S\rangle = \frac{1}{\sqrt{2}}\left(|eg\rangle + |ge\rangle\right) \tag{4.56b}$$

$$|A\rangle = \frac{1}{\sqrt{2}}\left(|eg\rangle - |ge\rangle\right) \tag{4.56c}$$

$$|E\rangle = |ee\rangle \tag{4.56d}$$

with their corresponding energies $E_E = 2\omega_0$, $E_S = \omega_0 + \Omega$, $E_A = \omega_0 - \Omega$, $E_G = 0$. Those states were first introduced by Dicke [140] and $|S\rangle$ and $|A\rangle$ are also referred to as Bell states, especially in quantum information. In such a spin-1-system, a triplet manifold with $|E\rangle$, $|S\rangle$ and $|G\rangle$, and a singlet manifold with $|A\rangle$ exists, The states $|S\rangle$ and $|A\rangle$ in the single-excitation manifold constitute a prime example for maximally entangled states, as they cannot be written as a product of single-atom states, which

is a result of the interatomic interaction. We can clearly see that $|G\rangle$ and $|E\rangle$ are not influenced by the collective couplings and remain at their respective energies, while the symmetric state $|S\rangle$ is shifted upwards by Ω and the asymmetric state $|A\rangle$ is shifted down by the same amount, thus implicitly lifting the degeneracy between the two. The shift Ω can become very large at small interatomic separations up to the point where the shift would become infinite and therefore the model breaks down. This would usually happen at the order of the Bohr radius $a_0 =$, where molecule formation comes into play.

Given the eigenstates of the system we can perform the following transformation,

$$\sigma_1^+ = \frac{1}{\sqrt{2}} \left(|E\rangle \langle S| - |E\rangle \langle A| + |S\rangle \langle G| + |A\rangle \langle G| \right) \tag{4.57a}$$

$$\sigma_2^+ = \frac{1}{\sqrt{2}} \left(|E\rangle \langle S| + |E\rangle \langle A| + |S\rangle \langle G| - |A\rangle \langle G| \right) \tag{4.57b}$$

allowing us to write down the Liouvillian as

$$\mathcal{L}[\rho] = \mathcal{L}_S[\rho] + \mathcal{L}_A[\rho] \tag{4.58}$$

with

$$\begin{aligned} \mathcal{L}_S[\rho] = & \frac{\Gamma + \gamma}{2} \left[2 \left(|S\rangle \langle E| + |G\rangle \langle S| \right) \rho \left(|E\rangle \langle S| + |S\rangle \langle G| \right) \right. \\ & \left. - \left(|E\rangle \langle E| + |S\rangle \langle S| \right) \rho - \rho \left(|E\rangle \langle E| + |S\rangle \langle S| \right) \right] \end{aligned} \tag{4.59a}$$

$$\begin{aligned} \mathcal{L}_A[\rho] = & \frac{\Gamma - \gamma}{2} \left[2 \left(|A\rangle \langle E| + |G\rangle \langle A| \right) \rho \left(|E\rangle \langle A| + |A\rangle \langle G| \right) \right. \\ & \left. - \left(|E\rangle \langle E| + |A\rangle \langle A| \right) \rho - \rho \left(|E\rangle \langle E| + |A\rangle \langle A| \right) \right] \end{aligned} \tag{4.59b}$$

and we define $\gamma_S := \Gamma + \gamma$ and $\gamma_A := \Gamma - \gamma$, where $\gamma = \Gamma F(k_0 r)$.

From these deliberations it is evident that our two-atom system features two independent, i.e., non-overlapping, decay channels. First, we have $|E\rangle \to |S\rangle \to |G\rangle$, which we will dub superradiant for $F(k_0 r) > 0$, as decay takes place with an increased spontaneous emission rate γ_S. Secondly, there is $|E\rangle \to |A\rangle \to |G\rangle$ with a decreased emission rate γ_A. Thus, we will call this channel subradiant. For $F(k_0 r) < 0$, the roles of the superradiant and the subradiant decay channel interchange. In the limit of $F(k_0 r \to 0) = 1$, decay of the asymmetric state will vanish completely and the entire system dynamic is captured by the three states $|E\rangle$, $|S\rangle$, $|G\rangle$. If we generalize this to larger systems, it suffices to investigate the so-called Dicke states on the surface of the collective Bloch sphere [140], which are basically the symmetric states in every excitation manifold as any other states will have zero decay rates and no overlapping matrix elements with the decaying states. Sometimes these are also called bright states as they are the only ones that couple to the radiation field and can therefore be populated by it. The non-decaying non-coupled states are then referred to as dark states. Figure 4.5 illustrates the energy shifts and decay cascades present in the system.

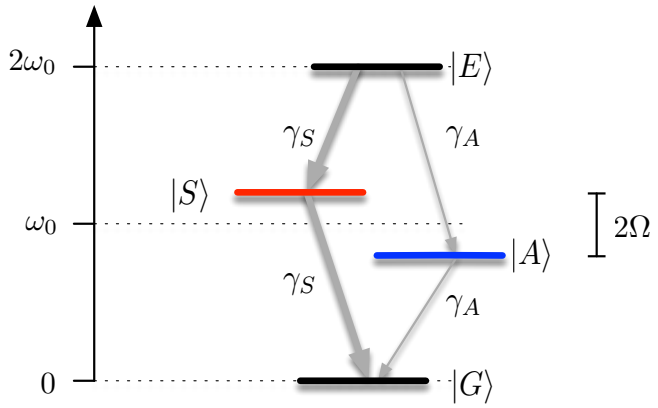

Figure 4.5: *Super- and subradiance in two atoms.* The symmetric state $|S\rangle$ and the asymmetric state $|A\rangle$ are shifted from the bare atomic energy by $\pm\Omega$. There are two non-interacting decay channels: the superradiant one involving the symmetric state with the rate $\gamma_S = \Gamma + \gamma$ and the subradiant one with $\gamma_A = \Gamma + \gamma$ involving the asymmetric state.

5 Publication: Cascaded Collective Decay in Regular Arrays of Cold Trapped Atoms

The present publication, which constitutes the first publication making up this doctoral thesis focuses on the study of super- and subradiance in extended toy models of up to four atoms. When looking at more than two atoms the situation quickly becomes drastically more involved as there are not just two decay channels anymore and the separation between them becomes far less simple. The aim of this paper is to investigate these toy models and, most importantly, study the effects of collective decay on spectroscopic techniques like the Ramsey procedure. The paper has been published in Optics Express on December 31st, 2012 [144].

Abstract

Energy and lifetime of collective optical excitations in regular arrays of atoms and molecules are significantly influenced by dipole-dipole interaction. While the dynamics of closely positioned atoms can be approximated well by the Dicke superradiance model, the situation of finite regular configurations is hard to access analytically. Most treatments use an exciton based description limited to the lowest excitation manifold. We present a general approach studying the complete decay cascade of a finite regular array of atoms from the fully inverted to the ground state. We explicitly calculate all energy shifts and decay rates for two generic cases of a three-atom linear chain and an equilateral triangle. In numerical calculations we show that despite fairly weak dipole-dipole interactions, collective vacuum coupling allows for superradiant emission as well as subradiant states in larger arrays through multi-particle interference. This induces extra dephasing and modified decay as important limitations for Ramsey experiments in lattice atomic clock setups as well as for the gain and frequency stability of superradiant lasers.

5.1 Introduction

The spontaneous decay of an excited atom arises due to its coupling to vacuum fluctuations of the electromagnetic field as first proposed by Dirac and later analyzed

by Wigner and Weisskopf. Dicke [145] showed that the vacuum coupling of several identical atoms at almost the same position leads to correlations among the atoms and as a result to collective superradiant spontaneous emission. In general, the decay rate of low energy collective excitations grows linearly with the particle number N. The resulting collective decay exhibits a delayed intensity maximum proportional to N^2 as a significant deviation from the exponential decay of individual atoms [146, 147] and is called '*superradiance*'. The phenomenon has been observed in a large number of experiments in gases and solids [146, 148] and recently also for ultracold quantum gases [149, 150].

The basic phenomenon of superradiance was widely studied theoretically already decades ago using a variety of analytical approximation methods [151, 152] with a particularly comprehensive and detailed review by Haroche [147]. These treatments are mostly based on spatially well-confined samples neglecting finite distance dipole-dipole interactions or other near-field effects as Van der Waals shifts by collisions (see [147] for the limits). While in such small-sample configurations all atoms are exposed to the same environment (vacuum fluctuations) and virtually indistinguishable, in extended systems of atoms or molecules, as e.g., in optical lattices, this approach has to be refined to account for finite interaction and correlation lengths. In systems with finite resonant dipole-dipole interactions along with a lattice symmetry, the lowest energy eigenstates are given by coherent collective electronic excitations in the material, called 'excitons' [153]. Due to their wave-like periodic structure excitons can feature superradiance as well [154]. Interestingly, it has been noted only very recently, that also subradiant exciton states can appear in regular optical lattices [155]. In previous work, we studied the energies and lifetimes of such excitons for ultracold atoms in 1D and 2D optical lattices [155, 156] and in more general configurations . In most cases it was sufficient to limit ourselves to electrostatic dipole-dipole interactions and consider coupling among nearest-neighbour sites only. Such collective states were also considered by other authors, e.g., [157].

In contrast to these treatments, in the present paper we will investigate the full model for the collective decay process of a few atoms involving multiple excitations up to the fully inverted state. We refrain from any limiting size and distance approximations and in particular do not restrict ourselves to the single-excitation manifold. While the underlying equations for the dynamics are well-established, exact analytic treatments of the full decay problem for more than two particles are hardly possible and apart from some special cases, we have to rely on numerical solutions. Besides exhibiting the underlying basic physical mechanisms of decay channels, correlation buildup and entanglement, our study aims at direct implications for atomic clock configurations based on magic wavelength lattices [40], optical storage of qubits in atomic ensembles and ultrastable superradiant lasers [158–160]. Here, super- and subradiance can play a decisive limiting or helpful role, as e.g., the Ramsey signal crucially depends on the remaining excited state population at the time of the second pulse.

To some extent important physical effects can be seen already in the simplest

configuration of two two-level atoms with identical transition wavelength λ_0 as a function of the interatomic distance r [138]. As each particle can decay, the doubly excited state exhibits twice the single atom damping rate to a singly excited state. Depending on the distance r the excitation distributes differently among the two single-excitation atomic eigenstates, which due to dipole-dipole interaction are given by a symmetric and an anti-symmetric superposition of the two dipoles. For small distances, i.e., $r/\lambda_0 \ll 1$, the symmetric state becomes populated dominantly and is superradiant, while the anti-symmetric one is almost dark. At large distances, $r/\lambda_0 \gg 1$, the damping rate of both states tends to the one of a single atom leading to quite different effective dynamics. Here, everything can be calculated explicitly in an analytical fashion.

For more particles the situation becomes much more difficult to solve immediately, since already for the first step we get an increasing number of intermediate states with the total physical Hilbert space growing as 2^N. We will show that analytical results can still be obtained for some special configurations, like a regular triangle, while most calculations need to be performed numerically.

The paper is organized as follows: in section 2 we describe the model and exhibit the dependence of the interaction terms on its geometry. In section 3 we review general properties and present an analytical solution for three atoms positioned in an equilateral triangle and compare it to the numerical solution for three atoms in a chain. Finally we study superradiance in larger systems and its implications on physical applications numerically.

5.2 Model

Let us consider N identical two-level systems held in a regular spaced configuration e.g., in a far detuned optical lattice. We describe the spontaneous decay process by common dipole coupling of the atoms to the free space radiation modes in vacuum state. Upon rotating wave and Markov approximation one ends up with a standard Lindblad type master equation including dipole-dipole interaction [136]. Explicitly, the time-evolution of the density operator is governed by

$$\frac{\partial\hat{\rho}}{\partial t} = -\frac{i}{\hbar}\left[\hat{H},\hat{\rho}\right] - \mathcal{L}_{\mathrm{cd}}\left[\hat{\rho}\right], \tag{5.1}$$

with the Hamiltonian

$$\hat{H} = \sum_i \hbar\omega_0 S_i^+ S_i^- + \sum_{i\neq j} \hbar\Omega_{ij} S_i^+ S_j^- . \tag{5.2}$$

The above master equation could also be formulated using a non-Hermitian Hamiltonian, as e.g., in [161], which is equivalent to our formulation. Here, S_i^+ and S_i^- are the rising and lowering operators for the atomic dipole of the i-th atom with the atomic transition energy given by $\hbar\omega_0$, and Ω_{ij} denotes the resonant dipole-dipole energy

transfer between the atoms i and j. The collective damping is accounted for by the Liouvillian

$$\mathcal{L}_{\mathrm{cd}}\left[\hat{\rho}\right] = \frac{1}{2}\sum_{i,j}\Gamma_{ij}\left(S_i^+ S_j^-\,\hat{\rho} + \hat{\rho}S_i^+ S_j^- - 2S_i^-\,\hat{\rho}S_j^+\right) \tag{5.3}$$

with Γ_{ij} being generalized spontaneous emission rates arising from the coupling of the atomic transition dipoles through the vacuum field [162].

Note, that collective coupling and decay matrices $[\Omega_{ij}]$ and $[\Gamma_{ij}]$ possess non-diagonal elements, which have to be calculated as a function of the system's geometry and its relative angle θ to the atomic dipoles μ_i. In many cases due to the finite correlation length of vacuum fluctuations these non-diagonal parts can be safely neglected. Here, we assume the same linear dipole moments and orientation for all particles ($\mu_i = \mu$) and $\mathbf{r}_{ij} = \mathbf{r}_i - \mathbf{r}_j$ denotes the vector connecting the atom's positions. Fortunately, the damping Liouvillian is bilinear in the dipole moment operators, so that the total interaction is composed of pairwise terms depending on the relative coordinates only. Thus, for identical atoms we have [138]

$$\Gamma_{ij} = \frac{3\Gamma}{2}F\left(k_0 r_{ij}\right) \text{ and } \Omega_{ij} = \frac{3\Gamma}{4}G\left(k_0 r_{ij}\right) \tag{5.4}$$

with Γ the single-atom linewidth, $k_0 = \omega_0/c = 2\pi/\lambda_0$ and

$$\begin{aligned} F\left(\xi\right) &= \left(1-\cos^2\theta\right)\frac{\sin\xi}{\xi} + \left(1-3\cos^2\theta\right)\left(\frac{\cos\xi}{\xi^2} - \frac{\sin\xi}{\xi^3}\right), \\ G\left(\xi\right) &= -\left(1-\cos^2\theta\right)\frac{\cos\xi}{\xi} + \left(1-3\cos^2\theta\right)\left(\frac{\sin\xi}{\xi^2} + \frac{\cos\xi}{\xi^3}\right), \end{aligned} \tag{5.5}$$

where $\xi = k_0 r_{ij}$.

It is noteworthy to point out that $F\left(\xi \to 0\right) = 2/3$, $G\left(\xi\right)$ diverges for $\xi \to 0$ and $F\left(\xi \to \infty\right) = G\left(\xi \to \infty\right) = 0$. As a reminder and for later reference the two (scaled) functions for $\theta = \pi/2$ are shown in fig. 5.1. For this work we will be concerned with lattice constants (atomic distances) large enough to keep the effect of the divergence small only. For the collective states of two atoms it is possible to find distances d at which there is either no energy shift, $G(k_0 d) = 0$, or no modified spontaneous emission, $F(k_0 d) = 0$. Due to the non-periodicity of F and G this cannot be achieved for more than two atoms in a periodic arrangement. Similarly one can expect the most significant effects to occur at distances where either F or G has an extremal value, which also cannot be fulfilled for all atoms in a regular array.

As a first step in investigating the decay properties of the collective states of the system, we will consider the energy eigenstates including the dipole-dipole couplings Ω_{ij}. In this basis the Hamiltonian can be rewritten in diagonal form

$$\hat{H} = \sum_k \hbar\omega_k S_k^+ S_k^-, \tag{5.6}$$

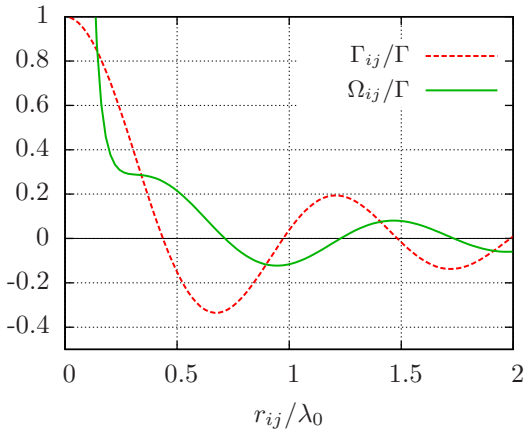

Figure 5.1: Collective spontaneous emission Γ_{ij}/Γ and resonant dipole-dipole coupling Ω_{ij}/Γ for $\theta = \pi/2$ as a function of inter-atomic distance in units of the resonant wavelength λ_0.

where the energies ω_k depend on the geometry. When we represent $\mathcal{L}_{\text{cd}}$ in this same basis, we see that only in very special cases the Liouvillian gets diagonal as well. In these special cases spontaneous decays occur between these same eigenstates only, which allows for a simple analytical treatment of the entire system. In the general case, however, $\hat{H}$ and $\mathcal{L}_{\text{cd}}$ have different eigenstates. Hence, spontaneous decay processes will lead to superpositions of energy eigenstates inducing oscillatory dynamics and we need to resort to a numerical analysis. An approach based on the damping basis leads to equivalent phenomena as it will not diagonalize the Hamiltonian. Despite these problems, a diagonalization of the $|\Gamma_{ij}]$ and $[\Omega_{ij}]$ matrices can be at least performed numerically, even for hundreds of atoms. Important properties of energy shifts and decay rates appearing in the system can be obtained from their eigenvalues without the need to solve the full dynamics in the excessively large corresponding Hilbert space. To get some intuitive insight intro their connection to the full system dynamics we will study this relation closely by investigating special fully solvable simple examples.

5.3 Collective System Dynamics and Examples

5.3.1 General Results

At first we will exhibit some general features of the dynamics. Interestingly, independent of the geometry we find that the totally inverted state $|e\rangle$ with all N atoms in the excited state will always decay with a collective emission rate of $\Gamma_e = \sum_i \Gamma = N\Gamma$. The state $|e\rangle$ is also a simultaneous eigenstate of the Hamiltonian with energy $E_e = N\hbar\omega_0$

without any interaction shifts and the Liouvillian with the decay

$$\sum_{i,j} \Gamma_{ij} S_i^+ S_j^- \left|e\right\rangle \left\langle e\right| = \sum_{i,j} \Gamma_{ij} \delta_{ij} \left|e\right\rangle \left\langle e\right| = \sum_i \Gamma_{ii} \left|e\right\rangle \left\langle e\right| = \Gamma_e \left|e\right\rangle \left\langle e\right|. \tag{5.7}$$

In physical terms this means that each atom decays independently as the emitted photon cannot be reabsorbed by any other atom and no atomic coherence or field is present to facilitate interference effects. This coincides with the Dicke state prediction of closely spaced atoms. The number of possible final states of this first decay process nevertheless grows with the atom number N and the rate Γ_e is split among many possible paths. The resulting state manifold is closely related to the exciton states containing only a single excitation, but with the role of ground and excited state reversed. This manifold now includes super- and subradiant states and in the successive steps even more channels become available until half of the energy is dissipated.

As a second general result we present the collective decay rate of the single-excitation symmetric state of N identical atoms,

$$\left|s\right\rangle = \frac{1}{\sqrt{N}} \sum_{i=1}^{N} \left|g_1 \ldots e_i \ldots g_n\right\rangle, \tag{5.8}$$

which corresponds to the zero-momentum exciton in a chain of lattice constant a. This decay rate can be derived analytically as shown in [163] and gives

$$\Gamma_s(N) = \Gamma \left[1 + 2 \sum_{n=1}^{N-1} \left(1 - \frac{n}{N}\right) F\left(k_0 a n\right)\right]. \tag{5.9}$$

We see that the spontaneous decay rate is collectively enhanced by pairwise interactions and can grow linearly with particle number for small chains as predicted by the Dicke model [147]. For longer chains the long-range contributions become small and the enhancement saturates with chain length. In fig. 5.2 the damping rate of the symmetric state for different lattice constants is shown for $\theta = 0$ and $\theta = \pi/2$ as a function of the number of atoms constituting the chain. The chain's length is $L = (N-1)a$. Let us remark here that the scattering intensity in a particular directional mode can still grow for large N but the solid angle of this mode shrinks so that the effect on the total decay rate decreases and the effective lifetime will saturate. This is good news for atomic lattice clocks, which in this case will not suffer too much from superradiant decay.

Throughout this work we will mainly concentrate on ^{87}Sr as a specific example. To trap these atoms one usually uses a 'magic wavelength' optical lattice, which refers to the specific wavelength to minimize or even eliminate the differential light shift in the ^{87}Sr $^1S_0 \rightarrow ^3P_0$ clock transition. This wavelength turns out to be $\lambda_m = 813.5 \pm 0.9\,\mathrm{nm}$ [164]. The optical lattice will confine the atoms at a distance of $\lambda_m/2$ [165] which given in units of the transition wavelength [166] will be

$$\frac{\lambda_m}{2\lambda_0} \approx 0.5824. \tag{5.10}$$

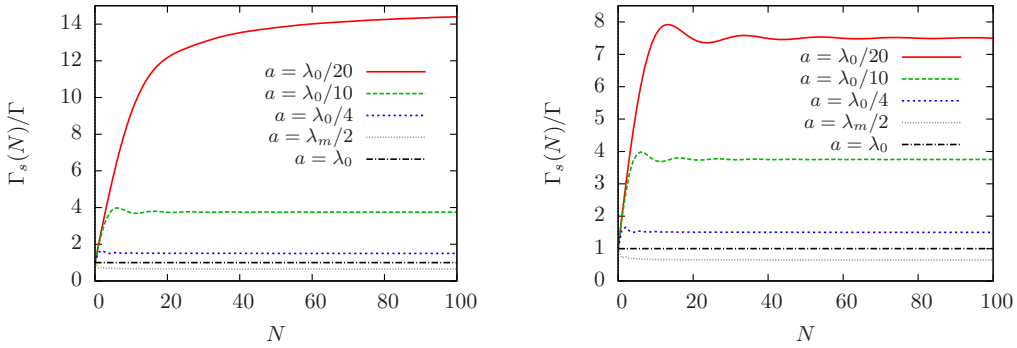

Figure 5.2: Symmetric exciton state decay rate $\Gamma_s(N)/\Gamma$ as function of atom number for $\theta = 0$ (left) and $\theta = \pi/2$ (right).

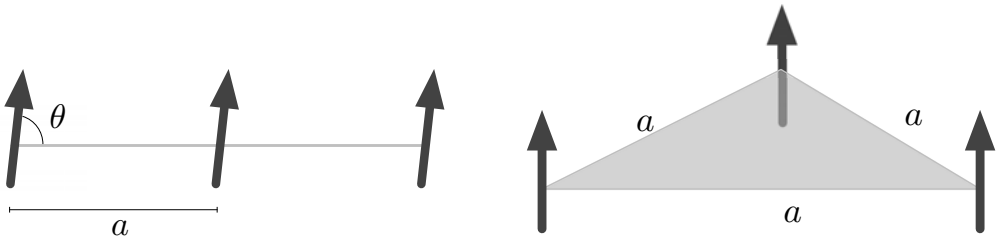

Figure 5.3: Linear chain and triangular array of three atoms with lattice constant a and angle θ.

As a matter of fact we will see that at the magic wavelength even subradiance can appear for long lattices, which should prolong the available T_1-time for readout.

5.3.2 Three Particle Regular Arrays

In this section we will investigate two different regular geometric arrangements for $N = 3$. We compare a linear chain, where we go beyond the single excitation and nearest-neighbour coupling limits, discussed in [155], to an equilateral triangle, which has the advantage of being fully analytically treatable. Let us point out, that for two atoms, e.g., [145], the particular relative arrangement is irrelevant, and therefore the system can always be handled analytically.

Linear Chain

First, we consider a linear chain of lattice constant a, where the angle between the atomic dipoles and the direction of the chain is given by θ (see fig. 5.3).

State	Involved bare states	E	$\Delta\left(\frac{\lambda_0}{2}\right)$	$\Delta\left(\frac{\lambda_m}{2}\right)$
$\|e\rangle$	$\|eee\rangle$	$3\omega_0$	0	0
$\|2_z\rangle$	$\|eeg\rangle + \beta_1 \|ege\rangle + \|gee\rangle$	$2\omega_0$	0.25	0.18
$\|2_x\rangle$	$-\|eeg\rangle + \|gee\rangle$	$2\omega_0$	0.12	0.04
$\|2_y\rangle$	$\|eeg\rangle - \beta_2 \|ege\rangle + \|gee\rangle$	$2\omega_0$	−0.37	−0.21
$\|1_z\rangle$	$\|gge\rangle + \beta_1 \|geg\rangle + \|egg\rangle$	ω_0	0.25	0.18
$\|1_x\rangle$	$-\|gge\rangle + \|egg\rangle$	ω_0	0.12	0.04
$\|1_y\rangle$	$\|gge\rangle - \beta_2 \|geg\rangle + \|egg\rangle$	ω_0	−0.37	−0.21
$\|g\rangle$	$\|ggg\rangle$	0	0	0

Table 5.1: Collective states (non-normalized) and energy shifts Δ [Hz] for lattice constants $a = \lambda_0/2$ and $a = \lambda_m/2$. $\beta_1 \approx 1.71$, $\beta_2 \approx 1.18$ (for $a = \lambda_0/2$).

The collective states that arise from the dipole-dipole interaction are listed in table 5.1, where the values that have been chosen for the numerical treatment are $\omega_0 = 10^{14}\,\mathrm{Hz}$, $\Gamma = 1\,\mathrm{Hz}$ and thus with $a = \lambda_0/2$ and $\theta = \pi/2$ we obtain $\Omega_{12} = \Omega_{23} = 0.21\,\mathrm{Hz}$ and $\Omega_{13} = -0.12\,\mathrm{Hz}$, as well as $\Gamma_{12} = \Gamma_{23} = -0.15\,\mathrm{Hz}$ and $\Gamma_{13} = 0.04\,\mathrm{Hz}$. The energy shifts Δ of the collective states are independent from ω_0 and can be expressed in terms of the collective parameters as $-\Omega_{13}$ and $\left(\Omega_{13} \pm \sqrt{8\Omega_{12}^2 + \Omega_{13}^2}\right)/2$.

With this we can now study the system's decay properties for arbitrary initial preparations. Figure 5.4 (right) depicts the decay from the $|2_z\rangle$ state, which involves all three single excitation states $|1_x\rangle$, $|1_y\rangle$ and $|1_z\rangle$ and finally populates the ground state $|g\rangle$. The initial state decays exponentially and 'feeds' the intermediate states whose populations (per feeding state) over time obey

$$\rho_{\mathrm{interm}}(t) = A\left[1 - \exp\left(-\nu t\right)\right]\exp\left(-\gamma t\right), \tag{5.11}$$

where A is the amplitude, ν denotes the feeding rate responsible for increasing the population and γ is the state's decay rate. In this manner we have studied the system's behaviour for arbitrary initial preparations, where our results are summarized in table 5.2. Here, the diagonal entries refer to the states' decay rates, while the off-diagonal ones describe the feeding rate from an upper to a lower state. A scheme visualizing the various decay channels is given in fig. 5.4 (left).

Let us point out that the decay rates of the single-excitation states correspond exactly to the eigenvalues of the matrix $[\Gamma_{ij}]$, that can be built up from the Γ_{ij}, since $\sigma\left([\Gamma_{ij}]\right) = \{1.23, 0.96, 0.81\}$, while the decay rates of the doubly excited states are larger by exactly one Γ.

Equilateral triangle

Now, we consider an arrangement of the atoms in an equilateral triangle of length a with the atomic dipoles drawing a right angle to the plane of the triangle (see fig. 5.3).

	e	2_z	2_x	2_y	1_z	1_x	1_y	g
e	3							
2_z	1.19	1.81						
2_x	1.04		196					
2_y	0.77			2.23				
1_z		0.99	1.18	1.38	0.81			
1_x		0.87	1.00	1.30		0.96		
1_y		0.52	0.76	1.00			1.23	
g					0.81	0.96	1.23	0

Table 5.2: [Hz] Decay (diagonal entries) and feeding rates for the collective states in a chain of lattice constant $a = \lambda_0/2$.

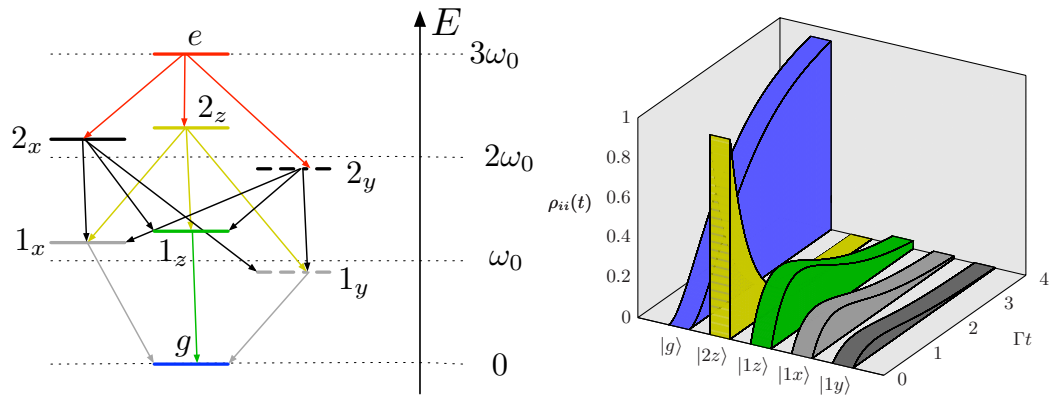

Figure 5.4: Decay scheme (left) and cascade dynamics from $|2_z\rangle$ state via the single-excitation states $|1_z\rangle$, $|1_x\rangle$ and $|1_y\rangle$ to the ground state for a chain with spacing $a = \lambda_0/2$.

State	Involved bare states	E	Δ
$\|e\rangle$	$\|eee\rangle$	$3\omega_0$	0
$\|s^2\rangle$	$\|eeg\rangle + \|ege\rangle + \|gee\rangle$	$2\omega_0$	2Ω
$\|a^2\rangle$	$\|eeg\rangle - 2\,\|ege\rangle + \|gee\rangle$	$2\omega_0$	$-\Omega$
$\|b^2\rangle$	$-\,\|eeg\rangle + \|gee\rangle$	$2\omega_0$	$-\Omega$
$\|s^1\rangle$	$\|gge\rangle + \|geg\rangle + \|egg\rangle$	ω_0	2Ω
$\|a^1\rangle$	$\|gge\rangle - 2\,\|geg\rangle + \|egg\rangle$	ω_0	$-\Omega$
$\|b^1\rangle$	$-\,\|gge\rangle + \|egg\rangle$	ω_0	$-\Omega$
$\|g\rangle$	$\|ggg\rangle$	0	0

Table 5.3: Collective states (non-normalized) in the equilateral triangle with $\Omega = 3\Gamma G(k_0 a)/4$.

Due to the fact that in this particular configuration $\Omega_{ij} = \Omega$ and $\Gamma_{ij} = \gamma$ for all $i \neq j$ the coefficient matrices $[\Omega_{ij}]$ and $[\Gamma_{ij}]$ assume the same structure. As a consequence, the Hamiltonian as well as the Liouvillian are diagonal in the same basis, which allows for an analytical discussion of the system.

Again, we diagonalize the Hamiltonian, where the diagonal states with their energy are put down in table 5.3. In this setup, since all mutual couplings have the same value Ω, the states $|a\rangle$ and $|b\rangle$ are degenerate, as they experience the same energy shift. Notice the fairly close correspondence to the states that appear in the chain (table 5.1). Moreover, the existence of two symmetric states $|s^1\rangle$ and $|s^2\rangle$ shall be pointed out, which is a consequence of the uniform mutual coupling as well.

Figure 5.5 shows the decay from the fully inverted state $|e\rangle$ for $a = \lambda_0/5$, corresponding to $\gamma = 0.71\Gamma$. Notice, that the majority of the population decays via the symmetric channels. For a negative γ the symmetric states $|s^i\rangle$ (yellow and green) feature a diminished decay rate, while the states $|a^i\rangle$ and $|b^i\rangle$, which employ the same behaviour (black and grey) become superradiant. As above, we show the decay and feeding rates in table 5.4.

The decay scheme for this situation looks quite similar to the one of the chain (Figure 5.4), except that for one and two excitations there is only one state with a positive energy shift, while the other two states are degenerate and shifted downwards.

In fig. 5.6 (left) we compare the decay process to the ground state for a magic wavelength distance ($a = \lambda_m/2$, dashed line) and close positioning of the atoms ($a = \lambda_0/5$, solid line). The decay of the fully inverted state is not affected by the system's geometry and will therefore show the same exponential decay for any configuration.

For $\gamma = \Gamma$ the symmetric decay channel $|e\rangle \to |s^2\rangle \to |s^1\rangle \to |g\rangle$ decouples from the two channels $|a^2\rangle \to |a^1\rangle$ and $|b^2\rangle \to |b^1\rangle$, where the latter two will not decay to the ground state, yielding two dark states in the single-excitation manifold. For

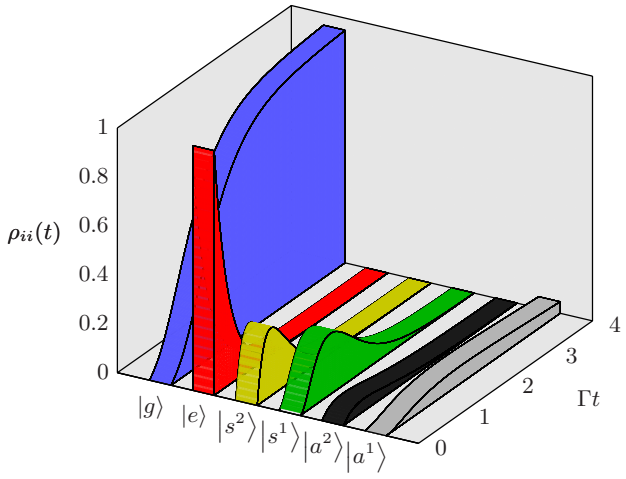

Figure 5.5: Decay from the fully inverted state via $|s^2\rangle$, $|a^2\rangle$ (and $|b^2\rangle$, which due to the degeneracy shows the sam behaviour) and the single-excitation states $|s^1\rangle$ and $|a^1\rangle$ (and $|b^1\rangle$) to the ground state for $\gamma = 0.71\Gamma$ ($a = \lambda_0/5$).

	e	s^2	a^2	b^2	s^1	a^1	b^1	g
e	3Γ							
s^2	$\Gamma - 2\gamma$	$2\Gamma + 2\gamma$						
a^2	$\Gamma + \gamma$		$2\Gamma - \gamma$					
b^2	$\Gamma + \gamma$			$2\Gamma - \gamma$				
s^1		Γ	$\Gamma - 3\gamma$	$\Gamma - 3\gamma$	$\Gamma + 2\gamma$			
a^1		$\Gamma + 3\gamma$	Γ	Γ		$\Gamma - \gamma$		
b^1		$\Gamma + 3\gamma$	Γ	Γ			$\Gamma - \gamma$	
g					$\Gamma + 2\gamma$	$\Gamma - \gamma$	$\Gamma - \gamma$	0

Table 5.4: Decay rates (diagonal entries) and feeding rates for the equilateral triangle where we have a uniform collective spontaneous emission rate $\gamma = \Gamma_{ij}$.

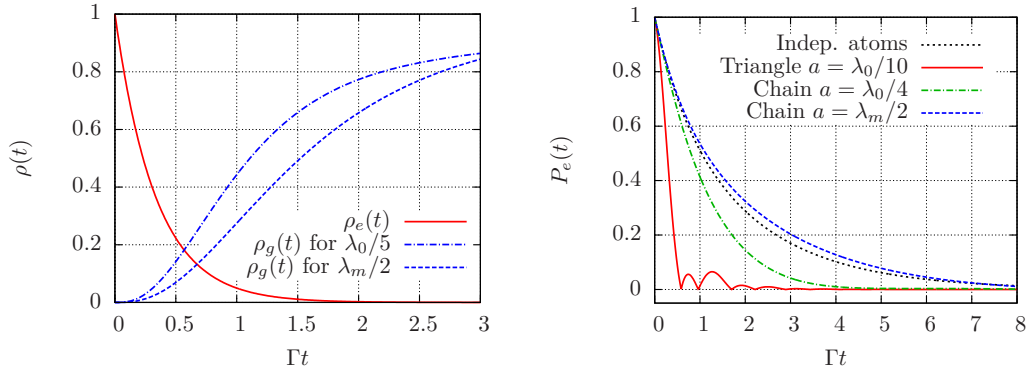

Figure 5.6: Collective decay from fully excited state to the ground state in the equilateral triangle for $a = \lambda_0/5$ and $a = \lambda_m/2$ (left) and its influence on the maximal Ramsey signal contrast for independent atoms, atoms closely positioned in a triangle as well as in a chain (green) and at magic wavelength-distance (right).

$\gamma = 0$ the system behaves as independent two-level subsystems and no distinction in terms of emission rates can be made. Again, we observe, that the decay rates for the single-excitation states coincide with the eigenvalues of the $[\Gamma_{ij}]$-matrix, which are $\sigma([\Gamma_{ij}]) = \{\Gamma + 2\gamma, \Gamma - \gamma\}$.

5.4 Superradiance in Larger Extended Arrays

One characteristic feature of Dicke superradiance is the pulsed emission with an increase of the energy emission as a function of time in an initial pulse buildup phase [160]. We will now study this phenomenon in our finite spaced arrays and look at the system's energy emission given by $W(t) = -\partial_t \langle \hat{H} \rangle_{\hat{\rho}(t)}$. For very close atoms in the Dicke limit where decay occurs only via the symmetric states, the maximum occurs exactly when half of the energy is lost and is given by $W_{\max}(N)/\Gamma = N(N+2)/4$. This is strongly modified when other decay channels get mixed due to finite atom-atom distance, even for two atoms only [167]. Surprisingly, as shown in the following numerical solutions of the master equation, one obtains an effectively much smaller maximum of the energy emission, $W_{\max}$, for finite lattice constants. In fig. 5.7 the maximum emission intensity relative to the initial decay rate of the fully inverted state is depicted as a function of the number of atoms in the chain for different lattice constants. The distance d_f is the first root of F, namely $F(k_0 d_f) = 0$, and d_g is the first root of G, analogously. We note that the closer the atoms are positioned in the chain the more obvious the superradiant nature of the system becomes, but even for $a\lambda_0/10$ we are far from the values of the Dicke case. Even a small contribution of

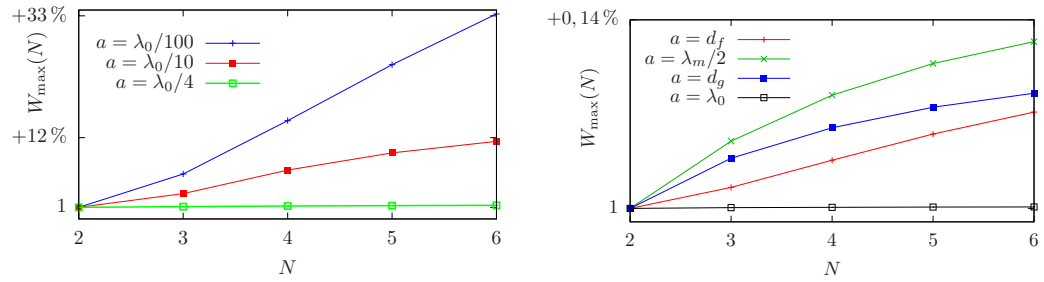

Figure 5.7: Maximum of the energy emission as a function of the number of atoms in the chain for small (left) and large (right) lattice constants a. The distances d_f and d_g refer to the first root of the functions F and G, respectively.

slowly decaying states has a a large influence due to their long lifetime. On the other hand, even for larger lattice constants, i.e., $a > \lambda_0/2$, the emission per atom increases with the number of atoms in contrast to independent decay.

5.4.1 Ramsey Signal

As the decay of excitation is directly accompanied by loss of atomic coherence, enhanced decay rates influence the spectroscopic properties of the collective system. As a practical example we consider two-pulse Ramsey spectroscopy, where the first $\pi/2$-pulse prepares a product state of half-exited atoms, which potentially exhibit strong superradiance. Using the two generic three-atom configurations discussed above, we now study the maximum possible Ramsey signal contrast, which emerges if we start with all atoms in the ground state, apply a resonant $\pi/2$-pulse ('Hadamard'-gate) with the same phase to each atom, then leave the systems to its free dynamics, and after a time t apply a second $\pi/2$-pulse (once in-phase and once with a phase shift of π), again to each atom with the same phase and look at the difference of these two signals. Figure 5.6 (right) shows the survival probability of the fully inverted state $|e\rangle$ as a function of the time t in between the two pulses for independent atoms (black), close positioning in a triangle (red), where dispersive dephasing via Ω_{ij} occurs, a chain of lattice constant $a = \lambda_0/4$ (green), where we observe a superradiant decay via Γ_{ij}, and the magic wavelength chain (blue), which is clearly subradiant.

5.5 Conclusions and Outlook

We have shown that despite the system size being much larger than a wavelength, collective effects in the decay and energy shifts of atoms in regular optical lattices will lead to important changes in the system dynamics. In conjunction with the appearance of fast decay via superradiant states, one usually also finds subradiant channels and states, where the population can be trapped and which feature different energy shifts. In general, we see that superradiance can persist in spatially distributed arrays to a surprising extent, but it will be accompanied by subradiant states, so that we get a large spread in the behaviour of individual trajectories. In contrast, for average quantities the changes get less and less significant.

The discussion in the present paper, even though presented in the language of ultracold atoms in optical lattices, can be adopted for any set-up of ordered active materials, e.g., an array of semiconductor quantum dots, a chain of colour centres in solids, or a cluster of organic molecules. Collective states in these structures can play a key role in the physical implementation of quantum information processing, and their lifetimes are critical in this context. Furthermore, these phenomena can be relevant in the context of cooling molecules by superradiant emissions [168].

Acknowledgements

We thank Sebastian Krämer for his help with the numerics and acknowledge support by DARPA through the QUASAR project.

6 Publication: Protected State Enhanced Quantum Metrology in Dense Ensembles of Two-Level Emitters

In this letter, we propose an alteration of the well-established Ramsey spectroscopy procedure in the presence of dipole-dipole interaction. We suggest to phase-spread the atomic coherences after the first $\pi/2$-pulse and undo the spread before the second $\pi/2$-pulse. As a proof of principle, we have investigated this idea for two atoms and see that the sensitivity could be improved significantly. We go on to analyzing the concept for larger systems and perform numerical simulations. This work was published in Physical Review Letters on September 18th, 2013 [169].

Abstract

Ramsey interferometry is routinely used in quantum metrology for the most sensitive measurements of optical clock frequencies. Spontaneous decay to the electromagnetic vacuum ultimately limits the interrogation time and thus sets a lower bound to the optimal frequency sensitivity. In dense ensembles of two-level systems the presence of collective effects such as superradiance and dipole-dipole interaction tends to decrease the sensitivity even further. We show that by a redesign of the Ramsey-pulse sequence to include different rotations of individual spins that effectively fold the collective state onto a state close to the centre of the Bloch sphere, partial protection from collective decoherence is possible. This allows a significant improvement in the sensitivity limit of a clock transition detection scheme over the conventional Ramsey method for interacting systems and even for non-interacting decaying atoms.

6.1 Introduction

The precise measurement of time using suitable atomic transitions is a major achievement of quantum metrology. The Ramsey interferometry procedure plays a crucial role as it allows an accurate locking of the microwave or optical oscillator to the transition frequency in the atom. Typical early realizations were based on atomic beams or later on laser-cooled atomic fountains [75], where the atoms would interact with two consecutive Rabi pulses. With optical lattices [40, 165] time measurements

were expected to become even more accurate due to longer interaction times and the elimination of collisions (see [170, 171] for recent reviews). To reduce quantum projection noise (scaling as $1/\sqrt{N}$ for N atoms) and to speed up the measurement, setups usually involve an as large as possible number of atoms. In a finite volume, of course, this brings collective effects like superradiance and dipole-dipole shifts to the table [144]. While some techniques rely on the engineering of particular geometries without the need to alter the internal atomic states [107], exploiting the uncertainty principle by employing squeezed states [172–174] can be helpful as well to achieve less noise with lower atom numbers [175, 176]. These techniques rely heavily on entanglement [177, 178] among atoms and require very careful preparation and isolation of the ensemble.

When, finally, interrogation times reached the lifetime of the excited state, spontaneous emission became a critical factor for the contrast of the Ramsey fringes. Interestingly, despite the use of long lived clock states, for multiple atoms in close proximity to each other, collective spontaneous emission can still reach a detrimental magnitude, namely proportional to the atom number [136, 138]. While this is usually limited to volumes of the order of a cubic wavelength, in regular arrays, such as an optical lattice, the effect can extend over tens of lattice sites [179].

In this paper, we propose a strategy that works on the level of the Ramsey pulses and which we dub the 'asymmetric Ramsey technique', in contrast to the conventional symmetric Ramsey technique that employs only identical $\pi/2$ pulses applied to all atoms. While the conventional Ramsey technique excites superposition states, which possess a maximum dipole moment and thus are most sensitive to superradiance, this new approach allows the selection of long-lived collective states (or 'dark states') to improve the sensitivity of the clock signal. The procedure requires a modification of the Ramsey steps: after the initial $\pi/2$ pulse is applied, each atomic coherence is rotated by a distinct phase, resulting in a subradiant collective state with vanishing classical dipole (with a lifetime which can be even longer than that of the independent atoms [156]). The detection procedure is then followed leading to a significant improvement in the sensitivity limit over the conventional Ramsey technique.

6.2 Model

We assume N identical two-level emitters with levels $|g\rangle$ and $|e\rangle$ separated by ω_0 in a geometry defined by $\mathbf{r}_i$ for $i = 1, ...N$. For the Pauli ladder operators $\sigma_i^{\pm}$ and subsequently $\sigma_i^x = \sigma_i^+ + \sigma_i^-$, $\sigma_i^y = -i(\sigma_i^+ - \sigma_i^-)$ and $\sigma_i^z = \sigma_i^+\sigma_i^- - \sigma_i^-\sigma_i^+$ unitary rotations $\mathcal{R}_\mu^{(j)}[\varphi] = \exp\left(i\varphi\,\sigma_j^\mu/2\right)$ where $\mu \in \{x, y, z\}$ are defined.

The independent atom decay rates are Γ; the cooperative nature of decay for atom pairs i, j is reflected by mutual decay rates Γ_{ij} (in the following we use $\Gamma_{ii} = \Gamma$). Via the vacuum, dipole-dipole interactions occur characterized by the frequency shifts Ω_{ij}. Both functions depend on r_{ij} [144]. The dynamics of the system can be described via

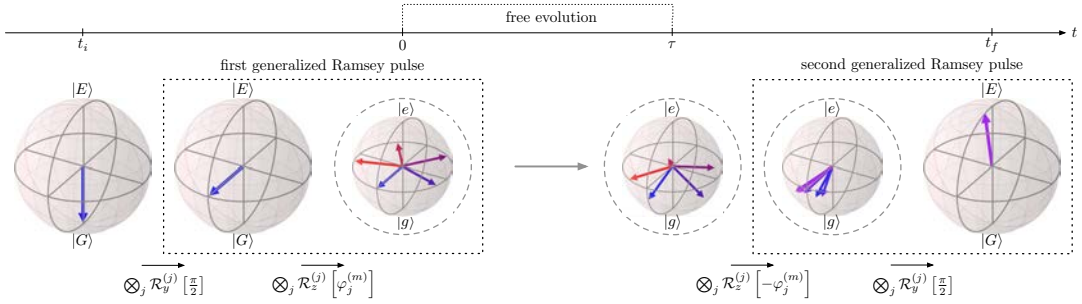

Figure 6.1: *State protective Ramsey sequence.* The ensemble of N spins starts with all spins down in a collective coherent pure spin state on the surface of the collective Bloch sphere (radius $N/2$). Individual $\pi/2$ pulses are followed by phase encoding operations of angles $\varphi_j^{(m)} = (2\pi m/N)(j-1)$ where $j = 1, ...N$ and $m = 1, ...[N/2]$, which brings the total spin close to the centre of the Bloch sphere (third-fifth steps are shown on small Bloch spheres of radius $1/2$). After time τ, the phase encoding operation is reversed and $\pi/2$ pulses prepare the ensemble (now in a mixed state shown on the large collective Bloch sphere) for the detection of the population difference signal.

the master equation

$$\frac{\partial \rho}{\partial t} i[\rho, H] + \mathcal{L}[\rho], \tag{6.1}$$

where the Hamiltonian is given by

$$H = \frac{\omega}{2} \sum_i \sigma_i^z + \sum_{i \neq j} \Omega_{ij}\, \sigma_i^+ \sigma_j^- \tag{6.2}$$

with $\omega = \omega_0 - \omega_l$ (ω_l is the reference frequency) and the Liouvillian is

$$\mathcal{L}[\rho] = \frac{1}{2} \sum_{i,j} \Gamma_{ij} \left[2\sigma_i^- \rho\, \sigma_j^+ - \sigma_i^+ \sigma_j^- \rho - \rho\, \sigma_i^+ \sigma_j^- \right]. \tag{6.3}$$

A typical procedure in spectroscopic experiments is the Ramsey method of separated oscillatory fields [64]. The sequence assumes the ensemble of spins initiated in the ground state at time t_i such that $\langle S^z \rangle(t_i) = -N/2$ where $S^z = \sum_i \sigma_i^z/2$. Three stages follow: (i) a quick pulse between t_i and $t = 0$ rotates the atoms into a collective state in the xy-plane that exhibits maximal dipole, (ii) free evolution for the time τ and (iii) a second quick pulse flips the spins up. The detected signal is a measure of population inversion and therefore proportional to $\langle S^z \rangle(t_f)$. Analysis of this signal gives the sensitivity as a figure of merit in metrology

$$\delta\omega = \min \left[\frac{\Delta S^z(\omega, \tau)}{|\partial_\omega \langle S^z \rangle(\omega, \tau)|} \right], \tag{6.4}$$

where the minimization is performed with respect to ω.

We follow the dynamics as described above in a density matrix formalism. We start with $\rho_i = |G\rangle\langle G|$, transform it into $\rho_0 = \mathcal{R}_1 \rho_i \mathcal{R}_1^\dagger$, evolve it into ρ_τ by solving eq. (6.1) and finally transform it into $\rho_f = \mathcal{R}_2 \rho_\tau \mathcal{R}_2^\dagger$. The detected signal and its variance are computed as $\langle S^z \rangle$ and ΔS^z from ρ_f.

As a basis of comparison, we take independent systems ($\Gamma_{ij} = 0$ and $\Omega_{ij} = 0$ for $i \neq j$). The rotation pulses are $\mathcal{R}_1 = \mathcal{R}_2 = \bigotimes_j \mathcal{R}_y^{(j)}[\pi/2]$ and the resulting sensitivity is

$$[\delta\omega]_{\text{indep}} = \min\left[\frac{\sqrt{e^{\Gamma\tau} - \cos^2(\omega\tau)}}{\sqrt{N}\,|\tau \cdot \sin(\omega\tau)|}\right] = \frac{e^{\Gamma\tau/2}}{\tau\sqrt{N}}. \tag{6.5}$$

Further optimization with respect to the interrogation time gives an optimal $\tau_{\text{opt}} = 2/\Gamma$ and optimal sensitivity $\Gamma e/2\sqrt{N}$, which shows that the main impediment of Ramsey interferometry is the limitation in the interrogation times owing to the decay of the dipoles.

As a principal advance of this paper, we propose a generalized Ramsey sequence (as illustrated in fig. 6.1) that deviates from the typical one by a redesign of the two pulses at times $t = 0$ and $t = \tau$, intended to drive the spin system into states that are protected from the environmental decoherence. To accomplish this, one complements the normal $\pi/2$ pulse with a phase distribution pulse, which for a particular atom j is represented by a rotation around the z-direction with the angle $\varphi_j^{(m)} = 2\pi m(j-1)/N$, where $m = 1, ...[N/2]$ and $[N/2]$ is the integer before $N/2$. The first Ramsey pulse operator is then

$$\mathcal{R}_1 = \bigotimes_j \mathcal{R}_z^{(j)}\left[\varphi_j^{(m)}\right] \cdot \mathcal{R}_y^{(j)}\left[\frac{\pi}{2}\right].$$

To justify the choice of the rotation angles notice that at time $t = 0$, for any set of $\varphi_j^{(m)}$, the system is in a state of zero average collective spin: at an intuitive level this means that the phase-spread operation folds the system collective state from the surface of the Bloch sphere onto a zone close to its centre. For small atom-atom separations, collective states of higher symmetry are shorter lived (culminating, at zero separation, with the maximally symmetric superradiant Dicke state [140] of rate $N\Gamma$). Let us then try to sketch how asymmetric states can be build by imposing orthogonality of a phase-spread state $|\psi_\varphi\rangle = \bigotimes_{j=1}^N \left[|g\rangle + \left(e^{i\varphi}\right)^{(j-1)}|e\rangle\right]/\sqrt{2}$ to the multitude of symmetric states of the system. While generally this is an unsolvable problem (see supplement), we can get some insight using the symmetric state in the single excitation subspace, the so-called W-state $|W\rangle$. From $\langle W|\psi_\varphi\rangle = \sum_{j=1}^N \left(e^{i\varphi}\right)^j = 0$ we get the solutions $\varphi = 2\pi m/N$ which justify the choice from above $\varphi_j^{(m)}$.

At time τ the phase spread is reversed and a $\pi/2$ pulse follows

$$\mathcal{R}_2 = \bigotimes_j \mathcal{R}_y^{(j)}\left[\frac{\pi}{2}\right] \cdot \mathcal{R}_z^{(j)}\left[-\varphi_j^{(m)}\right].$$

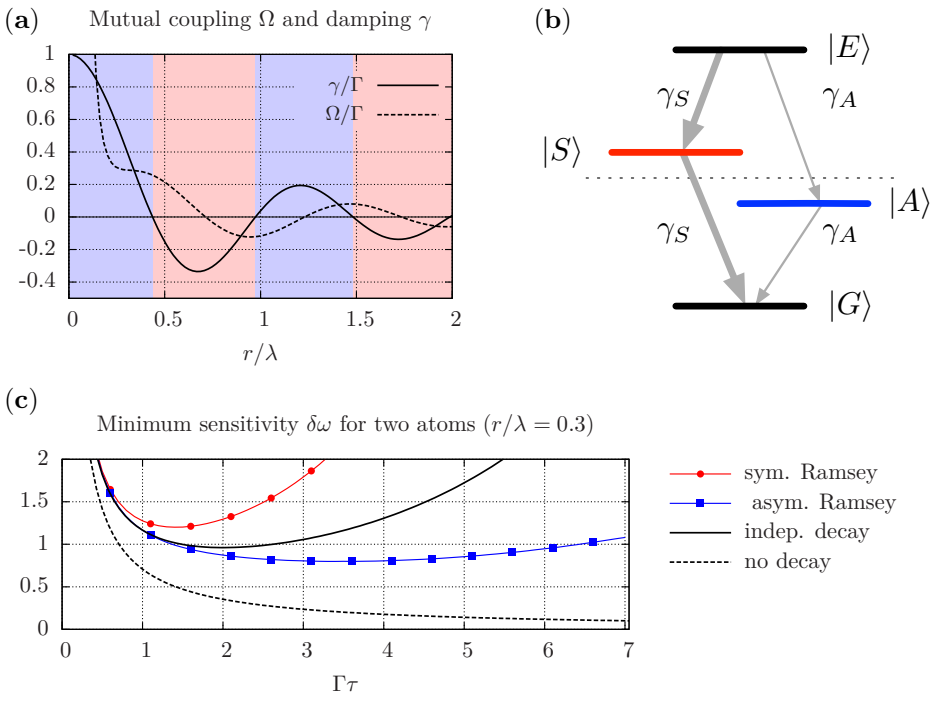

Figure 6.2: *Two atoms metrology.* (a) Normalized mutual decay rate and dipole-dipole frequency shift for a pair of atoms as a function of r/λ. For positive/negative γ, the asymmetric state is subradiant/superradiant (indicated by the colour-coded regions). (b) Level scheme in the dressed basis showing the two independent decay channels with modified rates γ_S and γ_A. (c) Optimal sensitivity as a function of $\tau\Gamma$. The atom separation is $r/\lambda = 0.3$ corresponding to $\gamma \approx 0.41\ \Gamma$ and $\Omega \approx 0.29\ \Gamma$. The minimum for the asymmetric addressing is reached around $\tau \simeq 2/\gamma_A$.

6.3 Two Atoms Case

Let us use a simple system to elucidate the differences between typical and asymmetric Ramsey sequences. We consider atoms 1 and 2 separated by a distance r with $\gamma = \Gamma_{12}(r)$ and $\Omega = \Omega_{12}(r)$ (their dependence on r is shown in fig. 6.2a). The diagonalization of the Hamiltonian is performed by a transformation from the bare basis $\{|gg\rangle, |ge\rangle, |eg\rangle, |ee\rangle\}$ to the collective basis $\{|G\rangle, |S\rangle, |A\rangle, |E\rangle\}$ with $|G\rangle = |gg\rangle$, $|S\rangle = (|eg\rangle + |ge\rangle)/\sqrt{2}$, $|A\rangle = (|eg\rangle - |ge\rangle)/\sqrt{2}$ and $|E\rangle = |ee\rangle$. This transformation diagonalizes the dissipative dynamics as well, and leads to two independent decay channels with damping rates $\gamma_S = \Gamma + \gamma$ and $\gamma_A = \Gamma - \gamma$ as illustrated in fig. 6.2b.

We follow the evolution of $\rho_i = |G\rangle\langle G|$ in the collective basis and compute the detected signal and its variance from ρ_τ. For the symmetric Ramsey sequence one obtains $\langle S^z\rangle_{\mathrm{S}} = 2\sqrt{2}\Re\left(\rho_\tau^{ES} + \rho_\tau^{SG}\right)$ which can be calculated by solving the evolution between 0 and τ from the following set of coupled equations

$$\dot{\rho}^{ES} = \left[-\frac{2\Gamma + \gamma_S}{2} - i(\omega - \Omega)\right]\rho^{ES}, \tag{6.6a}$$

$$\dot{\rho}^{SG} = \left[-\frac{\gamma_S}{2} - i(\omega + \Omega)\right]\rho^{SG} + \gamma_S\,\rho^{ES}. \tag{6.6b}$$

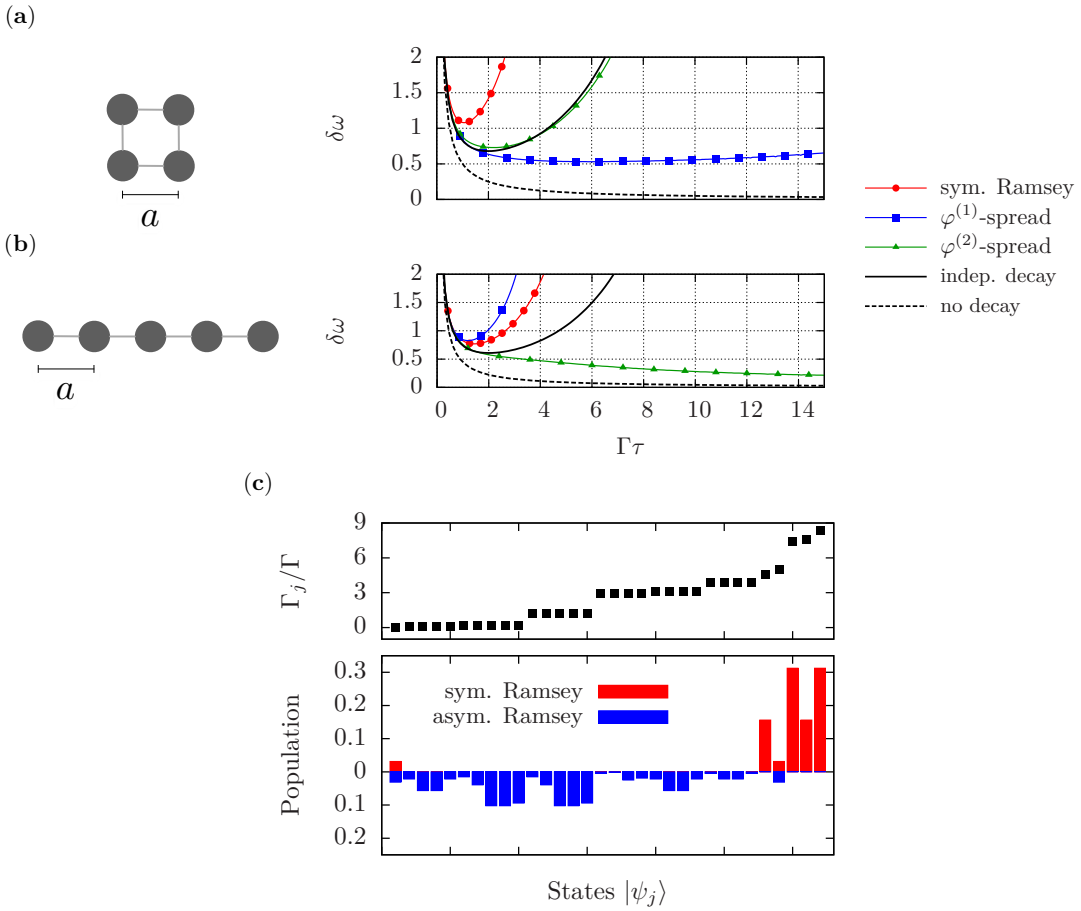

Figure 6.3: *Numerical investigations.* a) and b) Numerical results for the square and a 5 atom-chain. c) Results of diagonalization for an ideal system of 5 equally mutually coupled emitters. The states are ordered with increasing effective decay rate. The occupancy is shown in the histograms for symmetric vs. asymmetric Ramsey sequences.

The computation of the signal variance requires the derivation of

$$\left\langle (S^z)^2 \right\rangle_{\mathrm{S}} = 2\left[1 + \rho_\tau^{SS} - \rho_\tau^{AA} + 2\Re\left(\rho_\tau^{EG}\right)\right],$$

thus solving

$$\begin{aligned}
\dot{\rho}^{EE} &= -2\Gamma\rho^{EE}, \\
\dot{\rho}^{SS} &= -\gamma_S\left(\rho^{SS} - \rho^{EE}\right), \\
\dot{\rho}^{AA} &= -\gamma_A\left(\rho^{AA} - \rho^{EE}\right), \\
\dot{\rho}^{EG} &= -(\Gamma + 2i\omega)\rho^{EG}.
\end{aligned}$$

In contrast, for the asymmetric Ramsey sequence we get $\langle S^z\rangle_{\mathrm{A}} = 2\sqrt{2}\Re\left(\rho_\tau^{EA} - \rho_\tau^{AG}\right)$ and $\left\langle (S^z)^2 \right\rangle_{\mathrm{A}} = 2\left[1 + \rho_\tau^{AA} - \rho_\tau^{SS} - 2\Re\left(\rho_\tau^{EG}\right)\right]$, where the extra coherences can be derived from the solutions of

$$\dot{\rho}^{EA} = \left[-\frac{2\Gamma + \gamma_A}{2} - i(\omega + \Omega)\right]\rho^{EA}, \tag{6.7a}$$

$$\dot{\rho}^{AG} = \left[-\frac{\gamma_A}{2} - i(\omega - \Omega)\right]\rho^{AG} + \gamma_A\,\rho^{EA}. \tag{6.7b}$$

The minimum sensitivities depending on τ after optimization with respect to ω can be very well approximated by

$$[\delta\omega]_{\mathrm{S}} = \frac{\sqrt{2\left(1 + a_S e^{-2\Gamma\tau} + b_S e^{-\gamma_S\tau} - c_S e^{-\gamma_A\tau}\right)}}{\tau\cdot e^{-\gamma_S\tau/2}\left(e^{-\Gamma\tau}\mathcal{A}_S^- + \mathcal{A}_S^+\right)} \tag{6.8a}$$

$$[\delta\omega]_{\mathrm{A}} = \frac{\sqrt{2\left(1 + a_A e^{-2\Gamma\tau} + b_A e^{-\gamma_A\tau} - c_A e^{-\gamma_S\tau}\right)}}{\tau\cdot e^{-\gamma_A\tau/2}\left(e^{-\Gamma\tau}\mathcal{A}_A^+ + \mathcal{A}_A^-\right)}, \tag{6.8b}$$

where a, b, c and $\mathcal{A}^\pm$ are given by the system's geometry (see supplement).

Assuming a separation of timescales for example when $\gamma_A \ll \Gamma, \gamma_S$, the sensitivity $[\delta\omega]_{\mathrm{A}}$ scales similarly to the independent sensitivity of eq. (6.5) with Γ replaced by γ_A. This holds approximately even in the intermediate regime shown in fig. 6.2c where $\gamma_A \simeq 0.59\ \Gamma$, as transpiring from the scaling of the blue (squares) line. For closely spaced atoms, the result is easy to interpret and extremely encouraging since it allows for large interrogation times and direct improvement of the minimum sensitivity. In the general case, of varying the distance between atoms for example to the second region of fig. 6.2a, the symmetric state becomes subradiant instead and the symmetric procedure is the optimal one, however providing only a minimal gain over the independent atom case. This is relevant for the case of linear atom chains separated by a magic wavelength [180], where the conventional Ramsey technique is optimal.

6.4 Numerical Results

Let us now extend our model to more general configurations of a few two-level systems in various geometries. In principle, the configuration can be generalized to a 2D or 3D lattice but one ends up with large Hilbert spaces rather quickly that render simple numerical methods unfeasible. To illustrate the effectiveness of the asymmetric Ramsey method we particularize to the two situations depicted in fig. 6.3, i.e., square and linear geometries. The results are presented in fig. 6.3a,b for all possible phase-spread angle sets, i.e., varying the index m of $\varphi_j^{(m)}$ from 1 to $[N/2]$ ($N = 4$ for square and 5 for the chain) and for a lattice constant $a/\lambda = 0.3$.

To motivate further, we consider a simplified system of five closely positioned emitters ($a/\lambda = 0.2$) with uniform mutual couplings, i.e., $\Omega_{ij} = \Omega$ and $\Gamma_{ij} = \gamma$ for every $i \neq j$. Simultaneous diagonalization of the Hamiltonian and Liouvillian is then possible and it leads to 2^N states $|\psi_j\rangle$ each with an associated decay channel Γ_j, as shown in fig. 6.3c. The histograms show the state population after the first symmetric Ramsey pulse in contrast to the population after the first asymmetric ($\varphi^{(1)}$-spread) Ramsey pulse. Clearly, the conventional Ramsey procedure addresses the symmetric states only, which feature the highest decay rates, while the generalized method distributes the population among states with lower decay rates.

While the examples studied in fig. 6.3 are a proof-of-principle for the phase-spread mechanism we propose, a general optimization for arbitrary distances and geometries is not straightforward and needs to be accompanied by more sophisticated numerical simulations. For the linear chain case for a ratio $a/\lambda = 0.15$, the two nearest neighbours contribute positively while the outer ones feature a negative coupling (see fig. 6.2a). The strategy to be employed is therefore not clear; for instance, as seen in fig. 6.3b, a simple $\varphi_j^{(1)}$ phase distribution performs worse than the symmetric Ramsey sequence while great improvement is introduced by applying $\varphi_j^{(2)}$ shifts.

Experimental investigations of the mechanism described above must mainly address the question of individual phase writing on distinguishable emitters. As one particular realization, a chain of atoms excited by a laser tilted by some angle α opens up the possibility of imprinting a varying phase $\varphi_j = k_0(j-1)a/\cos(\alpha)$ for the j^{th} atom. Note, that interestingly for a strontium magic wavelength lattice, excitation at about 90° automatically excites long lived exciton states close to the optimum. In a 2D lattice this still is fulfilled quite well by excitation from the third direction perpendicular to the plane. For a cube the situation is more tricky and requires careful angle optimization for which preliminary calculations are promising and will be fully investigated in a future publication.

While the main focus of this paper is the case of ensembles of systems coupled via a naturally occurring bath (the electromagnetic vacuum), this formalism can treat general cases of engineered baths. For example, the common interaction of atoms with a decaying optical cavity field [181], combined with elimination of the cavity

mode can lead to equal mutual coupling between any pair of atoms. Another example is that of several superconducting qubits coupled to CPW transmission lines and resonators [182–184]. Here, on the one hand the distance of the particles is much smaller than a wavelength so the effects are very large, but on the other hand the individual transition frequencies, Rabi amplitudes and phases can be controlled very well.

Let us finally remark on multipartite entanglement. First, our technique hints towards the possibility of preparing multipartite entangled states via dissipative techniques. The phase-spreading technique prepares the initial state as a separable state with a large contribution from a quasi non-decaying state. After considerable evolution time τ the correlated environment filters out all other contributions except for the decoherence-free state which necessarily presents quantum correlations (as a basis of comparison consider the 2 atom case where the $|A\rangle$ is maximally entangled). Second, the state protection operation can as well be tested for the protection of entanglement stored in collective states. This can for example be employed in schemes where spin squeezed states are used for sensitive phase detection to minimize their degradation during pure dissipative evolution periods.

6.5 Concluding Remarks

We have described a state protective mechanism applied to a collection of vacuum-coupled two level systems that can be employed in quantum metrology applications for enhanced detection of transition frequencies. The generality of the mechanism opens the way for investigations into more complex engineered reservoirs (atoms in mode-structuring cavities, superconducting qubits coupled to CPW transmission lines) and different noise models such as phase-correlated noise (as treated in [185]). Applications involving multipartite entanglement are also envisioned, such as protection of spin squeezed states during dissipative evolution and the design of dissipation-induced entangling schemes.

Acknowledgements

We are grateful to H. Zoubi, M. Skotiniotis, W. Niedenzu and M. Holland for useful comments on the manuscript and to S. Krämer for assistance with numerics. We acknowledge the use of the QuTiP open-source software [186] to generate fig. 6.1. Support has been received from DARPA through the QUASAR project (L. O. and H. R.) and from the Austrian Science Fund (FWF) via project P24968-N27 (C. G.).

6.6 Supplementary Material

6.6.1 Analytical Expressions for the Two Atom Case

The parameters a, b, c and $\mathcal{A}^{\pm}$ depend on the relative distance r/λ between the two atoms via the decay rates $\gamma_S = \Gamma + \gamma$ and $\gamma_A = \Gamma - \gamma$ as well as the coherent dipole-dipole energy shift Ω. Their explicit functional dependence on r/λ and the angle θ (between the direction of the transition dipoles and the distance between the atoms) is given as

$$\frac{\gamma}{\Gamma} = \frac{3}{2}\left(1-\cos^2\theta\right)\frac{\sin\xi}{\xi} + \left(1-3\cos^2\theta\right)\left(\frac{\cos\xi}{\xi^2} - \frac{\sin\xi}{\xi^3}\right) \tag{6.9a}$$

$$\frac{\Omega}{\Gamma} = -\frac{3}{4}\left(1-\cos^2\theta\right)\frac{\cos\xi}{\xi} + \left(1-3\cos^2\theta\right)\left(\frac{\sin\xi}{\xi^2} + \frac{\cos\xi}{\xi^3}\right), \tag{6.9b}$$

where $\xi = kr = 2\pi r/\lambda$ and we have set $\theta = \pi/2$ for our calculations.

The expressions in the minimum sensitivity for the symmetric Ramsey procedure are then

$$a_S = \frac{1}{4}\left(\frac{\gamma_A}{\gamma_S} - \frac{\gamma_S}{\gamma_A}\right), \tag{6.10a}$$

$$b_S = \frac{4\Gamma - \gamma_S}{4\gamma_A}, \tag{6.10b}$$

$$c_S = \frac{\gamma_A}{4\gamma_S}, \tag{6.10c}$$

$$A_S^{\pm} = \sqrt{\left(\alpha_S^{\pm}\right)^2 + B_S^2}, \tag{6.10d}$$

where we have introduced the abbreviations

$$\alpha_S^{\pm} = 1 \pm \frac{\Gamma\gamma_S}{\Gamma^2 + 4\Omega^2}, \tag{6.11a}$$

$$B_S = \frac{2\Omega\gamma_S}{\Gamma^2 + 4\Omega^2}. \tag{6.11b}$$

For the asymmetric Ramsey procedure, i.e., a $\varphi^{(1)}$-spread,

$$a_A = -a_S = \frac{1}{4}\left(\frac{\gamma_S}{\gamma_A} - \frac{\gamma_A}{\gamma_S}\right), \tag{6.12a}$$

$$b_A = \frac{4\Gamma - \gamma_A}{4\gamma_S}, \tag{6.12b}$$

$$c_A = \frac{\gamma_S}{4\gamma_A}, \tag{6.12c}$$

$$A_A^{\pm} = \sqrt{\left(\alpha_A^{\pm}\right)^2 + B_A^2}, \tag{6.12d}$$

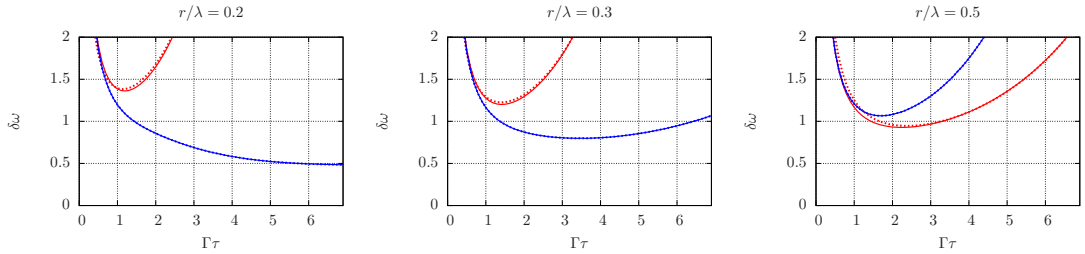

Figure 6.4: Analytical expressions (dashed) and numerical results (solid) for both the symmetric and asymmetric Ramsey procedures are compared showing almost perfect agreement (up to the small oscillations terms ignored in the derivation). Three distances have been chosen: $r/\lambda = 0.2, 0.3$ and 0.5.

where we again employ abbreviations

$$\alpha_A^{\pm} = 1 \pm \frac{\Gamma\gamma_A}{\Gamma^2 + 4\Omega^2}, \tag{6.13a}$$

$$B_A = \frac{2\Omega\gamma_A}{\Gamma^2 + 4\Omega^2}. \tag{6.13b}$$

The approximations that come into play are $\Omega \ll \omega$ and we neglect the phase shift that emerges between the expectation value and the variance due to the dipole-dipole interaction. The agreement between the analytical expressions above and numerical computations is obvious from fig. 6.4.

6.6.2 Phase-Spread Operation

After preparation of the initial collective state

$$|\psi\rangle = \bigotimes_{j=1}^{N} \left[\frac{|g\rangle + \left(e^{i\varphi}\right)^{j-1} |e\rangle}{\sqrt{2}} \right], \tag{6.14}$$

in the asymmetric Ramsey procedure, where $\varphi = \varphi^{(1)} = 2\pi/N$, it is easy to see that

$$\langle W|\psi\rangle = \sum_{j=1}^{N} \left(e^{i\varphi}\right)^{j-1} = 0, \tag{6.15}$$

corresponding to a division of the unit circle into N segments with equal angles, yielding an almost trivial vector sum of zero. This can be generalized to the μ-excitations symmetric state, where

$$\langle s^{(\mu)}|\psi\rangle = \sum_{j=0}^{M} p(j,\mu) \left(e^{i\varphi}\right)^{j} \tag{6.16}$$

with $M = \mu\left(N - \frac{\mu+1}{2}\right)$ and $p(j,\mu)$ is the integral partition of j restricted to μ summands, in essence counting how many possibilities there are to build up the number j from a sum of μ integers smaller than j. Unfortunately, this is a fractal function. One can show for concrete μ that $\langle s^{(\mu)}|\psi\rangle = 0$, but due to the fractal nature of $p(j,\mu)$ that statement cannot be written down in a closed way for arbitrary μ.

7 Publication: Protected Subspace Ramsey Spectroscopy

As a continuation and extension of the work that we did in the above letter, this more comprehensive article looks at the optimal phase-spread angles, which we have determined to be π between neighbouring atoms and, most importantly, at scaling laws of the benefit of our technique with the system size. We see that, in principle, the larger the system, the more pronounced subradiant states appear, which favours our idea of using these to improve the measurement sensitivity. The article was published in Physical Review A on November 11th, 2014 [187].

Abstract

We study a modified Ramsey spectroscopy technique employing slowly decaying states for quantum metrology applications using dense ensembles. While closely positioned atoms exhibit superradiant collective decay and dipole-dipole induced frequency shifts, recent results [Ostermann, Ritsch and Genes, Phys. Rev. Lett. **111**, 123601 (2013)] suggest the possibility to suppress such detrimental effects and achieve an even better scaling of the frequency sensitivity with interrogation time than for noninteracting particles. Here we present an in-depth analysis of this 'protected subspace Ramsey technique' using improved analytical middling and numerical simulations including larger 3D samples. Surprisingly we find that using sub-radiant states of N particles to encode the atomic coherence yields a scaling of the optimal sensitivity better than $1/\sqrt{N}$. Applied to ultracold atoms in 3D optical lattices we predict a precision beyond the single atom linewidth.

7.1 Introduction

Recent experimental setups have demonstrated Raman and Ramsey spectroscopy on narrow atomic clock transitions using cold atoms trapped in 1D magic wavelength optical lattices with unprecedented precision below one Hertz [42, 188]. While on the one hand in this extreme limit even weak atom-atom interactions cause perturbations, on the other hand such setups provide a unique testing ground for measuring such tiny corrections [189]. From the point of view of an atomic clock or a superradiant laser [190] interactions constitute a perturbation. In particular at higher particle

densities dipole-dipole interaction and collective decay tend to introduce shifts and dephasing [136, 138, 144, 156], which limit the useful interrogation time. As these are essentially bipartite interactions, they cannot be corrected simply by rephasing techniques. While for ^{87}Sr with its mHz-linewidth, decay is no major limitation at the moment, alternative approaches with e.g., calcium atoms have already reached this limit [191].

Over the past couple of years a considerable number of theoretical proposals to deal with metrology bounds have been put forward (see Refs. [185, 192–196]). In our recent theoretical proposal [169] we suggested that by a proper modification of the standard Ramsey interferometry technique (SRT) on interacting two-level ensembles, the detrimental effect of collective decay can be minimized and surprisingly to some extent even reversed. The technique takes advantage of the atomic interactions to suppress decay by transferring the atomic excitation to subradiant collective states. We dub this method protective Ramsey technique (PRT). It might be less surprising in hindsight, but still is puzzling, that an optically highly excited collective state of atomic dipoles can be prevented from decay via destructive interferences of the field emitted by the individual dipoles. Interestingly, one finds an unexpected fast growth of the lifetime of the excited states with the particle number. Employing the proposed techniques these long-lived states can then be used for an enhanced Ramsey spectroscopy allowing for a significantly higher precision than even for independently decaying atoms paving the way for implementations of this technique with 3D lattices.

The method requires an additional individually controlled single particle spin rotation, which is added after the first and reversed before the final Ramsey pulse. In consequence, the total ensemble spin is shifted towards zero by spreading the individual spins by predefined amounts almost homogeneously around the equatorial plane of the Bloch sphere. Thus the ensemble becomes classically nonradiative during free evolution. While this should obviously work for tightly packed ensembles confined within a cubic wavelength, we demonstrate that it works almost as well in 3D regular lattices. In this case it is not a priori clear which would be the most long lived configuration, but the minimum decay rate can be inferred from the eigenvalues of the collective decay Liouvillian operator. It is of course an extra technical challenge to implement the required optimal transformation as it in general requires individual spin addressing. In practise, however, in many cases, a proper use of phases introduced by a designed lattice and excitation geometry turns out to be sufficient to get very close to such an optimal state with a single laser applied at an optimal angle.

It is generally thought that, in order to beat the $1/\sqrt{N}$ scaling of the sensitivity of SRT applied on N noninteracting particles, the state preparation stage should involve the generation of nonclassical multipartite entangled states (such as spin squeezed states) [172–178]. Here we present numerical evidence that suggests that one can overcome this scaling by employing classical operations at the initial and final stages of the sequence only.

In Sec. II we describe our model and discuss the formalism, while Sec. III gives an

overview of the results of SRT applied to non decaying or independently decaying atoms. We introduce PRT in Sec. IV and elaborate on our choice of rotations. We also detail the method applied to simple interacting systems comprised of two atoms and three atoms in a triangular geometry. The main body of numerical results and analytical considerations for larger systems is presented in Sec. V, where chains of many atoms are considered, scaling laws are investigated and results for the fundamental cubic unit cell are presented. We conclude in Sec. VI.

7.2 Model

Our model assumes N identical two-level atoms with levels $|g\rangle$ and $|e\rangle$ separated by an energy of $\hbar\omega_0$ (transition wavelength λ_0) in a geometry defined by the position vectors $\{\mathbf{r}_i\}$ for $i = 1, ...N$. For each i, operations on the corresponding two-dimensional Hilbert space are written in terms of the Pauli matrices $\sigma_i^{x,y,z}$ and corresponding ladder operators $\sigma_i^{\pm}$ connected via

$$\sigma_i^x = \sigma_i^+ + \sigma_i^- \tag{7.1a}$$
$$\sigma_i^y = -i(\sigma_i^+ - \sigma_i^-) \tag{7.1b}$$
$$\sigma_i^z = \sigma_i^+\sigma_i^- - \sigma_i^-\sigma_i^+. \tag{7.1c}$$

Rotations about an axis μ are defined as

$$\mathcal{R}_\mu^{(j)}[\varphi] = \exp\left(i\varphi\,\sigma_j^\mu/2\right), \tag{7.2}$$

where $\mu \in \{x, y, z\}$. The coupling of the system to the common bath represented by the surrounding electromagnetic vacuum results in i) irreversible dynamics characterized by independent decay channels with rates $\Gamma_{ii} \equiv \Gamma$ as well as cooperative decay channels with rates Γ_{ij} (for atom pair $\{i, j\}$) and ii) dipole-dipole interactions through the exchange of virtual photons characterized by the frequency shifts Ω_{ij}. Assuming identical dipole moments for all atoms, we can write this explicitly [144] as

$$\Omega_{ij} = \frac{3\Gamma}{4}\,G(k_0 r_{ij}) \tag{7.3a}$$
$$\Gamma_{ij} = \frac{3\Gamma}{2}\,F(k_0 r_{ij}) \tag{7.3b}$$

for two atoms separated by a distance of r_{ij}. With the notations $\xi = k_0 r_{ij}$ (with the wavenumber $k_0 = 2\pi/\lambda_0$) for the normalized separation and $\alpha = \cos\theta =$

$(\mathbf{r}_{ij} \cdot \mu) / |\mathbf{r}_{ij}||\mu|$, one can put down the two functions

$$F(\xi) = \left(1-\alpha^2\right) \frac{\sin\xi}{\xi} + \left(1-3\alpha^2\right) \left(\frac{\cos\xi}{\xi^2} - \frac{\sin\xi}{\xi^3}\right), \tag{7.4a}$$

$$G(\xi) = -\left(1-\alpha^2\right) \frac{\cos\xi}{\xi} + \left(1-3\alpha^2\right) \left(\frac{\sin\xi}{\xi^2} + \frac{\cos\xi}{\xi^3}\right). \tag{7.4b}$$

We follow the evolution of the system both analytically and numerically in the framework of the master equation

$$\frac{\partial\rho}{\partial t} = i[\rho, H] + \mathcal{L}[\rho]. \tag{7.5}$$

The unitary dynamics of the system is described by the Hamiltonian

$$H = \frac{\omega}{2} \sum_i \sigma_i^z + \sum_{i \neq j} \Omega_{ij}\, \sigma_i^+ \sigma_j^- \tag{7.6}$$

with $\omega = \omega_0 - \omega_l$, where ω_l is a laser reference frequency. The dissipative dynamics can be written in (a nondiagonal) Lindblad form

$$\mathcal{L}[\rho] = \frac{1}{2} \sum_{i,j} \Gamma_{ij} \left[2\sigma_i^- \rho\, \sigma_j^+ - \sigma_i^+ \sigma_j^- \rho - \rho\, \sigma_i^+ \sigma_j^-\right]. \tag{7.7}$$

7.3 Standard Ramsey Interferometry

Let us review some fundamental aspects of a typical procedure in spectroscopic experiments, i.e., the Ramsey method of separated oscillatory fields [64]. As illustrated in fig. 7.1, the method consists of preparing an ensemble of spins in the ground state at time t_i such that their collective population $S^z = \sum_i \sigma_i^z/2$ starts at a value of $\langle S^z \rangle = -N/2$. A preparatory Ramsey pulse, applied between t_i and $t = 0$, rotates the state around the y-direction to achieve an alignment of the collective dipole with the x-axis. This is realized by applying a laser that is quasi resonant with the atomic transition with a Rabi frequency χ for the time $t_i - t_0$ such that the pulse area $\int_{t_0}^{t_i} \chi(t')\, \mathrm{d}t' \approx \pi/2$. As a simplification we assume that $\Omega_{ij}, \Gamma_{ij} \ll \chi$ such that no population redistribution among the atoms can occur during the pulse. Typically, for level shifts and decay rates on the order of MHz, a Rabi frequency in the GHz regime or more would ensure that this approximation is valid for laser pulses with a duration in the realm of ns. In the next step, the ensemble is allowed to evolve freely for what we refer to as 'interrogation time' τ. Note that, depending on the geometry of the

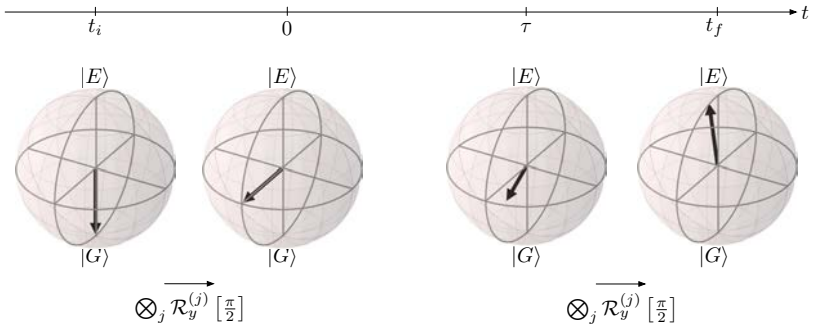

Figure 7.1: *Standard Ramsey metrology.* The ensemble of N spins starts with all spins down in a collective coherent pure spin state on the surface of the collective Bloch sphere (radius $N/2$). The first $\pi/2$ pulse aligns the average collective dipole along the x axis and free evolution is allowed. After the interrogation time τ, another $\pi/2$ pulse follows which attempts to align the state with the excited state and fails by an angle that depends on the accumulated phase during free evolution as well as on the total decay of the collective state. The detected signal to be analyzed is a measure of population inversion.

excitation scheme (whether the laser comes from the side or propagates through the ensemble) the signal will show oscillations in time either at laser-atom detuning ω or at the natural frequency ω_0. The next step is the same as the first one, where a second $\pi/2$ pulse rotates the collective state around the y-axis. At the end, the signal to be extracted is the population inversion as a function of the scanned laser detuning. Analysis of this signal gives the sensitivity as a figure of merit in metrology

$$\delta\omega = \min\left[\frac{\Delta S^z(\omega,\tau)}{|\partial_\omega \langle S^z\rangle(\omega,\tau)|}\right], \tag{7.8}$$

where the minimization is performed with respect to ω and $S^z = \sum_i \sigma_i^z$ is the detected signal, while $(\Delta S^z)^2 = \left\langle (S^z)^2 \right\rangle - \langle S^z\rangle^2$ refers to its rms deviation.

To start with, we assume independent systems ($\Gamma_{ij} = 0$ and $\Omega_{ij} = 0$ for $i \neq j$). The operations to be applied on the density matrix ρ at the times of the Ramsey pulses are

$$\mathcal{R}_1 = \mathcal{R}_2 = \bigotimes_j \mathcal{R}_y^{(j)}[\pi/2]. \tag{7.9}$$

It is easy to find the optimal sensitivity as a minimization over ω as

$$[\delta\omega]_{\text{indep}} = \min\left[\frac{\sqrt{e^{\Gamma\tau} - \cos^2(\omega\tau)}}{\sqrt{N}\,|\tau\cdot\sin(\omega\tau)|}\right] = \frac{e^{\Gamma\tau/2}}{\tau\sqrt{N}}. \tag{7.10}$$

Notice that, for nondecaying atomic excitations, the method allows for a perfect accuracy,. However, in the presence of decay, an optimal interrogation time $\tau_{\text{opt}} = 2/\Gamma$

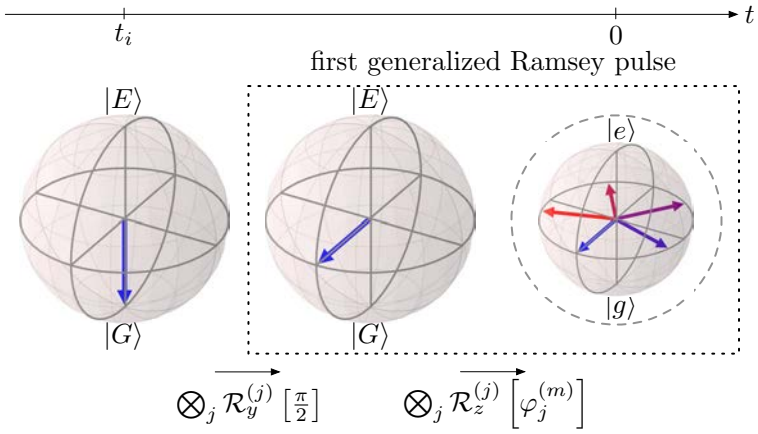

Figure 7.2: *Phase-spread operation.* Redesign of the first Ramsey pulse to include, in addition to the initial $\pi/2$ pulse, rotations of the individual spins with different angles such that the resulting overall dipole moment vanishes. Notice that the last Bloch sphere has a radius 1/2, corresponding to single spins.

suggests itself, where the corresponding optimal sensitivity is given by

$$[\delta\omega]_{\text{indep}}^{\text{opt}} = \frac{\Gamma \cdot e}{2\sqrt{N}}. \tag{7.11}$$

Thus, it becomes obvious that, given the atomic species (which determines Γ) one can improve the accuracy by an increase of the sample size only. Yet, due to the finite available volume, this would imply an increase of density which causes the assumption that the atoms are independent to break down. In the next section we analyze this high density limit where we observe that the collective behaviour can be exploited to reduce the effective Γ appearing in eq. (7.11) instead.

7.4 Protective Ramsey Technique

To counteract the effect of the collective coupling to the vacuum modes, it has been proposed [169] to make use of a generalized Ramsey sequence (as illustrated in fig. 7.2). In contrast to SRT, the generalized PRT contains extra rotations in conjunction with the Ramsey pulses that are intended to drive the spin system into states that are protected from the environmental decoherence. In a first step, one applies

$$\mathcal{R}_1^{(m)} = \bigotimes_j \mathcal{R}_z^{(j)}\left[\varphi_j^{(m)}\right] \cdot \mathcal{R}_y^{(j)}\left[\frac{\pi}{2}\right], \tag{7.12}$$

where the state of a particular atom j is rotated around the z-direction with the angle

$$\varphi_j^{(m)} = 2\pi m \frac{j-1}{N}. \tag{7.13}$$

The idea behind this choice of angles is to drive the system into a state which exhibits a vanishing dipole moment. This can be achieved by rotating the spins in the xy-plane in $\lfloor N/2 \rfloor$ distinct ways indexed by $m = 1, ...\lfloor N/2 \rfloor$ (where $\lfloor N/2 \rfloor$ is the first integer before $N/2$). The protection of the state is targeted at the period of its free evolution and in the final step, before the second Ramsey pulse, the state has to be brought back to the surface of the Bloch sphere to ensure a large contrast in the signal. This is accounted for by a reversal of the phase spread operation, i.e.,

$$\mathcal{R}_2^{(m)} = \bigotimes_j \mathcal{R}_y^{(j)} \left[\frac{\pi}{2}\right] \cdot \mathcal{R}_z^{(j)} \left[-\varphi_j^{(m)}\right]. \tag{7.14}$$

As stated previously, at time $t = 0$, for any set of $\varphi_j^{(m)}$, the system is in a state of zero average collective spin. At an intuitive level this choice comes from the observation that, for small atom-atom separations, collective states of higher symmetry are shorter lived (culminating at zero separation with the maximally symmetric superradiant Dicke state [140] of rate $N\Gamma$). Let us now try to sketch how asymmetric states can be built by imposing orthogonality of a phase-spread state

$$|\psi_\varphi\rangle = \bigotimes_{j=1}^{N} \frac{1}{\sqrt{2}} \left[|g\rangle + \left(e^{i\varphi}\right)^{(j-1)} |e\rangle\right], \tag{7.15}$$

to the multitude of symmetric states of the system. It is straight-forward to see that

$$\langle W|\psi_\varphi\rangle = \sum_{i=1}^{N} \left(e^{i\varphi}\right)^{(j-1)}, \tag{7.16}$$

where

$$|W\rangle = \left(|egg\ldots\rangle + |geg\ldots\rangle + \cdots + |g\ldots ge\rangle\right)/\sqrt{N}, \tag{7.17}$$

the so-called W-state, which is the fully symmetric state of a single excitation distributed equally among N atoms. Imposing orthogonality, i.e., $\langle W|\psi_\varphi\rangle = 0$ we find $\varphi = 2\pi/N$. Geometrically, this corresponds to a division of the unit circle into N pieces of angle $2\pi/N$, which when added up yields a trivial vector sum of zero. Generalizing this concept to higher energy states, where $\left|w^{(n)}\right\rangle$ is the symmetric state of n excitations, gives us

$$\left\langle w^{(n)}|\psi_\varphi\right\rangle = \sum_{j=1}^{M} p(j,n)\ \left(e^{i\varphi}\right)^{(j-1)} = 0 \tag{7.18}$$

with $p(j,n)$ being the integral partition of the number j comprised of n summands and $M = n\,(N - (n+1)/2) + 1$. Unfortunately, $p(j,n)$ is a fractal function and thus, Equation (7.18) cannot be solved for a general number of atoms and excitations, yet any concrete number gives the same result as above, i.e., $\varphi = 2\pi/N$. Hence, we see that for any symmetrically coupled system of N atoms the choice $\varphi = 2\pi/N$ results in a zero-occupation of the symmetric states.

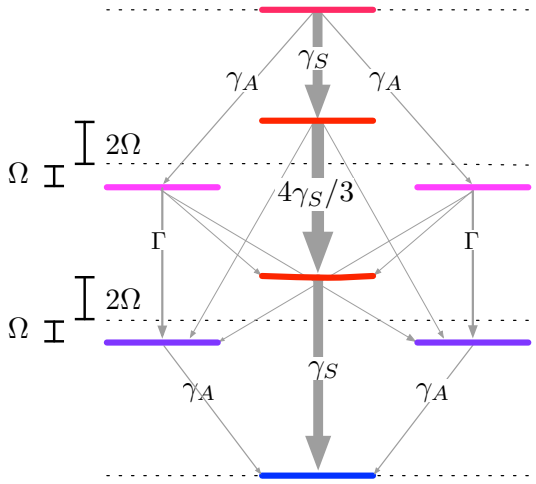

Figure 7.3: *Energy levels and decay channels for three equidistant atoms.* Results of the diagonalization of both the Hamiltonian and the Liouvillian for three atoms in an equidistant triangle configuration. The dipole-dipole shifts of levels are depicted with the corresponding decay channels and rates. Further details can be found in Ref. [144].

We will now look at systems of small atom numbers where the protected states $|p_N^{(m)}\rangle = \mathcal{R}_1^{(m)}|G\rangle$, with $|G\rangle$ being the ground state, can be readily expressed in both the collective and uncoupled bases. For two atoms the 'protected' state is unique ($m = 1$) and is simply the asymmetric state

$$|p_2^{(1)}\rangle = \frac{1}{\sqrt{2}}(|ge\rangle - |eg\rangle) = |A\rangle\,. \tag{7.19}$$

Observe that the transformation that diagonalizes the Hamiltonian automatically renders the Liouvillian in diagonal form. Denoting the mutual decay rate by $\gamma_{12} = \gamma$, two decay channels with $\gamma_A = \Gamma - \gamma$ and $\gamma_S = \Gamma + \gamma$ are obtained. For closely spaced atoms, γ can reach values close to Γ such that $\gamma_A \ll \Gamma$ and the state $|A\rangle$ can be protected from decoherence very well. Since analytical and numerical results for the two atom case are presented in Ref. [169], we will only stress one conclusion that emerges from this analysis, i.e., even for moderate distances the time for which the optimal sensitivity is obtained roughly scales as $2/\gamma_A$. This indicates that the evolution of the system is mainly within the protected subspace, a claim that will be investigated further in the next section.

For three atoms there is still only one choice of $m = 1$. However, the resulting state

is somewhat more complicated in both coupled and uncoupled bases, i.e.,

$$\begin{aligned}|p_3^{(1)}\rangle &= \frac{-1}{2\sqrt{2}}\left(|eee\rangle + |ggg\rangle + |egg\rangle + |gee\rangle\right) \\ &+ \frac{1}{4\sqrt{2}}\left(1+i\sqrt{3}\right)\left(|eeg\rangle + |geg\rangle\right) \\ &+ \frac{1}{4\sqrt{2}}\left(1-i\sqrt{3}\right)\left(|ege\rangle + |gge\rangle\right) \\ &= \frac{1}{2\sqrt{2}}\left(|\frac{3}{2},\frac{3}{2}\rangle + |\frac{3}{2},-\frac{3}{2}\rangle\right) \\ &+ \frac{\sqrt{3}}{4}\left(|\frac{1}{2},\frac{1}{2},1\rangle + |\frac{1}{2},-\frac{1}{2},1\rangle\right) \\ &+ i\frac{\sqrt{3}}{4}\left(|\frac{1}{2},\frac{1}{2},2\rangle - |\frac{1}{2},-\frac{1}{2},2\rangle\right).\end{aligned} \tag{7.20}$$

Above we have used the short form for the tensor products in the uncoupled basis and an additional index in the coupled basis. The complete label of a state (different from the ones with $J = N/2$) in the coupled basis as used here is $|J, M, \alpha\rangle$, where as usual $0 \leq J \leq N/2$ and $|M| \leq J$. In the symmetric subspace, characterized by $J = N/2$ (with states on the surface of the Bloch sphere), there are $N + 1$ states. The additional index α is needed in order to distinguish among degenerate states inside the Bloch sphere (note that there is a certain unitary freedom in how the change of basis is performed, i.e., in how the collective degenerate states are defined). These other states that lie inside the Bloch sphere (equal in number to $2^N - (N + 1)$), we loosely dub asymmetric states. For the three-particle example, as seen in fig. 7.3, states in the middle belong to the symmetric subspace. There are four such states with maximal $J = 3/2$, and therefore $2^3 - 4 = 4$ asymmetric states inside the sphere. Since there are only two combinations of $J = 1/2$ and $M = \pm 1/2$, the remaining states are degenerate and therefore distinguished by an additional index $\alpha = 1, 2$. These asymmetric state are depicted in fig. 7.3 on the sides and correspond to $|1/2, \pm 1/2, \alpha\rangle$ in the expression for $|p_3^{(1)}\rangle$.

It is however obvious that the number of asymmetric states grows drastically with N and so does the degeneracy. Consequently, the expressions for the protected states become vastly more complicated for larger N making it necessary to tackle the problem numerically.

For atoms in an equidistant triangle configuration where all mutual decay rates and couplings are equal and specified by γ and Ω, respectively, one can again simply use the transformation that diagonalizes the Hamiltonian to diagonalize the Liouvillian as well. The resulting states with their corresponding decay rates are depicted in fig. 7.3. Thee phase-spread transformation that leads to the protected state $|p_3^{(1)}\rangle$ simply ensures that the system's evolution mostly runs through the states on the side, characterized by smaller decay rates γ_A.

7.5 Larger Systems

We are now in the position to extend our investigations to larger systems in various configurations. First, we show results for six atoms in a chain, where the separation is varied and the scan over different rotations (i.e., over all possible sets of φ_j^m) is performed. We then explain the obtained results by taking a close look at the collective decay properties as derived from a diagonalization of the Liouvillian and find scaling laws for the characteristic timescale of the most protected subspace consistent with the numerical results. Then, we show that the performance of PRT can beat the typical $1/\sqrt{N}$ scaling. Finally, we extend our numerics to a cube configuration of eight atoms which should be the building block for understanding the application of this method to dense 3D lattices.

7.5.1 1D Chain Configuration

To begin with, we consider a linear chain of six atoms separated by various lattice constants a and subject to first SRT and than to PRT. We numerically compute the minimum sensitivity as a function of τ and scan over all possible rotation indexes m. The results are plotted in fig. 7.4 for separations of $0.2\lambda_0$, $0.3\lambda_0$ and for the magic wavelength. The obtained curves are compared to the independent atom case (shown in black in all plots).

As seen in fig. 7.4a and fig. 7.4b, for distances smaller than $\lambda_0/2$, there is at least one m for which the corresponding PRT method gives results better than SRT. More surprising and promising at the same time, the optimal PRT performs even better than the independent atom case. The immediate conclusion is that one can use such techniques to turn cooperative decay into an advantage instead of treating it as a detrimental effect. For distances larger than $\lambda_0/2$ (as illustrated in fig. 7.4c), the SRT beats any PRT we used for a fairly simple reason. At these distances the symmetric states are subradiant. Therefore, SRT naturally leads the system to subspaces which are more protected from the environment.

From fig. 7.4a and fig. 7.4b we notice that the $m = 3$ rotation performs best. More generally, as seen in the following subsections, the optimal PRT scheme seems to always be the one characterized by a maximum $m = \lfloor N/2 \rfloor$. Such rotations effectively create non-radiative subunits of atom pairs within the chain (exact for even N and an approximation for odd N where one atom is unpaired). This seems to agree with the mechanism described in Ref. [185] as well.

7.5.2 Diagonal Decay Channels – Scaling Laws

A key property for the improved performance of dense ensembles under PRT is the occurrence of subradiant states. To get some physical insight into the behaviour of these states with distance and particle number, we perform a diagonalization of the

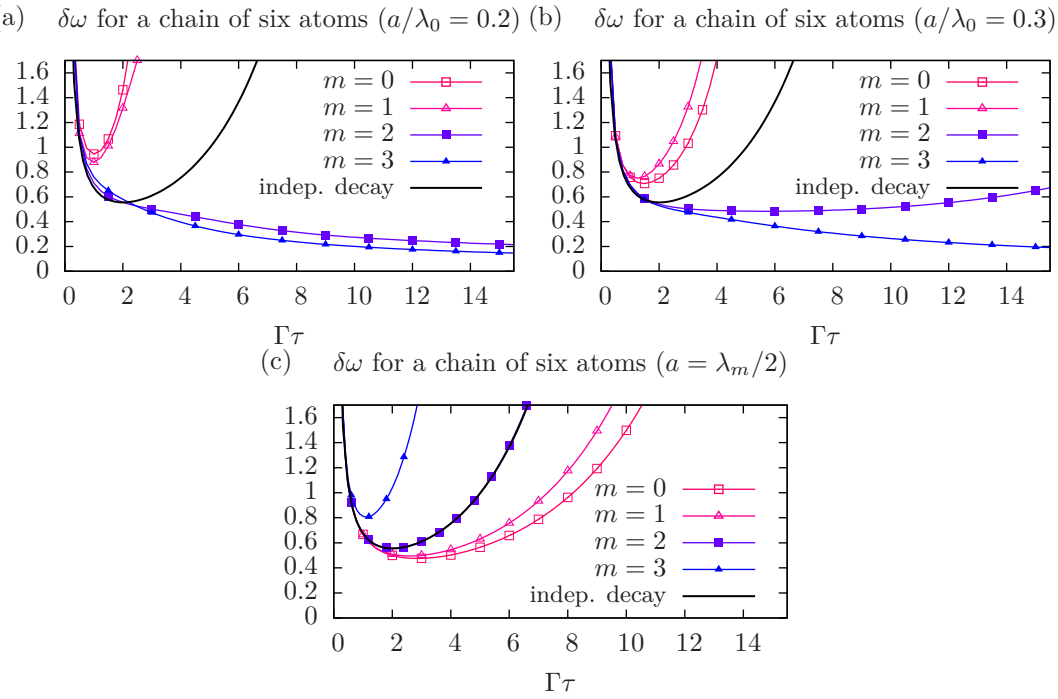

Figure 7.4: *Numerical investigations for a 1D chain of six atoms* Numerical results for the sensitivity as a function of τ for a 1D chain of six atoms separated by $a = 0.2\lambda_0$ in a), by $a = 0.3\lambda_0$ in b) and by half of the magic wavelength in c). The different curves correspond to independent decay (solid line), SRT with $m = 0$ (empty squares) and PRT with $m = 1$ (empty triangles), $m = 2$ (filled squares) and $m = 3$ (filled triangles). In c) the independent decay overlaps with the curve for $m = 2$.

decay matrix for N particles in a linear chain configuration. This is done by a unitary matrix T, such that

$$\Gamma = T\, D_\Gamma\, T^{-1}, \tag{7.21}$$

where D_Γ is a diagonal matrix containing the eigenvalues of the decay rate matrix $[\Gamma_{ij}]$, which we label λ_i for $i = 1, ...N$. With this, we can write the connection to collective ladder operators as

$$\sigma_i^{\pm} =: \sum_{k=1}^{N} T_{ik} \Pi_k^{\pm}. \tag{7.22}$$

Using eq. (7.22) in eq. (7.7) we obtain a diagonal form for the Liouvillian that shows a breakdown of the decay process into N different channels, i.e.,

$$\mathcal{L}[\rho] = \sum_{k=1}^{N} \frac{\lambda_k}{2} (2\Pi_k^- \rho \Pi_k^+ - \Pi_k^+ \Pi_k^- \rho - \rho \Pi_k^+ \Pi_k^-). \tag{7.23}$$

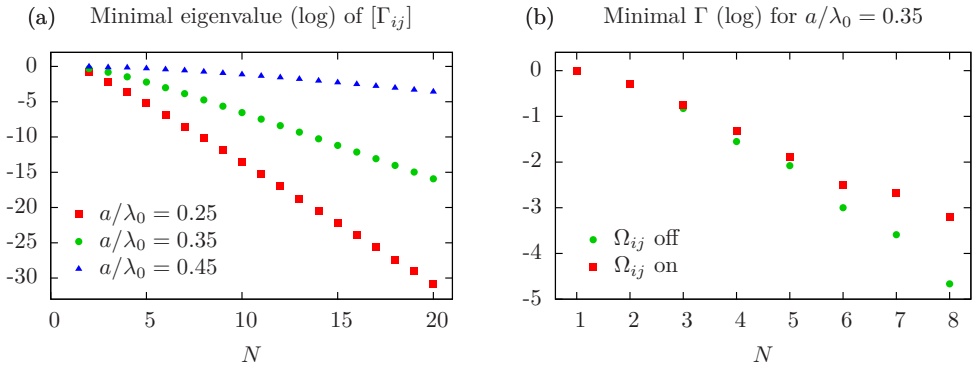

Figure 7.5: *Subradiant behaviour for increasing N.* a) Minimum decay rate (or eigenvalue) obtained from $[\Gamma_{ij}]$ with increasing atom number N in a linear chain configuration for different spacings a. Smaller distances show a close to exponential and drastic decrease of Γ_{min} with increasing N. b) Scaling of the Γ_{min} obtained via the population accumulation method (as detailed in the text) with and without coherent dipole-dipole energy exchange.

After establishing a description of the decay via independent decay channels, let us now investigate the scaling of the corresponding rates with N. Results of the numerical diagonalization of the decay matrix $[\Gamma_{ij}]$ are illustrated in fig. 7.5a for $a = 0.2\lambda_0$, $a = 0.35\lambda_0$ and $a = 0.45\lambda_0$. There, the logarithm of the minimum eigenvalue Γ_{min} (normalized with respect to Γ) is plotted against N. A closer and closer to exponential scaling emerges as a/λ_0 becomes smaller.

Having identified that there are decay channels with exponentially close to zero rates (with increasing N), the natural question is: does the system end up in such subspaces characterized by almost perfect protection from the environment? To this end, we simulate population accumulation dynamics, where the system is initialized in the fully inverted state and the population of the ground state is monitored. It is safe to assume that in the long time limit all but the channel with the very lowest decay rate will have damped out fully. Therefore, the population of the ground state will have the following approximate analytical form for large times,

$$p_G(t) \approx 1 - e^{-\Gamma_{\text{min}} t}. \tag{7.24}$$

The results are plotted in fig. 7.5b as green circles, where $\Omega_{ij} = 0$ is assumed. The values obtained perfectly overlap with the predicted values from fig. 7.5a (green circles). However, we have also investigated the effect of coherent dipole-dipole energy exchange on such dynamics and found the red squares line in fig. 7.5b. In the realistic case where $\Omega_{ij} \neq 0$, the Hamiltonian and Liouvillian cannot be diagonalized simultaneously and the system does not evolve to the fully protected subspace but to a combination of slowly decaying subspaces. The resulting scaling with increasing N is however still quite steep and close to an exponential.

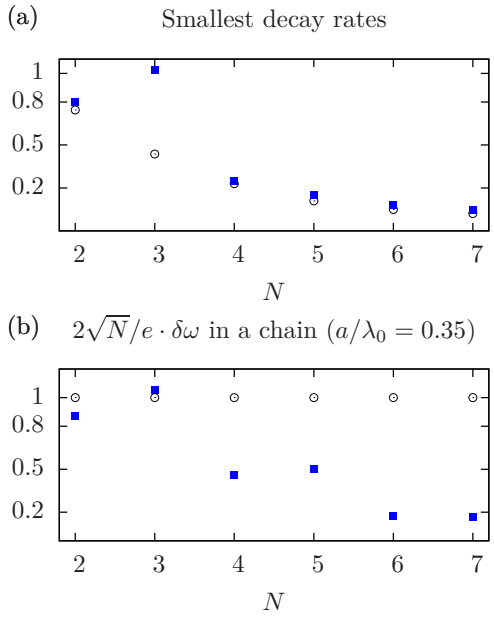

Figure 7.6: *Scaling laws.* a) Scaling of the extrapolated inverse timescale $2/\tau_{\text{opt}}$ with increasing N (squares) compared to the theoretical scaling of Γ_{min} (circles). b) Scaling of the minimum sensitivity (times $2\sqrt{N}/e$) obtained via PRT with particle number (always for the PRT with $m = \lfloor N/2 \rfloor$). The circles show the normal scaling of SRT on independent atoms $2\sqrt{N}/e \cdot \delta\omega = 1$. For an even particle number, the rotation with $m = N/2$ corresponds to a configuration where the system is composed of non-radiative atom pairs. For odd particle number, there is one unpaired spin and the resulting sensitivity is roughly the one obtained for $N - 1$ atoms (except for small systems where the effect of the unpaired atom is substantial).

7.5.3 Optimal Sensitivity via Protected Method – Scaling Laws

We are now in the position to extract scaling laws for the minimum sensitivity with atom number from numerical investigations of PRT on 1D lattices. First, we extract the optimal interrogation times τ_{opt} from the sensitivity curves such as those plotted in fig. 7.4. A simple fit of $2/\tau_{\text{opt}}$ with the minimum decay rate predicted theoretically for $a = 0.35\lambda_0$ (as read from fig. 7.5a shows a good agreement with increasing N (except for $N = 3$ for PRT with $m = 1$). The results are shown in fig. 7.6a. The conclusion is that, for long interrogation times, the system subjected to PRT is indeed mainly restricted to a protected subspace governed by the smallest theoretically predicted decay rate.

More importantly, we have analyzed the behaviour of the normalized optimal sensitivity $(2\sqrt{N}/e)\delta\omega$ with increasing N and compared it to the typical scaling for

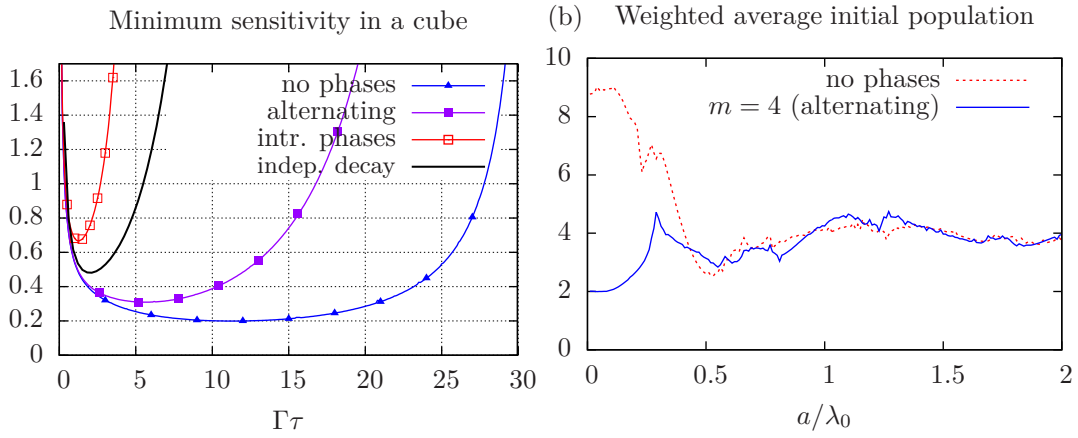

Figure 7.7: *Numerical investigations for the cube configuration.* a) Frequency sensitivity for the cube configuration in a magic wavelength lattice. b) Weighed average of decay rates with corresponding populations for SRT compared to PRT as a function of interatomic distance in a cube. As obvious from the plot, PRT outperforms SRT for distances roughly less than $\lambda_0/2$.

independently decaying atoms (shown as a constant function valued 1 in fig. 7.6b). The immediate conclusion is that PRT does indeed beat the usual scaling using independent ensembles with atoms in coherent spin states and suggests that even the improved scaling introduced by the use of spin squeezed states might be outperformed. However, extended numerical investigations are needed at this point and such an extrapolation will be deferred to a future publication. The chains of even and odd number behave differently, owing to the aforementioned fact that the PRT with $m = \lfloor N/2 \rfloor$ is the optimal one for $a = 0.35\lambda_0$. For even N the sensitivity outperforms the standard one as soon as $N > 1$ given that every two neighbouring atoms are paired into non-radiative cells when PRT is applied. For odd N there is an extra unpaired dipole that seems to strongly influence the results when N is small and will lead to the same $\delta\omega$ (as for the previous even integer) for large N.

7.5.4 3D Cube Configuration

As a further step towards a generalized view of a 3D configuration this section lays out the properties of a unit cell of a cubic lattice, where eight atoms reside in the corners of a cube. Here, the atoms are trapped equidistantly (lattice constant a), while their dipoles point into the direction that is transverse to the propagation direction of the excitation and readout laser pulses. Thus, different coupling strengths emerge, whereas the dominating contribution is still the nearest-neighbour distance with the dipole moment and the vector connecting the respective pairs drawing an angle of $\theta = \pi/2$. Note that symmetry renders all eight particles equivalent here.

Since, in such a configuration, a direct laser excitation of all eight atoms with

the same phase, is not possible, this setup offers a solid testing ground for a quasi-automatic phase imprinting due to finite distances. In a typical situation an excitation pulse would reach one face of the cube, i.e., four atoms, with some phase φ, while the other four atoms would receive a phase of $\varphi + ka$, where k is the laser's wavenumber and a denotes the length of the cube, as mentioned above. This, of course, can become arbitrarily complicated, if one allows for the cube to be addressed from any angle, where then each atom could obtain a distinct phase, simply because of the free propagation of the laser pulses between them.

In fig. 7.7a we depict the minimum sensitivity as a function of time for a lattice constant of $a \approx 0.58\lambda_0$, corresponding to ^{87}Sr in a magic wavelength lattice. We observe, that a Ramsey scheme, where every atom receives the same phase outperforms any other phase imprinting by a landslide. This might seems a bit counter-intuitive at first, as one is lead to assume that this situation is the standard Ramsey technique. Yet, a closer look reveals that due to the geometrically induced implicit phase imprinting, the above mentioned second face of the cube needs to pick up an extra phase of $-ka$, so that both faces, i.e., every atom in the cubic sample, indeed possesses the same imprinted phase. At the magic wavelength distance, the lowest order nearest-neighbour dissipative coupling has a negative value, thus favouring as many pairs of equal phase as possible. As mentioned before, the majority of the couplings is constituted by nearest neighbour pairs, but there are also couplings in the planar and cubic diagonal, which becomes quite evident when looking at the sensitivity for an alternating phase distribution, i.e., every nearest neighbour pair is separated by a phase of exactly π. Here, a trade off between the next-neighbour and diagonal couplings can be observed as the closest couplings decrease the sensitivity due to a negative sign and a phase difference of π while the diagonal ones, which are also negative in sign, yet possess no phase difference, increase the sensitivity.

Finally, the SRT sensitivity is obtained by including the implicit phase imprinting caused by a laser pulse that hits one face of the cube first, propagates further and hits the second face with an extra phase of ka. At magic wavelength distance this amounts to a phase of approximately 1.16π, which clearly yields the worst sensitivity as the contributions from the pairs with an unfavourable overall sign outweigh the advantageous ones.

To sum up, for the cubic unit cell, where an implicit geometric phase imprinting has been reversed, it is the blue line (filled triangles) of fig. 7.7a an experimental setup should strive for. This line competes against the SRT line (red, empty squares), which carries the geometrically induced phase difference.

To investigate this elementary building block a little further, fig. 7.7b illustrates the weighted average lifetimes of the initial Ramsey state as a function of the lattice constant for various phase distributions. The average lifetimes are calculated as

$$\Gamma_{\mathrm{av}} = \sum_{j=1}^{2^N} \Gamma_j \left|\langle \psi_j | \psi_0 \rangle\right|^2 . \tag{7.25}$$

For very small lattice constants we observe that the PRT yields the lowest average lifetime, while for larger distances having no phase difference between the individual atoms gives better results. Now, this does not necessarily mean that SRT beats PRT at those distances, since, as discussed above, SRT suffers from an implicit imprinting of a phase induced by the sample's geometry.

7.6 Conclusions

Despite the common expectation that pairwise interactions and collective dynamics will introduce shifts and noise to ultrahigh precision spectroscopy setups in dense ensembles, we have shown, that using appropriate intermediate preparation steps, these effects cannot only be minimized but sometimes even used to improve the signal to noise ratio for Ramsey type measurements. Transferring excitation to the so-called protected subspaces prevents errors which cannot be corrected by common rephasing pulse schemes. An important example is the prevention of superradiant decay by a population transfer to subradiant states. Surprisingly, the lifetime of these subradiant states grows very fast with particle density and number, which is reflected in the scaling of both the minimum sensitivity and the maximally allowed interrogation times. While the main focus of this paper is the case of ensembles of cold atoms coupled via dipole-dipole interaction through the electromagnetic vacuum, the idea of using protected subspaces to improve precision spectroscopy can be extended to more general cases of engineered baths. Enhancing the interaction of atoms by coupling to a highly confined field mode [181, 197] induces long range mutual interactions between any pair of atoms yielding even stronger effects. Recently, analogous implementations using NV-centres or superconducting qubits coupled to CPW transmission lines or resonators showed surprisingly strong effects [183, 184, 198, 199].

In principle, our method in the most general form requires single particle control of the excitation phase. Luckily, in many cases of experimental realizations of such a generalized Ramsey method the required phase pattern has a lot of regularity and symmetries, which can be used to simplify the procedure. As a first guess one can think of an automatic phase imprinting achieved by the sample's geometry, where the phase front of a plane wave laser hits each element of a regular lattice with a different phase $\exp(ikr_i)$, with k being the wavenumber of the laser and r_i denoting the positions of the atoms. Addressing a linear chain transversally at right angle from the side leads to an equal phase for all particles. By tilting the laser and thus introducing an angle α between the laser's propagation direction and the elongation of the chain the relative excitation phase can be tuned as $\varphi_j = k(j-1)a \cdot \cos(\alpha)$. Alternatively, a magnetic field gradient applied for a prescribed time, resulting in a spatial gradient of the difference in splitting of $|g\rangle$ and $|e\rangle$ among the individual two-level emitters, will facilitate the accumulation of a relative phase between the atoms much in the form desired in our scheme. Phase gradients could also be engineered by the differential light shift of off-resonant laser fields. In principle, these phases can be even tailored

in 3D. Finally, an implementation in the framework of engineered baths, e.g., with superconducting qubits coupled to CPW transmission lines, could also be realized. Here one has indeed individual spin control. A more thorough discussion on practical considerations has been provided in Ref. [169].

Acknowledgements

We acknowledge the use of the open-source software [186] to generate fig. 7.1 and fig. 7.2. Support has been received from DARPA through the QUASAR project (L. O. and H. R.) and from the Austrian Science Fund (FWF) via project P24968-N27 (C. G.).

8 Publication: Selective Protected State Preparation of Coupled Dissipative Quantum Emitters

In this article, where the larger part of calculations and analysis was performed by David Plankensteiner, we investigate the possibility of addressing subradiant states directly, instead of preparing superradiant ones and then changing the phases of their coherences. We could show that, given an external field or engineered phases in the excitation itself, this is in fact possible. My contribution to this work mainly lies in the calculation and interpretation of the Depth of Entanglement results. The article was published in Scientific Reports on November 9th, 2015 [200].

Abstract

Inherent binary or collective interactions in ensembles of quantum emitters induce a spread in the energy and lifetime of their eigenstates. While this typically causes fast decay and dephasing, in many cases certain special entangled collective states with minimal decay can be found, which possess ideal properties for spectroscopy, precision measurements or information storage. We show that for a specific choice of laser frequency, power and geometry or a suitable configuration of control fields one can efficiently prepare these states. We demonstrate this by studying preparation schemes for strongly subradiant entangled states of a chain of dipole-dipole coupled emitters. The prepared state fidelity and its entanglement depth is further improved via spatial excitation phase engineering or tailored magnetic fields.

8.1 Introduction

Ensembles of effective two-level quantum emitters consisting of single atoms, ions, or defects in solids are employed ubiquitously in quantum optics and quantum information [201]. They are the basis for precision spectroscopy or atomic clock setups, as well as for experiments testing fundamental concepts of quantum physics or implementations of the strong coupling cavity QED (quantum electrodynamics) regime [202, 203]. In the absence of direct particle-particle interactions, larger ensembles allow for faster, more precise measurements [173] via a scaling of the effective single photon to matter

coupling strength g by a factor $\sqrt{N}$ (with system size N) and a reduction of the quantum projection noise (by $1/\sqrt{N}$) [175, 204].

For any precise measurement one has to externally prepare, control and measure the particle dynamics. Hence, the emitters are almost unavoidably coupled to their environment. A suitable theoretical framework to model such experiments is open system dynamics with a coupling to a fluctuating thermal bath. At optical frequencies this can often be approximated by the zero effective temperature electromagnetic vacuum field [139, 205]. Still, extra perturbations by a thermal environment and background gas collisions cannot be avoided.

In a laboratory experiment the particles need to be confined in a finite spatial volume that can be addressed by laser beams. Thus, increasing particle numbers will lead to higher densities, where direct particle-particle interactions as well as environmentally induced collective decoherence can no longer be neglected. For optical transition frequencies a critical density is conventionally assumed at the point where the average particle separation is of the order of an optical wavelength [206]. Above this limit vacuum fluctuations tend to become uncorrelated and decay becomes independent. However, recent calculations have shown that collective states can exhibit superradiance and subradiance even at much larger distances [156] as long as the bandwidth of the emission is small enough.

In many typical configurations and in optical lattices in particular, the particle-particle interaction is dominated by binary dipole-dipole couplings, with its real part inducing energy shifts and its imaginary part being responsible for collective decay [136, 207]. Generally, this interaction is associated with dephasing and decay. However, recently it has been found that under special conditions also the opposite can be the case and these interactions can lead to a synchronization [208] or even a blockade of the decay [209].

Oftentimes it is assumed that while such states exist, they cannot be prepared by lasers as they are strongly decoupled from the radiation fields. However, it was recently proposed that individual instead of overall addressing of the atoms can push the many particle system to evolve towards subspaces protected from decay or dephasing [169]. When applied to Ramsey spectroscopy such states have been shown to exhibit frequency sensitivities superior even to those obtained from non-interacting ensembles [187]. However, apart from special cases with an optimal lattice size and excitation angle, it is not so obvious how to implement such precise a control.

In this work we highlight the surprising fact that interaction induced level shifts can be used to aid in preparing such states. In many cases the magnitude of the shifts a state experiences and its lifetime are tightly connected allowing one to identify and address interesting states via energy resolution. As a generic ensemble we particularize to a 1D regular chain of quantum emitters coupled by dipole-dipole interactions with a tunable magnitude (by varying the interparticle separation). Collective coupling to the vacuum leads to the occurrence of subradiant as well as superradiant excitonic states [156]. In particular, the subradiant states should prove extremely useful

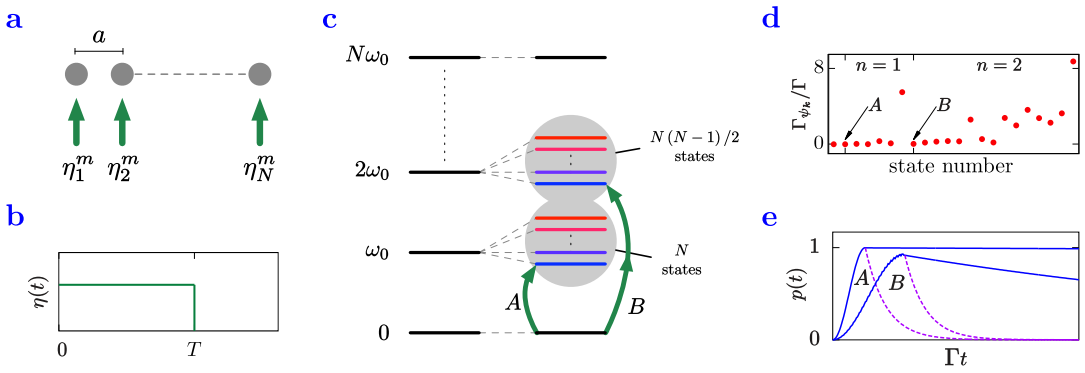

Figure 8.1: *Selective state preparation procedure.* a) A chain of N closely spaced quantum emitters (separation a with $ka \ll 1$, k being the laser wave number) are individually driven with a set of pumps $\{\eta_j^m\}$. b) The lasers are turned on for a time T, optimized such that an effective π-pulse into the desired subradiant target state is achieved. c) Level structure for the N systems where the C_n^N-fold degeneracy of a given n-excitation manifold is lifted by the dipole-dipole interactions. The target states are then reached by energy resolution (adjusting the laser frequency) and symmetry (choosing the proper m). d) Scaling of the decay rates of energetically ordered collective states starting from the ground state (state index 1) up to the single- and double-excitation manifolds for 6 particles at a distance of $a = 0.02\,\lambda_0$. The arrows identify the decay rates for the lowest energy states in the single (A) and double (B) excitation manifolds. e) Numerical results of the time evolution of the target state population for $N = 6$ and $a = 0.02\,\lambda_0$ during and after the excitation pulse. Near unity population is achieved for both example states A (where we used $\eta = 0.53\,\Gamma$) and B (for $\eta = 2.44\,\Gamma$) followed by a subradiant evolution after the pulse time T shown in contrast to the independent decay with a rate Γ (dashed line).

for quantum information as well as metrology applications as they exhibit robust, multipartite quantum correlations. As mentioned above, the atoms' interactions provide a first handle for target state selection as they lead to energy resolved collective states. Furthermore, using a narrow bandwidth laser excitation matched to the target states both in energy and symmetry allows for a selective population transfer from the ground state via an effective Rabi π-pulse.

In many cases, however, the required phase structure of the target state is not compatible with the excitation laser phase so that only a very weak coupling can be achieved. On the other hand, increasing the laser power reduces spectral selectivity by an unwanted addressing of off-resonant but strongly coupled states. Hence, to address a larger range of states of practical interest, we also propose and analytically study new methods of phase imprinting via a weak spatial magnetic field gradient. The

small relative phase shifts increase the effective coupling to groups of emitters via a nonuniform phase distribution. With this method any state may acquire a finite laser coupling to the ground state via the magnetically induced level shifts resulting in an efficient population transfer with a minimal compromise on lifetime.

The considered setup is a chain (see fig. 8.1a) of N identical two-level systems (TLS) with levels $|g\rangle$ and $|e\rangle$ separated by a frequency of ω_0 (transition wavelength λ_0) in a geometry defined by the position vectors $\{\mathbf{r}_i\}$ for $i = 1, ...N$. For each i, operations on the corresponding two-dimensional Hilbert space are written in terms of the Pauli matrices $\sigma_i^{x,y,z}$ and raising/lowering operators $\sigma_i^{\pm}$ connected via $\sigma_i^x = \sigma_i^+ + \sigma_i^-$, $\sigma_i^y = -i(\sigma_i^+ - \sigma_i^-)$ and $\sigma_i^z = \sigma_i^+\sigma_i^- - \sigma_i^-\sigma_i^+$. The complete Hamiltonian describing the coherent dynamics is

$$H = H_0 + H_{\text{dip}} = \omega_0 \sum_i \sigma_i^+\sigma_i^- + \sum_{i\neq j} \Omega_{ij}\sigma_i^+\sigma_j^-, \tag{8.1}$$

where H_0 is the free Hamiltonian and has degenerate energy levels (degeneracy $C_n^N = N!/(N-n)!n!$ for level n) ranging from 0 for the ground state to $N\omega_0$ for the highest excited state. The second term H_{dip} describes interactions between pairs of TLS which can be induced either by an engineered bath (such as a common, fast evolving optical cavity field) or by the inherent electromagnetic vacuum. We denote the couplings between emitters i and j by Ω_{ij} and particularize to the case of a free-space one dimensional equidistant chain of TLS with small interparticle distances a such that $a \ll \lambda_0$ (as depicted in fig. 8.1a).

For the sake of simplicity, we use dipole moments perpendicular to the chain for all numerical computations. To a good approximation, in the limit of $k_0 a \ll 1$, the nearest-neighbour (NN) assumption can be used (such that $\Omega_{ij} = \Omega\delta_{ij\pm1}$) and exact solutions in the single-excitation manifold can be found [210]. Within this subspace and approximation, the Hamiltonian assumes the form of a tridiagonal symmetric Toeplitz matrix with ω_0 on the diagonal and Ω above and below the diagonal. The solutions are readily available [211] with eigenvalues $\omega_0 + \epsilon_m$ for an index m running from 1 to N, where $\epsilon_m = 2\Omega\cos[\pi m/(N+1)]$ are the dipole-induced energy shifts. The corresponding eigenstates of the Hamiltonian are then

$$|m\rangle = \sum_j f_j^m \sigma_j^+ |G\rangle, \text{ with } f_j^m = \sqrt{\frac{2}{N+1}} \sin\left(\frac{\pi m j}{N+1}\right), \tag{8.2}$$

where we used $|G\rangle = |g\rangle^{\otimes N}$.

Spontaneous decay via a coupling to the free radiation modes in the evolution of the system can be included in a generalized Lindblad form [139],

$$\mathcal{L}[\rho] = \frac{1}{2}\sum_{i,j} \gamma_{ij}\left(2\sigma_i^-\rho\,\sigma_j^+ - \sigma_i^+\sigma_j^-\rho - \rho\,\sigma_i^+\sigma_j^-\right), \tag{8.3}$$

where the γ_{ij} denote collective damping rates arising from the coupling to a common radiation field. These rates also strongly depend on the atomic distances a with

two prominent limiting cases of $\gamma_{ij}(a \to \infty) = \Gamma\delta_{ij}$ (independent emitters limit) and $\gamma_{ij}(a \to 0) = \Gamma$ (the Dicke limit [140]). In general, one can perform a transformation of the Liouvillian into a new basis by diagonalizing the γ_{ij} matrix. This procedure leads to a decomposition into N independent decay channels with both superradiant ($> \Gamma$) and subradiant (robust) decay rates ($< \Gamma$) [187]. Note, however, that the states corresponding to these channels generally do not coincide with energy eigenstates of the Hamiltonian, so that we cannot reduce the system dynamics to simple rate equations.

8.2 Results

8.2.1 Selective State Preparation

Tailored coherent excitation. As mentioned above, our dipole coupled systems possess states with a large range of radiative lifetimes and energy shifts. Depending on the desired application particular states can be highly preferable over others. In a first straightforward approach we now illustrate that in principle it is possible to access a desired collective state simply by a selective coherent driving with a properly chosen amplitude and phase for each TLS. This is described by the Hamiltonian

$$H_m = \sum_j \eta_j^m (\sigma_j^+ e^{-i\omega_l t} + \sigma_j^- e^{i\omega_l t}), \tag{8.4}$$

with a suitably chosen set of η_j^m. For a targeted eigenstate in the single-excitation manifold, some analytical insight on how to choose these amplitudes can be gathered from the state's symmetry. For energy eigenstates this can be found quite reliably within the NN approximation [179]. In an equidistant finite chain our calculation suggests the following choice of driving fields at laser frequency ω_l,

$$\eta_j^m = \eta \sin\left(\frac{\pi m j}{N+1}\right), \tag{8.5}$$

chosen to fit the symmetry of a target state $|m\rangle$.

The selectivity of the excitation process can be further improved by an *energetically resolved excitation* of a given state $|m\rangle$ by a proper choice of the laser frequency $\omega_l = \omega_0 + \epsilon_m$ and its bandwidth. This is possible due to the interaction induced level splitting from H_{dip} (as depicted in fig. 8.1c). Indeed, in perturbation theory and in a frame rotating at ω_l the evolution of the system starting from the ground state up to a normalization factor leads to

$$e^{-iH_m t}\,|G\rangle \simeq |G\rangle - i\eta t\,|m\rangle\,. \tag{8.6}$$

The success of the corresponding process is illustrated in the sequence of plots in fig. 8.1, where the $|m = N\rangle$ state with $n = 1$ is considered (target state A) and accessed via the combination η_j^N of pumps lasting for a duration T.

Numerical simulations were performed on a six-atom chain with driving strength $\eta = 0.53\,\Gamma$ at an interatomic separation of $a = 0.02\,\lambda_0$. The time for which the pumps are switched on is $T = 1.58\,\Gamma^{-1}$ which is considerably shorter than the time scale governed by the decay rate of $0.0009\,\Gamma$ of the target state. The resulting dynamic is an effective π-pulse (efficiency of 99.94%) flipping the population into the state $|m = N\rangle$ followed by an extremely slow decay, indicating the robustness of the target state (as seen in curve A of fig. 8.1e).

It is, of course, desirable to target higher excitation manifolds as well. In the absence of analytical expressions or good approximations for the target states, we employ phases that yield maximal asymmetry, i.e., $\bar{\eta}_j = \eta(-1)^j$ for any $j = 1, ..., N$. Such a driving can be expected to address collective states, where the fields emitted by any two neighbouring particles interfere destructively [209] (similar to a previously investigated mechanism [169]). Numerical simulations show that the resulting collective states indeed exhibit the lowest energy shifts of the targeted manifold and can be expected to be long lived. The resonance condition for a specific state $|\psi\rangle$ within the manifold n is $n\omega_l = n\omega_0 + \delta\omega_\psi$, where $\delta\omega_\psi = \langle\psi| H_{\mathrm{dip}} |\psi\rangle$. As an illustration, the curve B in fig. 8.1e shows an almost perfect efficiency (98.36%) two-photon π-pulse allowing for a population transfer to the longest-lived collective state in the second excitation manifold of $N = 6$ emitters separated by $a = 0.02\,\lambda_0$. The chain was driven with a strength of $\eta = 2.44\,\Gamma$ for a time $T = 3.44\,\Gamma^{-1}$, which again is significantly shorter than the natural time scale given by the target state decay rate of $0.0402\,\Gamma$.

Let us add a comment on the practical implementation of such an addressing. In typical current experimental configurations for clocks based on 1D magic wavelength lattices [42, 212] the atoms are very close and hardly allow for an individual direct particle addressing. One is largely limited by a quasi plane wave driving, which typically addresses all particles with equal intensity. If the pump light is applied perpendicularly to the trap, the evolution is governed by a symmetric Hamiltonian H_{sym}, obtained from equation (8.4) with an equal pump amplitude $\eta_j^m = \eta$ for any m and j. A laser excitation from the ground state into the state $|m\rangle$ is connected to the coupling amplitude $\chi_m = \langle m| H_{\mathrm{sym}} |G\rangle = \eta \sum_i f_i^m$, which yields

$$\chi_m = \begin{cases} 0 & \text{if } m \text{ is even,} \\ \frac{\sqrt{2}\eta}{\sqrt{N+1}} \cot\left(\frac{m\pi}{2N+2}\right) & \text{if } m \text{ is odd.} \end{cases} \tag{8.7}$$

We will refer to states with even m as *dark states* as they cannot be accessed by the laser excitation and call the remaining ones *bright states* [209]. In the limit of large atom numbers $N \gg 1$, it is of interest to investigate the two cases, where $m \ll N$ and $m \sim N$, for states at the top/bottom of the manifold. In the first case, the function for the driving yields $\chi_m \approx \eta\sqrt{8N}/m\pi$, whereas in the other case we have $\chi_m \approx 0$.

Note, that sometimes geometry can change this behaviour. For a 1D string of equidistant emitters illumination at a chosen angle of incidence and polarization leads to a designable phase gradient of the excitation amplitudes. The situation becomes even more complex for a 3D cubic lattice, where the phases also differ in the different

lattice planes. As a lucky coincidence, a perpendicular plane illumination at the clock frequency in a magic lattice for Strontium (Sr) targets an almost dark state. This leads to subradiance and in principle allows for a spectral resolution better than the natural linewidth [190]. In not so favourable cases one could also think of a specific lattice design to facilitate a tailored dark state excitation.

Radiative properties. In order to be useful resources for quantum information applications, target states should exhibit *robustness* with respect to the environmental decoherence. To identify states of minimum decay rate, we scan through the eigenstates $|\psi_k\rangle$ of the Hamiltonian $H = H_0 + H_{\text{dip}}$ (for $k = 1, ..., 2^N$) and compute their decay rates Γ_{ψ_k} (see section Methods below). We find that generally, for a given manifold, the energetic ranking of the states closely indicates their robustness to decay (as illustrated by the colour-coding in fig. 8.1c) ranging from blue for subradiant states to red for superradiant states. This is due to the fact that both radiation and energetic shifts are strongly dependent on the symmetry of the states. In fig. 8.1d, for $N = 6$, we plot the decay rates of the collective states in the first ($n = 1$) and second ($n = 2$) excitation manifold arranged as a function of their increasing energy corresponding to the level structure of fig. 8.1c. Superradiant states are found at the upper sides of the manifolds while the ideal robust states lie at the bottom. In fig. 8.1d, the arrows indicate the optimal decay rates in the single- ($0.0009\,\Gamma$) and double-excitation manifolds ($0.0402\,\Gamma$) corresponding to target states A and B whose population evolution is depicted in fig. 8.1e.

Within the single-excitation manifold, an analytical expression for the decay rate of a state $|m\rangle$ can be found as $\Gamma_m = \sum_{i,j} \gamma_{ij} f_i^m f_j^m$. For small distances the state $m = 1$ (upper state) is superradiant, whereas states at the bottom of the manifold $m \sim N$ exhibit subradiant properties. In the Dicke limit where $a = 0$ we have $\gamma_{ij} = \Gamma$ for any i and j, and we can compute $\Gamma_m = 2\Gamma \cot^2 [m\pi/(2N + 2)]/(N + 1)$ for m odd and $\Gamma_m = 0$ for m even. Note, that in this particular limit, these are the same conditions as for the darkness and brightness of a state. For large numbers of emitters, we recover the expected superradiant scaling with N for the state with $m = 1$, i.e., $\Gamma_1 \approx 8\Gamma N/\pi^2$. On the other hand, large m yield a decay rate of $\Gamma_m \approx 0$ (perfect subradiance) in the same limit.

There are two important conclusions from these results: i) since in the considered limit the decay rate of the superradiant state $|m = 1\rangle$ scales with $\Gamma_1 \propto N$, whereas its driving is $\chi_1 \propto \sqrt{N}$, driving this state becomes more difficult with increasing atom number due to the reduced time-scale and ii) if the number of atoms is not too large, χ_m will remain finite, while Γ_m already indicates vast subradiance due to its scaling-down with N. Hence, there are robust states that remain bright, i.e., they can be driven directly even though the driving is not matched to their symmetry.

8.2.2 Accessing Dark States via Magnetic Field Gradients

The direct symmetric driving with $H_{\rm sym}$ allows access to bright states only. Given that nearby dark states can conceivably be more robust, we now employ a progressive level shifting mechanism that allows for a coupling between bright and dark states. This is achieved by subjecting the ensemble to a magnetic field with a positive spatial gradient along the chain's direction. The increasing energy shift of the upper atomic levels (as depicted in fig. 8.2a) plays a role similar to the individual phase imprinting mechanism described previously. For each particle the shift of the excited level induces a time-dependent phase proportional to the value of the magnetic field at its position. We demonstrate the mechanism for a particular two-atom example, where indirect near unity access to the dark subradiant asymmetric collective state is proved and extend it to the single-excitation manifold of N atoms.

Two-atom case. The eigenstates of the Hamiltonian $H_0 + H_{\rm dip}$ are $|E\rangle = |ee\rangle$, $|G\rangle = |gg\rangle$ and in the single-excitation subspace $|S\rangle = (|eg\rangle + |ge\rangle)/\sqrt{2}$ and $|A\rangle = (|eg\rangle - |ge\rangle)/\sqrt{2}$. The symmetric state $|S\rangle$ is superradiant ($\Gamma_S = \Gamma_1 = \Gamma + \gamma_{12}$) and bright, directly accessible via symmetric driving with strength $\chi_1 = \sqrt{2}\eta$. The asymmetric state $|A\rangle$, on the other hand, is subradiant ($\Gamma_A = \Gamma_2 = \Gamma - \gamma_{12}$) and dark. Indirect access can be achieved by shifting the second atom's excited state by $2\Delta_B$ (see schematics in fig. 8.2b), where Δ_B is tunable and quantifies the per-emitter shift for a given magnetic field amplitude. We first analyze the dynamics in the absence of decay by solving the time-dependent Schrödinger equation governed by the Hamiltonian $H = H_0 + H_{\rm dip} + H_{\rm sym} + H_B$, where $H_B = 2\Delta_B \sigma_2^+ \sigma_2^-$. We reduce the dynamics to three states, and assume a quasi-resonant Raman-like scheme where the population of $|E\rangle$ is at all times negligible. An effective two-level system arises (between the ground state and the asymmetric state; see section Methods below) and the resonance condition can be identified as

$$\Delta^{(2)} = -\Delta_B + \sqrt{\Delta_B^2 + \Omega^2 - 2\eta^2}, \tag{8.8}$$

with an effective Rabi frequency of

$$\nu_R^{(2)} = \frac{\sqrt{2}\eta\Delta_B}{\Omega + \sqrt{\Delta_B^2 + \Omega^2 - 2\eta^2}}. \tag{8.9}$$

To fulfil $|c_S|^2 \ll 1$, we need to restrict the driving to a parameter regime where $\eta, \Delta_B \ll \Omega$. A scan over the magnetic field is performed and the exact numerical results for the asymmetric state population are plotted in fig. 8.2d against the adiabatic solution showing near unity population transfer for an optimized Δ_B. Further restrictions are imposed when decay is considered. These stem from the fact that the coherent process described by ν_R should be faster than the incoherent one characterized by Γ_A. For close particles, the ability to tune the distance ensures that the scaling down of Γ_A is very fast and the above conditions are readily fulfilled.

For the particular example illustrated in fig. 8.2d we chose $a = 0.05\,\lambda_0$, resulting in $\Omega = 23.08\,\Gamma$, $\Gamma_A = 0.019\,\Gamma$. The 0.994 population is reached at $T = 16.19\,\Gamma^{-1}$, which is very close to the theoretical estimate of $T = \pi/2\nu_R^{(2)} = 16.179\,\Gamma^{-1}$ obtained from the adiabatic solution under the assumption of a π-pulse transferring the population to the target state.

Many-atom case. For a chain of N atoms, we consider the progressive shifting of excited levels along the chain depicted in fig. 8.2a. This is realized by the application of a magnetic field with a constant gradient and is described by the Hamiltonian $H_B = 2\Delta_B \sum_i (i-1)\sigma_i^+\sigma_i^-$. Let us consider a dark state $|d\rangle$ (d even) and the bright state $|b = d-1\rangle$ immediately above. Their coupling via H_B is quantified by $\Delta_{\rm db} = 2\Delta_B \sum_i (i-1) f_i^d f_i^b$, as shown in fig. 8.2c.

We develop a protocol where direct off-resonant driving into the bright state (amplitude χ_b) combined with a coupling between the bright and dark states via the magnetic field leads to an almost unity population transfer into the dark state. Given a sufficient energy separation, the problem can be reduced to solving the time-dependent Schrödinger equation for the three coupled state amplitudes c_b, c_d and c_G. Following the same adiabatic approximation as in the two-atom case we reduce the general dynamics to an effective two-level system between the states meant to be connected by an effective π-pulse, i.e., $|d\rangle$ and $|G\rangle$. The generalized resonance condition (with $\epsilon_{\rm db} = \epsilon_d - \epsilon_b$) reads

$$\Delta^{(N)} = -\Delta_B(N-1) - \frac{\epsilon_d + \epsilon_b}{2} + \sqrt{\frac{\epsilon_{db}^2}{4} + \Delta_{\rm db}^2 - \chi_b^2}, \tag{8.10}$$

and was obtained in the limit where the coupling of the dark state to the other adjacent bright state $|d+1\rangle$ was neglected owing to the relation $\chi_{d-1} \gg \chi_{d+1}$. The effective transition rate between the ground state and the state $|d\rangle$ is

$$\nu_R^{(N)} = \frac{\chi_b |\Delta_{\rm db}|}{\Delta + \epsilon_b + \Delta_B(N-1)}. \tag{8.11}$$

The addition of decay imposes a new constraint on the timescale of the process, i.e., $\nu_R^{(N)} \gg \Gamma_d$, required to ensure near unity population in the dark state. The fulfilment of this condition depends on the individual system under consideration. As an illustration of the procedure, fig. 8.2e presents the targeting of a robust dark state in the single excitation manifold of four particles. Note, that the numerical results are performed in an exact regime beyond the NN approximation and are in excellent agreement with our conclusions obtained from the NN treatment.

8.3 Discussions

8.3.1 Entanglement Properties

To justify the usefulness of collective states for quantum information purposes, we employ the von Neumann entropy to analyze their entanglement properties. More specifically, we compute the von Neumann entropy of the reduced density matrix ρ_s of a single two-level emitter (showing the degree of its bipartite entanglement with the rest of the system) defined by $S(\rho_s) = -\sum_i \lambda_i \log_2 \lambda_i$, where λ_i is the i-th eigenvalue of ρ_s and $0 \log_2 0 \equiv 0$. We furthermore minimize the set of values for all atoms to obtain a lower bound on the entanglement contained in the system. We compare the numerical results to the single-atom entropy of the symmetric Dicke state $|-N/2, -N/2+n\rangle$ [140]. For these particular states the entropy is maximized if the number of excitations in the state is $n = N/2$. It follows that it is highly desirable to drive the system into robust states as close as possible to $n = \lfloor N/2 \rfloor$ excitations (where $\lfloor N/2 \rfloor$ is the largest integer smaller or equal to $N/2$), since this manifold contains the most entangled state. A comparison of the exact numerical data and the analytical expression for the entropy is shown in fig. 8.3a.

Another way to characterize the entanglement of the prepared state is to investigate their *depth of entanglement* [213, 214], which does not quantify the entanglement itself but rather shows how many atoms of an ensemble are involved in the present entanglement. This measure has been used in recent experiments [214, 215] since it is a readily measurable quantity. The depth of entanglement is computed as follows: given an N-atom target state in which an arbitrary number of said N atoms is entangled, we compute the limit of how much population one can drive into this state such that the resulting density matrix ρ remains separable into a subset of density matrices that exhibit no more than k-atom entanglement ($1 \leq k \leq N$). This may be done by numerically maximizing the target state population P_t as a function of the ground state population P_G for different k. The boundaries themselves indicate how many atoms need to be entangled in order to prepare the pure target state, i.e., the boundary where the target state population is maximized to 1 corresponds to the number of atoms entangled in the (pure) target state. If a general prepared state has a target and ground state population such that the corresponding data point lies on or above the k-atom boundary, more than k atoms are entangled.

Obviously, for the pure target states considered in the above computation all atoms contribute to the entanglement, since otherwise the minimal von Neumann entropy as shown in fig. 8.3a would be zero. For a more interesting result, we can compute the depth of entanglement in order to demonstrate the efficiency of the driving procedure using a magnetic field gradient as in fig. 8.2e. From fig. 8.3b, where all boundaries have been plotted for the considered subradiant four-atom state, it is clear that the prepared state shows all-atom entanglement as the corresponding data point lies far above the boundary for three-atom entanglement.

8.3.2 Implementation Considerations

The proof-of-principle technique presented above has been particularized on a specific generic system of emitters in an equidistant chain. The choice is natural since the electromagnetic vacuum provides a simple example for both collective dispersive and dissipative dynamics. To exemplify a possible realization we consider a particular system [216] where bosonic Sr atoms are trapped in a magic wavelength optical lattice at separations of $a = 206.4$nm. The working transition is at $\lambda_0 = 2.6\mu$m, between the $^3P_0$ and $^3D_1$ electronic states. This amounts to a ratio of $a/\lambda_0 \approx 1/13$ which allows for an operation in the regime targeted by our scheme. The corresponding single atom decay rate is at the order of $\Gamma = 0.3$ MHz and circularly polarized light can allow for transitions between states with a difference of 1 in magnetic quantum number. We have numerically investigated a system of 4 atoms in such a configuration and found a sizable 73% target state population for $\eta = 2\,\Gamma$ and $\Delta_B = 0.5\,\Gamma$, under the conditions of a relatively small level shift between the dark and bright state around $6\,\Gamma$ which does not allow for large driving powers. For further optimization of the efficiency of the target state preparation one could envision a modified setup where a trapping transition of smaller wavelength can be chosen that would most importantly allow for better state separation (owing to larger dipole shifts). The corresponding magnetic field gradient required to produce the considerable $\Delta_B = 0.5\,\Gamma$ shift on a distance of $a = 206$ nm is around $5.2 \cdot 10^5$ G/m, not far from state-of-the-art values achievable in high magnetic field gradient magneto-optical trap experiments [217, 218]. Of course, there are many detrimental practical effects that can seriously limit the above technique such as light-assisted collision loss. We envision the extension of the described technique to systems where both the coherent and dissipative particle-particle interactions can be suitably tailored. For example, the same kind of dipole-dipole Hamiltonians can occur in 3D lattices of polar molecules [219] or between two different colour NV centres in diamonds [220].

8.3.3 Conclusions

Direct particle interactions are typically detrimental and limiting in precision measurement applications. Here, we have presented some specific opposite examples, where the *collective* nature of the decoherence combined with the coherent binary dipole-dipole interactions is used as a new resource for the controlled and efficient preparation of specially selected states. The excitation scheme can be tailored to address target states exhibiting both entanglement as well as robustness against decay. As a generic example we studied the case of a one-dimensional system of tightly spaced equidistant quantum emitters. Already the inherent dipole-dipole coupling allows for a targeted state preparation technique via energy selection. The performance of the excitation can be enhanced additionally via the *continuous* application of a spatially increasing magnetic field. The general principle of such a phase imprinting technique is potentially applicable in many specific environments such as optical lattices or atoms and ions

localized within one or more common optical cavity modes [181, 197], NV-centres or superconducting qubits coupled to CPW transmission lines or resonators [184, 198].

8.4 Methods

8.4.1 Decay Rate of the States

In order to arrive at an analytical expression for the decay rate of an eigenstate $|\psi_k\rangle$ of the Hamiltonian in equation (8.1), we consider the homogeneous part of the differential equation of the corresponding density matrix element that arises from the master equation. The solution of this differential equation yields an exponential decay. The rate at which the state population decays may be written as

$$\Gamma_{\psi_k} = -\langle\psi_k|\,\mathcal{L}\left[|\psi_k\rangle\langle\psi_k|\right]|\psi_k\rangle = \sum_{i,j}\gamma_{ij}\,\langle\psi_k|\,\sigma_i^+\sigma_j^-\,|\psi_k\rangle\,. \tag{8.12}$$

Note, that this is true only for states that contain a specific number of excitations, i.e., they are eigenstates of the operator $\sum_i \sigma_i^z$. Obviously, this is fulfilled for eigenstates of the considered Hamiltonian. Equation (8.12) was used in order to compute the rates depicted in fig. 8.1d and throughout the manuscript. For example, we used it in order to compute the decay rate of the eigenstates in the nearest neighbour approximation Γ_m.

8.4.2 Subradiance and Disorder

Let us consider the influence of spatial disorder on subradiant properties of the target states. To mimic disorder we perturb an equidistant chain of N emitters (average separation a) by introducing an uncertainty in each emitter position quantified by a defect parameter s (normal distribution of variance sa). We then write the randomized matrix of decay rates and find the minimum decay channel without, as well as in the presence of disorder of $s = 20\%$ and $s = 40\%$. For the $s = 0\%$ case, it has been shown [187] that the minimum decay rate scales exponentially with N even for distances up to $0.4\lambda_0$, while the linear scaling with N typical for superradiance is reached for $a \ll \lambda_0$ only. After averaging over 100 random configurations, we plot the logarithm of the minimal rates as a function of increasing N in fig. 8.4a.

As a somewhat surprising result, subradiance scales even better with N as the disorder increases. This might be understood as a destructive interference effect brought on by the cancellation of emitted photons stemming from the random positioning. As pointed out in previous investigations [187], the states of low symmetry (as, for example, the $m = N$ state) possess decay rates closest to the analytically derived minimal rate. We analyze the respective sensitivity of the state subradiance to disorder by initializing the system of N emitters in the $m = N$ state and allow it to

decay. The outcome is plotted in fig. 8.4b and shows remarkable robustness of the disordered systems on a long time-scale. While on a short time-scale disorder pushes the considered state into faster decaying channels, the long time limit shows that the remaining population accumulates in the disorder-enhanced robust states.

For short time-scales, the state still decays slowly (subradiantly), however, the decay rate increases with growing disorder ($s = 40\%$). More remarkable, though, is the behaviour the decaying states show for long time-scales, as the states subject to larger disorder become more robust than the unperturbed system. This is due to the fact that all population in the $m = N$ state that decays through more radiative channels have decayed at that point and only the most subradiant channel (minimal eigenvalue of the decay rate matrix) remains. As seen in fig. 8.4a, this eigenvalue is even further reduced by disorder which explains the long time-scale behaviour in fig. 8.4b.

8.4.3 Coherent Dynamics with a Magnetic Field Gradient

Two-atom case. To find the expressions in equation (8.8) and equation (8.9) we solve three coupled differential equations neglecting the population of the fully inverted state $|E\rangle$ as far off-resonant for all times. In the collective basis, where any state may then be written as $|\psi\rangle = c_S |S\rangle + c_A |A\rangle + c_G |G\rangle$, the equations are

$$i\dot{c}_S = (\Delta + \Delta_B + \Omega)c_S - \Delta_B c_A + \sqrt{2}\eta c_G, \tag{8.13}$$

$$i\dot{c}_A = (\Delta + \Delta_B - \Omega)c_A - \Delta_B c_S, \tag{8.14}$$

$$i\dot{c}_G = \eta c_S, \tag{8.15}$$

where $\Omega = \Omega_{12}$ is the coherent interaction between the atoms and Δ is the detuning between the atomic resonance frequency and the driving laser. For an efficient driving of $|A\rangle$ the population of the state $|S\rangle$ needs to be negligible which allows us to set a steady-state condition, namely $\dot{c}_S = 0$ yielding the desired effective two-level system between $|G\rangle$ and $|A\rangle$.

Many-atom case. The same approach as in the two-atom case may be used to describe the dynamics in the single-excitation manifold for an arbitrary number of atoms in a chain. Given sufficient energy separation we may neglect all states but the ones we aim to address. We can indirectly address a dark state $|d\rangle$ by driving the bright state $|b\rangle$ immediately above, which is coupled to the dark state by a magnetic field gradient. Neglecting all populations but c_b, c_d, and c_G and their respective couplings via the magnetic field gradient, the investigation reduces to the equations

$$i\dot{c}_b = \left[\Delta + \epsilon_b + \Delta_B(N-1)\right] c_b + \Delta_{\mathrm{db}} c_d + \chi_b c_G, \tag{8.16}$$

$$i\dot{c}_d = \left[\Delta + \epsilon_d + \Delta_B(N-1)\right] c_d + \Delta_{\mathrm{db}} c_b, \tag{8.17}$$

$$i\dot{c}_G = \chi_b c_b. \tag{8.18}$$

For an efficient driving of the dark state we may again invoke a steady-state condition on the bright state population $\dot{c}_b = 0$. This, again, yields an effective two-level system

between the ground and the dark state with resonance condition and Rabi frequency as displayed in equation (8.10) and equation (8.11), respectively.

8.4.4 Von Neumann Entropy

For a Dicke state an analytical expression for the von Neumann entropy of the reduced density matrix can be obtained. First, note that, since Dicke states are invariant under a permutation of the atoms, all reduced density matrices are identical. Hence, they all share the same von Neumann entropy for a given number of excitations n. We may choose to reduce the full density operator ρ to the density matrix of the first atom in the ensemble, i.e., $\rho_s^1 \equiv \rho_s = \mathrm{tr}_{2,\ldots,N}(\rho)$ which yields a von Neumann entropy of

$$S(\rho_s) = \frac{n}{N}\log_2\left(\frac{N}{n}\right) - \left(1-\frac{n}{N}\right)\log_2\left(1-\frac{n}{N}\right). \tag{8.19}$$

For the actual eigenstates of the Hamiltonian in equation (8.1) this computation needs to be done numerically. Furthermore, these states are not invariant under permutation of atoms and hence it is required to minimize the entropy with respect to the atomic chain index in order to find the lower bound.

8.4.5 Depth of Entanglement

The boundaries depicted in fig. 8.3b were found by maximizing the target state population with the condition on the density matrix of the prepared state to contain no more than k-atom entanglement, i.e., $\rho = \bigotimes_i \rho_i^{k_i}$ with $k_i \leq k$ and at least one $k_i = k$. To compute the boundaries we generalized the algorithm that was previously used solely for the W-state [214] to arbitrary states in the single-excitation manifold. For the computation of all boundaries we need to distinguish the two cases where $P_G = 0$ and $P_G > 0$. Considering a separable state ($k = 1$), the boundary for $P_G > 0$ is found to be

$$\max(P_t) = P_G \max_{\prod_i \alpha_i = \sqrt{P_G}} \left| \sum_i |c_i| \frac{\sqrt{1-\alpha_i^2}}{\alpha_i} \right|^2, \tag{8.20}$$

where $\alpha_i \in [0,1]$ and c_i are the coefficients of the target state. For $P_G = 0$ the maximization is much simpler, i.e., $\max(P_t) = \max|c_i|^2$, which is found by setting one $\alpha_i = 0$ and the remaining coefficients $\alpha_{j\neq i} = 1$. Note, that for both these and all following computations we neglect the symmetry of the state, i.e., the phases of the coefficients c_i by using $|c_i|$. This is valid due to the invariance of entanglement under local unitary operations and necessary if we restrict the coefficients α_i in the way we did.

For multiple-atom entanglement ($k > 1$) the matter of finding the corresponding boundary is no longer so simple. In order to find the maximum population, we assume

maximally allowed entanglement in the prepared state. We split the prepared state into $M = \lceil N/k \rceil$ sets, where $M-1$ sets are k-atom entangled and the remaining one is $k' = N - k(M-1)$-atom entangled. To find the maximum, one has to consider all possible positions of the k'-entangled state. If, for example, the k'-entangled state is at the last position, the population of the target state $|t\rangle$ in the prepared state reads

$$P_t = \left| \langle t | \left[\left(\bigotimes_{i=1}^{M-1} |\varphi_i^k\rangle \right) \otimes |\varphi_M^{k'}\rangle \right] \right|^2 , \tag{8.21}$$

where

$$|\varphi_i^k\rangle = \alpha_i |G_k\rangle + \sqrt{1-\alpha_i^2} \sum_{r=1}^{k} \lambda_r^i \sigma_r^+ |G_k\rangle \tag{8.22}$$

is a general non-separable state of k atoms in the single-excitation manifold. The state $|G_k\rangle$ is the k-atom ground state and the coefficients $\lambda_r^i \in [0,1]$ have to be normalized, i.e., $\sum_r (\lambda_r^i)^2 = 1 \; \forall \; i$. One then has to maximize the target state population with respect to the coefficients $\alpha_i \in [0,1]$ and λ_r^i with the condition $\prod_j \alpha_j = \sqrt{P_G}$. The number of these coefficients, however, grows vastly with the number of atoms, hence numerical computations are limited. For $P_G = 0$ one can again choose one $\alpha_i = 0$ and all $\alpha_{j \neq i} = 1$.

Note, that all boundaries computed via this maximization only hold for pure states. In order to find the boundaries for mixed states we need to compute the convex hulls of the respective boundaries [214]. The $k = N$ boundary is found when a perfect superposition between the ground and target state is reached.

In this work we considered the specific case of an exciton state of a four-atom chain. In that case, when investigating two-atom entanglement the permutation of the k'-entangled state is rendered unnecessary since $k' = k = 2$. Unfortunately, this is no longer true for $k = 3$, where we did have to account for all permutations.

Acknowledgements

We acknowledge financial support from the SFB through the FoQus project (D. P.), DARPA through the QUASAR project (L. O. and H. R.) and from the Austrian Science Fund (FWF) via project P24968-N27 (C. G.). Furthermore, we acknowledge the use of the QuTip open-source software [221]. H.R. thanks Vladan Vuletic for helpful discussions. C. G. thanks M. W. Mitchell for the suggestion of energetic addressing of collective states.

Author Contributions Statement

C. G. conceived the ideas and supervised the work. D. P. developed the concepts, conducted analytical calculations, took the main role in writing the manuscript and wrote numerical simulations, with support from L. O. especially in generalizing the depth of entanglement. H. R. provided guidance and expertise. The manuscript has been reviewed and edited by all authors.

Additional Information

No competing financial interests arise in the funding of this work.

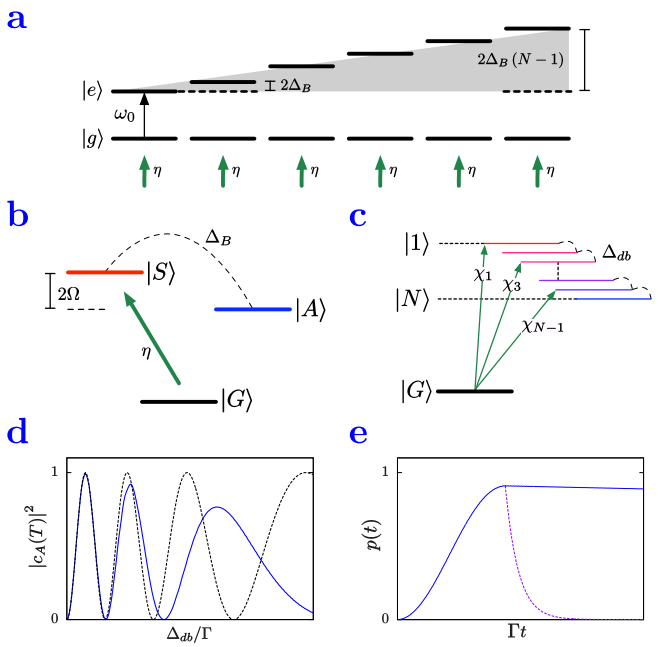

Figure 8.2: *Coupling to dark states via a magnetic field gradient.* a) Linearly increasing level shifts along the chain occurring in the presence of the magnetic field gradient. b) Illustration of the level structure and indirect dark state access for two coupled emitters. While symmetry selects the state $|S\rangle$, off-resonant addressing combined with bright-dark state coupling of strength Δ_B allows for a near-unity population transfer into the state $|A\rangle$. c) Dynamics in the single-excitation manifold of N coupled emitters where symmetric driving reaches the bright states with amplitudes χ_m while the magnetic field couples neighbouring dark and bright states. d) Plot of the asymmetric state population for the two-atom case as a function of the increasing magnetic field (solid line) compared to the steady-state approximation (dashed line) at numerically optimized time $T = 16.19\,\Gamma^{-1}$, with parameters $\eta = \Gamma$ and $a = 0.05\,\lambda_0$. e) For a chain of $N = 4$ emitters, a 91%-efficient π-pulse to the most robust state can be achieved as demonstrated in the population evolution plot. The separation is chosen to be $a = 0.025\,\lambda_0$, while $\eta = 40\,\Gamma$ and numerical optimization is employed to find $\Delta_B = 0.98\,\Gamma$.

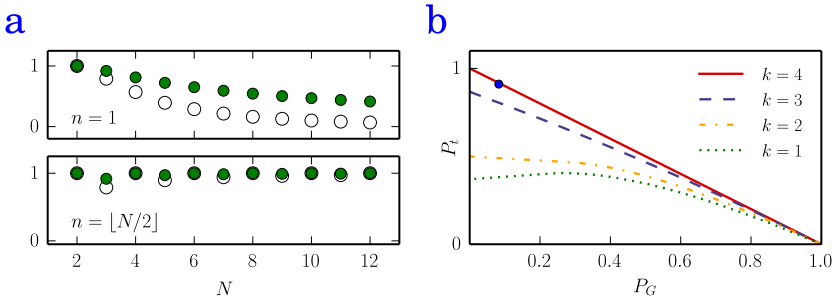

Figure 8.3: *Entanglement properties.* a) Comparison of the numerically computed von Neumann entropy (empty circles) of the reduced density matrix of the chain minimized over the atom index and the analytical expression for the entropy of the Dicke state (green circles), both for excitations $n = 1$ and $n = \lfloor N/2 \rfloor$ as a function of the atom number N at distance $a = 0.1\lambda_0$. b) Depth of entanglement of the subradiant four-atom state (blue dot) prepared by the magnetic field gradient scheme (see fig. 8.2e). It clearly lies above the $k = 3$ boundary indicating four-atom entanglement. The k-atom entanglement boundaries of the target state population P_t as a function of the ground state population P_G have been computed for the corresponding target state of a four-atom chain at distance $a = 0.025\,\lambda_0$.

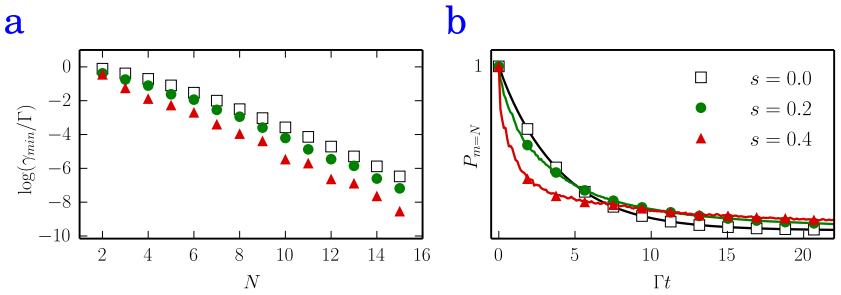

Figure 8.4: *Subradiance and disorder.* a) Plot of the logarithm of the minimal eigenvalue of the decay rate matrix (matrix with entries γ_{ij}) as a function of N at a distance of $a = 0.4\lambda_0$ for increasing levels of disorder ($s = 0, 0.2, 0.4$). b) Decay of the $|m = N\rangle$ state as a function of time. In the presence of disorder ($s = 0.2, 0.4$) the short time and long time behaviours are fundamentally different. At short times, disorder can push the state towards faster decaying channels while decay inhibition due to disorder occurs at larger times.

9 Publication: A Superradiant Laser on a Magic Wavelength Optical Lattice

In this article Thomas Maier and I numerically investigated properties of a laser, whose active medium is given by a collection of atoms that are coupled via dipole-dipole-interaction. The methods are quite similar to what we used in above publications, yet a cavity and a broadband pump are added. My contributions to this article were a plethora of discussions and guidance throughout the calculations as well as writing large parts of the text. The article was published in Optics Express on June 2nd, 2014 [190].

Abstract

An ideal superradiant laser on an optical clock transition of noninteracting cold atoms is predicted to exhibit an extreme frequency stability and accuracy far below mHz-linewidth. In any concrete setup sufficiently many atoms have to be confined and pumped within a finite cavity mode volume. Using a magic wavelength lattice minimizes light shifts and allows for almost uniform coupling to the cavity mode. Nevertheless, the atoms are subject to dipole-dipole interaction and collective spontaneous decay which compromises the ultimate frequency stability. In the high density limit the Dicke superradiant linewidth enhancement will broaden the laser line and nearest neighbour couplings will induce shifts and fluctuations of the laser frequency. We estimate the magnitude and scaling of these effects by direct numerical simulations of few atom systems for different geometries and densities. For Strontium in a regularly filled magic wavelength configuration atomic interactions induce small laser frequency shifts only and collective spontaneous emission weakly broadens the laser. These interactions generally enhance the laser sensitivity to cavity length fluctuations but for optimally chosen operating conditions can lead to an improved synchronization of the atomic dipoles.

9.1 Introduction

An essential and characteristic property of laser light, observed since its first generation, is its extraordinary coherence and frequency stability well below the width of the optical resonator used. Far above threshold the linewidth is limited by technical noise of the

gain medium and the mirrors only. Continuous technological advances have brought this limit down to an incredible stability below the Hz-level [222], which competes against the Q and the linewidth of long lived atomic clock states. At this point, further technological improvements seem extremely challenging. Therefore, it has been suggested recently [223] and to some extent demonstrated experimentally [159, 224] that an atomic clock transition could be used as a narrow band gain medium to run a laser. Due to the very feeble individual dipole moments of the atoms such a device can only be operated in the strong collective coupling regime, where superradiant emission into the field mode provides for the necessary gain [225]. In this domain of operation a huge collective dipole constituted by a large number of atoms, which are synchronized via their common coupling to the cavity field [160, 226], will build up.

The general idea of superradiant lasers and their properties have been discussed already two decades ago [167, 227], where a unique frequency stability scaling with the inverse square of the atom number N and squeezed output light was predicted. Their superb accuracy in the regime of a cavity linewidth much larger than the atomic linewidth were highlighted just recently [159]. Most importantly, in this case the laser becomes very insensitive to technical noise in the resonator and its properties are dominated by the intrinsic stability of the collective atomic dipole. Under favourable conditions, with only a few photons and millions of atoms present, a natural width of the system several orders of magnitude below the 1 Hz-level could be envisaged.

A central, yet open technical problem here is the implementation of a uniform collective coupling of the atoms to the field mode as well as the optical pumping in the atomic system without a considerable perturbation of the lasing levels, which in this case include the atomic ground state. Thus, a very careful choice of operating parameters is required. Here, we study another intrinsic source of perturbation in this sensitive system, namely direct dipole-dipole interaction between the laser active atoms, as they are densely confined within the optical resonator. Similar to atom-atom collisions in Ramsey experiments [116], dipole-dipole couplings tend to induce phase noise and decoherence of the collective atomic dipole. In particular in lattice setups at low filling, where collisions are strongly suppressed, this should constitute the most prominent source of noise for such a laser.

The basic phenomenon of superradiance was theoretically studied in detail, e.g., by Haroche and coworkers [147], about 50 years ago using a variety of analytical approximation methods [151, 152]. As an important effect one finds that the decay rate of low energy collective excitations grows linearly with the particle number N [228]. For multiply excited states the effect is increased further and the collective decay of a strongly inverted ensemble exhibits a delayed intensity maximum largely proportional to N^2 as a significant deviation from the exponential decay of individual atoms [144, 146, 147]. The phenomenon has been observed in a large number of experiments in gases and solids [146, 148] and more recently also for ultracold quantum gases [149, 150].

As in every laser setup, we naturally have to deal with inverted ensembles. Hence,

we can expect that superradiant effects will play an important role and the assumption of individual atomic decay at the independent free space single atom rate will lose its validity. Let us emphasize that the collective symmetric coupling of the atoms to the cavity mode does not require the atoms to occupy a small volume of the order of a cubic wavelength, but simply calls for an almost equal cavity coupling constant for all atoms. Dicke superradiant spontaneous decay, on the other hand, is maximal for closely spaced emitters, but still plays a decisive role in more extended geometries and in particular for regularly ordered ensembles. While this free space superradiant interaction and decay was incorporated intrinsically in the early works on superradiant lasing [227], it was neglected in the more recent considerations on superradiant lasing on ultra narrow atomic transitions [223].

In the present paper we investigate the full model for the collective decay process in a superradiant laser configuration. While the underlying Hamiltonian and dynamical master equations for the coupled atom-field dynamics are well established, exact treatments of the full decay problem for more than a few particles is hardly possible apart from some special cases. Numerical simulations can be performed for somewhat higher atom numbers in the fully collective limit. However, for more particles in a small but finite volume, collective and individual decay are present and the equations immediately become very cumbersome, as the number of occupied states within the total physical Hilbert space (growing as 2^N) gets prohibitively large. Interesting results can still be obtained for special finite configurations, which should exhibit the qualitative consequences of dipole-dipole coupling quite well. Besides demonstrating the underlying basic physical mechanisms, our study aims at direct implications for the laser linewidth of a magic wavelength lattice laser in the superradiant regime [40, 158–160].

9.2 Model

We consider N identical two-level atoms held in a regular spaced configuration, e.g., in a far detuned optical trap, each of them symmetrically coupled to a single mode of a high Q optical resonator. Due to the inherent exposure of the atoms to the vacuum bath the ensemble is affected by coherent dipole-dipole energy exchange processes and also by collective spontaneous emission [136]. Further, we employ a transverse incoherent pump, which allows us to use the atoms as an active medium, as well as another dissipative process, the cavity loss. Upon Born, rotating wave and Markov approximation we end up with a standard Lindblad type master equation. Explicitly the time-dependence of the N-atom density matrix is governed by ($\hbar = 1$)

$$\frac{\partial \rho}{\partial t} = i\,[\rho, H] + \mathcal{L}_{\rm cd}\,[\rho] + \mathcal{L}_{\rm pump}\,[\rho] + \mathcal{L}_{\rm cav}\,[\rho] = \mathcal{L}\,[\rho]\,, \tag{9.1}$$

with the Hamiltonian

$$H = \frac{\omega_0}{2}\sum_i \sigma_i^z + \sum_{i\neq j}\Omega_{ij}\,\sigma_i^+\sigma_j^- + \omega_c\,a^\dagger a + H_{\rm int}, \tag{9.2}$$

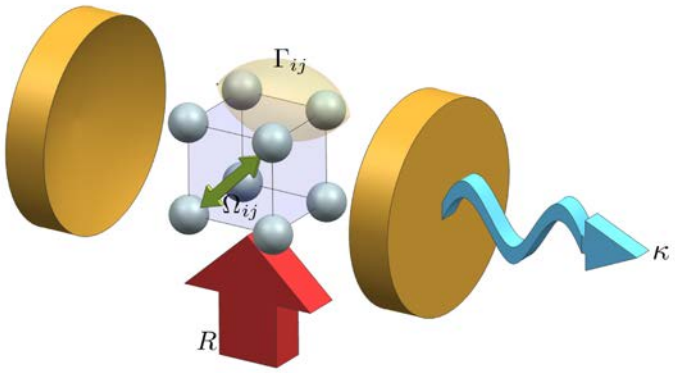

Figure 9.1: Schematics of a lattice laser setup. A transversely pumped (pumping rate R) finite atomic ensemble with dipole-dipole couplings Ω_{ij} and collective spontaneous emission Γ_{ij} inside an optical resonator with a loss rate of κ.

where σ_i^+ and σ_i^- are the raising and lowering operators for the atomic dipole of the i-th atom with the transition energy ω_0, the operators $a^\dagger$ and a correspond to the creation and annihilation of a photon with the frequency ω_c in the cavity mode , Ω_{ij} denotes the resonant dipole-dipole energy transfer between the atoms i and j, and

$$H_{\text{int}} = g \sum_i \left(a\sigma_i^+ + a^\dagger \sigma_i^- \right) \tag{9.3}$$

represents the Jaynes-Cummings type interaction between the individual atomic transition dipoles and the cavity mode with g being the coupling that emerges if a constant mode function is assumed. This approximation is justified in the situation where the atomic ensemble is aligned transversely to the propagation direction of the cavity mode or its dimensions are much smaller than the length of the resonator.

The collective atomic damping is accounted for by the Liouvillian

$$\mathcal{L}_{\text{cd}}[\rho] = \frac{1}{2} \sum_{i,j} \Gamma_{ij} \left(2\sigma_i^- \rho \sigma_j^+ - \sigma_i^+ \sigma_j^- \rho - \rho \sigma_i^+ \sigma_j^- \right) \tag{9.4}$$

with generalized spontaneous emission rates Γ_{ij} arising from the coupling of the atomic transition dipoles through the vacuum field [162]. The incoherent transverse broadband pumping, which in our model acts on each atom in the same way, leads to

$$\mathcal{L}_{\text{pump}}[\rho] = \frac{R}{2} \sum_i \left(2\sigma_i^+ \rho \sigma_i^- \sigma_i^- \sigma_i^+ \rho - \rho \sigma_i^- \sigma_i^+ \right) \tag{9.5}$$

with R quantifying the pumping rate and cavity loss with the rate κ is described by

$$\mathcal{L}_{\text{cav}}[\rho] = \kappa \left(2a\rho a^\dagger - a^\dagger a \rho - \rho a^\dagger a \right). \tag{9.6}$$

Observe that the collective coupling and decay matrices $[\Omega_{ij}]$ and $[\Gamma_{ij}]$ possess non-diagonal elements, which have to be calculated as a function of the system's geometry [144]. In many other cases, due to the finite correlation length of vacuum fluctuations, these nondiagonal parts can be safely neglected. Explicitly, for identical atoms we have [138]

$$\Gamma_{ij} = \frac{3\Gamma}{2} F\left(k_0 r_{ij}\right) \qquad \Omega_{ij} = \frac{3\Gamma}{4} G\left(k_0 r_{ij}\right) \tag{9.7}$$

with Γ the single atom linewidth, $k_0 = \omega_0/c = 2\pi/\lambda_0$ and

$$\begin{aligned} F(\xi) &= \left(1-\cos^2\theta\right)\frac{\sin\xi}{\xi} + \left(1-3\cos^2\theta\right)\left(\frac{\cos\xi}{\xi^2} - \frac{\sin\xi}{\xi^3}\right), \\ G(\xi) &= -\left(1-\cos^2\theta\right)\frac{\cos\xi}{\xi} + \left(1-3\cos^2\theta\right)\left(\frac{\sin\xi}{\xi^2} + \frac{\cos\xi}{\xi^3}\right), \end{aligned} \tag{9.8}$$

where $\xi = k_0 r_{ij}$. Here, r_{ij} denotes the relative distance between the atoms i and j and θ is the angle the transition dipole draws with the vector connecting the two atoms.

A crucial property of a laser is its spectrum in the steady state. In order to calculate the spectral distribution of the light field inside the cavity we employ the Wiener-Khinchin theorem [229], where

$$S(\omega, t) = \int e^{-i\omega\tau} \left\langle a^\dagger(t+\tau) a(t) \right\rangle \mathrm{d}\tau. \tag{9.9}$$

Numerically, this is achieved by at first determining the steady state ρ_S, which can be calculated as the kernel of the Liouvillian, i.e., solving $\mathcal{L}\left[\rho_S\right] = 0$. Now, the annihilation operator a is applied and we let this state evolve. After a time τ has elapsed, we apply the creation operator $a^\dagger$ and Fourier-transform the trace of this aggregate, as the Fourier transformation of the expectation value of the field correlation function equates to the spectrum of the intra cavity and output light field.

9.3 Superradiant Laser Dynamics with Confined Ensembles

9.3.1 General Properties of Superradiant Lasing

First, let us exhibit some general features of the dynamics of a laser with all atoms coupled equally to the cavity mode in the two idealized limiting cases of (a) fully collective and (b) individual independent spontaneous decay. Mathematically, this is implemented simply by setting (a) $\Gamma_{ij} = \Gamma$ for the collective case as discussed in [227] and (b) $\Gamma_{ij} = \Gamma\delta_{ij}$ for independent decay as studied in [223]. Surprisingly, the fully collective case is much easier to deal with numerically as the total collective spin magnitude is conserved and the Hilbert space for N atoms is restricted to the $N+1$ states of a spin-$N/2$ system. The effective pumping of the atoms can also be

described as an independent or collective , which results in analogous expressions as those describe the respective decay processes, see 9.4. Here we refrain from including dipole-dipole induced excitonic shifts of the energy levels. This assumption can be justified for a completely homogeneous atomic density [147] but has to be reconsidered for concrete finite size implementations. We will explicitly account for this in the finite lattice geometries discussed below.

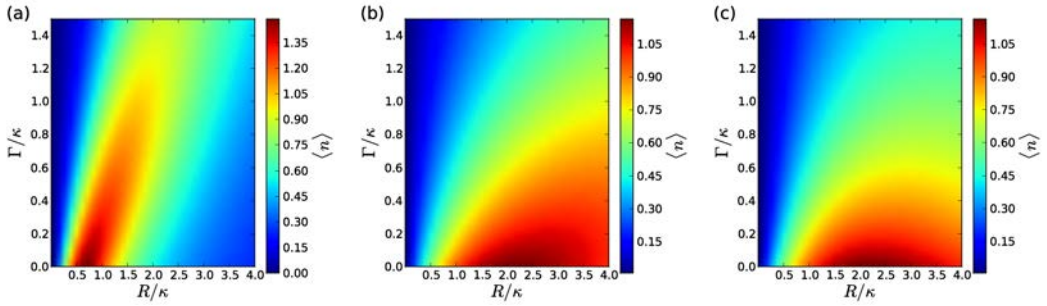

Figure 9.2: Stationary photon number as a function of the pump strength R and the spontaneous decay rate Γ for collectively pumped and collectively decaying atoms (a), individually pumped but collectively decaying atoms (b) and individually pumped and individually decaying atoms (c).

Figure 9.2 shows the mean photon number as a function of the pump strength R and the single atom decay rate Γ for the three cases of collective pump and collective decay, individual pump and collective decay and independent pump and independent decay for $N = 4$ atoms. We see that the maximum photon number is not so different for the three cases and appears at small spontaneous decay rates. For fully collective pump and collective spontaneous decay fig. 9.2(a) superradiant emission into free space limits the optimal operation regime to a lower pump intensity, though.

Now, it is of course most interesting to look at the frequency stability or line-width of this laser. As seen in fig. 9.3 the output intensity spectrum exhibits a nonlinear growth with the atom number (green line), as expected, until it saturates (red line). Remarkably, however, the linewidth does not narrow with the photon or atom number, but is even increased by superradiant spontaneous emission. Thus, the optimal case seems to be collective emission into the lasing mode without superradiant spontaneous decay. We will investigate this in more detail in the following sections.

9.3.2 The Superradiant Lattice Laser

Above we have seen that collective decay and collective pump strongly change the laser dynamics and its properties. Besides modified decay rates governed by eq. (9.4) in any finite size geometry dipole-dipole interaction as given by eq. (9.2) has to be taken into account as well. To study the basic physical effects, in this section we will

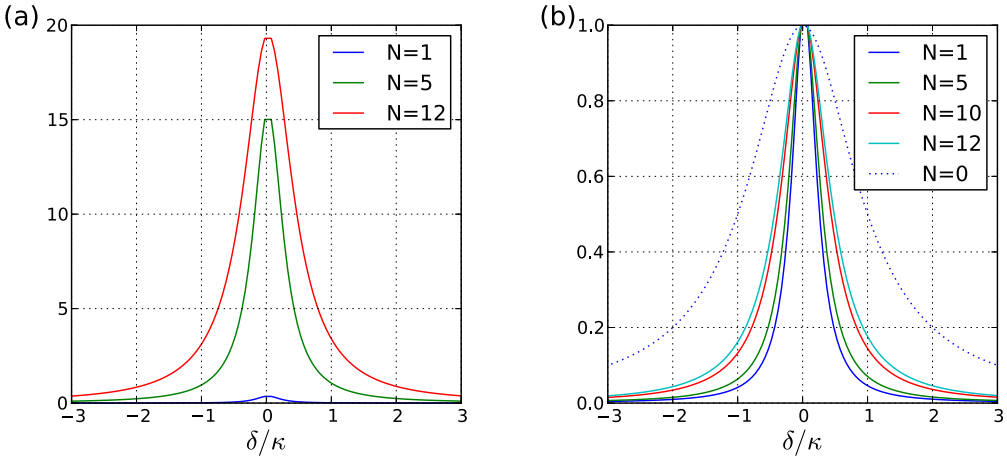

Figure 9.3: Output spectrum of a fully collective laser with different atom numbers N for $\Gamma = \kappa/20$ and $R = \kappa/5$ compared to the empty cavity linewidth ($N = 0$), absolute (a) and normalized (b).

investigate three different regular geometric arrangements for the laser active atoms. We compare a linear chain, where we go beyond the single excitation and nearest-neighbour coupling limits discussed in [228], to an equilateral triangle and a square configuration. Let us point out, that for two atoms, e.g., [145], the particular relative arrangement is irrelevant, and therefore the system can be handled analytically.

A square lattice of four atoms

As a generic example we first show the photon number, the inversion of the active medium atoms and the $g^{(2)}(0)$ correlation function for a fixed cavity loss κ while tuning the pumping rate R and the individual atom decay rate Γ for a four atom laser in a square lattice. The chosen lattice constant is half of the magic wavelength for Strontium, $\lambda_{\text{magic}}/(2\lambda_0) \approx 0.58$ [40, 166]. For the photon number shown in fig. 9.4(a) the maximum appears at a pumping ratio of $R/\kappa = 2.2$, which is equal to the result from above for individual pumping and collective decay as depicted in fig. 9.2(b).

In fig. 9.4(b) the expectation value of the σ_z operator is illustrated, where the black line represents the crossover to population inversion. On the right-hand side of the line the atom population is inverted, corresponding to the lasing case. Figure 9.4(c) presents the $g^2(0)$ function, where the white line highlights a value of $g^2(0) = 1$, indicating a perfectly coherent light field. The area where $g^2(0) < 1$ could be referred to as an anti-bunching regime.

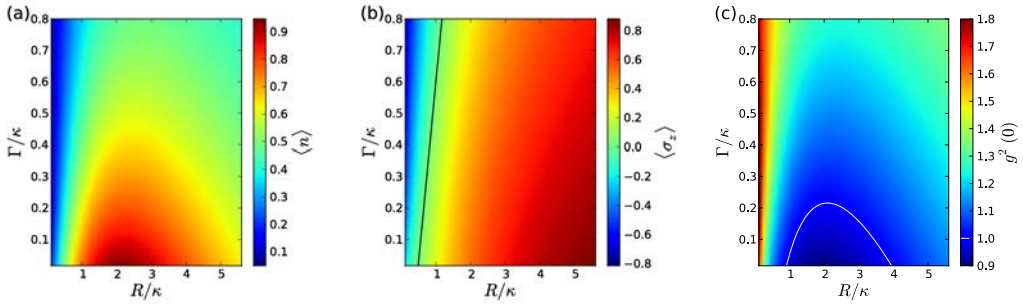

Figure 9.4: Stationary operation of a four atom laser on a square lattice. (a) photon number, (b) atomic inversion, where the black line indicates equal population of the excited and the ground state, (c) $g^2(0)$ function, with the white line at $g^{(2)}(0) = 1$ representing a coherent state.

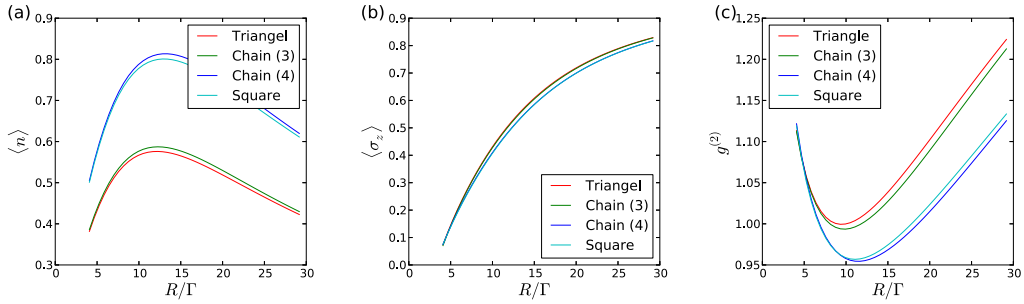

Figure 9.5: Photon number (a), atomic inversion (b) and g^2 function (c) of the laser as a function of the pump strength R for different atomic arrangements and a fixed spontaneous decay rate $\Gamma = 0.2\kappa$.

Comparison of different geometrical configurations

Let us study the influence of the geometric arrangement of the particles for different numbers of atoms and compare the results for the square discussed above to an equilateral triangle of atoms and a three and four atom chain. In order to obtain a substantial effect despite our small atom numbers, we choose a smaller lattice constant of $d = \lambda_0/10$ and a fixed atomic decay rate of $\Gamma/\kappa = 0.2$.

In fig. 9.5 we show, that for the average values the atom number is more important than the particular geometric arrangement. Interestingly for four atoms one can even reach sub Poissonian photon statistics.

Naturally, the results depend on the average distance of the atoms, which is shown in the following set of pictures in fig. 9.6 for a square of different lattice constants d with a fixed spontaneous emission rate of $\Gamma/\kappa = 0.2$. As one might have expected, fig. 9.6 demonstrates a much more pronounced effect when varying the distance as

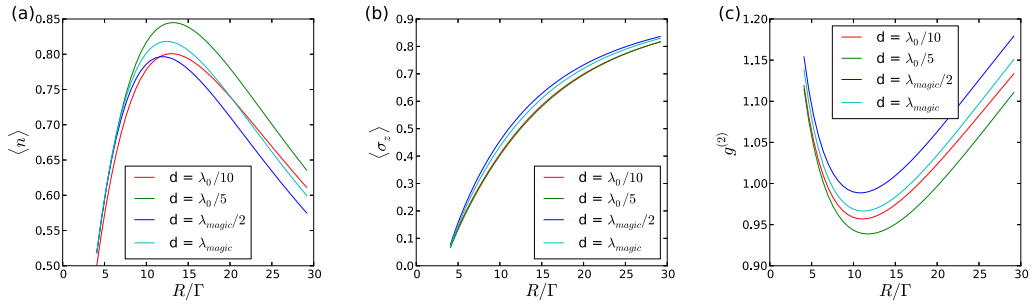

Figure 9.6: Photon number (a), atomic inversion (b) and g^2 function (c) of the laser as a function of the pump strength R for a square of different lattice constants d and a fixed spontaneous decay rate $\Gamma = 0.2\kappa$.

opposed to changing the geometry.

Overall, despite fairly strong interactions of the atoms at small distances, the laser seems to be very robust against such pairwise perturbations, which appear to average out quite well once the oscillation threshold is surpassed. The differences increase with pump strength where, on average, more particles are excited.

9.4 Laser Stability and Frequency Shifts for Different Atomic Distances

Of course, the most sought after quality of a superradiant laser is its superb frequency stability and accuracy. In the first section we have seen that collective spontaneous decay can broaden the laser line. As dipole-dipole interactions shift the atomic energy levels, this might as well change the laser line position, which we will now study for a lattice laser in more detail in the following. Now, we will study this effect for a lattice laser.

9.4.1 Laser Linewidth and Frequency Shift

As is well known, the spectrum of a laser in the bad cavity limit deviates from the idealized Shawlow-Townes result, but the centre of the line still approximately follows a Lorentzian [160] so that in our numerical analysis the linewidth and its centre position relative to the bare atom line can be determined from a Lorentzian fit to the steady state spectrum, as described in sec. 2. Therefore, the width of the Lorentzian corresponds to the laser's linewidth while the offset in the maximum describes the energy shift, which is the energy of the light field in the cavity relative to the cavity ground frequency. Figure 9.7 and fig. 9.8 present the fitted width γ_L and the energy shift δ for different interatomic distances and geometrical configurations as

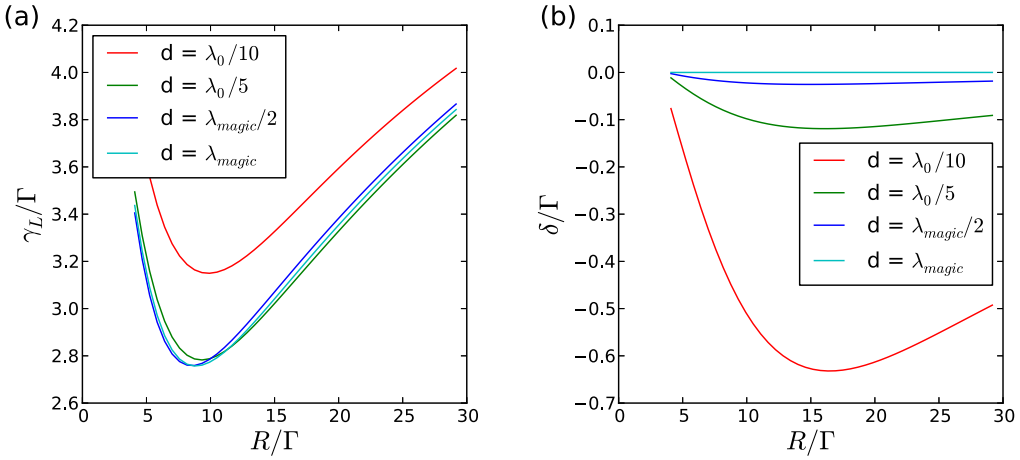

Figure 9.7: Laser linewidth (a) and frequency shift (b) for a square atom arrangement at different distances as a function of the pump strength for a fixed atomic decay rate of $\Gamma = 0.2\kappa$.

a function of the pumping rate R. For these calculations we used the same parameters as above and we don't include a detuning between the atoms and the cavity mode ($\Delta = \omega_c - \omega_0 = 0$).

In fig. 9.7 we depict the linewidth and frequency shift of a laser with four atoms in a square configuration as a function of the pump strength for different inter atomic distances. We observe a minimum linewidth at a moderate pump strength of $R/\kappa \approx 1.9$, which corresponds to an operation at the maximally achievable photon number, as shown in fig. 9.4.

For a stronger pump the perturbations due to collective interactions dominate, though significant effects appear for very closely positioned atoms, i.e., $d < \lambda_0/2$, only. Even with just four atoms it is possible to achieve a linewidth significantly below the resonator's linewidth. The predicted frequency shift with respect to the bare atom frequency (as depicted in fig. 9.7) remains very small for larger interatomic distances and reaches a maximum value when the laser is operated at $R/\kappa \approx 3$, close to the maximum photon number. This could certainly be an observable phenomenon, but it is not detrimental for the operation of such a laser. Obviously, for a realistic setup we assume much too high a value for the atom-mode coupling g, which however seems justified as one of our individual atoms could represents 10^3 to 10^4 atoms in an experiment.

Interestingly, for the linewidth and shift properties, geometrical effects are more important than they are for the average intensity. A square arrangement of the atoms creates a much larger shift than a triangular or a linear array, as can be seen in fig. 9.8. Note that the increased shift with the atom number could lead to observable perturbations for larger ensembles. Again, operation at a lower pump intensity could

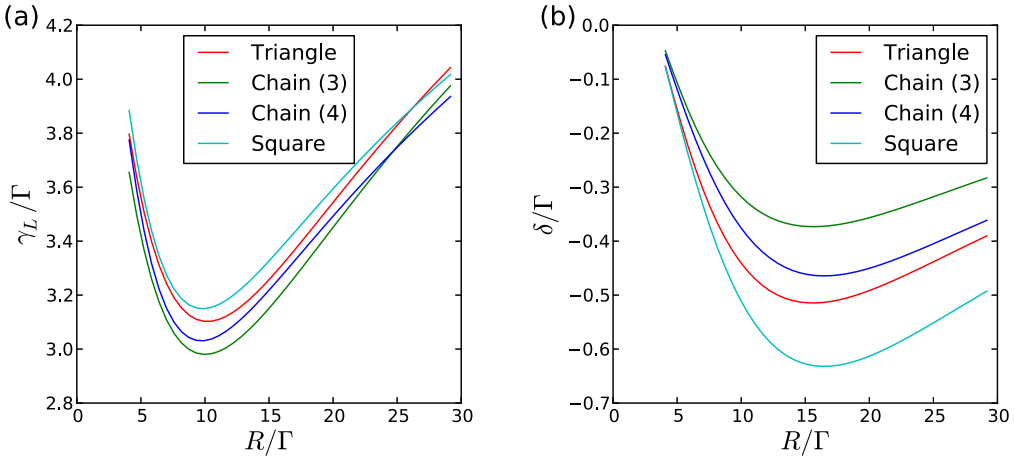

Figure 9.8: Laser linewidth (a) and frequency shift (b) for different geometric configurations but same lattice constant ($d = \lambda_0/10$) as a function of the pump strength for a fixed atomic decay rate of $\Gamma = 0.2\kappa$.

help to minimize the effect.

9.4.2 Laser Sensitivity to Cavity Length Fluctuations

A central criterion for the stability of a laser is its sensitivity to fluctuations of the effective cavity length, which at present is one of the main limitations of reference oscillator stabilized lasers. Despite spectacular recent progress [42], comprehensive control at this level is still an extraordinary technical challenge. With the atoms acting as reference oscillators less effort in order to achieve technical stabilization is expected in an ideal superradiant laser. In the following we will study the effect of a varying cavity frequency described by an effective detuning (Δ) on the average photon number fig. 9.9 and the frequency mismatch between the bare atomic transition frequency and the laser field ($\delta_a = \omega_0 - \omega_L$) as seen in fig. 9.10 depending on the average atomic distance. As shown in fig. 9.9(a) for closely positioned atoms the interaction evokes a significant blue shift of the cavity frequency, generating the maximum photon number with respect to the clock transition. For atoms in a magic wavelength lattice fig. 9.9(b) this shift is much smaller and close to the interaction-free case. The detuning sensitivity of the laser output spectrum in these two cases is depicted in fig. 9.10.

We see that the laser frequency pulling via the cavity changes with the interaction and increases with pumping and the intracavity photon number. Nevertheless, as indicated by the solid and dashed lines, the effective laser frequency change remains within an atomic linewidth even for cavity fluctuations on the order of the cavity width. At low pump strength and small inversion a sort of self-synchronization of the atomic dipoles via direct interactions can lead to very strong suppression of cavity

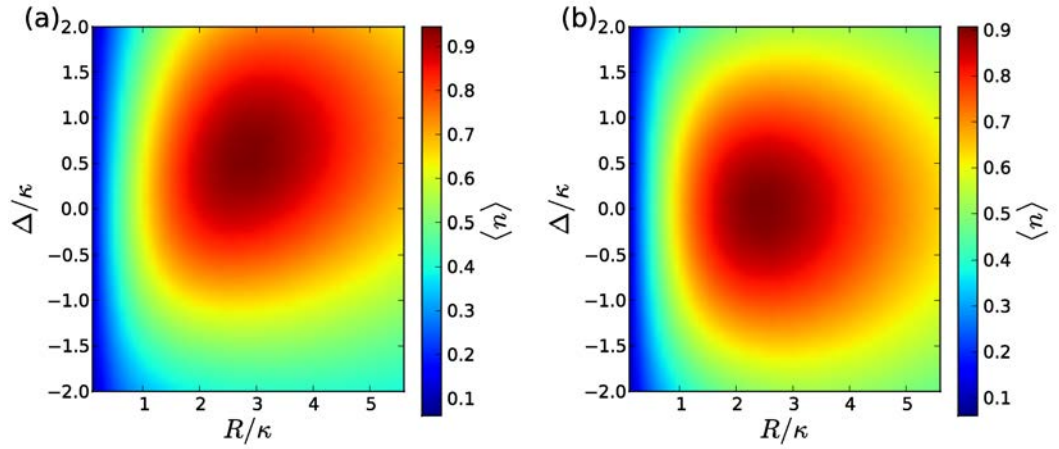

Figure 9.9: Average photon number for atoms on a square with $d = \lambda_0/10$ (a) and $d = \lambda_{\text{magic}}/2$ (b) for variable cavity detuning and an atomic decay rate $\Gamma = 0.2\kappa$.

fluctuations at the expense of very little output light, while for stronger pumping interaction effects are suppressed and the cavity drifts produce a more significant impact on the laser frequency. Overall, we observe that by choosing optimal operating conditions a decoupling of the cavity fluctuations from the laser frequency can be suppressed very effectively, even in the case of atomic interactions. However, this decoupling generally also reduces the output power of the laser.

9.5 Conclusions and Outlook

By means of numerically solvable examples involving a few particles only, we have evaluated the influence of dipole-dipole interaction and collective spontaneous emission on the radiative properties of a superradiant laser in a lattice geometry. In general, even for fairly closely spaced atoms, shifts and frequency uncertainties are of the order of the free space atomic linewidth. Only for very densely packed ensembles superradiant free space decay will substantially broaden the laser line and increase the sensitivity of the laser frequency to cavity drifts. Quantitatively, the various limiting cases of a completely collective laser as opposed to an independent atom system can lead to a different scaling behaviour of the photon number and the linewidth with substantially different photon statistics. Fortunately, for a Strontium setup based on a magic wavelength lattice, the detrimental effects remain very small, although they could attain an observable magnitude at high filling. At optimally chosen operating conditions dipole dipole interaction can be exploited to reduce laser frequency fluctuations via direct phase stabilization even at very low photon numbers.

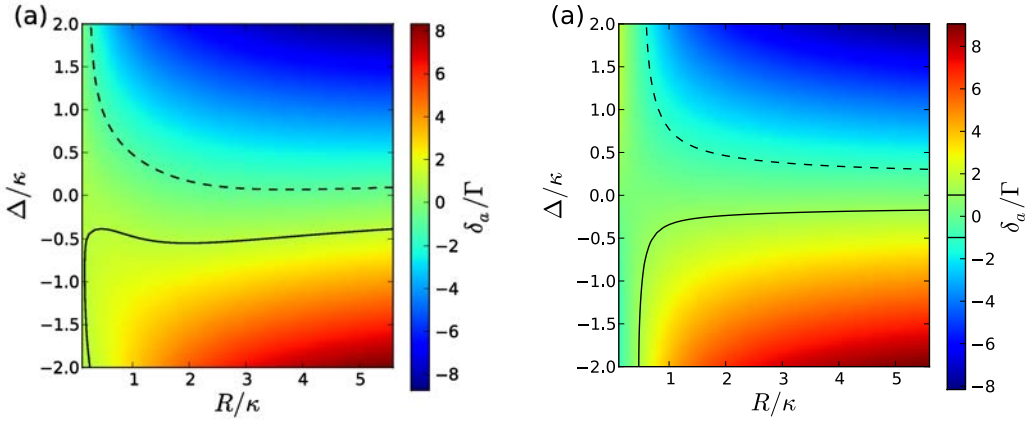

Figure 9.10: Frequency shift for a square atom configuration with $d = \lambda_0/10$ (a) and $d = \lambda_{\text{magic}}/2$ (b) for variable detuning and a fixed atomic decay rate of $\Gamma = 0.2\kappa$. The dashed line represents $\delta_a/\Gamma = -1$ and the solid line corresponds to $\delta_a/\Gamma = 1$.

In this work we still assumed a rather ideal and to some extent artificial pumping mechanism, replenishing the upper atomic state by introducing the minimum necessary decoherence only, while also neglecting light shifts from the pump lasers. Any more realistic pumping via extra levels or an injection of excited atoms would, of course, add extra noise and has to be designed very carefully. This is one of the major remaining challenges for the implementation of such an optical version of the hydrogen maser. In any case, from the point of view of stability and shifts, the operation at weak pump strength seems favourable, although the very weak output field could be a technical challenge for practical use.

Acknowledgements

We thank M. Holland, D. Meiser, J. Ye, C. Genes and A. M. Rey for stimulating discussions and acknowledge support by DARPA through the QUASAR project and the Austrian Science Fund via the SFB Foqus project F4013.

10 Conclusions

The publications presented above constitute the main body of this thesis and have followed each other on a fairly straight path. Let us now summarize these papers and present general conclusions and an outlook on further research opportunities in their realm.

10.1 Summary and Conclusions

Throughout this thesis we have seen that dipole-dipole interaction and the resulting enhanced or decreased collective spontaneous emission rates can have a large effect on spectroscopic measurements.

We began with an investigation of dipole-dipole interaction in somewhat extended toy models of three, four and five emitters. We saw that moving from the arguably simple case of two atoms, where super- and subradiance can be treated straightforwardly, more than two emitters becomes much more involved rather quickly. We have performed analytical investigations of a equilateral triangle and numerical calculations for a three-atom chain. Our main results were that the closer the emitters are to each other, the more detrimental their interactions are to a Ramsey spectroscopy setup and that for the magic wavelength of ^{87}Sr the nearest-neighbour dissipative coupling becomes negative, resulting in subradiant behaviour.

In the next part, we have presented and investigated the idea of using subradiant as opposed to superradiant states in a Ramsey spectroscopy setup. We did this by improving the measurement procedure to include an extra step, namely the phase separation of individual emitters after the first $\pi/2$-pulse. In this way, the superradiant states, where the coherence between all emitters is perfectly in phase, are replaced by their subradiant counterparts, which results in a vast improvement of measurement precision. We have demonstrated the concept for two emitters, both numerically and analytically and we have conducted numerical investigations for larger systems of different geometries, all showing an increase in precision when using the altered Ramsey technique.

Further investigations with a focus on scalability and larger systems have shown that a phase shift of π in the coherence between next neighbours seems to yield the best overall precision. Additionally, we could show that subradiant decay rates scale almost exponentially with the system size and thus hint at very promising results for large systems. Lastly, a cube, posing as the unit cell for a 3D lattice, has been looked

at and we found that for small lattice constants a phase altered Ramsey procedure as we proposed clearly outperforms the regular Ramsey technique.

Now, we focused on preparing subradiant states directly, in contrast to altering the phase of the coherence after the first half excitation to obtain subradiant states. We saw that by using an excitation scheme, which features a direct phase imprinting onto the individual emitters, we could realize an almost perfect Rabi π-pulse from the ground state to a targeted subradiant state, both for the single- and the two-excitation manifold. We could verify numerically that these states are in fact subradiant as they feature a vastly decreased spontaneous emission rate. We have suggested a concrete realization with a magnetic field gradient in order to implement our scheme experimentally.

Lastly, we have applied our methods and insights from free space optical lattices to the investigation of a superradiant laser. Here, we basically took the same systems we had been looking at before and put an optical cavity around them. We found that a laser device with atoms in an optical lattice as its active medium is fairly insensitive to the collective effects among the atoms as long as they are placed sufficiently far apart from each other. At very narrow atomic densities the laser suffers from collective shifts and increased spontaneous emission, though, which makes it more sensitive to other outside perturbations. For ^{87}Sr in a magic wavelength lattice, however, these effects can safely be ignored.

In conclusion we found that using subradiant states in spectroscopy can dramatically improve the sensitivity and precision of a setup relying on the Ramsey measurement scheme. In that sense, it seems possible to achieve stabilities below the single atom linewidth in future optical lattice atomic clocks. But, of course, long-lived states can also be used in other applications. Long-time quantum memories for quantum computing and quantum information as well as quantum communication setups could all benefit from slowly decaying subradiant states.

10.2 Future Research Questions

A first and straight-forward next research target is optical lattices with a filling factor of less than unity. This means a, so to say, random distribution of N emitters onto M lattices sites with $N < M$. At larger distances, dipole-dipole interaction ebbs away in general, yet, clusters of emitters can build up and act as one effective dipole with effective shifts and decay rates. Numerical and possibly analytical calculations, reducing the clusters to effective dipoles, could be carried out. Additionally, employing the mean-field approach of chp. 11 more involved calculations and actual simulations of the measurement procedure could be performed.

Another idea would be to include atomic motion or temperature in our treatments. So far, we have assumed the dipoles to be at fixed positions, characterized by a position vector. Yet, classical or even quantum mechanical motional degrees of freedom could

be included in the models. Of course, this quickly becomes very involved as the Hilbert space would grow drastically. Yet, toy models or approximate larger models should be tractable.

In terms of a superradiant laser, a more involved model could be developed. This includes a realistic pumping mechanism, where phase factors and shifts introduced by the pump laser are taken into account. A expanded level structure of the individual atoms, i.e., three or four instead of just two levels, may be of interest. Also larger atom numbers for the effective medium could provide further insights into realistic systems.

To name another area of interest, it could be worthwhile to look at the effects of dipole-dipole interaction in optical fibers in contrast to free space. Here, not every wave vector is permitted, which should alter the results of the dipole-induced shifts and collective emission rates noticeably. Experiments investigating superradiance in fibers are currently being performed at various institutions.

11 Publication: Optimized Geometries for Future Generation Optical Lattice Clocks

In this letter, which has been submitted to EPL, Sebastian Krämer and I tackle the question of which geometry of an optical lattice is most favourable for subradiance and thus a long probe time in a Ramsey spectroscopy setup. Sebastian came up with our mean-field approach to the dipole-dipole coupled emitters and my contribution was the idea to use this formalism for looking at optimal geometries as well as lots of discussions and writing the article itself. This work has been published on May, 6th 2016 [230].

Abstract

Atoms deeply trapped in magic wavelength optical lattices provide a Doppler- and collision-free dense ensemble of quantum emitters ideal for high precision spectroscopy and they are the basis of some of the best optical atomic clocks to date. However, despite their minute optical dipole moments the inherent long range dipole-dipole interactions in such lattices still generate line shifts, dephasing and modified decay. We show that in a perfectly filled lattice line shifts and decay are resonantly enhanced depending on the lattice constant and geometry. Potentially, this yields clock shifts of many atomic linewidths and reduces the measurement by optimizing the lattice geometry, such collective effects can be tailored to yield zero effective shifts and prolong dipole lifetimes beyond the single atom decay. In particular, we identify dense 2D hexagonal or square lattices as most promising configurations for an accuracy and precision well below the independent ensemble limit. This geometry should also be an ideal basis for related applications such as superradiant lasers, precision magnetometry or long lived quantum memories.

11.1 Introduction

Since the turn of the century the technology of manipulating and controlling ultracold atoms with lasers has seen breathtaking advances [231–233]. Following the seminal demonstration of a quantum phase transition in an optical lattice [234], nowadays the

so-called Mott insulator state with exactly one atom per site can now be prepared routinely [165, 235]. Experiments with photo-associated ultracold molecules have reached a comparable control [219, 236–238]. Coherent interactions between the atoms at neighbouring sites can be tailored [239] and using large and sufficiently dense ensembles one overcomes the weak single atom field coupling in free space [203].

For some of the world's best optical clocks [240–242], atoms with a long-lived transition are prepared in an optical lattice using a differential light shift free (magic) trapping wavelength [40, 95]. In principle, this provides for a Doppler free and, for 3D confinement, also a collision free cold and dense ensemble with negligible inhomogeneous broadening, eliminating major clock accuracy limitations. However, when excited optically, emitters are still not completely independent as they will inevitably interact via a long range resonant dipole-dipole coupling [243].

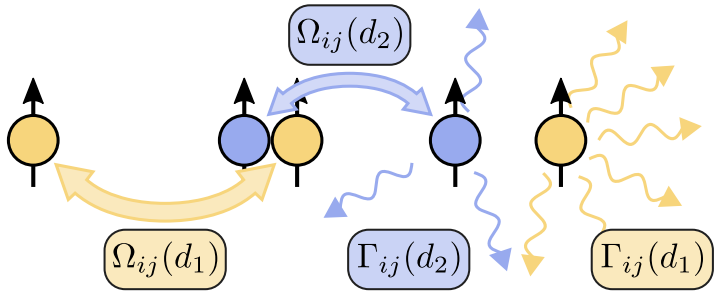

Figure 11.1: (Colour online) Scheme of a 2D optical lattice filled with clock atoms interacting via dipole-dipole energy exchange Ω_{ij} and a collectively modified spontaneous emission Γ_{ij} at two different lattice constants shown in blue and yellow. In a mean field treatment with translation invariance the sum over all interaction terms yields two effective couplings Ω^{eff} and Γ^{eff} only, which govern the approximate system dynamics.

At sufficient densities, i.e., small lattice constants, this dipole-dipole interaction strength surpasses the excited state lifetime and collective excitations analogous to excitons appear [179]. For distances much smaller than the wavelength as for polar molecules in optical lattices they dominate the dynamics [244] and allow for studying generic phenomena of solid state physics [231]. For clock transitions the extremely tiny dipole moment keeps these interactions small. However, the excitons effective transition frequencies and their spontaneous decay rate is still dominated by dipole-dipole interaction [144] substantially deviating from the bare atom case. Although not fully reached in current setups, this constitutes a fundamental limit for the accuracy and precision of corresponding clock setups.

In an idealized Ramsey sequence for a clock setup, the first laser pulse creates a product state of all atoms prepared in a 50% superposition of ground and excited state with equal phase and all dipoles aligned in parallel. This state features the maximally possible dipole moment and typically exhibits superradiance. Even a tiny single particle spontaneous emission rate thus can be that strongly enhanced, that collective decay becomes the dominant factor limiting measurement time and precision [169]. In current setups based on 1D lattices with low filling this perturbation is often negligible compared to other noise like collisions, transverse motion, black body shifts or reference cavity fluctuations. However, in lattices with 3D confinement and unit filling, these dipole-dipole interaction shifts are much larger than the atomic linewidth and represent a significant inherent perturbation. Note that their absolute magnitude scales with the atomic dipole moment and thus strongly depends on the chosen transition lifetime, which can change by almost 6 orders of magnitude from a calcium to a strontium clock. This, however, is very different from the single excitation case, which has been investigated in recent experiments in Boulder [245].

In this work we quantitatively study such collective effects on Ramsey spectroscopy in perfect optical lattice configurations. As a key quantity to capturing the collective modifications of the system dynamics, we use the decay and phase shift of the collective dipole generated by the first Ramsey pulse, which determines the contrast and shift of the central Ramsey fringes. Note, that due to the pairwise nature of dipole-dipole interactions a simple rephasing pulse cannot correct these errors. We ignore interaction induced perturbations during the Ramsey pulses, which introduce extra noise but could be reduced by very fast pulses or improved sequences [246]. In practise we set out to numerically solve the well established master equation for the atomic density matrix ρ including optical dipole-dipole interaction obtained by tracing over the electromagnetic vacuum field [136, 139, 243, 247],

$$\dot{\rho} = i\,[\rho, H] + \mathcal{L}[\rho]. \tag{11.1}$$

As previously shown for small atom numbers ($N < 12$) a numerical solution of the full master equation yields non-negligible shifts already [107, 144]. Unfortunately, as the Hilbert space grows exponentially with atom number, the full equation cannot be solved for ensembles of a realistic size. Since for precision measurements we need to evaluate collective effects precisely, reliable and in a converging manner alternative numerical methods are required. For larger ensembles at low densities a cluster approach has produced first estimates of the scaling of the dephasing with the system's size and density [240]. In the opposite limit of a very high density, important self synchronization effects through dipole coupling were studied recently using strongly simplifying assumptions for the coupling [208]. Synchronization via spin-spin coupling can also occur via collisions at high density [248] or within an optical resonator [249].

In this letter we present an extensive numerical analysis of the collective dynamics for fully populated lattices of different geometries and sizes containing a large or even an infinite number of particles. Our primary goal is to estimate the magnitude of the dipole phase shift and collective decay as a function of lattice and excitation

geometry. Most interestingly, besides a resonant enhancement of shifts, decay and dephasing at certain lattice spacings, we find cases where collective interactions even lead to improvements of the maximally achievable measurement precision beyond the independent particle level by virtue of subradiant states. Our considerations are based on an idealized setup ignoring lattice shifts, thermal effects or the hopping of atoms.

Numerically we apply an enhanced mean field approach related to cumulant expansion methods. It was developed in a recent paper, where we have also checked its validity extensively [250]. Using this method we can scale up the ensemble towards experimentally relevant atom numbers of up to $N \approx 10^5$ particles. If the particle distribution exhibits symmetries numbers up to even 10^{10} are possible, well approximating infinite systems in 1D and 2D. The accuracy of the approach, however, breaks down at very close distances, as it cannot correctly capture high order correlations. Similar deliberations for classical dipoles have recently been put forward [251].

11.2 Model

We consider an ensemble of N identical effective two-level atoms with transition frequency ω_0 and inverse lifetime γ at positions r_i $(i = 1..N)$ interacting via optical dipole-dipole coupling described by the Hamiltonian [136, 243]

$$H = \sum_{ij;i\neq j} \Omega_{ij}(r_{ij})\sigma_i^+\sigma_j^-. \tag{11.2}$$

Here, $\sigma_i^\pm$ denotes the raising (lowering) operator of the i-th atom and $\Omega_{ij} = \frac{3}{4}\gamma G\left(k_0 r_{ij}\right)$ represents the energy exchange with $k_0 = \omega_0/c = 2\pi/\lambda_0$ and $r_{ij} = |r_i - r_j|$ being the distance between atoms i and j. Collective spontaneous emission is accounted for by a Liouvillian of the form [139, 243]

$$\mathcal{L}[\rho] = \frac{1}{2}\sum_{i,j}\Gamma_{ij}(r_{ij})(2\sigma_i^-\rho\sigma_j^+ - \sigma_i^+\sigma_j^-\rho - \rho\sigma_i^+\sigma_j^-), \tag{11.3}$$

where the off-diagonal rates $\Gamma_{ij} = \frac{3}{2}\gamma F\left(k_0 r_{ij}\right)$ introduce super- and subradiant decay [136] and $\Gamma_{ii} = \gamma$. Explicitly we have

$$F(\xi) = \alpha\frac{\sin\xi}{\xi} + \beta\left(\frac{\cos\xi}{\xi^2} - \frac{\sin\xi}{\xi^3}\right) \tag{11.4a}$$

$$G(\xi) = -\alpha\frac{\cos\xi}{\xi} + \beta\left(\frac{\sin\xi}{\xi^2} + \frac{\cos\xi}{\xi^3}\right) \tag{11.4b}$$

with $\alpha = 1 - \cos^2\theta$ and $\beta = 1 - 3\cos^2\theta$, where θ represents the angle between the line connecting atoms i and j and the common atomic dipole orientation.

11.3 Mean Field Approximation

To study large particle numbers we derive the equations of motion for the expectation values of the Pauli operators for the k-th atom as detailed in the supplement [252]. Assuming a separable density operator and factorizing the two-particle correlations via $\langle\sigma_i^\mu\sigma_j^\nu\rangle \approx \langle\sigma_i^\mu\rangle\langle\sigma_j^\nu\rangle$ for $\mu, \nu \in \{x, y, z\}$ they transform to a closed set. As shown previously [250] these equations still capture the major part of the interaction up to a moderate interaction strength. To obtain even more accurate results one can add second order pair correlation corrections. As we have shown in some earlier work, these corrections significantly increase the precision of the results at increased computational effort [250] but do not induce qualitative changes.

11.4 Symmetric Configurations

For symmetric geometries with each atom initially in the same state and subject to the same effective interactions, the equations of motion for all particles become identical and read

$$\langle\dot{\sigma^x}\rangle = \Omega^{\text{eff}}\langle\sigma^y\rangle\langle\sigma^z\rangle - \frac{1}{2}\Big(\gamma - \Gamma^{\text{eff}}\langle\sigma^z\rangle\Big)\langle\sigma^x\rangle, \tag{11.5a}$$

$$\langle\dot{\sigma^y}\rangle = -\Omega^{\text{eff}}\langle\sigma^x\rangle\langle\sigma^z\rangle - \frac{1}{2}\Big(\gamma - \Gamma^{\text{eff}}\langle\sigma^z\rangle\Big)\langle\sigma^y\rangle, \tag{11.5b}$$

$$\langle\dot{\sigma^z}\rangle = -\gamma\big(1 + \langle\sigma^z\rangle\big) - \frac{1}{2}\Gamma^{\text{eff}}\Big(\langle\sigma^x\rangle^2 + \langle\sigma^y\rangle^2\Big). \tag{11.5c}$$

Hence instead of solving a huge set of coupled nonlinear equations we need to determine the effective couplings, i.e.,

$$\Omega^{\text{eff}} = \sum_{j=2}^{N}\Omega_{1j} \qquad \Gamma^{\text{eff}} = \sum_{j=2}^{N}\Gamma_{1j}. \tag{11.6}$$

Of course, such a rigorous symmetry condition is fulfilled for very few atomic distributions only. In these cases, however, the essence of the interactions within the entire lattice is captured solely by two real numbers, the effective coupling Ω^{eff} and the collective decay rate Γ^{eff}. In a clock setup one seeks to minimize the energy shifts Ω^{eff} and find configurations with a maximally negative Γ^{eff}, minimizing decay and allowing for an as long as possible interrogation time.

11.5 Finite Systems

Firstly, for finite symmetric configurations the effective quantities can be calculated easily. The most obvious symmetric structures are regular polygons. This might not be the most practical example but nicely displays the underlying physics [253]. In fig. 11.2

we compare the parameters for a square, a ten-sided and a 100000-sided polygon. The square shows a behaviour quite similar to the underlying functions $F(\xi)$ and $G(\xi)$, while the two larger polygons exhibit strong size dependent variations, particularly at integral values of d/λ_0 emerging from the accumulation of many $1/\xi$ contributions. Note that even with a relatively large atom spacing, cooperative collective effects are sizable and vary strongly with distance.

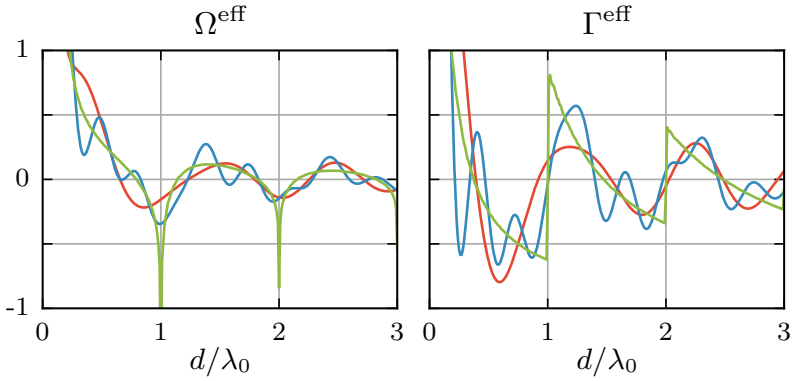

Figure 11.2: (Colour online) Distance dependence of the effective dipole coupling Ω^{eff} and Γ^{eff} for a square (red), a ten-sided (blue) and a 100000-sided (green) regular polygon. The fewer particles the closer the functions resemble the underlying couplings Ω_{ij} and Γ_{ij}. The divergences at integral d/λ_0 result from the $1/\xi$ terms in $F(\xi)$ and $G(\xi)$.

11.6 Infinite Systems

In practise, extended regular systems, i.e., large periodic lattices, are experimentally more relevant. Figure 11.3 depicts the effective couplings for an infinite chain, a square lattice and a hexagonal lattice. For comparison, we have overlaid the results for smaller atom numbers to demonstrate finite size effects, where even unphysical values of $\Gamma^{\text{eff}} < -1$ can appear. We observe stronger variations and again divergences at integral values of d/λ_0 . These manifest themselves in a much more pronounced way at huge atom numbers and therefore underpin the importance of properly treating long range interactions.

Note that for the two-dimensional square lattice and the hexagonal lattice Γ^{eff} exhibits a broad minimum for the effective decay close to $\Gamma^{\text{eff}} = -1$ for $d < \lambda_0$, where atomic decay is strongly inhibited. This favours such two-dimensional setups for lattice clocks as subradiant decay will dominate the system dynamics allowing for much longer Ramsey delay times and thus offering a higher overall precision [169]. Similarly we can identify lattice constants with a zero effective shift and therefore increased clock accuracy. Extending these calculations to three dimensional lattices, we find

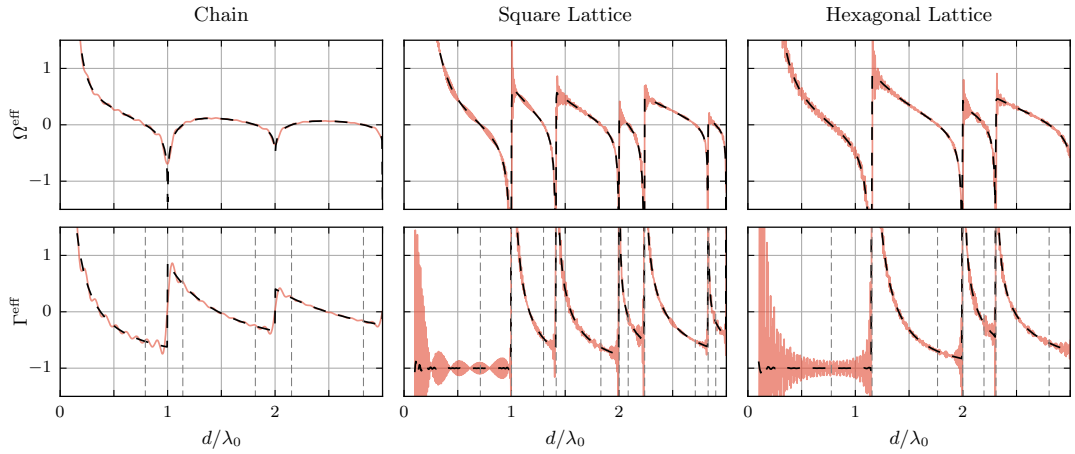

Figure 11.3: (Colour online) Distance dependence of the effective quantities Ω^{eff} and Γ^{eff} for an infinite equidistant chain, a square lattice and a hexagonal lattice (dashed black) compared to their not yet converged finite counterparts of 10, $4 \cdot 10^4$ and 10^5 particles respectively (solid red). Again, we find divergences at integral d/λ_0 owing to the $1/\xi$-terms in $F(\xi)$ and $G(\xi)$. In the 2D configurations Γ^{eff} plateaus at -1 for $d < \lambda_0$, suggesting that this parameter range will be the most favourable for clock setups as decay is strongly suppressed. Finite sample sizes in our numerics can lead to strong oscillations of the effective quantities at small distances and even to unphysical values of $\Gamma^{\text{eff}} < -1$.

that the necessary atom numbers to obtain smooth converging behaviour are beyond our current numerical capabilities. For particle numbers of about 10^{12} the resulting effective quantities still fluctuate strongly, predicting potential problems for such 3D clock setups. A demonstration of this effect can be found in the supplement [252].

11.7 Tailoring Atomic Excitations

So far we have assumed a phase-symmetric excitation of all atoms by the first Ramsey pulse. In a practical excitation scheme this corresponds to illumination at right angle. In general, however, the effective couplings Ω^{eff} and Γ^{eff} will change, when we allow for a local phase shift imprinted on the atoms. In a $\pi/2$ Ramsey sequence [3] the excitation phase appears on the excited state directly, i.e.,

$$|\Psi\rangle = \bigotimes_{j=1}^{N} \frac{1}{\sqrt{2}} \left(|g\rangle + e^{i\Delta\phi(j-1)} |e\rangle \right). \tag{11.7}$$

In our treatment we can exploit the system's symmetry and absorb this phase into the effective couplings [252]. For $\Delta\phi = 0$ we recover the above results. The closer the phase

shift gets to $\Delta\phi = \pi$, however, the more half-integral values of d/λ_0 yield minimal shifts and the maximally negative Γ^{eff} as seen in fig. 11.4. Since the emitted light has interfered constructively at integral and destructively at half-integral distances for $\Delta\phi = 0$, it will do exactly the opposite at $\Delta\phi = \pi$. Furthermore, addressing atoms transversally ($\Delta\phi = 0$) seems more favourable at typical magic wavelength trapping distances, e.g., $d/\lambda_0 \approx 0.58$ for ^{87}Sr [40, 144, 166]. Again, for $d \ll \lambda_0$ the mean field approach breaks down and one should rather turn to the Dicke model [140], reducing N two-level emitters to one effective spin $N/2$-system [208].

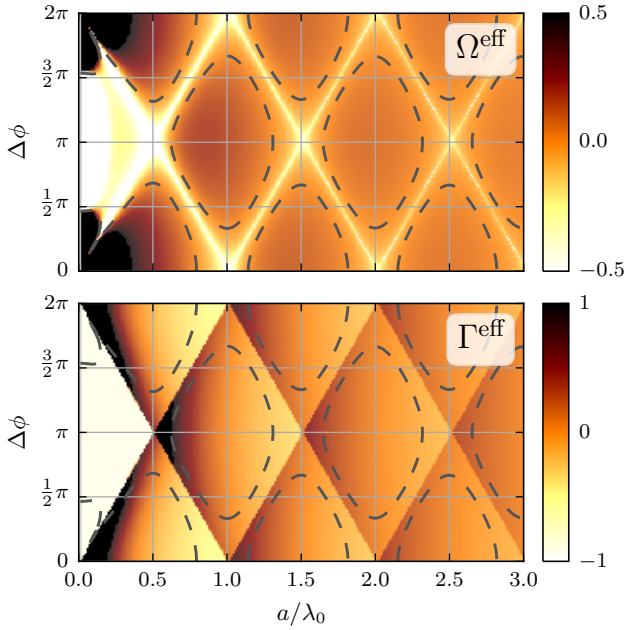

Figure 11.4: (Colour online) Effective interactions Ω^{eff} and Γ^{eff} for an infinite chain with spacing a where the spins are initially prepared with phase shift $\Delta\phi$ between neighbouring spins. The dashed lines indicate parameters with $\Omega^{\text{eff}} = 0$ optimal for an optical clock.

Let us finally discuss the consequences for typical cases. Figure 11.5 shows the time evolution of the average spin for an infinite chain initialized in a symmetric Ramsey state with either no phase shift or a phase shift of $\Delta\phi = \pi$ between neighbouring atoms. The lattice constants have been chosen to be approximately $\lambda_0/2$ as would be typical [165]. We refrain from choosing exactly $\lambda_0/2$ to avoid the $1/\xi$ divergence. We observe that the dipoles' lifetimes vary strongly, comparing the subradiant behaviour (red) where the collective dipole lives much longer than the natural lifetime of the atom to the superradiant (green) regime where the excitation vanishes very quickly. Additionally, to highlight the validity of the mean field approach, we add the results of a second order expansion simulation. Corresponding results for a full Ramsey sequence are shown in the supplement.

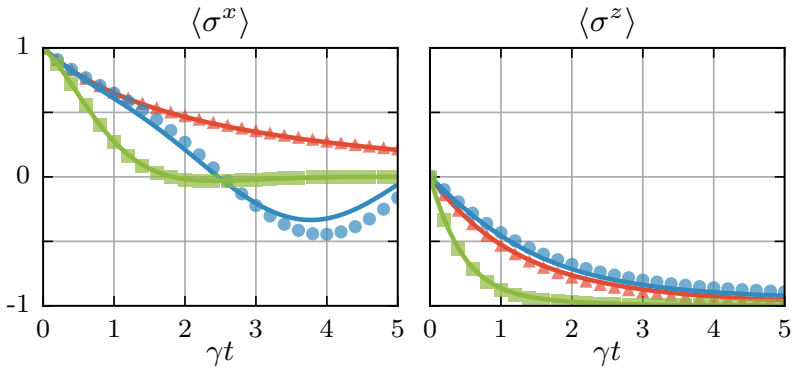

Figure 11.5: (Colour online) Three different examples for the time evolution of the spin expectation values for a chain with spacing d where initially all spins are prepared in a coherent superposition of ground and excited state with a phase shift of $\Delta\phi$. The parameters used are $d = 0.792\lambda_0$ with $\Delta\phi = 0$ (red triangles), where $\Omega^{\text{eff}} = 0$ and Γ^{eff} is nearly optimal, as well as $d = 0.49\lambda_0$ (green squares) and $d = 0.51\lambda_0$ (blue circles), both with $\Delta\phi = \pi$ which are close to a Γ^{eff} discontinuity. The solid lines correspond to a solution of a second order cumulant expansion model with 200 particles and demonstrate a very good agreement with the infinite mean field description.

11.8 Conclusions

In densely filled optical lattices dipole-dipole interaction and collective decay significantly change the evolution of an induced collective dipole strongly affecting Ramsey spectroscopy. Due to the long range-nature of the coupling, sizable shifts appear even for long lived clock states despite their minute dipole moment, which limits the accuracy and precision of Ramsey spectroscopy. Shifts and dephasing in large systems strongly depend on the dimensionality and geometry of the lattice, exhibiting resonant enhancements at particular lattice constants. While at current operating densities for Strontium [240–242] these shifts are smaller than other technical imperfections, they constitute inherent fundamental perturbations even in perfectly filled lattice clocks.

In this work, we have identified optimal operation geometries, which combine a negligible effective shift with a strong suppression of decay. In particular, for a 1D lattice with a tailored excitation angle and for a 2D hexagonal lattice favourable operation parameters for future generation clock setups were found. These results appear to be robust against small position fluctuations or a few lattice defects. In this sense it seems possible to implement a high density dark exciton based atomic clock geometry, where the fundamental limit to line shifts is many orders of magnitude below a single Hz and one gets almost unlimited exciton life times. In 3D the interactions are particularly sensitive to a change in lattice constant and boundary effects, which

dominate even for billions of particles rendering such setups very challenging [252].

We have considered perfectly filled and designed optical lattices, while in any experimental setup some imperfections in the form of defects or position fluctuations will be present. This can be of fundamental quantum nature [254, 255] or simply stem from technical imperfections. Interestingly, at least in 1D geometries we found that this even leads to strong subradiant behaviour and thus could be a useful resource [200, 210]. This effect has to be confirmed for higher dimensions, though.

While for most considerations we have focused on the case of clock transitions, the same physics is present in a more prominent and experimentally easier observable form for broader transitions. Optimizing geometries will also be relevant for devices such as superradiant lasers [159, 190] or lattice based optical memories.

Acknowledgements

The authors acknowledge funding by the Austrian Science Fund FWF project SFB FoQus F4006-N13 (S.K., H.R.) and the DARPA QUASAR project (L.O., H.R.).

11.9 Supplementary Material

11.9.1 Derivation of the Mean-Field Equations

Starting from the full multiparticle density operator ρ our master equation allows to obtain the following equations for the individual spin expectation values immediately

$$\dot{\langle\sigma_k^x\rangle} = \sum_{j;j\neq k} \Omega_{kj}\langle\sigma_j^y\sigma_k^z\rangle - \frac{1}{2}\gamma\langle\sigma_k^x\rangle + \frac{1}{2}\sum_{j;j\neq k}\Gamma_{kj}\langle\sigma_j^x\sigma_k^z\rangle \tag{11.8a}$$

$$\dot{\langle\sigma_k^y\rangle} = \sum_{j;j\neq k} \Omega_{kj}\langle\sigma_j^x\sigma_k^z\rangle - \frac{1}{2}\gamma\langle\sigma_k^y\rangle + \frac{1}{2}\sum_{j;j\neq k}\Gamma_{kj}\langle\sigma_j^y\sigma_k^z\rangle \tag{11.8b}$$

$$\begin{aligned}\dot{\langle\sigma_k^z\rangle} = &\sum_{j;j\neq k} \Omega_{kj}\Big(\langle\sigma_j^x\sigma_k^y\rangle - \langle\sigma_j^y\sigma_k^x\rangle\Big) - \gamma\big(1+\langle\sigma_k^z\rangle\big)\\ &- \frac{1}{2}\sum_{j;j\neq k}\Gamma_{kj}\Big(\langle\sigma_j^x\sigma_k^x\rangle + \langle\sigma_j^y\sigma_k^y\rangle\Big).\end{aligned} \tag{11.8c}$$

Assuming a spatially separable state $\rho = \bigotimes_k \rho_k$ leads to the lowest order mean field equations used in the letter.

11.9.2 Mean Field Equations with Tailored Excitation Phase

At zero temperature the ground state $\rho = \bigotimes_k (|g\rangle)(\langle g|)_k$ is separable and in an idealized standard Ramsey procedure the first pulse would create a product state

of equal weighted superpositions $\rho = \bigotimes_k 1/2\,((|g\rangle + |e\rangle)(\langle e| + \langle g|))_k$. This is the generic initial state we use in our work to study dipole-dipole interaction. In fact, this state possesses the maximal collective dipole moment and therefore shows strong interactions.

Of course, in any real setup this preparation step is not perfect as interactions are present during the excitation pulse and the excitation laser carries an intensity and phase gradient. Some of the errors can be corrected in improved excitation schemes [169,246]. However, particularly in extended systems a phase gradient is hard to avoid and will strongly influence the system dynamics. Fortunately, one can show, that a known phase gradient will not complicate the calculations too much. If we allow for the individual atomic states to bare a spatially dependent phase of $\Delta\phi$ on the excited state, i.e., $|\psi_k\rangle = \frac{1}{\sqrt{2}}\,(|g\rangle + \exp(i\phi_k)\,|e\rangle)$, we can absorb this into our equations efficiently. Using the abbreviations $\Omega_{kj}^{\cos} = \Omega_{kj}\cos(\phi_k - \phi_j)$ and $\Omega_{kj}^{\sin} = \Omega_{kj}\sin(\phi_k - \phi_j)$ we obtain the following modified equations of motion

$$\begin{aligned}\frac{d}{dt}\langle\tilde{\sigma}_k^x\rangle &= \sum_{j;j\neq k}\Omega_{kj}^{\sin}\langle\tilde{\sigma}_j^x\sigma_k^z\rangle + \sum_{j;j\neq k}\Omega_{kj}^{\cos}\langle\tilde{\sigma}_j^y\sigma_k^z\rangle - \frac{1}{2}\gamma\langle\tilde{\sigma}_k^x\rangle \\ &\quad + \frac{1}{2}\sum_{j;j\neq k}\Gamma_{kj}^{\cos}\langle\tilde{\sigma}_j^x\sigma_k^z\rangle - \frac{1}{2}\sum_{j;j\neq k}\Gamma_{kj}^{\sin}\langle\tilde{\sigma}_j^y\sigma_k^z\rangle \end{aligned} \tag{11.9a}$$

$$\begin{aligned}\frac{d}{dt}\langle\tilde{\sigma}_k^y\rangle &= -\sum_{j;j\neq k}\Omega_{kj}^{\cos}\langle\tilde{\sigma}_j^x\sigma_k^z\rangle + \sum_{j;j\neq k}\Omega_{kj}^{\sin}\langle\tilde{\sigma}_j^y\sigma_k^z\rangle - \frac{1}{2}\gamma\langle\tilde{\sigma}_k^y\rangle \\ &\quad + \frac{1}{2}\sum_{j;j\neq k}\Gamma_{kj}^{\sin}\langle\tilde{\sigma}_j^x\sigma_k^z\rangle + \frac{1}{2}\sum_{j;j\neq k}\Gamma_{kj}^{\cos}\langle\tilde{\sigma}_j^y\sigma_k^z\rangle \end{aligned} \tag{11.9b}$$

$$\begin{aligned}\frac{d}{dt}\langle\sigma_k^z\rangle &= -\sum_{j;j\neq k}\Omega_{kj}^{\sin}(\langle\tilde{\sigma}_j^x\tilde{\sigma}_k^x\rangle + \langle\tilde{\sigma}_j^y\tilde{\sigma}_k^y\rangle) + \sum_{j;j\neq k}\Omega_{kj}^{\cos}(\langle\tilde{\sigma}_j^x\tilde{\sigma}_k^y\rangle - \langle\tilde{\sigma}_j^y\tilde{\sigma}_k^x\rangle) \\ &\quad - \gamma(1+\langle\sigma_k^z\rangle) - \frac{1}{2}\sum_{j;j\neq k}\Gamma_{kj}^{\cos}(\langle\tilde{\sigma}_j^x\tilde{\sigma}_k^x\rangle + \langle\tilde{\sigma}_j^y\tilde{\sigma}_k^y\rangle) \\ &\quad - \frac{1}{2}\sum_{j;j\neq k}\Gamma_{kj}^{\sin}(\langle\tilde{\sigma}_j^x\tilde{\sigma}_k^y\rangle - \langle\tilde{\sigma}_j^y\tilde{\sigma}_k^x\rangle). \end{aligned} \tag{11.9c}$$

We see that the following definitions prove to be very helpful

$$\Omega_k^{\cos} = \sum_{j;j\neq k}\Omega_{kj}\cos(\phi_k - \phi_j) \qquad \Omega_k^{\sin} = \sum_{j;j\neq k}\Omega_{kj}\sin(\phi_k - \phi_j) \tag{11.10a}$$

$$\Gamma_k^{\cos} = \sum_{j;j\neq k}\Gamma_{kj}\cos(\phi_k - \phi_j) \qquad \Gamma_k^{\sin} = \sum_{j;j\neq k}\Gamma_{kj}\sin(\phi_k - \phi_j). \tag{11.10b}$$

Again, if we consider highly symmetric configurations where $\Omega^{\mathrm{f}} = \Omega_k^{\mathrm{f}}$ and $\Gamma^{\mathrm{f}} = \Gamma_k^{\mathrm{f}}$ and

the rotated states are initially identical we can define the effective rotated quantities

$$\tilde{\Omega}^{\text{eff}} = \Omega^{\cos} - \frac{1}{2}\Gamma^{\sin} \tag{11.11}$$

$$\tilde{\Gamma}^{\text{eff}} = \Gamma^{\cos} + 2\Omega^{\sin} \tag{11.12}$$

which lead to a closed set of simplified effective equations as well, i.e.,

$$\frac{d}{dt}\langle\tilde{\sigma}^x\rangle = \tilde{\Omega}^{\text{eff}}\langle\tilde{\sigma}^y\rangle\langle\sigma^z\rangle - \frac{1}{2}\gamma\langle\tilde{\sigma}^x\rangle + \frac{1}{2}\tilde{\Gamma}^{\text{eff}}\langle\tilde{\sigma}^x\rangle\langle\sigma^z\rangle \tag{11.13a}$$

$$\frac{d}{dt}\langle\tilde{\sigma}^y\rangle = -\tilde{\Omega}^{\text{eff}}\langle\tilde{\sigma}^x\rangle\langle\sigma^z\rangle - \frac{1}{2}\gamma\langle\tilde{\sigma}^y\rangle + \frac{1}{2}\tilde{\Gamma}^{\text{eff}}\langle\tilde{\sigma}^y\rangle\langle\sigma^z\rangle \tag{11.13b}$$

$$\frac{d}{dt}\langle\sigma^z\rangle = -\gamma\big(1 + \langle\sigma^z\rangle\big) - \frac{1}{2}\tilde{\Gamma}^{\text{eff}}\Big(\langle\tilde{\sigma}^x\rangle^2 + \langle\tilde{\sigma}^y\rangle^2\Big). \tag{11.13c}$$

Note that such a phase gradient tends to mix the real and imaginary part of the interaction terms.

11.9.3 Effective Quantities for Cubic Lattices in 3D

In a cubic 3D lattice the number of neighbours at a given distance r grows approximately as r^2. Hence, one cam expect a slower convergence with distance. This problem is increased as the number of emitters to be considered grows with the third power of the system size. In contrast to 1D and 2D, together these two scalings prevent a convergence of the effective interaction parameters in the range of tractable lattices sizes of up to $N = (10^4)^3 = 10^{12}$ sites. Anyway, this is beyond experimentally realistic atom numbers so that we have to live with finite size effects.

In order to demonstrate the very slow convergence of the infinite range mean field model, we present some typical intermediate result for a 3D cubic lattice. In fig. 11.6 we depict the effective coupling strengths Ω^{eff} and Γ^{eff} for the innermost two-level system in a cubic lattice of about $8 \cdot 10^9$ particles, i.e., 2000 particles in each direction. We obtain strong and very rapid oscillations of the shifts as a function of the lattice constant. Notice, that $1/r$-contributions as discussed in the letter will show up for planar and cubic diagonal distances of $\sqrt{2} \cdot r$ and $\sqrt{3} \cdot r$ as well. Increasing the atom number further still leads to changes of this pattern, so no final conclusions about physical properties and the behaviour of a 3D cubic lattice can be obtained. However, perturbations of up to an order of magnitude larger than the linewidth as well as strong finite size shifts can be expected. In this case it is difficult to suggest an optimal lattice constant for a clock setup, except for avoiding certain resonances and choosing a region of about $d \approx 3\lambda/4$.

11.9.4 Ramsey Spectroscopy

The effective coupling and decay parameters $\Omega^{\text{eff}}, \Gamma^{\text{eff}}$ characterize the interaction induced perturbation of the individual spin dynamics. Consequently, they will alter the

Ramsey signal by introducing shifts of the fringes and modifications of the maximally obtainable contrast. As the actual connection between the magnitude of these effective couplings and their quantitative effect on the signal is nontrivial, we demonstrate the alterations of the Ramsey signal in the following examples. Using the previously derived equations of motion, it is straight forward to simulate the results of an ideal Ramsey sequence. By starting with a $\pi/2$-pulse all spins are rotated into the x-direction of the Bloch sphere. For a time γt the system evolves according to the equations

$$\langle \dot{\sigma^x} \rangle = -\Delta_a \langle \sigma_k^y \rangle + \Omega^{\text{eff}} \langle \sigma^y \rangle \langle \sigma^z \rangle - \frac{1}{2}\gamma \langle \sigma^x \rangle + \frac{1}{2}\Gamma^{\text{eff}} \langle \sigma^x \rangle \langle \sigma^z \rangle \tag{11.14a}$$

$$\langle \dot{\sigma^y} \rangle = \Delta_a \langle \sigma_k^x \rangle - \Omega^{\text{eff}} \langle \sigma^x \rangle \langle \sigma^z \rangle - \frac{1}{2}\gamma \langle \sigma^y \rangle + \frac{1}{2}\Gamma^{\text{eff}} \langle \sigma^y \rangle \langle \sigma^z \rangle \tag{11.14b}$$

$$\langle \dot{\sigma^z} \rangle = -\gamma\big(1 + \langle \sigma^z \rangle\big) - \frac{1}{2}\Gamma^{\text{eff}} \Big(\langle \sigma^x \rangle^2 + \langle \sigma^y \rangle^2 \Big), \tag{11.14c}$$

where $\Delta_a = \omega_0 - \omega_L$ is the detuning between the probe laser and the atomic transition frequency. After this free evolution a second $\pi/2$-pulse is applied and, finally, the expectation value of σ^z is measured. For a given system characterized by the effective quantities Ω^{eff} and Γ^{eff} the result of this measurement depends on the waiting time as well as on the detuning Δ_a. In fig. 11.7 the outcome of this numerical experiment is shown for three different realistic sets of effective quantities. The decisive quantity for the accuracy with regards to atomic clocks is the shift of the fringes due to the dipole-dipole interaction which can be obtained by measuring the shift of the maxima of the Ramsey fringes. The shifts for the chosen examples are shown in fig. 11.8. On the other hand the slope of the fringes at their roots is the determining factor for the best achievable experimental precision. The numerical results are shown in fig. 11.9. As seen in fig. 11.10 the maximal shifts depend on Ω^{eff} only, while the maximal slope at zero points is governed by Γ^{eff}. For realistic values for the effective quantities this means the accuracy can be limited to γ and the achievable precision can vary by a factor of 5.

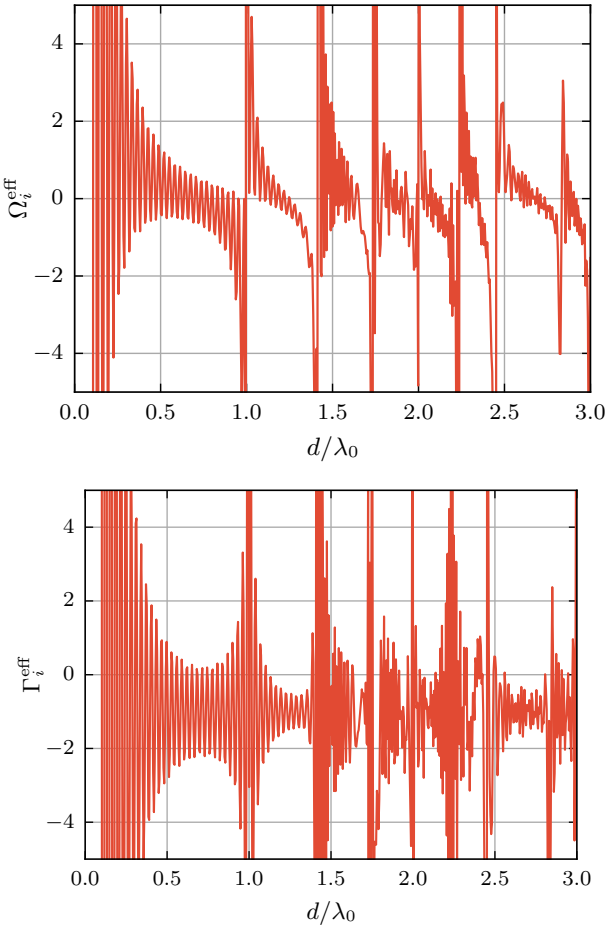

Figure 11.6: Effective quantities Ω_i^{eff} and Γ_i^{eff} as experienced for the innermost spin inside a cube consisting of $2001 \times 2001 \times 2001$ spins in a cubic lattice configuration depending on the lattice spacing d. Even for very small changes of the lattice spacing the mean net-effect of all other spins will change dramatically. Unphysical values of $\Gamma^{\text{eff}} < -1$ emerge due to numerical artifacts and too slow a convergence.

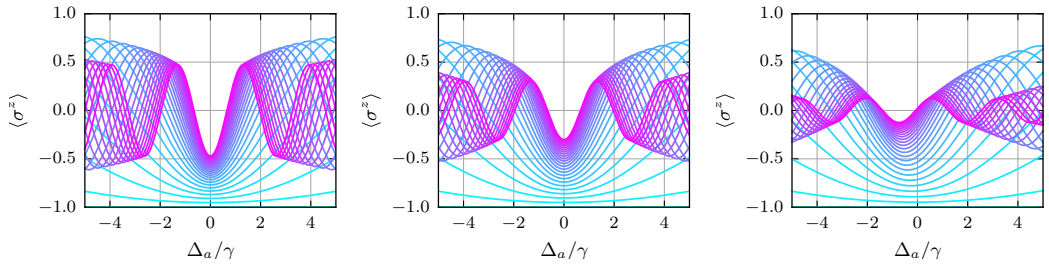

Figure 11.7: Simulated idealized Ramsey spectroscopy for different sets of effective cooperative interaction strengths, from left to right: subradiant case without shift ($\Omega^{\text{eff}} = 0, \Gamma^{\text{eff}} = -0.75$), independent atom limit ($\Omega^{\text{eff}} = 0, \Gamma^{\text{eff}} = 0$) and superradiant case with shift ($\Omega^{\text{eff}} = 1, \Gamma^{\text{eff}} = 1$). The colours indicate the free evolution time with cyan representing a very short time and magenta meaning times up to $2.5\gamma^{-1}$.

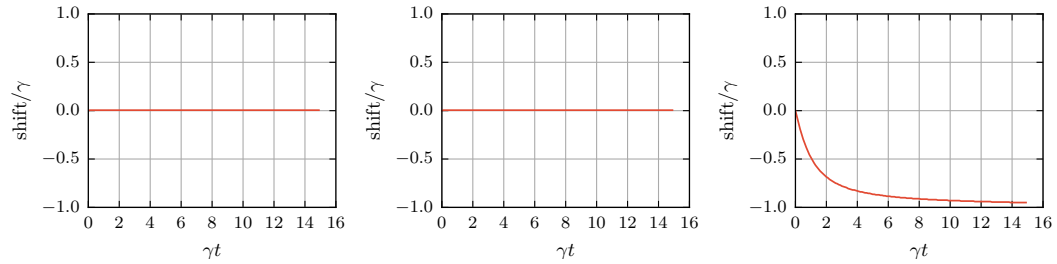

Figure 11.8: Shifts of the maxima after the free evolution time γt for different sets of effective interaction strengths as above, from left to right: ($\Omega^{\text{eff}} = 0, \Gamma^{\text{eff}} = -0.75$), ($\Omega^{\text{eff}} = 0, \Gamma^{\text{eff}} = 0$) and ($\Omega^{\text{eff}} = 1, \Gamma^{\text{eff}} = 1$).

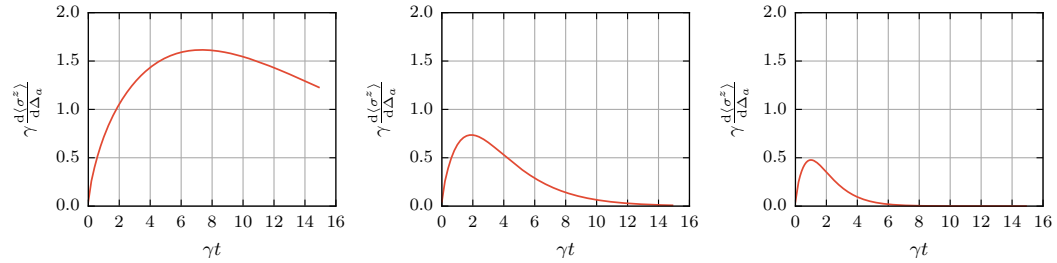

Figure 11.9: Slope of the signal at the zero crossing of the first fringe after a free evolution time of γt for different sets of effective interaction strengths as above, from left to right: ($\Omega^{\text{eff}} = 0, \Gamma^{\text{eff}} = -0.75$), ($\Omega^{\text{eff}} = 0, \Gamma^{\text{eff}} = 0$) and ($\Omega^{\text{eff}} = 1, \Gamma^{\text{eff}} = 1$).

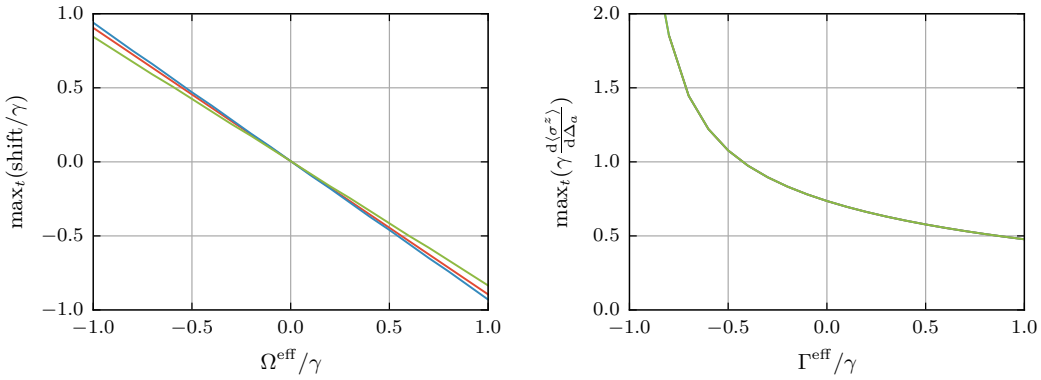

Figure 11.10: (a) Shift of Ramsey fringes depending on the effective coupling Ω^{eff} after $t = 15\gamma^{-1}$. The different lines represent different choices of Γ^{eff}, which hardly influence the result. The fringe shifts follow the effective mean field dipole coupling Ω^{eff} almost linearly and thus can be read off from the figures in the main manuscript. (b) Maximally achievable slope at roots depending on Γ^{eff}. The result is independent of the choice of Ω^{eff}. Note that a negative Γ^{eff} improves the measurement precision beyond the independent atom value.

12 Publication: Coherence and Degree of Time-bin Entanglement from a Quantum Dot

In this letter Ana Predojevic, Gregor Weihs and their team look at coherence and time-bin entanglement from a quantum dot. They have approached our group for theory support and my contribution lies in developing and investigating a model, where intensity-dependent dephasing causes a decrease in the pair photon signal that can be obtained from emissions of the quantum dot. The manuscirpt has been published in PRB on May, 12th 2016 [256].

Abstract

We report a study on coherence of excitation of single quantum dots. We address the coherent excitation of biexciton, the process that is indispensable for deterministic photon pair generation in quantum dots. Based on theoretical modelling we optimized the duration of the excitation pulse in our experiment to minimize the laser-induced dephasing and increase the biexciton-to-background single exciton occupation probability. An additional effect of this approach is a high degree of time-bin entanglement with a concurrence of up to 0.78(6) and a 0.88(3) overlap with a maximally entangled state.

12.1 Introduction

Single semiconductor quantum dots, due to their discrete energy structure, constitute an antibunched single photon source at a well defined frequency and with inherently sub-Poissonian statistics [257, 258]. They generate single photons through a recombination of an electro-hole pair formed by an electron from the conduction band and a hole from the valence band. In a more refined operation mode employing biexcitons, quantum dots can provide pairs of photons emitted in a fast cascade very similar to the original atomic cascade experiment by Aspect *et al.* [259]. It has been demonstrated that in the absence of the fine structure splitting of the bright exciton levels, such a cascade exhibits polarization entanglement [260–265].

Entanglement of photons is a fundamental resource for long distance quantum

communications [266, 267], where it forms the central part of various quantum communication protocols like teleportation [268] and entanglement swapping [269]. In addition, it is an essential element of linear optical quantum computing [270].

The ability to achieve entanglement of photons from a quantum dot is not limited to polarization. Recently, it has been shown that the biexciton-exciton cascade can also be entangled in its emission time (time-bin) [271]. Apart from the obvious goal to generate entangled photon pairs, there are further reasons for investigating the time-bin entanglement in photons emerging from a quantum dot. Namely, this method of entanglement calls for a coherent excitation and therefore is an excellent tool for investigating the coherence properties of a quantum dot system. Specifically, a quantum dot system that exhibits a high degree of coherence that can be combined with resonant excitation (especially two photon-resonant excitation of the biexciton [272, 273]) is a sine qua non for optimal use of quantum dot photons in quantum information processing.

Here, we report a study that relates the properties of the excitation pulse to the excitation coherence, photon generation probability, and the degree of entanglement in quantum dots. Our study addresses yet unexplored behaviour of resonantly excited quantum dot systems when exposed to varied excitation conditions. We indicate an optimized operation regime for the system under consideration and provide guidelines on how to extend this study to other similar systems (see supplementary material). Our study also shows a generalized method to achieve a very high photon pair generation probability from quantum dots. Furthermore, we report on an unprecedented degree of time-bin entanglement from a single quantum dot. The requirements to generate this type of entanglement include the suppression of the single exciton probability amplitude in the excitation pulse and the lowest possible degree of dephasing caused by the laser excitation. These conditions constitute contradictory demands on the excitation pulse-length and its intensity. We include a study of these limitations from an experimental and a theoretical point of view and we indicate key parameters required in order to achieve a high degree of time-bin entanglement.

12.2 Biexciton Generation

The central goal of the photon pair generation from the quantum dot systems is to get exactly one photon at the biexciton and one photon at the exciton frequency that are produced within a short time interval and with a well defined sum phase. In fact, the exciton and biexciton transition frequencies are well separated, so that excitation light that is tuned between these two frequencies produces a resonant two-photon coupling between the ground and the biexciton state (inset fig. 12.1).

To predominantly generate single pairs of photons from biexciton decay, one needs to avoid populating the single exciton state as well as the decay and re-excitation of the biexciton state within one laser pulse. This creates conflicting requirements for

the excitation pulse length. Namely, short pulses suppress dephasing and decay within the pulse duration but have large bandwidth and high intensity, which enhances the off-resonant generation of single excitons and power induced phase shifts. Longer pulses make the system more vulnerable to background dephasing, decay, and multiple excitations. A typical method to characterize the coherence of the excitation process is a study of the Rabi oscillations. Additionally to Rabi oscillations, here, we used time-bin entanglement to test the coherence of excitation. In particular, the creation of time-bin entanglement requires a phase stable generation of subsequent photon pairs, which is hampered by the phase uncertainty in the biexciton generation as well as any phase instability of the pump interferometer; the latter being very small in our system.

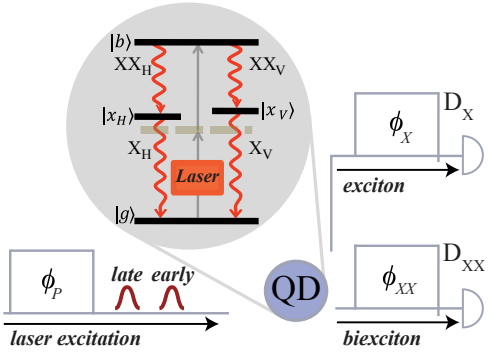

Figure 12.1: (Colour online) Schematic of time-bin entanglement. The quantum dot system (QD) is excited by two consecutive pulses obtained from an unbalanced Michelson interferometer shown on the left. The relative phase between these pulses is ϕ_P. The state analysis is performed using additional two interferometers, one for the exciton and the other for the biexciton photons. These two interferometers have their respective phases, ϕ_X and ϕ_{XX}. The photons are detected upon leaving the analysis interferometers using detectors D_X and D_{XX}. The level scheme depicts the quantum dot excited resonantly from the ground state $|g\rangle$ to the biexciton state $|b\rangle$ using a two-photon excitation. A pulsed laser populates the biexciton via a virtual level (dashed grey line). The system decays emitting a biexciton-exciton photon cascade (XX_V and X_V or XX_H and X_H).

12.3 Time-Bin Entanglement

This technique encodes quantum states in a superposition of the system's excitation within two distinct time-bins *early* and *late*. This type of entanglement (encoding) is important for optical-fibre based quantum communication [274] due to the fact that polarization entanglement can suffer from degradation in an optical fibre outside

laboratory conditions [275]. In addition, a method to perform linear optical quantum computing with photons entangled in time-bin has been demonstrated recently [276]. Time-bin entanglement is generated in a very similar manner for both parametric down-conversion [277] and atom-like systems [271] and in its simplest form it relies on post-selection in order to be measured. Such a scheme is depicted in fig. 12.1. The system is addressed by two excitation pulses, denoted the *early* and the *late* pulse. These are derived from an unbalanced interferometer, the so-called pump interferometer. If the system is driven with a very low probability to be excited, on average only one of these two pulses will actually create a photon pair. In other words, the system is placed in a superposition of being excited by the early or by the late pulse. The relative phase, ϕ_P, between the pulses determines the phase of the entangled state. This phase is written onto the quantum dot system using a coherent resonant excitation from the ground to the biexciton state. For comparison, note that in the process of parametric down-conversion the phase stability of the laser combined with the phase matching process in the extended medium ensures a constant phase relation between subsequent photon pairs. The time-bin entangled state reads

$$|\Phi\rangle = \frac{1}{\sqrt{2}}(|early\rangle_{XX}|early\rangle_X + e^{i\phi_P}|late\rangle_{XX}|late\rangle_X), \tag{12.1}$$

where ϕ_P is the phase of the pump interferometer generating the two excitation pulses and $|early\rangle$ ($|late\rangle$) denote photons generated in an *early* (*late*) time-bin. The subscripts XX and X identify biexciton and exciton photons, respectively. The analysis of the generated state is performed by two additional unbalanced interferometers, one for the exciton and one for the biexciton photons. The schematics of the three interferometers is presented in fig. 12.1.

12.4 Theoretical Model

To determine an optimized parameter regime we use a standard Lindblad master equation $\dot{\rho} = i\left[\rho, H\right] + \mathcal{L}\left(\rho\right)$ based upon an effective quantum dot Hamiltonian of the form

$$\begin{aligned} H = &\frac{1}{2}\Omega(t)\left(|g\rangle\langle x| + |x\rangle\langle b| + h.c.\right) \\ &+ \left(\Delta_x - \Delta_b\right)|x\rangle\langle x| - 2\Delta_b|b\rangle\langle b| \end{aligned} \tag{12.2}$$

and a Liouvillian damping operator

$$\mathcal{L} = \sum_i \mathcal{L}_i = \sum_i \frac{\gamma_i}{2}\left(2A_i^\dagger \rho A_i - A_i A_i^\dagger \rho - \rho A_i A_i^\dagger\right), \tag{12.3}$$

where

$$\hat{A}_1 = |b\rangle\langle x|, \quad \hat{A}_2 = |x\rangle\langle g| \tag{12.4}$$

describe biexciton and exciton decay, respectively, and the corresponding dephasing mechanisms are

$$\hat{A}_{bb} = \quad (|b\rangle \langle b| - |x\rangle \langle x|) \tag{12.5}$$

$$\hat{A}_{xx} = \quad (|x\rangle \langle x| - |g\rangle \langle g|)\,. \tag{12.6}$$

In eq. 2, Δ_x is the energy difference between the virtual level of the two-photon transition and the exciton energy, while Δ_b is the detuning between the two-photon resonance and the energy of the laser driving the system. More details can be found in the supplementary material.

We assume a Gaussian excitation laser pulse of a width σ and a time-dependent amplitude $\Omega(t) = \Omega_0 \cdot \exp\left(-\ln(2)\,(t-t_0)^2/\sigma^2\right)$. We calculate the emission probabilities ($P_x(t_f)$ and $P_b(t_f)$) as

$$P_i(t_f) = \gamma_i \int_0^{t_f} \langle i|\,\rho(t')\,|i\rangle \;\mathrm{d}t' \tag{12.7}$$

for different pulse lengths and dephasing models.

The most important and straightforward result of our model is shown in fig. 12.2. It shows the theoretically predicted Rabi oscillations for different pulse length. The constant dephasing parameters are taken from the $g^{(1)}(\tau)$ field correlation function measurements performed on exciton and biexciton photons. From this plot is obvious that the pulse length influences the coherence of the Rabi oscillations.

Besides a constant background dephasing rate of the freely evolving quantum dot, we also investigated the presence of the pump laser that leads to an extra and often dominant intensity-dependent dephasing rate

$$\gamma_\Omega(t) = \gamma_{I_0} \cdot \left(\frac{\Omega(t)}{\Omega_0}\right)^{n_p} \tag{12.8}$$

as detailed in [278], where Ω_0 is 1 THz in the natural units of our treatment and γ_{I_0} is the amplitude of the intensity-dependant dephasing rate. Depending on the exponent n_p of this type of dephasing, either longer or shorter pulses lead to less phase uncertainty in the generated photon pair.

However, as shown in fig. 12.3a, we found that compared to γ_{I_0}, the magnitude of the exponent n_p does not play such a great role in damping of the Rabi oscillations. Fitting the theory model to our measurement results shows that γ_{I_0} already yields strongly damped Rabi oscillations, while both exponents $n_p = 2$ and 4 are consistent with the experimental data, as shown in fig. 12.3b and fig. 12.3c. From fitting the Rabi oscillations data we obtain $\gamma_{I_0} \approx 0.0349$ and $\gamma_{I_0} \approx 0.0219$ for exciton and biexciton, respectively. Although our model is phenomenological γ_{I_0} is our only free parameter. The remaining parameters (in detail given in supplementary information) are experimentally measured values. Using these rates we can predict the ratio of biexcitons generated via a two-photon excitation to direct single excitons, see fig. 12.4a. Note, that as the first is a two-photon and the latter a single-photon process, the

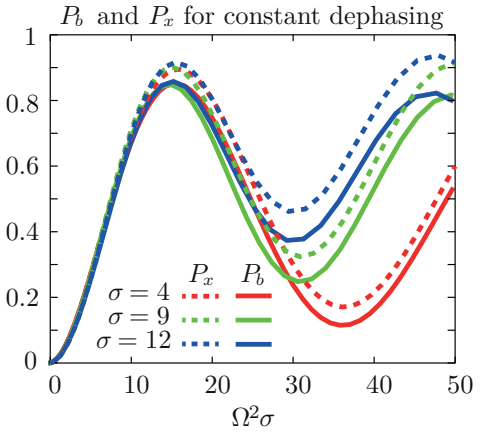

Figure 12.2: (Colour online) Rabi oscillations for constant dephasing as a function of $\Omega^2\sigma$. The emission probability for the biexciton, P_b, (left) and the exciton, P_x, (right) level are shown. The Rabi oscillations damping is very dependant on the length of the excitation pulse.

second one will dominate at low powers despite of being non-resonant. As shown in fig. 12.4a better ratios are obtained at longer pulse durations. In fig. 12.4b the total exciton photon generation is depicted, which includes photons from a direct excitation of the exciton as well as those generated from the decay of the biexcitons.

12.5 Entanglement

In the experiment the length of the laser pulses (4 ps to 20 ps) was varied by means of a pulse-stretcher. The laser wavelength was 918.7 nm, which is half way between biexciton and exciton emission (Figure 12.1). The distance between the exciton and the biexciton line in the quantum dot emission spectrum is 1.8 nm. We measured the degree of time-bin entanglement for five different pulse lengths: 4 ps, 9 ps, 12 ps, 15 ps and 20 ps. To characterize the entanglement we performed state tomography where 16 projective measurements are made in three orthogonal bases (one time basis and two energy bases) [279, 280]. For a 12 ps long pulse the fidelity of the reconstructed two-photon density matrix with the maximally entangled state was found to be $F = 0.88(3)$ while the concurrence was $C = 0.78(6)$. The reconstructed density matrix for this measurement is shown in fig. 12.5. The values for fidelity, concurrence, and coherence of the reconstructed density matrix for the other applied pulse lengths are given in tbl. 12.1.

pulse length (ps)	concurrence	fidelity	coherence
4	0.56(7)	0.78(3)	−0.28(3)
9	0.71(6)	0.83(3)	−0.36(3)
12	0.78(6)	0.88(3)	−0.39(3)
15	0.78(5)	0.88(3)	−0.40(3)
20	0.61(5)	0.80(3)	−0.32(3)

Table 12.1: Values for the fidelity with the maximally entangled Bell state, concurrence, and coherence (maximal off-diagonal element of the density matrix)

12.6 Entanglement Requirements

There are two types of factors limiting the degree of time-bin entanglement obtainable from an atom-like system: those associated with excitation and those associated with the intrinsic system coherence. The first type includes the so-called double excitations. In our measurements we drive the system with 6% probability to be excited, therefore, it will happen in 0.06^2 of the cases that the system is excited by both the early and the late pulse. These events cause the time-basis correlations to be less than unity and they also contribute to an incoherent background in both energy bases. The effect of double excitations can be eliminated through the use of deterministic schemes for generation of time-bin entanglement [281–283].

The time-basis measurements are not affected by the decoherence-induced reduction of the visibility, while the energy-bases measurements are. An intuitive picture of how the decoherence affects the time-bin entanglement is the following: the pump interferometer phase, ϕ_P, is transferred onto the quantum dot by means of resonant excitation. Any incoherence in the process of resonant excitation as well as in the relation between the ground and the biexciton state will lead to an uncertainty in the phase of the biexciton amplitude, which determines the relative phase of the entangled state components. This will reduce the visibility contrast and decrease the values of entanglement measures and indicators like concurrence and fidelity.

12.7 Conclusion

We have investigated the problem of decoherence of excitation process in quantum dots. Our theoretical study indicates that with respect to the parameters of our quantum dot system we can choose an optimized pulse duration and minimize the decoherence. Our measurements are consistent with the theoretical study that indicates the conditions needed to achieve coherent excitation and high photon pair generation probability. Additionally, using the same approach, we observed a very high degree of time-bin entanglement of the emitted photon pairs. This is possible because a high degree of time-bin entanglement is in a direct relation with coherence of excitation process. The

same theoretical study can be readily extended to other quantum dot systems where it can be used to determine the set of optimal parameters.

Theoretical study we presented here addresses a system that is driven by means of two-photon resonant excitation of the biexciton. Here, the non-resonant excitation of the exciton has emerged as the dominant dephasing process. We did not address the decoherence mechanisms that have microscopic origin, which were in depth studied in [284] and references within. Such decoherence mechanisms are easier to study through resonant excitation of a single exciton.

Beyond the decoherence induced by the excitation laser pulse quantum dots often face the decoherence that depends predominantly on the degree of interaction of the quantum dot with its semiconductor environment. Here the coherence can be increased relative to the lifetime of the emitted photons by the use of quantum dots embedded in micro-cavities [261, 285], particularly ones that are resonant to both exciton and biexciton photons [261].

Our result has one more important consequence. It indicates an existence of a trade-off between the excitation-pulse length and the biexciton binding energy. In particular it favours the use of quantum dots with large biexciton binding energy that in return allow for use of short excitation pulses. Such excitation pulses reduce the excitation jitter and are therefore more favourable for quantum information applications [286].

This work was funded by the European Research Council (project EnSeNa) and the Canadian Institute for Advanced Research through its Quantum Information Processing program. G.S.S. acknowledges partial support through the Physics Frontier Center at the Joint Quantum Institute (PFC@JQI). A. P. would like to thank the Austrian Science Fund for the support provided through project number V-375. L.O. and H.R. would also like to thank the Austrian Science Fund for support provided through SFB FoQus S4013. T. H. is receiving a DOC scholarship from the Austrian Academy of Sciences.

12.8 Supplemental Material

The quantum dot sample was held at a temperature of 4.8 K. It contained low density self-assembled InAs quantum dots embedded in a planar micro-cavity, increasing the vertical collection of photons. The excitation light was derived from a tunable 82 MHz repetition rate Ti:Sapphire pulsed laser.

To give a comparison to time-bin entanglement results obtained using parametric down-conversion we measured visibilities in three orthogonal bases. For the state generated using 12 ps pulses we find the visibilities of 94(2) % in the classically correlated basis (time basis) and 74(5) % and 67(5) % in the bases that indicate entanglement (energy bases).

12.8.1 Theoretical Model

The quantum dot system having a ground state $|g\rangle$, an intermediate exciton state $|x\rangle$ and a biexciton state $|b\rangle$ is described by the Hamiltonian

$$H = \frac{1}{2}\left(\Omega_1 |g\rangle \langle x| + h.c.\right) + \frac{1}{2}\left(\Omega_2 |x\rangle \langle b| + h.c.\right) + (\Delta_x - \Delta_b)|x\rangle \langle x| - 2\Delta_b |b\rangle \langle b|, \quad (12.9)$$

where Ω_1 and Ω_2 are the (identical) Rabi frequencies emerging from the coupling of the ground and exciton and the exciton and biexciton state, respectively, by the excitation laser pulse. Here, Δ_x is the difference between the virtual two-photon level and the exciton state of the quantum dot, while Δ_b is the detuning between the virtual two-photon level and the laser driving the quantum dot. In our experiment, we drive the two-photon virtual level resonantly, therefore $\Delta_b = 0$. Δ_x has been measured to be $\Delta_x = 2\pi \cdot 0.335\text{THz}$.

Our quantum dot system is subject to dissipative processes, therefore, we introduce the definition of a dissipator for the operator $\hat{A}$ as

$$D(\hat{A}) := 2\hat{A}\rho\hat{A}^\dagger - \hat{A}^\dagger\hat{A}\rho - \rho\hat{A}^\dagger\hat{A}. \quad (12.10)$$

With this definition we can now easily write down the loss processes in the system, which are

$$\mathcal{L}_1 = \frac{\gamma_b}{2} D\left(|b\rangle \langle x|\right) \quad (12.11)$$

$$\mathcal{L}_2 = \frac{\gamma_x}{2} D\left(|x\rangle \langle g|\right) \quad (12.12)$$

$$\mathcal{L}_3 = \frac{\gamma_b^{\text{deph}}}{2} D\left(|b\rangle \langle b| - |x\rangle \langle x|\right) \quad (12.13)$$

$$\mathcal{L}_4 = \frac{\gamma_x^{\text{deph}}}{2} D\left(|x\rangle \langle x| - |g\rangle \langle g|\right), \quad (12.14)$$

where the first two expressions consider population loss by spontaneous emission with the rates γ_b for the biexciton and γ_x for the exciton. These rates were measured to be $\gamma_b = 1/771\text{THz}$ and $\gamma_x = 1/405\text{THz}$. On the other hand, $\mathcal{L}_3$ and $\mathcal{L}_4$ account for the dephasing between the biexciton and exciton and the exciton and ground state, respectively. The rates have been assumed equal and are of the form

$$\gamma_b^{\text{deph}} = \gamma_x^{\text{deph}} = \gamma_{I_0} \cdot \Omega^{n_p} \quad (12.15)$$

where γ_{I_0} is the amplitude of the intensity-dependent dephasing and n_p represents the exponent of the intensity dependence. In our study we investigated $n_p = 2$ and $n_p = 4$, hence the linear ($n_p = 2$) and the quadratic ($n_p = 4$) intensity dependence of the dephasing. The value of γ_{I_0} has been obtained by fitting the model to the experimental data.

The full Liouvillian is hence

$$\mathcal{L} = \mathcal{L}_1 + \mathcal{L}_2 + \mathcal{L}_3 + \mathcal{L}_4 \quad (12.16)$$

and the time evolution of our system is governed by the master equation

$$\dot{\rho} = i\,[\rho, H] + \mathcal{L}. \tag{12.17}$$

The coherent excitation is described by time-dependent Rabi frequencies that for a Gaussian laser pulse envelope follow

$$\Omega_1 = \Omega_2 = \Omega \cdot \exp\left(-\frac{2\ln(2)\,(t-t_i)^2}{\sigma^2}\right), \tag{12.18}$$

where σ is the pulse length. In the experiment the pulse length can be varied from 4 ps to 20 ps. t_i is the center of the Gaussian pulse in the time domain.

12.8.2 Rabi Oscillations

In order to gain some insight into the dynamics of our system we plot the normalized emission probabilities

$$P_b(t_f) = \gamma_b \int_0^{t_f} \langle b|\,\rho(t')\,|b\rangle\ \mathrm{d}t' \tag{12.19}$$

$$P_x(t_f) = \gamma_x \int_0^{t_f} \langle x|\,\rho(t')\,|x\rangle\ \mathrm{d}t' \tag{12.20}$$

as a function of $\Omega^2\sigma$, which is proportional to the energy per pulse (Figure 12.6). Here, t_f is the time at which the photon is detected. For the constant dephasing the numbers $\gamma_x^{\mathrm{deph}} = 1/119\mathrm{THz}$ and $\gamma_b^{\mathrm{deph}} = 1/211\mathrm{THz}$ were used. These specific numbers are chosen in congruence with the $g^{(1)}(\tau)$ field correlation function measurements performed on exciton and biexciton photons, respectively.

As also explained in the manuscript, the population loss does not necessary need to originate exclusively from constant dephasing. If we introduce the intensity-dependent dephasing, given by eq. 8 in the manuscript, such that $\gamma_{I_0} = 0.05$ for $n_p = 2$ and $n_p = 4$, we obtain the normalized emission probabilities depicted in fig. 12.7.

12.8.3 Population at Low Excitation Power

Using second order time-dependent perturbation theory we can calculate the ratio between P_b and P_x for small driving strengths Ω. For this we will consider only the coherent part of the time evolution and neglect damping and dephasing. Our Hamiltonian therefore will have the following form

$$H = H_0 + V = \begin{pmatrix} 0 & 0 & 0 \\ 0 & \Delta & 0 \\ 0 & 0 & 0 \end{pmatrix} + \begin{pmatrix} 0 & \Omega & 0 \\ \Omega & 0 & \Omega \\ 0 & \Omega & 0 \end{pmatrix}.$$

The formal solution of the Schrödinger equation in the interaction picture for a time-dependent perturbation V in the basis $\{|n\rangle\}$ is

$$c_n(t) = c_n(0) - i\sum_k \int_0^t \mathrm{d}t' \, \langle n| \, V(t') \, |k\rangle \exp\left(-i(E_k - E_n)t'\right) c_k(t').$$

By recursively inserting this equation into itself we obtain the first-order

$$c_n(t) = c_n(0) - i\sum_k \int_0^t \mathrm{d}t' \, \langle n| \, V(t') \, |k\rangle \exp\left(-i(E_k - E_n)t'\right) c_k(0)$$

and the second order perturbative solution, i.e.,

$$\begin{aligned} c_n(t) =& c_n(0) - i\sum_k \int_0^t \mathrm{d}t' \, \langle n| \, V(t') \, |k\rangle \exp\left(-i(E_k - E_n)t'\right) \\ & \cdot \left[c_k(0) - i\sum_{k'} \int_0^{t'} \mathrm{d}t'' \, \langle k| \, V(t'') \, \left|k'\right\rangle \exp\left(-i(E_{k'} - E_k)t''\right) c_{k'}(0) \right]. \end{aligned}$$

When multiplying this expression we use that $V(t)$ is time-independent, while $E_{ab} = E_a - E_b$. We obtain

$$\begin{aligned} c_n(t) =& c_n(0) + \sum_k \langle n| \, V \, |k\rangle \, c_k(0) \frac{\exp\left(-iE_{kn}t\right) - 1}{E_{kn}} \\ & + \sum_{k,k'} \langle n| \, V \, |k\rangle \, \langle k| \, V \, \left|k'\right\rangle \frac{c_{k'}(0)}{E_{k'k}} \left(\frac{\exp\left(-iE_{k'n}t\right) - 1)}{E_{k'n}} - \frac{\exp\left(-iE_{kn}t\right) - 1)}{E_{kn}} \right). \end{aligned}$$

Our quantum dot system has three states $|g\rangle$, $|x\rangle$ and $|b\rangle$. This system is initially in the ground state, which means $c_g(0) = 1$. This condition together with the structure of our perturbation (i.e., only coupling ground and exciton and exciton and biexciton states) immediately reduces the sums to exactly one single term. Hence,

$$\begin{aligned} c_x(t) =& \frac{\Omega}{\Delta} \sin\left(\frac{\Delta t}{2}\right) \exp\left(-i\frac{\Delta t}{2}\right) \\ c_b(t) =& \frac{\Omega^2}{\Delta} \left[\frac{\sin\left(\frac{\Delta t}{2}\right)\cos\left(\frac{\Delta t}{2}\right)}{\Delta} - i\left\{ \frac{\sin\left(\frac{\Delta t}{2}\right)^2}{\Delta} + t \right\} \right] \end{aligned}$$

and the emission probability ratio therefore yields

$$\frac{P_b}{P_x} = \frac{\gamma_b \int_0^t |c_b(t')|^2 \, \mathrm{d}t'}{\gamma_x \int_0^t |c_x(t')|^2 \, \mathrm{d}t'} \sim \frac{\frac{\Omega^4}{\Delta^5}}{\frac{\Omega^2}{\Delta^3}} = \frac{\Omega^2}{\Delta^2},$$

which goes to zero for $\Omega \to 0$.

12.8.4 Detection Probabilities for Two Pulse Excitation

Up to a geometric factor, the field emitted by a single quantum emitter at a position $\vec{x}$ is proportional to its dipole operator $\hat{\sigma}$ evaluated at the proper retarded time, i.e.,

$$\hat{E}^+(\vec{x},t) \sim \vec{e}(\vec{x}) \cdot \hat{\sigma}(t - R/c), \tag{12.21}$$

where $\vec{e}(\vec{x})$ represents the geometrical emission distribution and R the optical path length between emitter and detector. In our case we have the two emission dipoles that correspond to the exciton transition $\hat{\sigma}_x = |g\rangle\langle x|$ and the biexciton transition $\hat{\sigma}_b = |x\rangle\langle b|$. If we assume that the frequencies of the biexciton and the exciton photon are sufficiently distinct to allow distinguishable detection at separate detectors, we can approximate the fields at the detectors by

$$\hat{E}_x^+(t) = \eta(\hat{\sigma_x}(t - R_x/c) + e^{i\phi_x}\hat{\sigma_x}(t - R_x/c - \tau)) \tag{12.22}$$
$$\hat{E}_b^+(t) = \eta(\hat{\sigma_b}(t - R_b/c) + e^{i\phi_{xx}}\hat{\sigma_b}(t - R_b/c - \tau)). \tag{12.23}$$

Here, η is a general detection efficiency subsuming geometry and the actual detector efficiency η_D. The angles ϕ_x and ϕ_{xx} are the individual phase shifts in the x and xx interferometers and τ is the delay time between the two pulses. Using these expressions and assuming a sufficient time delay between the two pulses, so that all excitations have decayed in the dot upon arrival of the second pulse, we can factorize some expectation values and obtain the following average count rates,

$$I_x(t) = \left\langle \hat{E}_x^-(t)\hat{E}_x^+(t) \right\rangle = \eta^2 \left\langle e^{-i\phi_x}(\sigma_x^\dagger(t+\tau)\sigma_x(t) + e^{i\phi_x}\sigma_x^\dagger(t)\sigma_x(t+\tau)) \right. \tag{12.24}$$
$$\left. + P_x(t) + P_x(t+\tau) \right\rangle \tag{12.25}$$
$$\approx \eta^2 \left(\cos(\phi_x)\,\rho_{gx}\rho_{xg} + \rho_{xx}\right) \tag{12.26}$$
$$I_b(t) = \eta^2 \left\langle \hat{E}_b^-(t)\hat{E}_b^+(t) \right\rangle \approx \eta^2 \left(\cos(\phi_{xx})\rho_{xb}\rho_{bx} + \rho_{bb}\right). \tag{12.27}$$

The corresponding probabilities can be obtained from our above calculations by integration over the pulse duration. Note, that some phase dependence of the signal can survive from the interference of the Rayleigh component of the scattering. In a similar way, for the two photon coincidence count probabilities we find

$$\begin{aligned} P_{bx}(t) = \eta^4 \left\langle \hat{E}_b^-(t)\hat{E}_x^-(t)\hat{E}_x^+(t)\hat{E}_b^+(t) \right\rangle &= \eta^4 \left(\cos\left(\phi_x + \phi_{xx}\right)\rho_{gb}\rho_{bg}\right. \\ &\left. + (1 + \rho_{xx})\rho_{bb} + 2\cos(\phi_{xx})\rho_{xb}\rho_{bx}\right) \end{aligned} \tag{12.28}$$
$$P_{xb}(t) = \eta^4 \left\langle \hat{E}_b^+(t)\hat{E}_x^-(t)\hat{E}_x^+(t)\hat{E}_b^+(t) \right\rangle = \eta^4 \rho_{xx}\rho_{bb}, \tag{12.29}$$

where $P_{bx}(t)$ corresponds to detecting the biexciton photon before the exciton photon and $P_{xb}(t)$ is the other way round. The dominant contribution comes from the ground state – biexciton coherence, which is induced by the phase of the excitation pulses and depends on the sum phase of the two interferometers. This behaviour is in an close

analogy to the results obtained in experiments using down-conversion by a nonlinear crystal. The quantities presented here have to be averaged at least over the detector response time. Note, that we can also get the probability for four simultaneous counts P_4, which simply reads $P_4 \approx 16\eta^8\rho_{bb}^2$ giving the product probability of a biexciton generated by a single pulse. This quantity is independent of any phase settings and we cannot detect more than four photons at exactly the same time, independent of how strong a pump we employ, due to pairwise anti-bunching.

In fig. 12.8 we depict the evolution of the populations and coherences of the density matrix for a Gaussian pulse as a function of the pulse duration in an ideal system without any dephasing. We see that the initially coherence follows the population until a gap opens and incoherent biexciton population builds up.

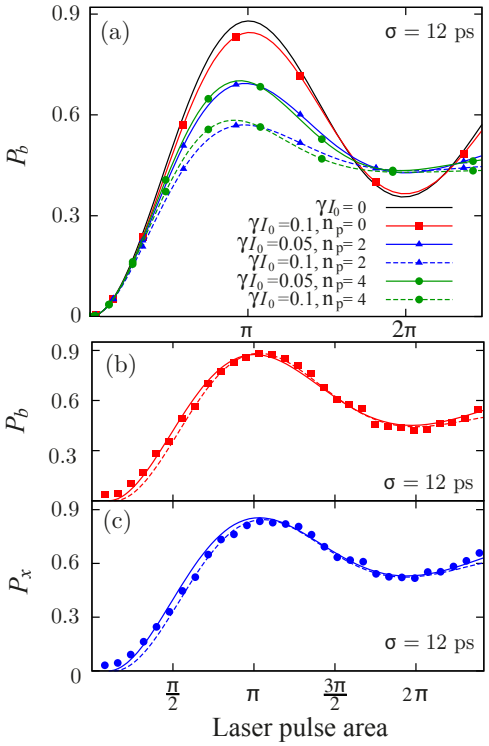

Figure 12.3: (Colour online) a) Biexciton emission probability, P_b (theory) for different dephasing models. We observe a strong damping of the Rabi oscillations even at moderate γ_{I_0}. From this it is clear that the amplitude of the intensity-dependant dephasing rate plays a much greater role than the exponent n_p. b) Emission probability for a biexciton, P_b, and exciton photon, P_x, as a function of the laser pulse area for linear (solid line) and quadratic (dashed line) intensity-dependent dephasing compared to the experimental data, respectively. The error bars are smaller than symbols. The theoretical parameters, γ_{I_0}, are obtained by fitting the ratio of the first maximum and minimum of the Rabi cycle.

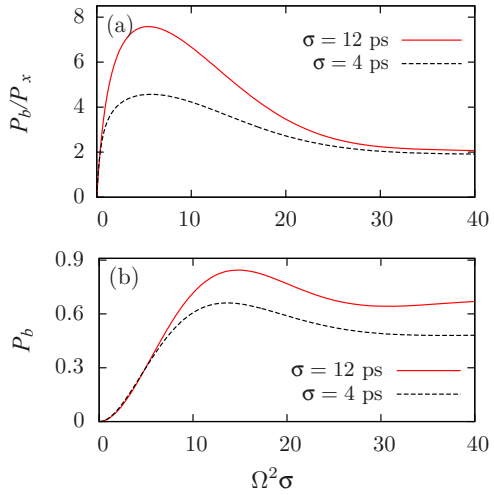

Figure 12.4: (Colour online) Relative probability for biexciton versus single exciton excitation in the quantum dot as a function of $\Omega^2\sigma$ for two different pulse lengths (upper plot). The choice of $\Omega^2\sigma$, which is proportional to the energy per pulse, as x-axis allows for easier comparison of the maxima. We see an optimum ratio of about 8 at a still moderate excitation rate. The lower plot gives the biexciton photon emission probability as a function of $\Omega^2\sigma$.

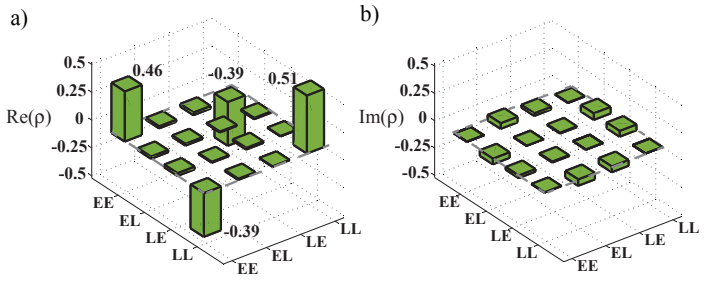

Figure 12.5: (Colour online) An example of (a) real and (b) imaginary part of the reconstructed density matrix. Measurements used to obtain this density matrix were performed using 12 ps excitation pulses while the emission probability was kept at 6 %. Here, *E (early)* and *L (late)* denote the measurement basis.

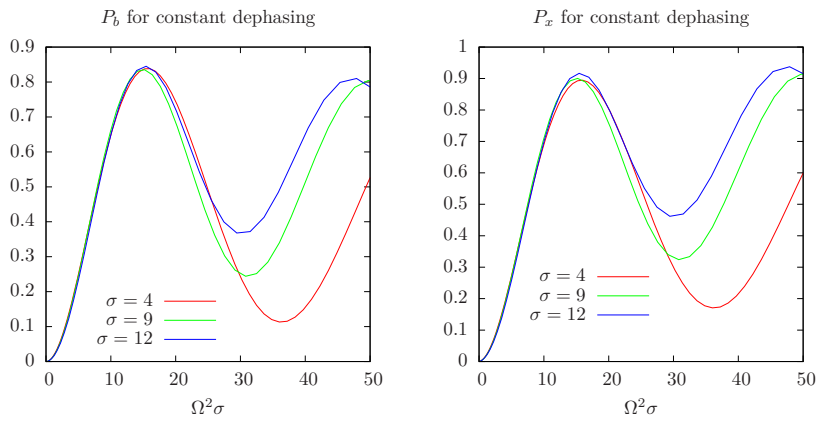

Figure 12.6: Rabi oscillations for constant dephasing as a function of $\Omega^2\sigma$. The emission probability for the biexciton, P_b, (left) and the exciton, P_x, (right) level are shown.It is obvious that short pulses introduce damping of the Rabi oscillations.

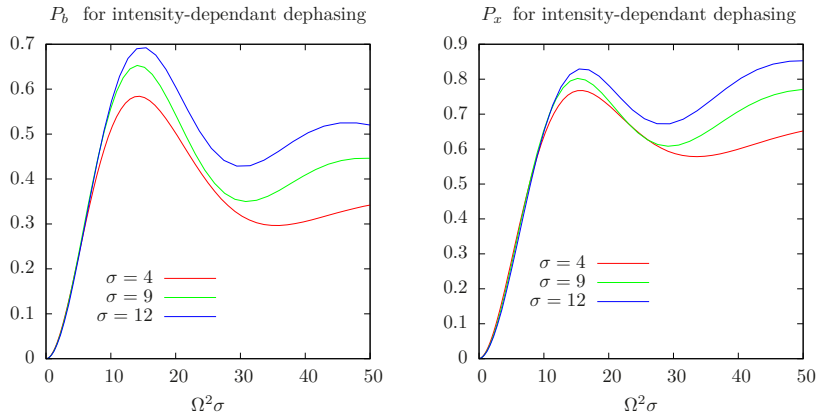

Figure 12.7: Rabi oscillations for linearly intensity-dependent dephasing with an amplitude of $\gamma_{I_0} = 0.05$ as a function of the deposited energy. The emission probability from the biexciton (left) and the exciton (right) level is shown. From this it is clear that the ratio between the first Rabi maximum and its first minimum is largely determined by γ_{I_0}. The figure for $n_p = 4$ looks fairly similar and is therefore omitted.

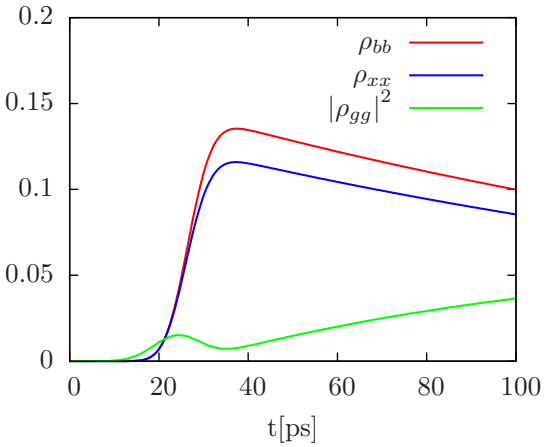

Figure 12.8: Time evolution of exciton ρ_{xx} and biexciton ρ_{bb} population as well as the biexciton-ground coherence as a function of time for a Gaussian pulse of $\sigma = 12$ ps.

Bibliography

[1] C. Cohen-Tannoudji, B. Diu, and F. Laloe, *Quantum Mechanics Volume 1*. Hermann, 1977.

[2] C. Cohen-Tannoudji, B. Diu, and F. Laloe, *Quantum Mechanics Volume 2*. Hermann, 1977.

[3] S. Haroche and J. M. Raimond, *Exploring the quantum*. Oxford University Press, 2006.

[4] J. Sakurai and J. Napolitano, *Modern Quantum Mechanics*. Pearson new international edition, Pearson, 2013.

[5] V. Fock, "Konfigurationsraum und zweite Quantelung," *Zeitschrift für Physik*, vol. 75, no. 9-10, pp. 622–647, 1932.

[6] E. T. Jaynes and F. W. Cummings, "Comparison of quantum and semiclassical radiation theories with application to the beam maser," *Proceedings of the IEEE*, vol. 51, no. 1, pp. 89–109, 1963.

[7] E. Schrödinger, "An undulatory theory of the mechanics of atoms and molecules," *Physical Review*, vol. 28, no. 6, p. 1049, 1926.

[8] C. W. Gardiner *et al.*, *Handbook of stochastic methods*, vol. 3. Springer Berlin, 1985.

[9] C. Gardiner and P. Zoller, *The Quantum World of Ultra-Cold Atoms and Light: Foundations of Quantum Optics*. Cold Atoms, Imperial College Press, 2014.

[10] C. Gardiner and P. Zoller, *Physics of Quantum Devices*. Cold Atoms, Imperial College Press, 2015.

[11] M. Fox, *Quantum Optics : An Introduction: An Introduction*. Oxford Master Series in Physics, Oxford University Press, 2006.

[12] C. Gerry and P. Knight, *Introductory Quantum Optics*. Cambridge University Press, 2005.

[13] M. Scully and M. Zubairy, *Quantum Optics*. Cambridge University Press, 1997.

[14] D. Walls and G. Milburn, *Quantum Optics*. Springer Study Edition, Springer Berlin Heidelberg, 2012.

[15] Y. Yamamoto and A. Imamoglu, *Mesoscopic Quantum Optics*. Wiley, 1999.

[16] W. Eichelberger, *Clocks, Ancient and Modern*. Gibson Bros., 1908.

[17] T. Bowie, *The sketchbook of Villard de Honnecourt*. Indiana University Press, (1959), 1960.

[18] D. Hill, *A History of Engineering in Classical and Medieval Times*. Routledge, 1996.

[19] D. West, *Galileo Galilei - a Short Biography*. 30 Minute Book, CreateSpace Independent Publishing Platform, 2015.

[20] J. Taylor, *Classical Mechanics*. University Science Books, 2005.

[21] A. Bell, *Christian Huygens*. Read Books, 2007.

[22] H. Lloyd, *The Anchor Escapement, William Clement Or Robert Hooke ? By H. Alan Lloyd,...* British Horological Institute, 1952.

[23] M. . W. Christie, *The Mostyn Tompion : the Year-going Spring Clock Made by Thomas Tompion for William III: Vente À Londres, Christie, Manson & Woods, 14 Juillet 1982*. J. A. Floyd, 1982.

[24] R. T. Gould, *The Marine Chronometer: Its History and Development*. Antique Collectors' Club, 2013.

[25] W. P. Mason, "Piezoelectricity, its history and applications," *The Journal of the Acoustical Society of America*, vol. 70, no. 6, pp. 1561–1566, 1981.

[26] W. A. Marrison, "A high precision standard of frequency," *Bell system technical journal*, vol. 8, no. 3, pp. 493–514, 1929.

[27] D. Sullivan, "Time and frequency measurement at nist: The first 100 years," in *Frequency Control Symposium and PDA Exhibition, 2001. Proceedings of the 2001 IEEE International*, pp. 4–17, IEEE, 2001.

[28] L. Carr, "The mks or giorgi system of units. the case for its adoption," *Proceedings of the IEE-Part I: General*, vol. 97, no. 107, pp. 235–240, 1950.

[29] G. Dunnington, J. Gray, and F. Dohse, *Carl Friedrich Gauss: Titan of Science*. MAA spectrum, Mathematical Association of America, 2004.

[30] F. Jenkin, W. Kelvin, J. Joule, J. Maxwell, and B. A. for the Advancement of Science, *Reports of the Committee on Electrical Standards Appointed by the British Association for the Advancement of Science*. E. & F.N. Spon, 1873.

[31] K. Soman, *International System Of Units: A Handbook On S.I. Unit For Scientists And Engineers*. Prentice-Hall Of India Pvt. Limited, 2009.

[32] I. B. of Weights, Measures, C. Page, and P. Vigoureux, *The International System of Units (SI)*. NBS special publication, U.S. Department of Commerce, National Bureau of Standards, 1974.

[33] A. French and E. Taylor, *An Introduction to Quantum Physics*. The M.I.T. introductoctory physics series, Nelson, 1978.

[34] J. S. Rigden, *Rabi, scientist and citizen*. Harvard University Press, 2000.

[35] B. Blair, A. Morgan, and U. S. N. B. of Standards, *Frequency and Time*. NBS special publication, U.S. Government Printing Office, 1972.

[36] S. Leschiutta, "The definition of the 'atomic' second," *Metrologia*, vol. 42, no. 3, p. S10, 2005.

[37] M. Kochsiek and M. Gläser, *Handbook of Metrology*. John Wiley & Sons, 2010.

[38] S. R. Jefferts, T. Heavner, T. Parker, and J. Shirley, "Nist cesium fountains: current status and future prospects," in *Optical Engineering and Applications*, pp. 667309–667309, International Society for Optics and Photonics, 2007.

[39] C. Gohle, T. Udem, M. Herrmann, J. Rauschenberger, R. Holzwarth, H. A. Schuessler, F. Krausz, and T. W. Hänsch, "A frequency comb in the extreme ultraviolet," *Nature*, vol. 436, no. 7048, pp. 234–237, 2005.

[40] M. Takamoto, F.-L. Hong, R. Higashi, and H. Katori, "An optical lattice clock," *Nature*, vol. 435, no. 7040, pp. 321–324, 2005.

[41] M. Boyd and U. of Colorado at Boulder. Physics, *High Precision Spectroscopy of Strontium in an Optical Lattice: Towards a New Standard for Frequency and Time*. University of Colorado at Boulder, 2007.

[42] B. Bloom, T. Nicholson, J. Williams, S. Campbell, M. Bishof, X. Zhang, W. Zhang, S. Bromley, and J. Ye, "An optical lattice clock with accuracy and stability at the 10^{-18} level," *Nature*, vol. 506, no. 7486, pp. 71–75, 2014.

[43] D. W. Allan, "Statistics of atomic frequency standards," *Proceedings of the IEEE*, vol. 54, no. 2, pp. 221–230, 1966.

[44] N. F. Ramsey, "History of atomic clocks," *Journal of Research of the National Institute of Standards and Technology*, vol. 88, p. 301, 1983.

[45] J. C. Camparo, "The rubidium atomic clock and basic research," tech. rep., DTIC Document, 2007.

[46] J. C. Hafele and R. E. Keating, "Around-the-world atomic clocks: predicted relativistic time gains," *Science*, vol. 177, no. 4044, pp. 166–168, 1972.

[47] C.-W. Chou, D. Hume, T. Rosenband, and D. Wineland, "Optical clocks and relativity," *Science*, vol. 329, no. 5999, pp. 1630–1633, 2010.

[48] S. Reinhardt, G. Saathoff, H. Buhr, L. A. Carlson, A. Wolf, D. Schwalm, S. Karpuk, C. Novotny, G. Huber, M. Zimmermann, *et al.*, "Test of relativistic time dilation with fast optical atomic clocks at different velocities," *Nature Physics*, vol. 3, no. 12, pp. 861–864, 2007.

[49] J. D. Prestage, R. L. Tjoelker, and L. Maleki, "Atomic clocks and variations of the fine structure constant," *Physical Review Letters*, vol. 74, no. 18, p. 3511, 1995.

[50] B. Hofmann-Wellenhof, H. Lichtenegger, and J. Collins, *Global Positioning System: Theory and Practice*. Springer Vienna, 2012.

[51] C. Cohen-Tannoudji, J. Dupont-Roc, and G. Grynberg, *Atom-Photon Interactions: Basic Processes and Applications*. A Wiley-Interscience publication, Wiley, 1998.

[52] H. Lyons, "The atomic clock: a universal standard of frequency and time," *The American Scholar*, pp. 159–168, 1950.

[53] R. Solarz and J. Paisner, *Laser Spectroscopy and its Applications*. Optical Science and Engineering, Taylor & Francis, 1986.

[54] R. Wynands, A. Bauch, D. Griebsch, R. Schroeder, and S. Weyers, *The new PTB caesium fountain clock CSF2*. Defense Technical Information Center, 2005.

[55] C. Salomon, N. Dimarcq, M. Abgrall, A. Clairon, P. Laurent, P. Lemonde, G. Santarelli, P. Uhrich, L. Bernier, G. Busca, *et al.*, "Cold atoms in space and atomic clocks: Aces," *Comptes Rendus de l'Académie des Sciences-Series IV-Physics*, vol. 2, no. 9, pp. 1313–1330, 2001.

[56] R. Li, K. Gibble, and K. Szymaniec, "Improved accuracy of the npl-csf2 primary frequency standard: evaluation of distributed cavity phase and microwave lensing frequency shifts," *Metrologia*, vol. 48, no. 5, p. 283, 2011.

[57] F.-L. Hong, M. Musha, M. Takamoto, H. Inaba, S. Yanagimachi, A. Takamizawa, K. Watabe, T. Ikegami, M. Imae, Y. Fujii, *et al.*, "Measuring the frequency of a sr optical lattice clock using a 120 km coherent optical transfer," *Optics letters*, vol. 34, no. 5, pp. 692–694, 2009.

[58] Y. Somayajulu, B. Mathur, P. Banerjee, S. Garg, L. Singh, P. Sood, T. R. Tyagi, C. Jain, and K. Kumar, "Clock synchronization experiment in india using symphonie satellite," *IETE Journal of Research*, vol. 25, no. 12, pp. 481–487, 1979.

[59] M. A. Lombardi, T. P. Heavner, and S. R. Jefferts, "Nist primary frequency standards and the realization of the si second," *Journal of Measurement Science*, vol. 2, no. 4, pp. 74–89, 2007.

[60] P. Forman, "Atomichron®: the atomic clock from concept to commercial product," *Proceedings of the IEEE*, vol. 73, no. 7, pp. 1181–1204, 1985.

[61] S. Millman and P. Kusch, "On the radiofrequency spectra of sodium, rubidium and caesium," *Physical Review*, vol. 58, no. 5, p. 438, 1940.

[62] H. Metcalf and P. van der Straten, *Laser Cooling and Trapping*. Graduate Texts in Contemporary Physics, Springer New York, 2012.

[63] D. Sullivan, J. Bergquist, J. Bollinger, R. Drullinger, *et al.*, "Primary atomic frequency standards at nist," *Journal of Research of the National Institute of Standards and Technology*, vol. 106, no. 1, p. 47, 2001.

[64] N. Ramsey, *Molecular Beams*. International series of monographs on physics, Oxford University Press, 1956.

[65] D. J. Wineland, R. E. Drullinger, and F. L. Walls, "Radiation-pressure cooling of bound resonant absorbers," *Physical Review Letters*, vol. 40, no. 25, p. 1639, 1978.

[66] D. Wineland and H. Dehmelt, "Proposed 1014 delta upsilon less than upsilon laser fluorescence spectroscopy on t1+ mono-ion oscillator iii," in *Bulletin of the American Physical Society*, vol. 20, pp. 637–637, AMER INST PHYSICS CIRCULATION FULFILLMENT DIV, 500 SUNNYSIDE BLVD, WOODBURY, NY 11797-2999, 1975.

[67] M. A. Kasevich, E. Riis, S. Chu, and R. G. DeVoe, "Rf spectroscopy in an atomic fountain," *Physical Review Letters*, vol. 63, no. 6, p. 612, 1989.

[68] K. Gibble and S. Chu, "Laser-cooled cs frequency standard and a measurement of the frequency shift due to ultracold collisions," *Physical Review Letters*, vol. 70, no. 12, p. 1771, 1993.

[69] A. Clarion, P. Laurent, G. Santarelli, S. Ghezali, S. Lea, and M. Bahoura, "A cesium fountain frequency standard: Recent results," *IEEE Transactions on Instrumentation and Measurement*, vol. 44, pp. 128–131, 1995.

[70] P. D. Lett, W. D. Phillips, S. Rolston, C. E. Tanner, R. Watts, and C. Westbrook, "Optical molasses," *Journal of the Optical Society of America B*, vol. 6, no. 11, pp. 2084–2107, 1989.

[71] S. Jefferts, D. Meekhof, J. Shirley, T. Parker, and F. Levi, "Preliminary accuracy evaluation of a cesium fountain primary frequency standard at nist," in *Frequency and Time Forum, 1999 and the IEEE International Frequency Control Symposium, 1999., Proceedings of the 1999 Joint Meeting of the European*, vol. 1, pp. 12–15, IEEE, 1999.

[72] T. P. Heavner, E. A. Donley, F. Levi, G. Costanzo, T. E. Parker, J. H. Shirley, N. Ashby, S. Barlow, and S. Jefferts, "First accuracy evaluation of nist-f2," *Metrologia*, vol. 51, no. 3, p. 174, 2014.

[73] F. Levi, A. Godone, and L. Lorini, "Reduction of the cold collisions frequency shift in a multiple velocity fountain: a new proposal," *Ultrasonics, Ferroelectrics, and Frequency Control, IEEE Transactions on*, vol. 48, no. 3, pp. 847–850, 2001.

[74] A. D. Ludlow, M. M. Boyd, J. Ye, E. Peik, and P. O. Schmidt, "Optical atomic clocks," *Reviews of Modern Physics*, vol. 87, no. 2, p. 637, 2015.

[75] R. Wynands and S. Weyers, "Atomic fountain clocks," *Metrologia*, vol. 42, no. 3, p. S64, 2005.

[76] T. Rosenband, D. Hume, P. Schmidt, C. Chou, A. Brusch, L. Lorini, W. Oskay, R. Drullinger, T. Fortier, J. Stalnaker, *et al.*, "Frequency ratio of al+ and hg+ single-ion optical clocks; metrology at the 17th decimal place," *Science*, vol. 319, no. 5871, pp. 1808–1812, 2008.

[77] S. Diddams, T. Udem, J. Bergquist, E. Curtis, R. Drullinger, L. Hollberg,

W. Itano, W. Lee, C. Oates, K. Vogel, *et al.*, "An optical clock based on a single trapped 199hg+ ion," *Science*, vol. 293, no. 5531, pp. 825–828, 2001.

[78] N. Hinkley, J. Sherman, N. Phillips, M. Schioppo, N. Lemke, K. Beloy, M. Pizzocaro, C. Oates, and A. Ludlow, "An atomic clock with 10−$^{-18}$ instability," *Science*, vol. 341, no. 6151, pp. 1215–1218, 2013.

[79] J. L. Hall, M. Zhu, and P. Buch, "Prospects for using laser-prepared atomic fountains for optical frequency standards applications," *Journal of the Optical Society of America B*, vol. 6, no. 11, pp. 2194–2205, 1989.

[80] H. Katori, M. Takamoto, V. Pal'Chikov, and V. Ovsiannikov, "Ultrastable optical clock with neutral atoms in an engineered light shift trap," *Physical Review Letters*, vol. 91, no. 17, p. 173005, 2003.

[81] S. Friebel, C. D'andrea, J. Walz, M. Weitz, and T. Hänsch, "Co 2-laser optical lattice with cold rubidium atoms," *Physical Review A*, vol. 57, no. 1, p. R20, 1998.

[82] S. Falke, H. Schnatz, J. V. Winfred, T. Middelmann, S. Vogt, S. Weyers, B. Lipphardt, G. Grosche, F. Riehle, U. Sterr, *et al.*, "The ^{87}Sr optical frequency standard at ptb," *Metrologia*, vol. 48, no. 5, p. 399, 2011.

[83] M. M. Boyd, T. Zelevinsky, A. D. Ludlow, S. Blatt, T. Zanon-Willette, S. M. Foreman, and J. Ye, "Nuclear spin effects in optical lattice clocks," *Physical Review A*, vol. 76, no. 2, p. 022510, 2007.

[84] P. G. Westergaard, J. Lodewyck, L. Lorini, A. Lecallier, E. Burt, M. Zawada, J. Millo, and P. Lemonde, "Lattice-induced frequency shifts in sr optical lattice clocks at the 10- 17 level," *Physical Review Letters*, vol. 106, no. 21, p. 210801, 2011.

[85] V. Ovsyannikov, V. G. Pal'chikov, H. Katori, and M. Takamoto, "Polarisation and dispersion properties of light shifts in ultrastable optical frequency standards," *Quantum Electronics*, vol. 36, no. 1, p. 3, 2006.

[86] A. Brusch, R. Le Targat, X. Baillard, M. Fouché, and P. Lemonde, "Hyperpolarizability effects in a sr optical lattice clock," *Physical Review Letters*, vol. 96, no. 10, p. 103003, 2006.

[87] Z. W. Barber, J. E. Stalnaker, N. D. Lemke, N. Poli, C. Oates, T. Fortier, S. Diddams, L. Hollberg, C. Hoyt, A. Taichenachev, *et al.*, "Optical lattice induced light shifts in an yb atomic clock," *Physical Review Letters*, vol. 100, no. 10, p. 103002, 2008.

[88] A. Taichenachev, V. Yudin, C. Oates, C. Hoyt, Z. Barber, and L. Hollberg, "Magnetic field-induced spectroscopy of forbidden optical transitions with application to lattice-based optical atomic clocks," *Physical Review Letters*, vol. 96, no. 8, p. 083001, 2006.

[89] L. Olschewski, "Messung der magnetischen Kerndipolmomente an freien43ca-,

87sr-, 135ba-, 137ba-, 171yb-und173yb-Atomen mit optischem Pumpen," *Zeitschrift für Physik*, vol. 249, no. 3, pp. 205–227, 1972.

[90] P. Brix and H. Kopfermann, "Isotope shift studies of nuclei," *Reviews of Modern Physics*, vol. 30, no. 2, p. 517, 1958.

[91] M. M. Boyd, T. Zelevinsky, A. D. Ludlow, S. M. Foreman, S. Blatt, T. Ido, and J. Ye, "Optical atomic coherence at the 1-second time scale," *Science*, vol. 314, no. 5804, pp. 1430–1433, 2006.

[92] B. Lahaye and J. Margerie, "G-factor of the metastable 6*sup*3 p *sub*0 level of odd isotopes of mercury," tech. rep., Caen Univ., 14 (France), 1975.

[93] T. Becker, J. v. Zanthier, A. Y. Nevsky, C. Schwedes, M. Skvortsov, H. Walther, and E. Peik, "High-resolution spectroscopy of a single in+ ion: Progress towards an optical frequency standard," *Physical Review A*, vol. 63, no. 5, p. 051802, 2001.

[94] X. Baillard, M. Fouché, R. Le Targat, P. G. Westergaard, A. Lecallier, Y. Le Coq, G. D. Rovera, S. Bize, and P. Lemonde, "Accuracy evaluation of an optical lattice clock with bosonic atoms," *Optics Letters*, vol. 32, no. 13, pp. 1812–1814, 2007.

[95] A. D. Ludlow, T. Zelevinsky, G. Campbell, S. Blatt, M. Boyd, M. H. de Miranda, M. Martin, J. Thomsen, S. M. Foreman, J. Ye, *et al.*, "Sr lattice clock at $1 \times 10-^{-16}$ fractional uncertainty by remote optical evaluation with a ca clock," *Science*, vol. 319, no. 5871, pp. 1805–1808, 2008.

[96] S. G. Porsev and A. Derevianko, "Multipolar theory of blackbody radiation shift of atomic energy levels and its implications for optical lattice clocks," *Physical Review A*, vol. 74, no. 2, p. 020502, 2006.

[97] E. Simon, P. Laurent, and A. Clairon, "Measurement of the stark shift of the cs hyperfine splitting in an atomic fountain," *Physical Review A*, vol. 57, no. 1, p. 436, 1998.

[98] T. Rosenband, W. Itano, P. Schmidt, D. Hume, J. Koelemeij, J. Bergquist, and D. Wineland, "Blackbody radiation shift of the 27 al+ $^1s_0 \rightarrow^3 p_0$ transition," in *Frequency and Time Forum (EFTF), 2006 20th European*, pp. 289–292, IEEE, 2006.

[99] T. Middelmann, S. Falke, C. Lisdat, and U. Sterr, "High accuracy correction of blackbody radiation shift in an optical lattice clock," *Physical Review Letters*, vol. 109, no. 26, p. 263004, 2012.

[100] M. Safronova, S. Porsev, and C. W. Clark, "Ytterbium in quantum gases and atomic clocks: van der waals interactions and blackbody shifts," *Physical Review Letters*, vol. 109, no. 23, p. 230802, 2012.

[101] M. Safronova, S. Porsev, U. Safronova, M. Kozlov, and C. W. Clark, "Blackbody-radiation shift in the sr optical atomic clock," *Physical Review A*, vol. 87, no. 1,

p. 012509, 2013.

[102] T. Nicholson, S. Campbell, R. Hutson, G. Marti, B. Bloom, R. McNally, W. Zhang, M. Barrett, M. Safronova, G. Strouse, *et al.*, "Systematic evaluation of an atomic clock at 2 [times] 10-18 total uncertainty," *Nature Communications*, vol. 6, 2015.

[103] T. Middelmann, C. Lisdat, S. Falke, J. S. Winfred, F. Riehle, and U. Sterr, "Tackling the blackbody shift in a strontium optical lattice clock," *Instrumentation and Measurement, IEEE Transactions on*, vol. 60, no. 7, pp. 2550–2557, 2011.

[104] P. J. Leo, P. S. Julienne, F. H. Mies, and C. J. Williams, "Collisional frequency shifts in 133 cs fountain clocks," *Physical Review Letters*, vol. 86, no. 17, p. 3743, 2001.

[105] F. P. Dos Santos, H. Marion, S. Bize, Y. Sortais, A. Clairon, and C. Salomon, "Controlling the cold collision shift in high precision atomic interferometry," *Physical Review Letters*, vol. 89, no. 23, p. 233004, 2002.

[106] K. Szymaniec, W. Chałupczak, E. Tiesinga, C. J. Williams, S. Weyers, and R. Wynands, "Cancellation of the collisional frequency shift in caesium fountain clocks," *Physical Review Letters*, vol. 98, no. 15, p. 153002, 2007.

[107] D. Chang, J. Ye, and M. Lukin, "Controlling dipole-dipole frequency shifts in a lattice-based optical atomic clock," *Physical Review A*, vol. 69, no. 2, p. 023810, 2004.

[108] G. Campbell, M. Boyd, J. Thomsen, M. Martin, S. Blatt, M. Swallows, T. Nicholson, T. Fortier, C. Oates, S. Diddams, *et al.*, "Probing interactions between ultracold fermions," *Science*, vol. 324, no. 5925, pp. 360–363, 2009.

[109] Y. Band and A. Vardi, "Collisional shifts in optical-lattice atom clocks," *Physical Review A*, vol. 74, no. 3, p. 033807, 2006.

[110] K. Gibble, "Decoherence and collisional frequency shifts of trapped bosons and fermions," *Physical Review Letters*, vol. 103, no. 11, p. 113202, 2009.

[111] A. Rey, A. Gorshkov, and C. Rubbo, "Many-body treatment of the collisional frequency shift in fermionic atoms," *Physical Review Letters*, vol. 103, no. 26, p. 260402, 2009.

[112] Z. Yu and C. Pethick, "Clock shifts of optical transitions in ultracold atomic gases," *Physical Review Letters*, vol. 104, no. 1, p. 010801, 2010.

[113] M. Bishof, Y. Lin, M. D. Swallows, A. V. Gorshkov, J. Ye, and A. M. Rey, "Resolved atomic interaction sidebands in an optical clock transition," *Physical Review Letters*, vol. 106, no. 25, p. 250801, 2011.

[114] N. Lemke, J. Von Stecher, J. Sherman, A. Rey, C. Oates, and A. Ludlow, "p-wave cold collisions in an optical lattice clock," *Physical Review Letters*, vol. 107, no. 10, p. 103902, 2011.

[115] A. Ludlow, N. Lemke, J. Sherman, C. Oates, G. Quéméner, J. von Stecher, and A. Rey, "Cold-collision-shift cancellation and inelastic scattering in a yb optical lattice clock," *Physical Review A*, vol. 84, no. 5, p. 052724, 2011.

[116] M. D. Swallows, M. Bishof, Y. Lin, S. Blatt, M. J. Martin, A. M. Rey, and J. Ye, "Suppression of collisional shifts in a strongly interacting lattice clock," *Science*, vol. 331, no. 6020, pp. 1043–1046, 2011.

[117] T. Nicholson, M. Martin, J. Williams, B. Bloom, M. Bishof, M. Swallows, S. Campbell, and J. Ye, "Comparison of two independent sr optical clocks with 1× 10- 17 stability at 10 3 s," *Physical Review Letters*, vol. 109, no. 23, p. 230801, 2012.

[118] T. Zanon-Willette, V. Yudin, and A. Taichenachev, "Generalized hyper-ramsey resonance with separated oscillating fields," *Physical Review A*, vol. 92, no. 2, p. 023416, 2015.

[119] T. Kohno, M. Yasuda, K. Hosaka, H. Inaba, Y. Nakajima, and F.-L. Hong, "One-dimensional optical lattice clock with a fermionic 171yb isotope," *Applied Physics Express*, vol. 2, no. 7, p. 072501, 2009.

[120] N. Lemke, A. Ludlow, Z. Barber, T. Fortier, S. Diddams, Y. Jiang, S. Jefferts, T. Heavner, T. Parker, and C. Oates, "Spin-1/2 optical lattice clock," *Physical Review Letters*, vol. 103, no. 6, p. 063001, 2009.

[121] P. Lemonde and P. Wolf, "Optical lattice clock with atoms confined in a shallow trap," *Physical Review A*, vol. 72, no. 3, p. 033409, 2005.

[122] L.-S. Ma, P. Jungner, J. Ye, and J. L. Hall, "Delivering the same optical frequency at two places: accurate cancellation of phase noise introduced by an optical fiber or other time-varying path," *Optics Letters*, vol. 19, no. 21, pp. 1777–1779, 1994.

[123] H. Eklund, A. Roos, and S. Eng, "Rotation of laser beam polarization in acousto-optic devices," *Optical and Quantum Electronics*, vol. 7, no. 2, pp. 73–79, 1975.

[124] C. Degenhardt, T. Nazarova, C. Lisdat, H. Stoehr, U. Sterr, and F. Riehle, "Influence of chirped excitation pulses in an optical clock with ultracold calcium atoms," *IEEE transactions on instrumentation and measurement*, vol. 54, no. 2, pp. 771–775, 2005.

[125] M. D. Swallows, M. J. Martin, M. Bishof, C. Benko, Y. Lin, S. Blatt, A. M. Rey, and J. Ye, "Operating a ^{87}Sr optical lattice clock with high precision and at high densit," *Ultrasonics, Ferroelectrics, and Frequency Control, IEEE Transactions on*, vol. 59, no. 3, pp. 416–425, 2012.

[126] J. Lodewyck, M. Zawada, L. Lorini, M. Gurov, and P. Lemonde, "Observation and cancellation of a perturbing dc stark shift in strontium optical lattice clocks," *Ultrasonics, Ferroelectrics, and Frequency Control, IEEE Transactions on*, vol. 59, no. 3, pp. 411–415, 2012.

[127] M. Naval Ordnance Laboratory, (White Oak and E. Winkler, *Analytical studies*

of the Mach-Zehnder interferometer. No. Bd. 1-2 in Report (Naval Ordnance Laboratory (White Oak, Md.))), U.S. Dept. of Commerce, Office of Technical Services, 1947.

[128] A. Einstein, "Strahlungsemission und -absorption nach der quantentheorie," *Deutsche Physikalische Gesellschaft*, vol. 18, 1916.

[129] A. Einstein, "Zur quantentheorie der strahlung," *Physikalische Gesellschaft Zürich*, vol. 18, 1916.

[130] H. Kreuzer and I. Tamblyn, *Thermodynamics*. World Scientific, 2010.

[131] G. Plunien, B. Müller, and W. Greiner, "The casimir effect," *Physics Reports*, vol. 134, no. 2, pp. 87–193, 1986.

[132] R. Loudon, *The Quantum Theory of Light*. Oxford University Press, 2000.

[133] J. Orear and E. Fermi, *Nuclear physics: a course given by Enrico Fermi at the University of Chicago*. University of Chicago Press, 1950.

[134] V. Weisskopf and E. Wigner, "Berechnung der natürlichen Linienbreite auf Grund der Diracschen Lichttheorie," *Zeitschrift für Physik*, vol. 63, no. 1-2, pp. 54–73, 1930.

[135] D. Van Oosten, P. Van der Straten, and H. Stoof, "Quantum phases in an optical lattice," *Physical Review A*, vol. 63, no. 5, p. 053601, 2001.

[136] R. Lehmberg, "Radiation from an n-atom system. i. general formalism," *Physical Review A*, vol. 2, no. 3, p. 883, 1970.

[137] R. Lehmberg, "Radiation from an n-atom system. ii. spontaneous emission from a pair of atoms," *Physical Review A*, vol. 2, no. 3, p. 889, 1970.

[138] Z. Ficek and R. Tanaś, "Entangled states and collective nonclassical effects in two-atom systems," *Physics Reports*, vol. 372, no. 5, pp. 369–443, 2002.

[139] C. Gardiner and P. Zoller, *Quantum Noise: A Handbook of Markovian and Non-Markovian Quantum Stochastic Methods with Applications to Quantum Optics*. Springer Series in Synergetics, Springer, 2004.

[140] R. H. Dicke, "Coherence in spontaneous radiation processes," *Physical Review*, vol. 93, no. 1, p. 99, 1954.

[141] Y. V. Sokhotski, "On definite integrals and functions employed in expansions into series." Sokhotski, 1873.

[142] J. Plemelj, *Problems in the sense of Riemann and Klein*, vol. 16. John Wiley & Sons, 1964.

[143] S. Weinberg, *The Quantum Theory of Fields*. No. Bd. 1 in The Quantum Theory of Fields 3 Volume Hardback Set, Cambridge University Press, 1995.

[144] L. Ostermann, H. Zoubi, and H. Ritsch, "Cascaded collective decay in regular arrays of cold trapped atoms," *Optics Express*, vol. 20, no. 28, pp. 29634–29645,

2012.

[145] R. H. Dicke, "Coherence in Spontaneous Radiation Processes," *Physical Review*, vol. 93, pp. 99–110, Jan 1954.

[146] J. MacGillivray and M. Feld, "Theory of superradiance in an extended, optically thick medium," *Physical Review A*, vol. 14, no. 3, p. 1169, 1976.

[147] M. Gross and S. Haroche, "Superradiance: An essay on the theory of collective spontaneous emission," *Physics Reports*, vol. 93, no. 5, pp. 301–396, 1982.

[148] N. Skribanowitz, I. P. Herman, J. C. MacGillivray, and M. S. Feld, "Observation of Dicke Superradiance in Optically Pumped HF Gas," *Physical Review Letters*, vol. 30, pp. 309–312, Feb 1973.

[149] S. Inouye, A. Chikkatur, D. Stamper-Kurn, J. Stenger, D. Pritchard, and W. Ketterle, "Superradiant rayleigh scattering from a bose-einstein condensate," *Science*, vol. 285, no. 5427, pp. 571–574, 1999.

[150] M. Moore and P. Meystre, "Theory of superradiant scattering of laser light from Bose-Einstein condensates," *Physical Review Letters*, vol. 83, no. 25, pp. 5202–5205, 1999.

[151] R. Bonifacio, P. Schwendimann, and F. Haake, "Quantum statistical theory of superradiance. I," *Physical Review A*, vol. 4, no. 1, p. 302, 1971.

[152] N. E. Rehler and J. H. Eberly, "Superradiance," *Physical Review A*, vol. 3, pp. 1735–1751, May 1971.

[153] A. Davydov and S. Dresner, *Theory of molecular excitons*, vol. 1. Plenum Press New York, 1971.

[154] V. Agranovich, *Excitations in organic solids*, vol. 142. Oxford University Press, 2009.

[155] H. Zoubi and H. Ritsch, "Lifetime and emission characteristics of collective electronic excitations in two-dimensional optical lattices," *Physical Review A*, vol. 83, no. 063831, 2011.

[156] H. Zoubi and H. Ritsch, "Metastability and directional emission characteristics of excitons in 1D optical lattices," *Europhysics Letters*, vol. 90, no. 2, p. 23001, 2010.

[157] I. Carusotto, M. Antezza, F. Bariani, S. De Liberato, and C. Ciuti, "Optical properties of atomic Mott insulators: From slow light to dynamical Casimir effects," *Physical Review A*, vol. 77, no. 6, p. 063621, 2008.

[158] L. Casperson, "Spectral narrowing in double-pass superradiant lasers," *Optics Communications*, vol. 8, no. 1, pp. 85–87, 1973.

[159] J. G. Bohnet, Z. Chen, J. M. Weiner, D. Meiser, M. J. Holland, and J. K. Thompson, "A steady-state superradiant laser with less than one intracavity photon," *Nature*, vol. 484, no. 7392, pp. 78–81, 2012.

[160] K. Henschel, J. Majer, J. Schmiedmayer, and H. Ritsch, "Cavity QED with an ultracold ensemble on a chip: Prospects for strong magnetic coupling at finite temperatures," *Physical Review A*, vol. 82, no. 3, p. 033810, 2010.

[161] J. Guo and J. Cooper, "Cooling and resonance fluorescence of two atoms in a one-dimensional optical molasses," *Physical Review A*, vol. 51, no. 4, pp. 3128–3135, 1995.

[162] Z. Ficek, R. Tanaś, and S. Kielich, "Quantum beats and superradiant effects in the spontaneous emission from two nonidentical atoms," *Physica A: Statistical Mechanics and its Applications*, vol. 146, no. 3, pp. 452–482, 1987.

[163] H. Zoubi, "Collective Light Emission of a Finite Size Atomic Chain," *arXiv preprint arXiv:1203.2094*, 2012.

[164] M. Takamoto and H. Katori, "Spectroscopy of the $^1s_0 \rightarrow ^3 p_0$ clock transition of ^{87}Sr in an optical lattice," *Physical Review Letters*, vol. 91, no. 22, p. 223001, 2003.

[165] I. Bloch, "Ultracold quantum gases in optical lattices," *Nature Physics*, vol. 1, no. 1, p. 23, 2005.

[166] G. K. Campbell, A. D. Ludlow, S. Blatt, J. W. Thomsen, M. J. Martin, M. H. de Miranda, T. Zelevinsky, M. M. Boyd, J. Ye, S. A. Diddams, *et al.*, "The absolute frequency of the ^{87}Sr optical clock transition," *Metrologia*, vol. 45, no. 5, p. 539, 2008.

[167] P. Horak, K. Gheri, and H. Ritsch, "Quantum dynamics of a single-atom cascade laser," *Physical Review A*, vol. 51, no. 4, p. 3257, 1995.

[168] G. Lin and S. Yelin, "Superradiance in spin-j particles: Effects of multiple levels," *Physical Review A*, vol. 85, no. 3, p. 033831, 2012.

[169] L. Ostermann, H. Ritsch, and C. Genes, "Protected state enhanced quantum metrology," *Physical Review Letters*, vol. 111, p. 123601, 2013.

[170] C. Oates, "Optical lattice clocks," *Bulletin of the American Physical Society*, vol. 57, 2012.

[171] P. Lemonde, "Optical lattice clocks," *The European Physical Journal Special Topics*, vol. 172, no. 1, p. 81, 2009.

[172] D. Oblak, P. G. Petrov, C. L. Alzar, *et al.*, "Quantum-noise-limited interferometric measurement of atomic noise: Towards spin squeezing on the cs clock transition," *Physical Review A*, vol. 71, no. 4, p. 043807, 2005.

[173] D. Wineland, J. Bollinger, W. Itano, F. Moore, and D. Heinzen, "Spin squeezing and reduced quantum noise in spectroscopy," *Physical Review A*, vol. 46, no. 11, p. R6797, 1992.

[174] D. Meiser, J. Ye, and M. J. Holland, "Spin squeezing in optical lattice clocks via lattice-based QND measurements," *New Journal of Physics*, vol. 10, no. 7,

p. 073014, 2008.

[175] I. Leroux, M. Schleier-Smith, and V. Vuletić, "Focus: Atomic clock beats the quantum limit," *Physical Review Focus*, vol. 25, p. 24, 2010.

[176] I. Leroux, M. Schleier-Smith, and V. Vuletić, "Orientation-dependent entanglement lifetime in a squeezed atomic clock," *Physical Review Letters*, vol. 104, no. 25, p. 250801, 2010.

[177] A. Louchet-Chauvet, J. Appel, J. J. Renema, D. Oblak, N. Kjaergaard, and E. S. Polzik, "Entanglement-assisted atomic clock beyond the projection noise limit," *New Journal of Physics*, vol. 12, no. 6, p. 065032, 2010.

[178] J. Borregaard and A. S. Sørensen, "Near heisenberg limited atomic clocks in the presence of decoherence," *arXiv preprint arXiv:1304.2288*, 2013.

[179] H. Zoubi and H. Ritsch, "Excitons and cavity optical lattice ultracold atoms," *Advances in Atomic, Molecular, and Optical Physics*, vol. 62, p. 171, 2013.

[180] M. Takamoto and H. Katori, "Spectroscopy of the s 0 1- p 0 3 clock transition of s r 87 in an optical lattice," *Physical review letters*, vol. 91, no. 22, p. 223001, 2003.

[181] D. Meiser and M. Holland, "Steady-state superradiance with alkaline-earth-metal atoms," *Physical Review A*, vol. 81, no. 3, p. 033847, 2010.

[182] A. Wallraff, "Private communication," 2013.

[183] K. Lalumière, A. Blais, B. Sanders, A. van Loo, A. Fedorov, and A. Wallraff, "Cooperative effects for qubits in a transmission line: Theory," in *APS Meeting Abstracts*, vol. 1, p. 29004, 2012.

[184] K. Lalumière, B. C. Sanders, A. F. van Loo, A. Fedorov, A. Wallraff, and A. Blais, "Input-output theory for waveguide QED with an ensemble of inhomogeneous atoms," *Physical Review A*, vol. 88, p. 043806, 2013.

[185] U. Dorner, "Noise-assisted ramsey interferometry," *Physical Review A*, vol. 88, p. 062113, 2013.

[186] J. R. Johansson, P. D. Nation, and F. Nori, "Qutip framework," *Computer Physics Communications*, vol. 184, p. 1234, 2013.

[187] L. Ostermann, D. Plankensteiner, H. Ritsch, and C. Genes, "Protected subspace Ramsey spectroscopy," *Physical Review A*, vol. 90, p. 053823, 2014.

[188] D. Akamatsu *et al.*, "Spectroscopy and frequency measurement of the ^{87}Sr clock transition by laser linewidth transfer using an optical frequency comb," *Applied Physics Express*, vol. 7, no. 1, p. 012401, 2014.

[189] A. M. Rey *et al.*, "Probing many-body interactions in an optical lattice clock," *Annals of Physics*, vol. 340, pp. 311–351, 2014.

[190] T. Maier, S. Krämer, L. Ostermann, and H. Ritsch, "A superradiant clock laser

on a magic wavelength optical lattice," *Optics Express*, vol. 22, pp. 13269–13279, 2014.

[191] N. Poli, C. W. Oates, P. Gill, and G. M. Tino, "Optical atomic clocks," *arXiv preprint arXiv:1401.2378*, 2014.

[192] M. Xu and M. J. Holland, "Conditional ramsey spectroscopy with synchronized atoms," *arXiv preprint arXiv:1407.5132*, 2014.

[193] L. Zhang, A. Datta, and I. A. Walmsley, "Precision metrology using weak measurements," *arXiv preprint arXiv:1310.5302*, 2014.

[194] W. Dür, M. Skotiniotis, F. Fröwis, and B. Kraus, "Improved quantum metrology using quantum error correction," *Physical Review Letters*, vol. 112, p. 080801, 2014.

[195] Z. Zhang and L. Duan, "Quantum metrology with dicke squeezed states," *arXiv preprint arXiv:1406.7626*, 2014.

[196] D.-W. Wang and M. O. Scully, "Heisenberg limit superradiant super-resolving metrology," *arXiv preprint arXiv:1403.3647*, 2014.

[197] H. Zoubi and H. Ritsch, "Hybrid quantum system of a nanofiber mode coupled to two chains of optically trapped atoms," *New Journal of Physics*, vol. 12, no. 10, p. 103014, 2010.

[198] K. Sandner, H. Ritsch, R. Amsüss, C. Koller, T. Nöbauer, S. Putz, J. Schmiedmayer, and J. Majer, "Strong magnetic coupling of an inhomogeneous nitrogen-vacancy ensemble to a cavity," *Physical Review A*, vol. 85, no. 5, p. 053806, 2012.

[199] J. Mlynek, A. Abdumalikov Jr, C. Eichler, and A. Wallraff, "Observation of superradiance in a small ensemble of artificial atoms," *Bulletin of the American Physical Society*, vol. 59, 2014.

[200] D. Plankensteiner, L. Ostermann, H. Ritsch, and C. Genes, "Selective protected state preparation of coupled dissipative quantum emitters," *Scientific Reports*, vol. 5, 2015.

[201] M. Lukin, "Colloquium: Trapping and manipulating photon states in atomic ensembles," *Reviews of Modern Physics*, vol. 75, no. 2, p. 457, 2003.

[202] M. Lukin, M. Fleischhauer, R. Cote, L. Duan, D. Jaksch, J. Cirac, and P. Zoller, "Dipole blockade and quantum information processing in mesoscopic atomic ensembles," *Physical Review Letters*, vol. 87, no. 3, p. 037901, 2001.

[203] K. Hammerer, A. Sørensen, and E. Polzik, "Quantum interface between light and atomic ensembles," *Reviews of Modern Physics*, vol. 82, no. 2, p. 1041, 2010.

[204] N. Sangouard, C. Simon, H. De Riedmatten, and N. Gisin, "Quantum repeaters based on atomic ensembles and linear optics," *Reviews of Modern Physics*, vol. 83, no. 1, p. 33, 2011.

[205] E. Davies, *Quantum theory of open systems*. Academic Press, 1976.

[206] K. Gheri, W. Alge, and P. Grangier, "Quantum analysis of the photonic blockade mechanism," *Physical Review A*, vol. 60, no. 4, p. R2673, 1999.

[207] H. Freedhoff, "Collective atomic effects in resonance fluorescence: Dipole-dipole interaction," *Physical Review A*, vol. 19, no. 3, p. 1132, 1979.

[208] B. Zhu, J. Restrepo, A. Rey, and M. Holland, "Quantum synchronization of ultracold atoms with dipole-dipole interactions in an optical lattice," *Bulletin of the American Physical Society*, vol. 59, 2014.

[209] H. Zoubi and H. Ritsch, "Bright and dark excitons in an atom-pair–filled optical lattice within a cavity," *EPL*, vol. 82, no. 1, p. 14001, 2008.

[210] H. Zoubi and H. Ritsch, "Optical properties of collective excitations for an atomic chain with vacancies," *The European Physical Journal D*, vol. 66, no. 11, p. 292, 2012.

[211] A. Böttcher and B. Silbermann, *Introduction to large truncated Toeplitz matrices*. Springer Science & Business Media, 2012.

[212] I. Ushijima, M. Takamoto, M. Das, T. Ohkubo, and H. Katori, "Cryogenic optical lattice clocks," *Nature Photonics*, vol. 9, no. 3, p. 185, 2015.

[213] A. Sørensen and K. Mølmer, "Entanglement and extreme spin squeezing," *Physical Review Letters*, vol. 86, no. 20, p. 4431, 2001.

[214] F. Haas, J. Volz, *et al.*, "Entangled states of more than 40 atoms in an optical fiber cavity," *Science*, vol. 344, no. 6180, p. 180, 2014.

[215] R. McConnell, H. Zhang, *et al.*, "Entanglement with negative Wigner function of almost 3,000 atoms heralded by one photon," *Nature*, vol. 519, no. 7544, p. 439, 2015.

[216] B. Olmos, D. Yu, Y. Singh, F. Schreck, K. Bongs, and I. Lesanovsky, "Long-range interacting many-body systems with alkaline-earth-metal atoms," *Physical Review Letters*, vol. 110, no. 14, p. 143602, 2013.

[217] B. Ueberholz, S. Kuhr, D. Frese, V. Gomer, and D. Meschede, "Cold collisions in a high-gradient magneto-optical trap," *Journal of Physics B*, vol. 35, no. 23, p. 4899, 2002.

[218] S. Yoon, Y. Choi, S. Park, W. Ji, J.-H. Lee, and K. An, "Characteristics of single-atom trapping in a magneto-optical trap with a high magnetic-field gradient," in *Journal of Physics: Conference Series*, vol. 80, p. 012046, IOP Publishing, 2007.

[219] B. Yan, S. A. Moses, B. Gadway, J. P. Covey, K. R. Hazzard, A. M. Rey, D. S. Jin, and J. Ye, "Observation of dipolar spin-exchange interactions with lattice-confined polar molecules," *Nature*, vol. 501, no. 7468, pp. 521–525, 2013.

[220] P. Neumann, R. Kolesov, B. Naydenov, J. Beck, F. Rempp, M. Steiner, V. Jacques, G. Balasubramanian, M. Markham, D. Twitchen, *et al.*, "Quantum

register based on coupled electron spins in a room-temperature solid," *Nature Physics*, vol. 6, no. 4, pp. 249–253, 2010.

[221] J. Johansson, P. Nation, and F. Nori, "Qutip 2: A Python framework for the dynamics of open quantum systems," *Computer Physics Communications*, vol. 184, no. 4, p. 1234, 2013.

[222] T. Kessler, C. Hagemann, C. Grebing, T. Legero, U. Sterr, F. Riehle, M. Martin, L. Chen, and J. Ye, "A sub-40-mHz-linewidth laser based on a silicon single-crystal optical cavity," *Nature Photonics*, vol. 6, no. 10, pp. 687–692, 2012.

[223] D. Meiser, J. Ye, D. Carlson, and M. Holland, "Prospects for a millihertz-linewidth laser," *Physical Review Letters*, vol. 102, no. 16, p. 163601, 2009.

[224] J. G. Bohnet, Z. Chen, J. M. Weiner, K. C. Cox, and J. K. Thompson, "Active and passive sensing of collective atomic coherence in a superradiant laser," *Physical Review A*, vol. 88, no. 1, p. 013826, 2013.

[225] V. Vuletic, "Atomic physics: An almost lightless laser," *Nature*, vol. 484, no. 7392, pp. 43–44, 2012.

[226] M. Xu, D. Tieri, and M. Holland, "Simulating Open Quantum Systems using the Simple Lie Group SU (4)," *arXiv preprint arXiv:1302.6284*, 2013.

[227] F. Haake, M. I. Kolobov, C. Fabre, E. Giacobino, and S. Reynaud, "Superradiant laser," *Physical Review Letters*, vol. 71, no. 7, p. 995, 1993.

[228] H. Zoubi, "Collective light emission of a finite-size atomic chain," *Europhysics Letters*, vol. 100, no. 2, p. 24002, 2012.

[229] P. Meystre and M. Sargent, *Elements of Quantum Optics*. Springer-Verlag, 1990.

[230] S. Krämer, L. Ostermann, and H. Ritsch, "Optimized geometries for future generation optical lattice clocks," *Europhysics Letters*, vol. 114, no. 1, p. 14003, 2016.

[231] I. Bloch, J. Dalibard, and S. Nascimbène, "Quantum simulations with ultracold quantum gases," *Nature Physics*, vol. 8, no. 4, pp. 267–276, 2012.

[232] M. Lewenstein, A. Sanpera, V. Ahufinger, B. Damski, A. Sen, and U. Sen, "Ultracold atomic gases in optical lattices: mimicking condensed matter physics and beyond," *Advances in Physics*, vol. 56, no. 2, pp. 243–379, 2007.

[233] A. Micheli, G. Brennen, and P. Zoller, "A toolbox for lattice-spin models with polar molecules," *Nature Physics*, vol. 2, no. 5, pp. 341–347, 2006.

[234] M. Greiner, O. Mandel, T. Esslinger, T. W. Hänsch, and I. Bloch, "Quantum phase transition from a superfluid to a mott insulator in a gas of ultracold atoms," *Nature*, vol. 415, no. 6867, pp. 39–44, 2002.

[235] W. S. Bakr, J. I. Gillen, A. Peng, S. Fölling, and M. Greiner, "A quantum gas microscope for detecting single atoms in a hubbard-regime optical lattice," *Nature*, vol. 462, no. 7269, pp. 74–77, 2009.

[236] C. Ospelkaus, S. Ospelkaus, L. Humbert, P. Ernst, K. Sengstock, and K. Bongs, "Ultracold heteronuclear molecules in a 3d optical lattice," *Physical Review Letters*, vol. 97, no. 12, p. 120402, 2006.

[237] L. D. Carr, D. DeMille, R. V. Krems, and J. Ye, "Cold and ultracold molecules: science, technology and applications," *New Journal of Physics*, vol. 11, no. 5, p. 055049, 2009.

[238] J. G. Danzl, M. J. Mark, E. Haller, M. Gustavsson, R. Hart, J. Aldegunde, J. M. Hutson, and H.-C. Nägerl, "An ultracold high-density sample of rovibronic ground-state molecules in an optical lattice," *Nature Physics*, vol. 6, no. 4, pp. 265–270, 2010.

[239] L.-M. Duan, E. Demler, and M. Lukin, "Controlling spin exchange interactions of ultracold atoms in optical lattices," *Physical Review Letters*, vol. 91, no. 9, p. 090402, 2003.

[240] M. Martin, M. Bishof, M. Swallows, X. Zhang, C. Benko, J. Von-Stecher, A. Gorshkov, A. Rey, and J. Ye, "A quantum many-body spin system in an optical lattice clock," *Science*, vol. 341, no. 6146, pp. 632–636, 2013.

[241] I. Ushijima, M. Takamoto, M. Das, T. Ohkubo, and H. Katori, "Cryogenic optical lattice clocks with a relative frequency difference of 1×10^{-18}," *arXiv preprint arXiv:1405.4071*, 2014.

[242] X. Zhang, M. Bishof, S. Bromley, C. Kraus, M. Safronova, P. Zoller, A. Rey, and J. Ye, "Spectroscopic observation of su (n)-symmetric interactions in sr orbital magnetism," *Science*, vol. 345, no. 6203, pp. 1467–1473, 2014.

[243] Z. Ficek, R. Tanas, and S. Kielich, "Cooperative effects in the spontaneous emission from two non-identical atoms," *Optica Acta*, vol. 33, no. 9, pp. 1149–1160, 1986.

[244] L. Pollet, J. Picon, H. Büchler, and M. Troyer, "Supersolid phase with cold polar molecules on a triangular lattice," *Physical Review Letters*, vol. 104, no. 12, p. 125302, 2010.

[245] S. L. Bromley, B. Zhu, M. Bishof, X. Zhang, T. Bothwell, J. Schachenmayer, T. L. Nicholson, R. Kaiser, S. F. Yelin, M. D. Lukin, *et al.*, "Collective atomic scattering and motional effects in a dense coherent medium," *arXiv preprint arXiv:1601.05322*, 2016.

[246] V. Yudin, A. Taichenachev, C. Oates, Z. Barber, N. Lemke, A. Ludlow, U. Sterr, C. Lisdat, and F. Riehle, "Hyper-ramsey spectroscopy of optical clock transitions," *Physical Review A*, vol. 82, no. 1, p. 011804, 2010.

[247] W. J. Meath, "Retarded interaction energies between like atoms in different energy states," *Journal of Chemical Physics*, vol. 48, pp. 227–235, 1968.

[248] C. Deutsch, F. Ramirez-Martinez, C. Lacroûte, F. Reinhard, T. Schneider, J.-N. Fuchs, F. Piéchon, F. Laloë, J. Reichel, and P. Rosenbusch, "Spin self-rephasing

and very long coherence times in a trapped atomic ensemble," *Physical Review Letters*, vol. 105, no. 2, p. 020401, 2010.

[249] M. Xu, D. Tieri, E. Fine, J. K. Thompson, and M. Holland, "Synchronization of two ensembles of atoms," *Physical Review Letters*, vol. 113, no. 15, p. 154101, 2014.

[250] S. Krämer and H. Ritsch, "Generalized mean-field approach to simulate large dissipative spin ensembles with long range interactions," *The European Physical Journal D*, 2015.

[251] R. J. Bettles, S. A. Gardiner, and C. S. Adams, "Cooperative ordering in lattices of interacting two-level dipoles," *arXiv preprint arXiv:1410.4776*, 2014.

[252] S. Krämer, L. Ostermann, and H. Ritsch, "Supplementary material," *arXiv preprint arXiv:1506.09079*, 2015.

[253] B. Olmos, R. González-Férez, and I. Lesanovsky, "Collective rydberg excitations of an atomic gas confined in a ring lattice," *Physical Review A*, vol. 79, no. 4, p. 043419, 2009.

[254] C. Menotti and H. Ritsch, "Mean-field approach to dipole-dipole interaction in an optical lattice," *Physical Review A*, vol. 60, no. 4, p. R2653, 1999.

[255] B. Olmos, R. González-Férez, and I. Lesanovsky, "Fermionic collective excitations in a lattice gas of rydberg atoms," *Physical Review Letters*, vol. 103, no. 18, p. 185302, 2009.

[256] T. Huber, L. Ostermann, M. Prilmüller, G. S. Solomon, H. Ritsch, G. Weihs, and A. Predojević, "Coherence and degree of time-bin entanglement from quantum dots," *Physical Review B*, vol. 93, p. 201301, May 2016.

[257] A. Predojević, M. Ježek, T. Huber, H. Jayakumar, T. Kauten, G. S. Solomon, R. Filip, and G. Weihs, "Efficiency vs. multi-photon contribution test for quantum dots," *Optics Express*, vol. 22, no. 4, pp. 4789–4798, 2014.

[258] S. Scheel, "Single-photon sources–an introduction," *Journal of Modern Optics*, vol. 56, no. 2-3, pp. 141–160, 2009.

[259] A. Aspect, J. Dalibard, and G. Roger, "Experimental test of bell's inequalities using time-varying analyzers," *Physical Review Letters*, vol. 49, no. 25, p. 1804, 1982.

[260] R. J. Young, R. M. Stevenson, P. Atkinson, K. Cooper, D. A. Ritchie, and A. J. Shields, "Improved fidelity of triggered entangled photons from single quantum dots," *New Journal of Physics*, vol. 8, no. 2, p. 29, 2006.

[261] A. Dousse, J. Suffczyński, A. Beveratos, O. Krebs, A. Lemaître, I. Sagnes, J. Bloch, P. Voisin, and P. Senellart, "Ultrabright source of entangled photon pairs," *Nature*, vol. 466, no. 7303, pp. 217–220, 2010.

[262] M. Ghali, K. Ohtani, Y. Ohno, and H. Ohno, "Generation and control of

polarization-entangled photons from gaas island quantum dots by an electric field," *Nature Communications*, vol. 3, p. 661, 2012.

[263] G. Juska, V. Dimastrodonato, L. O. Mereni, A. Gocalinska, and E. Pelucchi, "Towards quantum-dot arrays of entangled photon emitters," *Nature Photonics*, vol. 7, no. 7, pp. 527–531, 2013.

[264] R. Trotta, J. S. Wildmann, E. Zallo, O. G. Schmidt, and A. Rastelli, "Highly entangled photons from hybrid piezoelectric-semiconductor quantum dot devices," *Nano Letters*, vol. 14, no. 6, pp. 3439–3444, 2014.

[265] A. Muller, W. Fang, J. Lawall, and G. S. Solomon, "Creating polarization-entangled photon pairs from a semiconductor quantum dot using the optical stark effect," *Physical Review Letters*, vol. 103, no. 21, p. 217402, 2009.

[266] H.-J. Briegel, W. Dür, J. I. Cirac, and P. Zoller, "Quantum repeaters: The role of imperfect local operations in quantum communication," *Physical Review Letters*, vol. 81, no. 26, p. 5932, 1998.

[267] A. K. Ekert, "Quantum cryptography based on bell's theorem," *Physical Review Letters*, vol. 67, no. 6, p. 661, 1991.

[268] C. H. Bennett, G. Brassard, C. Crépeau, R. Jozsa, A. Peres, and W. K. Wootters, "Teleporting an unknown quantum state via dual classical and einstein-podolsky-rosen channels," *Physical Review Letters*, vol. 70, no. 13, p. 1895, 1993.

[269] M. Zukowski, A. Zeilinger, M. Horne, and A. Ekert, "Event-ready-detectors: Bell experiment via entanglement swapping," *Physical Review Letters*, vol. 71, no. 26, pp. 4287–4290, 1993.

[270] E. Knill, R. Laflamme, and G. J. Milburn, "A scheme for efficient quantum computation with linear optics," *Nature*, vol. 409, no. 6816, pp. 46–52, 2001.

[271] H. Jayakumar, A. Predojević, T. Kauten, T. Huber, G. S. Solomon, and G. Weihs, "Time-bin entangled photons from a quantum dot," *Nature Communications*, vol. 5, 2014.

[272] H. Jayakumar, A. Predojević, T. Huber, T. Kauten, G. S. Solomon, and G. Weihs, "Deterministic photon pairs and coherent optical control of a single quantum dot," *Physical Review Letters*, vol. 110, no. 13, p. 135505, 2013.

[273] M. Müller, S. Bounouar, K. D. Jöns, M. Glässl, and P. Michler, "On-demand generation of indistinguishable polarization-entangled photon pairs," *Nature Photonics*, vol. 8, no. 3, pp. 224–228, 2014.

[274] T. Honjo, H. Takesue, H. Kamada, Y. Nishida, O. Tadanaga, M. Asobe, and K. Inoue, "Long-distance distribution of time-bin entangled photon pairs over 100 km using frequency up-conversion detectors," *Optics Express*, vol. 15, no. 21, pp. 13957–13964, 2007.

[275] M. Brodsky, E. C. George, C. Antonelli, and M. Shtaif, "Loss of polarization entanglement in a fiber-optic system with polarization mode dispersion in one

optical path," *Optics Letters*, vol. 36, no. 1, pp. 43–45, 2011.

[276] P. C. Humphreys, B. J. Metcalf, J. B. Spring, M. Moore, X.-M. Jin, M. Barbieri, W. S. Kolthammer, and I. A. Walmsley, "Linear optical quantum computing in a single spatial mode," *Physical Review Letters*, vol. 111, no. 15, p. 150501, 2013.

[277] J. Brendel, N. Gisin, W. Tittel, and H. Zbinden, "Pulsed energy-time entangled twin-photon source for quantum communication," *Physical Review Letters*, vol. 82, no. 12, p. 2594, 1999.

[278] A. Muller, E. B. Flagg, P. Bianucci, X. Wang, D. G. Deppe, W. Ma, J. Zhang, G. Salamo, M. Xiao, and C.-K. Shih, "Resonance fluorescence from a coherently driven semiconductor quantum dot in a cavity," *Physical Review Letters*, vol. 99, no. 18, p. 187402, 2007.

[279] D. F. James, P. G. Kwiat, W. J. Munro, and A. G. White, "Measurement of qubits," *Physical Review A*, vol. 64, no. 5, p. 052312, 2001.

[280] H. Takesue and Y. Noguchi, "Implementation of quantum state tomography for time-bin entangled photon pairs," *Optics Express*, vol. 17, no. 13, pp. 10976–10989, 2009.

[281] C. Simon and J.-P. Poizat, "Creating single time-bin-entangled photon pairs," *Physical Review Letters*, vol. 94, no. 3, p. 030502, 2005.

[282] P. Pathak and S. Hughes, "Coherent generation of time-bin entangled photon pairs using the biexciton cascade and cavity-assisted piecewise adiabatic passage," *Physical Review B*, vol. 83, no. 24, p. 245301, 2011.

[283] P. B. Nisbet-Jones, J. Dilley, A. Holleczek, O. Barter, and A. Kuhn, "Photonic qubits, qutrits and ququads accurately prepared and delivered on demand," *New Journal of Physics*, vol. 15, no. 5, p. 053007, 2013.

[284] L. Monniello, C. Tonin, R. Hostein, A. Lemaitre, A. Martinez, V. Voliotis, and R. Grousson, "Excitation-induced dephasing in a resonantly driven inas/gaas quantum dot," *Physical Review Letters*, vol. 111, no. 2, p. 026403, 2013.

[285] M. Lermer, N. Gregersen, F. Dunzer, S. Reitzenstein, S. Höfling, J. Mørk, L. Worschech, M. Kamp, and A. Forchel, "Bloch-wave engineering of quantum dot micropillars for cavity quantum electrodynamics experiments," *Physical Review Letters*, vol. 108, no. 5, p. 057402, 2012.

[286] A. Kiraz, M. Atatüre, and A. Imamoğlu, "Quantum-dot single-photon sources: Prospects for applications in linear optics quantum-information processing," *Physical Review A*, vol. 69, no. 3, p. 032305, 2004.

List of Publications

Publications during PhD

- T. Huber, L. Ostermann, M. Prilmüller, G. S. Solomon, H. Ritsch, G. Weihs, and A. Predojević, "Coherence and degree of time-bin entanglement from quantum dots," *Physical Review B*, vol. 93, p. 201301, May 2016.
- S. Krämer, L. Ostermann, and H. Ritsch, "Optimized geometries for future generation optical lattice clocks," *Europhysics Letters*, vol. 114, no. 1, p. 14003, 2016.
- D. Plankensteiner, L. Ostermann, H. Ritsch, and C. Genes, "Selective protected state preparation of coupled dissipative quantum emitters," *Scientific Reports*, vol. 5, 2015.
- L. Ostermann, D. Plankensteiner, H. Ritsch, and C. Genes, "Protected subspace Ramsey spectroscopy," *Physical Review A*, vol. 90, p. 053823, 2014.
- T. Maier, S. Krämer, L. Ostermann, and H. Ritsch, "A superradiant clock laser on a magic wavelength optical lattice," *Optics Express*, vol. 22,pp. 13269–13279, 2014.
- L. Ostermann, H. Ritsch, and C. Genes, "Protected state enhanced quantum metrology," *Physical Review Letters*, vol. 111, p. 123601, 2013.
- L. Ostermann, H. Zoubi, and H. Ritsch, "Cascaded collective decay in regular arrays of cold trapped atoms," *Optics Express*, vol. 20, no. 28, pp. 29634–29645, 2012.

Publications before PhD

- G. Grübl, and L. Ostermann, "Reaching Fleming's discrimination bound," *arXiv preprint arXiv:1204.2998*, 2012.
- L. Ostermann, "Fleming's Quantum-Master-Inequality in Spin-1/2-Systems," *Diploma Theses*, Universität Innsbruck, 2010.